

INFORMATION TO USERS

This manuscript has been reproduced from the microfilm master. UMI films the text directly from the original or copy submitted. Thus, some thesis and dissertation copies are in typewriter face, while others may be from any type of computer printer.

The quality of this reproduction is dependent upon the quality of the copy submitted. Broken or indistinct print, colored or poor quality illustrations and photographs, print bleedthrough, substandard margins, and improper alignment can adversely affect reproduction.

In the unlikely event that the author did not send UMI a complete manuscript and there are missing pages, these will be noted. Also, if unauthorized copyright material had to be removed, a note will indicate the deletion.

Oversize materials (e.g., maps, drawings, charts) are reproduced by sectioning the original, beginning at the upper left-hand corner and continuing from left to right in equal sections with small overlaps.

Photographs included in the original manuscript have been reproduced xerographically in this copy. Higher quality 6" x 9" black and white photographic prints are available for any photographs or illustrations appearing in this copy for an additional charge. Contact UMI directly to order.

ProQuest Information and Learning
300 North Zeeb Road, Ann Arbor, MI 48106-1346 USA
800-521-0600

UMI[®]

University of Alberta

New Ternary Pnictides at the Zintl Border

by

Robert Lam



A thesis submitted to the Faculty of Graduate Studies and Research in partial fulfillment
of the requirements for the degree of Doctor of Philosophy

Department of Chemistry

Edmonton, Alberta

Fall 2000



National Library
of Canada

Acquisitions and
Bibliographic Services

395 Wellington Street
Ottawa ON K1A 0N4
Canada

Bibliothèque nationale
du Canada

Acquisitions et
services bibliographiques

395, rue Wellington
Ottawa ON K1A 0N4
Canada

Your file Votre référence

Our file Notre référence

The author has granted a non-exclusive licence allowing the National Library of Canada to reproduce, loan, distribute or sell copies of this thesis in microform, paper or electronic formats.

The author retains ownership of the copyright in this thesis. Neither the thesis nor substantial extracts from it may be printed or otherwise reproduced without the author's permission.

L'auteur a accordé une licence non exclusive permettant à la Bibliothèque nationale du Canada de reproduire, prêter, distribuer ou vendre des copies de cette thèse sous la forme de microfiche/film, de reproduction sur papier ou sur format électronique.

L'auteur conserve la propriété du droit d'auteur qui protège cette thèse. Ni la thèse ni des extraits substantiels de celle-ci ne doivent être imprimés ou autrement reproduits sans son autorisation.

0-612-59618-4

Canada

University of Alberta

Library Release Form

Name of Author: Robert Lam

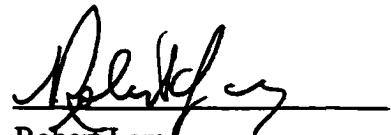
Title of Thesis: New Ternary Pnictides at the Zintl Border

Degree: Doctor of Philosophy

Year this Degree Granted: 2000

Permission is hereby granted to the University of Alberta Library to reproduce single copies of this thesis and to lend or sell such copies for private, scholarly or scientific research purposes only.

The author reserves all other publication and other rights in association with the copyright in the thesis, and except as herein before provided, neither the thesis nor any substantial portion thereof may be printed or otherwise reproduced in any material form whatever without the author's prior written permission.


Robert Lam
12206 - 92 Street
Edmonton, Alberta
T5G 1B3

Aug. 28, 2000

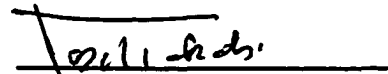
University of Alberta

Faculty of Graduate Studies and Research

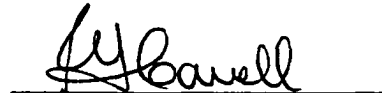
The undersigned certify that they have read, and recommend to the Faculty of Graduate Studies and Research for acceptance, a thesis entitled *New Ternary Pnictides at the Zintl Border* submitted by Robert Lam in partial fulfillment of the requirements for the degree of Doctor of Philosophy.



Prof. A. Mar



Prof. J. Takats



Prof. R. G. Cavell



Prof. N. Branda



Prof. F. Marsiglio



Prof. T. Hughbanks

Aug. 23, 2000

ABSTRACT

Increased interest in non-oxides, particularly those containing heavier main-group elements, derives from the lack of understanding of and the need to systematize their structures and properties. A series of new compounds containing a combination of electropositive and electronegative elements has been synthesized through reaction of the elements, and their structures have been determined by single-crystal X-ray diffraction methods. These polar intermetallic compounds provide a unique opportunity for studying bonding between main-group atoms as well as testing the validity of the Zintl concept.

The compounds EuSn_3Sb_4 and $\text{Ba}_2\text{Sn}_3\text{Sb}_6$ crystallize with new structure types characterized by three-dimensional channels constructed from shared tetrahedra, trigonal pyramids, and zigzag chains. Cation size has been found to be a structure-influencing factor in this series. The arsenide $\text{Ba}_3\text{Sn}_4\text{As}_6$ represents an intermediate structure type between the hypothetical limiting structures “ $\text{Ba}_4\text{Sn}_2\text{As}_6$,” containing one-dimensional corner-sharing chains of Sn-centered tetrahedra and “ $\text{Ba}_2\text{Sn}_6\text{As}_6$,” featuring two-dimensional corrugated layers with pentagonal channels. The structures of these weakly metallic compounds can be rationalized using the Zintl concept.

The nonstoichiometric arsenide $\text{Ba}_{0.8}\text{Hf}_{12}\text{As}_{17.7}$ adopts a structure that is a variant of the Cr_{12}P_7 structure type containing six-atom wide ribbons of As atoms inserted between assemblies of As-centered trigonal prismatic columns of Hf atoms. Electronic band structure calculations confirm the metallic behavior observed in the resistivity measurements. The structures of the weakly metallic antimonides $\text{RE}_6\text{Ge}_{5-x}\text{Sb}_{11+x}$ ($\text{RE} = \text{La-Nd, Sm, Gd-Dy}$) feature columns of Sb-centered face-sharing RE_6 trigonal prisms, separated by interconnecting walls of Ge and Sb atoms. A wide array of Ge-Ge, Ge-Sb,

and Sb–Sb interactions is found within these walls, ranging from strong covalent bonds, to intermediate one-electron partial bonds, to weak van der Waals forces. $\text{ZrSi}_{0.7}\text{Sb}_{1.3}$ and ZrGeSb represent new members, having one of the lowest total valence electron counts, of the large class of compounds that adopt the ZrSiS -type structure containing stacked square nets. Owing to the larger size of tin, the compound $\text{ZrSn}_{0.4}\text{Sb}_{1.6}$ adopts a slightly different structure that is a disordered variant of the known binary compound $\beta\text{-ZrSb}_2$. The Zintl concept is not applicable for the compounds in this second group.

To my parents

ACKNOWLEDGMENTS

I wish to thank my supervisor and mentor, Professor A. “3-D Eyes” Mar, for his patience and support during the five years it took to produce this thesis. I am also grateful for his willingness to share with me his endless knowledge on (and enthusiasm for) crystal structures and above all, for showing me that there is great beauty beyond the carbon horizon. Furthermore, his meticulous attention to detail and impeccable writing style are truly inspirational. I credit my ability to *read*, *write*, and *speak* more effectively upon completion of this degree to my supervisor’s influence. Future members will benefit greatly from the high standards already set by Professor Mar.

I have been fortunate to have had the opportunity to work alongside talented colleagues who have also become my friends. I wish to extend my gratitude towards the following members and alumni of the Mar group (in alphabetical order): E. J. “Helium” Anderson, G. “Monsieur Sure” Bolloré, D. T. “Chili D” Chow, Dr. L. “Madame Magneto” Deakin, R. E. “Christmas Time” Ellenwood, J. “Mysterio” Eulert, Dr. M. J. “Java Beans” Ferguson, R. W. “Plate Tectonics” Hushagen, A. M. “Peanut Butter” Mills, D. “Ubu’s Heated Centrifuge” Moore, M. J. “Penn State” Sprague, M. “Brontosaurus Ribs” Wang, and Dr. J. “Eyes of Steel” Zhang. I appreciate their support, encouragement, and numerous insightful discussions.

Also, I wish to thank the following individuals who have enriched my graduate school experience and earned my respect. Professor J. Takats for his friendship and wisdom. Professor M. Cowie (and Professor Mar) for setting up the Crystallographer’s Assistant position for me. Professor R. G. Cavell for agreeing to serve on my Ph.D. Committee on such short notice. Professor N. Branda for his kind words and support.

Professor P.-N. Roy for his contagious enthusiasm. Dr. J. Cooke for being an awesome laboratory coordinator and good friend. J. Jorgensen for her relentlessly cheerful, caring and thoughtful ways. J. Loiselle and R. Benson for being so nice and helpful. P. Tiege for his friendship. Q. Major for being himself. S. Trepanier for his sense of humour. Dr. D. S. A. George and C. Leong for providing additional moral support during Ph.D. Defense week. And finally, all my students for their making teaching fun.

This work was supported by the Natural Sciences and Engineering Research Council (NSERC) of Canada and the University of Alberta. I am grateful to the following individuals for their valuable contributions to this project. Dr. R. McDonald (Faculty Service Officer, Structure Determination Laboratory) for the X-ray data collection as well as taking me under his wing during my brief stay in the SDL as his assistant. H. W. Tan and Professor J. Beamish (Department of Physics) for access to the resistivity measurement facility and assistance with some of the measurements. Christina Barker (Department of Chemical and Materials Engineering) for assistance with the EDX analyses but also for entertaining conversations. Professor J. A. Ibers (Department of Chemistry, Northwestern University) and Professor F. W. B. Einstein (Department of Chemistry, Simon Fraser University) for helpful discussions on the structure determination of $Ba_3Sn_4As_6$ and $RE_6Ge_{5-x}Sb_{11+x}$ ($RE = La-Nd, Sm, Gd-Dy$), respectively.

Finally, I must thank my family for their support. C. A. Bridges for encouragement. And D. T. Chow for reminding me to smile and believing in me from the beginning.

– R. Lam (August, 2000)

TABLE OF CONTENTS

Chapter 1: Introduction	1
Solid State Chemistry	1
The Zintl Concept: Structure and Bonding	5
Methods of Procedure	11
Synthesis	11
Characterization	15
Physical Properties	16
References	25
Chapter 2: Synthesis and Structure of Ba₂Sn₃Sb₆, a Zintl Phase Containing Channels and Chains	28
Introduction	28
Experimental Section	29
Synthesis	29
Structure Determination	30
Results and Discussion	32
Description of the Structure	32
Structural Relationships and Bonding	34
References	45

Chapter 3: Ternary Antimonide EuSn_3Sb_4 and Related Metallic Zintl Phases	49
Introduction	49
Experimental Section	50
Synthesis	50
Structure Determination	51
Electrical Resistivity	52
Band Structure	52
Results and Discussion	53
Description of the Structure	53
Resistivity	54
Band Structure	54
References	70
Chapter 4: Synthesis and Structure of the Metallic Zintl Phase $\text{Ba}_3\text{Sn}_4\text{As}_6$	72
Introduction	72
Experimental Section	74
Synthesis	74
Structure Determination	75
Electrical Resistivity	78
Results and Discussion	79
Description of the Structure	79
Electrical Resistivity	83
Structural Relationships	84
References	99
Chapter 5: The Ternary Arsenide $\text{Ba}_{0.8}\text{Hf}_{12}\text{As}_{17.7}$, a Variant of the Cr_{12}P_7 Structure Type with Inserted Arsenic Ribbons	102
Introduction	102

Experimental Section	103
Synthesis	103
Structure Determination	104
Electrical Resistivity	105
Band Structure	105
Results and Discussion	106
Description of the Structure	106
Structural Relationships	108
Electrical Resistivity	109
Bonding	109
References	126
Chapter 6: Rare-Earth Germanium Antimonides $RE_6Ge_{5-x}Sb_{11+x}$ ($RE = La-Nd,$	
 Sm, Gd-Dy): Syntheses and Structures	129
Introduction	129
Experimental Section	131
Synthesis	131
Structure Determination	132
Transport Measurements	137
Results and Discussion	137
Trends	137
Description of the Structures	138
Structural Relationships	144
Transport Properties	145
References	167

Chapter 7: New Ternary Zirconium Antimonides: $ZrSi_{0.7}Sb_{1.3}$, $ZrGeSb$, and $ZrSn_{0.4}Sb_{1.6}$. A Family Containing ZrSiS-Type and β-ZrSb₂-Type Compounds	171
Introduction	171
Experimental Section	173
Synthesis	173
Structure Determination	175
Results and Discussion	178
Synthesis	178
Structure of $ZrSi_{0.7}Sb_{1.3}$ and $ZrGeSb$	179
Structure of $ZrSn_{0.4}Sb_{1.6}$	182
Implications	184
References	197
Chapter 8: Conclusion	200
Structural Diversity	200
Limits of Zintl Concept	202
Future Directions	204
References	207
Appendix	208

LIST OF TABLES

Table 1–1. Common Geometries of Sb Anionic Networks in Selected Zintl Compounds	20
Table 2–1. Crystallographic Data for $\text{Ba}_2\text{Sn}_3\text{Sb}_6$	38
Table 2–2. Atomic Coordinates, Occupancies, and Equivalent Isotropic Displacement Parameters (\AA^2) for $\text{Ba}_2\text{Sn}_3\text{Sb}_6$	40
Table 2–3. Selected Interatomic Distances (\AA) and Angles ($^\circ$) for $\text{Ba}_2\text{Sn}_3\text{Sb}_6$	41
Table 3–1. Crystallographic Data for EuSn_3Sb_4	58
Table 3–2. Atomic Coordinates, Occupancies, and Equivalent Isotropic Displacement Parameters (\AA^2) for EuSn_3Sb_4	60
Table 3–3. Selected Interatomic Distances (\AA) and Angles ($^\circ$) for EuSn_3Sb_4	61
Table 3–4. Comparison of Distances (\AA) and Angles ($^\circ$) in SnSb_4 Tetrahedra, SnSb_3 Trigonal Pyramids, and Sb–Sb Zigzag Chains in $A\text{Sn}_3\text{Sb}_4$ ($A = \text{Eu, Sr}$) and $\text{Ba}_2\text{Sn}_3\text{Sb}_6$	62
Table 4–1. Crystallographic Data for $\text{Ba}_3\text{Sn}_4\text{As}_6$	87
Table 4–2. Atomic Coordinates, Occupancies, and Equivalent Isotropic Displacement Parameters (\AA^2) for $\text{Ba}_3\text{Sn}_4\text{As}_6$	89
Table 4–3. Selected Interatomic Distances (\AA) and Angles ($^\circ$) for $\text{Ba}_3\text{Sn}_4\text{As}_6$	90
Table 5–1. Crystallographic Data for $\text{Ba}_{0.8}\text{Hf}_{12}\text{As}_{17.7}$	112
Table 5–2. Atomic Coordinates, Occupancies, and Equivalent Isotropic Displacement Parameters (\AA^2) for $\text{Ba}_{0.8}\text{Hf}_{12}\text{As}_{17.7}$	114
Table 5–3. Extended Hückel Parameters	114
Table 5–4. Selected Interatomic Distances (\AA) and Angles ($^\circ$) for $\text{Ba}_{0.8}\text{Hf}_{12}\text{As}_{17.7}$	115
Table 5–5. Comparison of Site Occupation	116
Table 6–1. Elemental (EDX) Analyses for Compounds $\text{RE}_6\text{Ge}_{5-x}\text{Sb}_{11+x}$ ($\text{RE} = \text{La–Nd, Sm, Gd–Dy}$)	147
Table 6–2. Cell Parameters for Compounds $\text{RE}_6\text{Ge}_{5-x}\text{Sb}_{11+x}$ ($\text{RE} = \text{La–Nd, Sm, Gd–Dy}$)	148

Table 6–3. Crystallographic Data for $\text{La}_6\text{Ge}_{2.8(1)}\text{Sb}_{13.2(1)}$, $\text{Nd}_6\text{Ge}_{3.6(1)}\text{Sb}_{12.4(1)}$, and $\text{Gd}_6\text{Ge}_{4.3(1)}\text{Sb}_{11.7(1)}$	149
Table 6–4. Atomic Coordinates, Occupancies, and Equivalent Isotropic Displacement Parameters (\AA^2) for $\text{RE}_6\text{Ge}_{5-x}\text{Sb}_{11+x}$ ($\text{RE} = \text{La, Nd, Gd}$)	152
Table 6–5. Selected Interatomic Distances (\AA) in $\text{RE}_6\text{Ge}_{5-x}\text{Sb}_{11+x}$ ($\text{RE} = \text{La, Nd, Gd}$)	154
Table 6–6. Summary of Residual Resistivity Ratios ($\rho_{300\text{K}}/\rho_{2\text{K}}$) for $\text{RE}_6\text{Ge}_{5-x}\text{Sb}_{11+x}$	154
Table 7–1. Representative Ternary Compounds That Adopt the ZrSiS-Type (or PbFCl-Type) Structure	186
Table 7–2. Crystallographic Data for $\text{ZrSi}_{0.7}\text{Sb}_{1.3}$, ZrGeSb , and $\text{ZrSn}_{0.4}\text{Sb}_{1.6}$	187
Table 7–3. Atomic Coordinates, Occupancies, and Equivalent Isotropic Displacement Parameters (\AA^2) for $\text{ZrSi}_{0.7}\text{Sb}_{1.3}$, ZrGeSb , and $\text{ZrSn}_{0.4}\text{Sb}_{1.6}$	190
Table 7–4. Selected Interatomic Distances (\AA) and Angles ($^\circ$) in $\text{ZrSi}_{0.7}\text{Sb}_{1.3}$ and ZrGeSb	191
Table 7–5. Selected Interatomic Distances (\AA) and Angles ($^\circ$) in $\text{ZrSn}_{0.4}\text{Sb}_{1.6}$	192
Table 8–1. Summary of Structural Features of Selected Arsenides and Antimonides	206
Table A–1. Powder X-Ray Diffraction Data for $\text{Ba}_2\text{Sn}_3\text{Sb}_6$	208
Table A–2. Anisotropic Displacement Parameters (\AA^2) for $\text{Ba}_2\text{Sn}_3\text{Sb}_6$	210
Table A–3. Anisotropic Displacement Parameters (\AA^2) for EuSn_3Sb_4	211
Table A–4. Anisotropic Displacement Parameters (\AA^2) for $\text{Ba}_3\text{Sn}_4\text{As}_6$	212
Table A–5. Crystallographic Data for $\text{Ba}_3\text{Sn}_4\text{As}_6$ (subcell)	213
Table A–6. Atomic Coordinates, Occupancies, and Equivalent Isotropic Displacement Parameters (\AA^2) for $\text{Ba}_3\text{Sn}_4\text{As}_6$ (subcell)	215
Table A–7. Anisotropic Displacement Parameters (\AA^2) for $\text{Ba}_3\text{Sn}_4\text{As}_6$ (subcell)	216
Table A–8. Powder X-Ray Diffraction Data for $\text{Ba}_{0.8}\text{Hf}_{12}\text{As}_{17.7}$	217
Table A–9. Anisotropic Displacement Parameters (\AA^2) for $\text{Ba}_{0.8}\text{Hf}_{12}\text{As}_{17.7}$	219
Table A–10. Powder X-Ray Diffraction Data for $\text{La}_6\text{Ge}_{2.8(1)}\text{Sb}_{13.2(1)}$	220
Table A–11. Powder X-Ray Diffraction Data for $\text{Ce}_6\text{Ge}_{5-x}\text{Sb}_{11+x}$	223
Table A–12. Powder X-Ray Diffraction Data for $\text{Pr}_6\text{Ge}_{5-x}\text{Sb}_{11+x}$	226

Table A–13. Powder X-Ray Diffraction Data for $\text{Nd}_6\text{Ge}_{3.6(1)}\text{Sb}_{12.4(1)}$	228
Table A–14. Powder X-Ray Diffraction Data for $\text{Sm}_6\text{Ge}_{5-x}\text{Sb}_{11+x}$	231
Table A–15. Powder X-Ray Diffraction Data for $\text{Gd}_6\text{Ge}_{4.3(1)}\text{Sb}_{11.7(1)}$	234
Table A–16. Powder X-Ray Diffraction Data for $\text{Tb}_6\text{Ge}_{5-x}\text{Sb}_{11+x}$	237
Table A–17. Powder X-Ray Diffraction Data for $\text{Dy}_6\text{Ge}_{5-x}\text{Sb}_{11+x}$	240
Table A–18. Anisotropic Displacement Parameters (\AA^2) for $\text{La}_6\text{Ge}_{2.8(1)}\text{Sb}_{13.2(1)}$, $\text{Nd}_6\text{Ge}_{3.6(1)}\text{Sb}_{12.4(1)}$, and $\text{Gd}_6\text{Ge}_{4.3(1)}\text{Sb}_{11.7(1)}$	242
Table A–19. Powder X-Ray Diffraction Data for $\text{ZrSi}_{0.7}\text{Sb}_{1.3}$	244
Table A–20. Powder X-Ray Diffraction Data for ZrGeSb	245
Table A–21. Powder X-Ray Diffraction Data for $\text{ZrSn}_{0.4}\text{Sb}_{1.6}$	246
Table A–22. Anisotropic Displacement Parameters (\AA^2) for $\text{ZrSi}_{0.7}\text{Sb}_{1.3}$, ZrGeSb , and $\text{ZrSn}_{0.4}\text{Sb}_{1.6}$	247

LIST OF FIGURES

Figure 1–1. Diamond-like lattice of NaTl that inspired Eduard Zintl to formulate a set of valence rules that later became known as the <i>Zintl concept</i>	21
Figure 1–2. Examples of zero- and one-dimensional “classical” geometries adopted by Sb: (a) Sb ₂ dumbbell; (b) Sb ₄ square; (c) helical chain; and (d) planar zigzag chain.	22
Figure 1–3. Examples of two-dimensional “classical” Sb networks in (a) BaSb ₃ and (b) elemental Sb.	23
Figure 1–4. “Nonclassical” structural features in anionic Sb networks: (a) linear Sb ₃ segment; (b) one-dimensional linear chain; and (c) two-dimensional square sheet.	24
Figure 2–1. View down the <i>b</i> axis of Ba ₂ Sn ₃ Sb ₆ , with the unit cell outlined.	42
Figure 2–2. Detailed view of part of the anionic framework of Ba ₂ Sn ₃ Sb ₆	43
Figure 2–3. Coordination of the (a) Ba(1) and (b) Ba(2) atoms in Ba ₂ Sn ₃ Sb ₆	44
Figure 3–1. View down the <i>b</i> axis of the structures of (a) <i>ASn₃Sb₄</i> (<i>A</i> = Eu, Sr) and (b) Ba ₂ Sn ₃ Sb ₆ , with the unit cells outlined.	63
Figure 3–2. Plot of resistivity vs. temperature for <i>ASn₃Sb₄</i> (<i>A</i> = Eu, Sr) and Ba ₂ Sn ₃ Sb ₆	64
Figure 3–3. Density of states (DOS) for isolated one-dimensional channels $\frac{1}{2}[\text{Sn}_{14}\text{Sb}_{22}]$ in (a) <i>ASn₃Sb₄</i> (<i>A</i> = Eu, Sr) and (b) Ba ₂ Sn ₃ Sb ₆ without and (c) with internal $\frac{1}{2}[\text{Sb}_2]$ zigzag chains included.	65
Figure 3–4. (a) Portion of the one-dimensional channel in <i>ASn₃Sb₄</i> (<i>A</i> = Eu, Sr) being connected to a neighbouring channel through formation of Sn–Sb bonds (dashed lines). (b) A terminal Sb atom in one of the SnSb ₄ tetrahedra loses electrons in the formation of Sn–Sb bonds to avoid repulsive interactions.	66
Figure 3–5. Total density of states (DOS) for the full three-dimensional anionic substructure of (a) <i>ASn₃Sb₄</i> (<i>A</i> = Eu, Sr) and (b) Ba ₂ Sn ₃ Sb ₆	67
Figure 3–6. Band dispersion curves along special symmetry directions for the full three-dimensional anionic substructure of (a) <i>ASn₃Sb₄</i> (<i>A</i> = Eu, Sr) and (b) Ba ₂ Sn ₃ Sb ₆	68

Figure 3–7. Crystal orbital overlap population (COOP) curves for ~2.9 Å Sn–Sb (solid line) and Sb–Sb (dashed line) interactions in the full three-dimensional anionic substructure of (a) ASn_3Sb_4 ($A = \text{Eu, Sr}$) and (b) $Ba_2Sn_3Sb_6$	69
Figure 4–1. View of $Ba_3Sn_4As_6$ down the a axis with the unit cell outlined.	93
Figure 4–2. Projection down the b axis showing the relative distributions of Ba and Sn–Sn pairs in planes running along $[101]$	94
Figure 4–3. View of the hypothetical limiting structures (a) “ $Ba_4Sn_2As_6$ ” and (b) “ $Ba_2Sn_6As_6$ ”, showing one-dimensional chains of corner-sharing tetrahedra and two-dimensional corrugated layers with pentagonal channels, respectively.	95
Figure 4–4. Coordination environments around Ba atoms in $Ba_3Sn_4As_6$	96
Figure 4–5. Plot of the electrical resistivity of $Ba_3Sn_4As_6$, measured along the needle axis a	97
Figure 4–6. Comparison of the structures of (a) $GeAs_2$, (b) $Ba_4In_8Sb_{16}$, (c) $Ba_3Si_4P_6$, and (d) $Ba_3Sn_4As_6$	98
Figure 5–1. View of $Ba_{0.8}Hf_{12}As_{17.7}$ down the c axis with the unit cell outlined.	117
Figure 5–2. View of the As ribbon in $Ba_{0.8}Hf_{12}As_{17.7}$ running along c and built up from As(2), As(4), and As(1).	118
Figure 5–3. Coordination environment around (a) monocapped square antiprismatic Hf(1), and (b) square antiprismatic Hf(2) in $Ba_{0.8}Hf_{12}As_{17.7}$	119
Figure 5–4. Coordination environment around Ba atom in $Ba_{0.8}Hf_{12}As_{17.7}$, disordered among symmetry-equivalent sites along the sixfold axis.	120
Figure 5–5. Comparison of the structures of (a) $Cr_{12}P_7$, (b) “ $BaHf_{12}As_{24}$ ” (idealized formula), and (c) $Ho_6Ni_{20}P_{13}$, shown in projection down the hexagonal c axis.	121
Figure 5–6. Plot of the electrical resistivity of $Ba_{0.8}Hf_{12}As_{17.7}$, measured along the needle axis c	122
Figure 5–7. DOS curve (and its Hf and As projections) for the $[Hf_{12}As_{24}]$ framework in idealized “ $BaHf_{12}As_{24}$ ”.	123
Figure 5–8. Crystal orbital overlap population curves for As–As contacts within the As ribbon of the $[Hf_{12}As_{24}]$ framework.	124
Figure 5–9. Crystal orbital overlap population curve for Hf–As contacts in the $[Hf_{12}As_{24}]$ framework.	125

Figure 6–1. Plot of unit cell volume for $RE_6Ge_{5-x}Sb_{11+x}$ compounds.	157
Figure 6–2. View of $La_6Ge_{2.8(1)}Sb_{13.2(1)}$ down the a axis showing the unit cell outline and the labeling scheme.	158
Figure 6–3. A schematic diagram illustrating the process of “retrotheoretical analysis” of the $RE_6Ge_{5-x}Sb_{11+x}$ structure.	159
Figure 6–4. Comparison of the symmetrical and asymmetrical three-atom wide Sb ribbons, built up of Sb(3) and Sb(4), in (a) $Gd_6Ge_{4.3(1)}Sb_{11.7(1)}$ and (b) $La_6Ge_{2.8(1)}Sb_{13.2(1)}$, respectively, as viewed perpendicular to the plane of the strips.	161
Figure 6–5. Comparison of the six-atom wide sections making up the kinked sheets in (a) $Gd_6Ge_{4.3(1)}Sb_{11.7(1)}$ and (b) $La_6Ge_{2.8(1)}Sb_{13.2(1)}$, respectively, as viewed perpendicular to the plane of the atoms.	162
Figure 6–6. Coordination environments around $RE(1)$ and $RE(2)$ atoms, showing bicapped trigonal prism and monocapped square antiprism geometries, respectively.	163
Figure 6–7. Comparison of the structures of (a) La_6MnSb_{15} and (b) $RE_6Ge_{5-x}Sb_{11+x}$ shown in projection down the shortest axis.	164
Figure 6–8. Electrical resistivity of $RE_6Ge_{5-x}Sb_{11+x}$ measured along the a axis between 2 and 300 K. (a) $RE = La, Ce, Pr$; (b) $RE = Nd, Sm, Gd$. Insets show low-temperature behavior, the arrows indicating changes in slope arising from magnetic ordering.	165
Figure 6–9. Electrical resistivity of single crystals of $RE_6Ge_{5-x}Sb_{11+x}$ measured along the a axis between 2 and 300 K. (a) $RE = Tb$; (b) $RE = Dy$	166
Figure 7–1. Coordination of Zr atoms in (a) $ZrSi_{0.7}Sb_{1.3}$ and $ZrGeSb$ and (b) $ZrSn_{0.4}Sb_{1.6}$, showing the monocapped square antiprismatic geometry.	193
Figure 7–2. ZrSiS-type structure of $ZrSi_{0.7}Sb_{1.3}$ and $ZrGeSb$, as viewed down the b axis, with the unit cell outlined.	194
Figure 7–3. View down the b axis of $ZrSn_{0.4}Sb_{1.6}$ with the unit cell outlined.	195
Figure 7–4. Connectivity of monocapped square antiprismatic building blocks in (a) $ZrSi_{0.7}Sb_{1.3}$ and $ZrGeSb$ and (b) $ZrSn_{0.4}Sb_{1.6}$	196

LIST OF CRYSTALLOGRAPHIC ABBREVIATIONS AND SYMBOLS

a, b, c	lengths of basis vectors, lengths of cell edges
α, β, γ	interaxial (lattice) angles between b and c , a and c , and a and b axes, respectively
Å	angstrom
d_{hkl}	interplanar distance, or spacing, of neighboring net planes (hkl)
F_c	calculated structure factor
F_o	observed structure factor
hkl	indices of the Bragg reflection (Laue indices) from the set of parallel equidistant net planes (hkl)
(hkl)	indices of a crystal face, or of a single net plane (Miller indices)
$[hkl]$	indices of a lattice direction
λ	wavelength
μ	linear absorption coefficient
P	experimental instability factor in weighting scheme (used in the calculation of $\sigma(I)$ to downweight intense reflections)
R	residual index
R_w	weighted residual index
R_{int}	residual index for averaged symmetry equivalent reflections
ρ	density
σ	standard deviation
U_{eq}	equivalent isotropic atomic displacement parameter
U_{ij}	elements of anisotropic atomic displacement parameter tensor
V	cell volume of the direct lattice
w	weighting factor applied to structure factor
Z	number of formula units per unit cell

CHAPTER 1

Introduction

SOLID STATE CHEMISTRY

History has shown that human development is driven by significant advancements in technology, as illustrated by the different Ages of human progress: Stone, Bronze, Iron, Industrial, and Atomic. Several trends are apparent as we enter the new millennium and the Information Age. First, the evolution of the Internet is becoming less of a novelty and more an integral part of our lives. The infrastructure for this new technology was made possible by advances in materials research, as shown by the doubling of processor speeds every 18 months (“Moore’s Law”) and continuously increasing capacities of memory devices. As progress is made in the area of materials science, we will also witness breakthroughs in such diverse endeavours as space exploration and medicine as technology will become available to overcome great challenges in these areas. The current emphasis on functional materials and materials chemistry in the chemical sciences, as shown by the recent flourish of activity in the fields of nanotechnology, superconductivity, thermoelectric materials, supramolecular and self-assembling systems, colossal magnetoresistance, and high-strength materials, is consistent with our need to adapt to a highly complex and technologically advanced society.

Solid state chemistry, a “rediscovered chemical frontier,”¹ plays a pivotal role in this search for new and useful materials. This subdivision of the solid state sciences, which also include solid state physics, materials science, ceramics and ceramic engineering, mineralogy, and metallurgy,² represents one of the least understood branches of the chemical sciences despite being perhaps one of the oldest, originating in prehistoric times with the firing of clay or smelting of ores during the Bronze Age.¹ Solid state chemistry involves the preparation, structure, properties, and applications of solid materials. By striving to understand the structures of solid state compounds, one hopes to gain insight on the origin of their unique properties. The development of structure-property relationships is a challenging task, but its success may lead to the possibility of predicting and designing new materials with specific structures and properties. It is the promise of the latter that is responsible for the recent growth of this emerging discipline.

The types of materials investigated by solid state chemists are diverse, ranging from *molecular solids*, in which discrete aggregates of atoms are packed together to form solid compounds, to *extended solids*, in which atoms are bonded to near neighbours to form infinite arrays that expand in one, two, or three dimensions. For the purposes of the present study, only the latter will be considered even though both classes of solids are scientifically and technologically interesting. Given the large number of elements in the Periodic Table, any combination of two (binary), three (ternary), four (quaternary), or more elements, under favorable conditions, can potentially form solid state compounds with extended structures. Even unlikely groupings of elements, such as those involving two very electropositive metals, have resulted in new compounds with well-defined

structures. The intermetallic Laves phases KNa_2 , CaLi_2 , CaMg_2 , and BaMg_2 , possessing the MgZn_2 structure type, provide good examples.³ It is the unpredictable and seemingly irrational manner in which solid state reactions occur that distinguishes this field from other fields of chemistry, such as organic or polymer, where there is a greater understanding of synthetic techniques and reaction mechanisms.

Considering the overwhelming number of permutations, it is not surprising that research efforts in *synthetic* solid state chemistry have been primarily focused on binary systems. In contrast, only about 5% of all possible ternary phase diagrams⁴ and even fewer quaternary systems have been extensively studied. Furthermore, the majority of these investigations have focused on oxides and halides owing to the natural tendency of most elements to form stable compounds with oxygen or the halogens. Fueling the continuing activity in oxide and halide crystal chemistry are important discoveries such as high T_c superconductivity in the cuprate $\text{YBa}_2\text{Cu}_3\text{O}_{7-x}$,⁵ catalytic and ion-exchange properties in the aluminosilicate zeolites (which can also act as molecular sieves),⁵ ferroelectricity in the barium titanate BaTiO_3 ,⁵ or superionic conductivity in the iodide RbAg_4I_5 .² In recent decades, more attention has been given to the synthesis and characterization of ternary and quaternary non-oxides, particularly those of the heavier elements. This has resulted in the discovery of new materials with novel structures and properties such as colossal magnetoresistance in $A_{14}\text{MnPn}_{11}$ ($A = \text{Eu, Sr}$; $\text{Pn} = \text{Sb, Bi}$),⁶⁻⁸ superconductivity in ZrRuP ,^{9,10} thermoelectricity in $\text{REFe}_{4-x}\text{Co}_x\text{Sb}_{12}$ ($\text{RE} = \text{La, Ce}$),¹¹ and heavy fermions in CeNiSb_2 .¹²

There exists a large family of polar intermetallic compounds with general compositions M_xA_y or $M_xA_yB_z$ ($M = \text{alkali or alkaline-earth metal}$; $A, B = p\text{-block}$

elements) whose structures and chemical bonding can be rationalized using a set of electron counting rules known as the *Zintl concept*.¹³ Recently considered to be among “the most important and useful paradigms in solid state chemistry,”¹⁴ this deceptively simple and convenient approach for interpreting the structures of extended solids has allowed a vast array of diverse structure types to be understood with the level of ease normally experienced by molecular chemists with similar empirical schemes such as the octet rule or the 18-electron rule. As a result, significant progress has been made in the structural and theoretical chemistry of solid state compounds, whose bonds usually consist of a complex interplay of ionic, covalent, and metallic aspects. Thus, the search for new ternary Zintl phases presents fertile ground for studying the crystal chemistry of the lesser known heavier main-group elements as well as developing better theories for interpreting or predicting new structure types with unusual modes (“non-classical” or hypervalent)¹⁴ of bonding.

The major goal of the present study is to synthesize and characterize new ternary Zintl compounds in the systems $M_xA_yB_z$ and $M_xM'_yB_z$, where M and M' represent electropositive elements (alkaline-earth, rare-earth, or group 4 transition metal) and A and B are electronegative main-group atoms ($A = \text{Si, Ge, Sn}$; $B = \text{As, Sb}$), with the additional aim of measuring their physical properties (resistivity). It is hoped that the mixture of three elements, in addition to varying their relative size and electronegativity, will result in complex structures that will serve to test the limits of the Zintl concept. Using electronic band structure calculations and crystal structure data as the tools, structure-property relationships will be developed through an understanding of the bonding and electronic structures of these compounds. The heavier pnictogens As and Sb were chosen

because they represent the less-explored part of the Periodic Table and, as such, there is a greater need to systematize their chemistry.

THE ZINTL CONCEPT: STRUCTURE AND BONDING^{13,14}

The foundation for the Zintl concept was established in the 1930s when Eduard Zintl, a German chemist who was studying intermetallic phases, observed that the structure of the binary compound NaTl, described as two interpenetrating diamond lattices of Na and Tl atoms, could be interpreted in terms of an anionic Tl^- network and Na^+ cations (Figure 1–1).¹³ Using this simple scheme, he proposed that the Na atoms donate their lone valence electron to the more electronegative Tl atoms which each form covalent bonds to four neighbours in a tetrahedral fashion. According to formal charge convention, the overall formula can be represented as $(\text{Na}^+)_3[\text{Tl}^-]$, emphasizing the two important components in Zintl compounds: the anionic network, in this case, the three-dimensional diamond lattice of Tl atoms, and the charge-neutralizing metal cations. The realization that compounds containing a combination of electropositive (alkali or alkaline-earth metals) and electronegative elements (groups 13–17) tend to form structures that can be readily understood in terms of a closed-shell configuration (8– N or octet rule) for each atom led to the motivation to synthesize and subsequently develop a vast library of novel compounds with diverse structural features.^{13–21}

Zintl compounds may be distinguished from traditional *intermetallic compounds* as well as *ionic compounds* on the basis of the electronegativity difference between the constituent elements. Intermetallic compounds are characterized by a relatively small

electronegativity difference among the metallic elements that make up the composition of these materials. Their structures are more influenced by metallic bonding and close packing factors than localized covalent bonding. As a result, the Zintl concept is typically not applicable for these compounds for which other more effective electron counting schemes exist (*i.e.*, valence electron concentration (*vec*) rules for Hume-Rothery phases). At the other extreme, ionic solids such as Na^+Cl^- or $\text{Ca}^{2+}(\text{F}^-)_2$ adopt structures that are characterized by regular packing arrays (lattices) of cations and anions owing to the large electronegativity difference between the components. Although the Zintl concept can be successfully implemented to assign charges to the atoms in ionic compounds, there is a lack of anion-anion bonding in their structures, which is a characteristic of Zintl compounds. Thus, these classic insulators are usually placed in a separate category to distinguish them from Zintl compounds. Accordingly, Zintl phases are found in the intermediate range along this continuum and are sometimes referred to as *polar intermetallic compounds*.¹⁵ Interestingly, their electronic properties also reflect their position between these two limiting classes by residing at the metal-insulator border.

An implied characteristic of Zintl phases, arising from the assumption of complete electron transfer from one component to the other, is that they must possess a definite composition with a *locally* ordered structure. Unlike intermetallic compounds, which may display nonstoichiometric or disordered behavior as a result of defects or solid solution formation, the requirement of a charge-neutral formulation must hold for the successful application of this approach. Furthermore, the relatively large difference in electronegativity between the electropositive and the electronegative atoms gives rise to the expectation that these compounds should behave as semiconductors, an intuition

based on the implication of an energy gap between occupied (bonding and nonbonding) and unoccupied (antibonding) states. Indeed, one of the original criteria for the definition of a Zintl phase was that it must be a semiconductor.¹³ This expectation may have discouraged the actual measurement of the electronic properties of these intriguing compounds.²²

Recent discoveries of numerous Zintl compounds that display metallic behavior, such as the ternary transition metal compounds $A_{14}\text{MnBi}_{11}$ ($A = \text{Ca}, \text{Sr}, \text{Ba}$)⁶⁻⁸ or the binary phase La_3In_5 ,²³ have prompted an extension of the classical Zintl concept to include these species. The modified *Zintl-Klemm concept*,¹³ which sets an *upper* limit of 2.0 eV for the band gap, can now be invoked to account for Zintl phases with semiconducting, semimetallic, as well as poorly metallic properties, but at the same time, effectively exclude classic valence insulators. Thus, borderline examples with partially delocalized bonding such as deltahedral clusters or certain intermetallic phases may even be considered as potential Zintl phases. For the vast majority of traditional Zintl compounds, the assumption of a small band gap is likely accurate, in spite of the fact that their properties have been meagerly investigated. As will be illustrated later, however, metallic behavior can often emerge as a result of increased band overlap or partial electron transfer from the cations to the Zintl anions.²² The labels *Zintl concept* and *Zintl-Klemm concept* are used interchangeably in the literature to refer to the new definition which includes metallic as well as semiconducting phases.

Much of the interest in the crystal chemistry of Zintl compounds comes about as a result of their structural diversity. In particular, pnictogen (P, As, Sb, and Bi) systems have attracted increasing attention because of their unusual structures and diverse

physical properties. Although many binary and ternary phases have been discovered with polyphosphide Zintl anions serving as the structural framework, the chemistry of the heavier elements remain increasingly less explored as we descend the group 15 elements. Owing to the ability of the heavier main-group elements to engage in diverse modes of bonding afforded by reduced s-p mixing of their orbitals,¹⁴ their crystal chemistry is expected to be structurally rich, as confirmed by the growing number of studies on antimonides. Following the Zintl concept, the heavier elements utilize electrons donated from their electropositive partners to satisfy the octet rule by forming lone pairs or bonds with neighbouring atoms from groups 13 to 17. As a result, the synthesis of new Zintl compounds of the heavier pnicogens offers a unique opportunity for studying homoatomic and heteroatomic bonding between main-group atoms, an interest that is frequently pursued in parallel by molecular main-group chemists.

Papouian and Hoffmann¹⁴ have constructed a useful theory to account for the prevalence of hypervalent or “nonclassical” bonding in the heavier main-group elements. As shown in Table 1–1, Sb condenses with remarkable versatility into anionic networks in the structures of Zintl compounds, forming “classical” as well as “nonclassical” (hypervalent) types of geometries.¹⁴ Although the emphasis here is on homoatomic (Sb–Sb) bonding, it should be expected that similar geometries may be constructed using heteroatomic (*A–B*) bonds. The simplest classical geometries that are adopted by Sb are the isolated atom and the Sb₂ dumbbell (Figure 1–2a).¹⁴ These substructures may be analyzed using the Zintl concept as follows: in order to fulfill the requirement of a complete octet, an isolated Sb atom necessarily possesses four lone pairs and each atom in an Sb₂ dumbbell must have three lone pairs and a bonding pair of electrons. Therefore,

we arrive at the formal charge assignments of Sb^{3-} and $[\text{Sb-Sb}]^{4-}$ for the two units. As an example, the structure of the Zintl compound $\text{Ba}_5\text{Sb}_4^{24}$ (Table 1-1) contains an anionic sublattice with two isolated Sb atoms and a Sb_2 pair per formula unit. Therefore, we can represent its formula as $(\text{Ba}^{2+})_5[(\text{Sb}^{3-})_2(\text{Sb}_2^{4-})]$, which clearly shows the structural relationship of the atoms. Another classical geometry observed for Sb is the isolated Sb_4 square (Figure 1-2b).¹⁴ Assigning a closed-shell configuration for each atom in the square leads to a formal charge of -1 for each atom, resulting in a net formulation of $[\text{Sb}_4]^{4-}$ for this unit. The Zintl compound $\text{Ca}_{11}\text{Sb}_{10}^{25}$ (Table 1-1) provides an illustration of a structure that incorporates isolated Sb_4 squares, as well as Sb_2 dumbbells and isolated Sb atoms. Its chemical formulation, adhering to the Zintl model, is $(\text{Ca}^{2+})_{22}[(\text{Sb}_4^{4-})(\text{Sb}_2^{4-})_4(\text{Sb}^{3-})_8]$. In all of these examples, Sb-Sb bond distances within the anionic frameworks fall within the range considered to be full single bonds (2.80 – 2.90 Å).

Continuing with other examples of classical geometries of Sb, there exists in the structure of the Zintl phases $A_2\text{Sb}_3$ ($A = \text{Sr}, \text{Ba}, \text{Eu}$)²⁶⁻²⁸ (Table 1-1) isolated Sb_6 zigzag segments.¹⁴ The terminal atoms of such units will have an assigned formal charge of -2 while the internal atoms making up the rest of the truncated chain will have a value of -1 . Thus, the charge-neutral formulation for these compounds is represented by $(\text{Ba}^{2+})_2[\text{Sb}^{2-}\text{Sb}^-\text{Sb}^-]$, where half of the Sb_6 zigzag segment is related to the other half by symmetry. If we extend the current segment to infinity along the two ends, we obtain the classical feature of one-dimensional zigzag chains (Figure 1-2d) that are often observed in numerous antimonide structures, such as in $A\text{Sb}_2$ ($A = \text{Ca}, \text{Eu}$)^{29,30} (Table 1-1).¹⁴ In this case, each atom in the chain is two-bonded and therefore can be assigned a formal

charge of -1 . There are also examples of one-dimensional helical chains (Figure 1-2c),¹⁴ such as those found in the compound KSb^{31} (Table 1-1), which differ in conformation from the planar zigzag chains mentioned previously. Since the Sb atoms in KSb are also two-bonded, they possess a formal charge of -1 . The chemical formulations for these Zintl compounds can be denoted as $(A^{2+})_{\infty}^1 [\text{Sb}^-]_2$ and $(\text{K}^+)_{\infty}^1 [\text{Sb}^-]$, respectively.

The richness of the structural features of Sb extends to classical two-dimensional nets such as the 2,3-connected Sb nets seen in the Zintl phase BaSb_3^{32} (Figure 1-3a), which may be compared to the 3-connected Sb nets encountered in elemental Sb (Figure 1-3b).¹⁴ Since two- and three-bonded Sb atoms are given formal charge assignments of -1 and neutral, respectively, we confirm that the compound $(\text{Ba}^{2+})[(\text{Sb}^0)(\text{Sb}^{1-})_2]$ indeed follows the Zintl concept.

In addition to forming classical bonding features, Sb also has the propensity to participate in “hypervalent” or “nonclassical” structural arrangements such as linear chains or planar square nets (Figure 1-4).¹⁴ The simplest example of these is offered by the Zintl compound $\text{Ca}_{14}\text{AlSb}_{11}^{33}$ (Table 1-1), which features, in addition to eight other isolated Sb atoms, a *linear* Sb_3 segment (Figure 1-4a). If the Ca^{2+} and Al^{3+} cations contribute a total of $+31$ positive charges to the structure, then the Sb_3 segment must have a -7 charge since the eight isolated Sb atoms must carry a formal charge of -3 each. Therefore, the Sb_3^{7-} substructure is isoelectronic with I_3^- and XeF_2 ,¹⁴ which also feature the four-electron, three-center bonding motif. The observation of long Sb–Sb bonds (3.20 \AA) within the linear Sb_3 segment is consistent with the MO picture determined for these hypervalent species, which involves an electron pair residing in a nonbonding orbital.¹⁴ The Sb_3 segment may be considered to be derived from one-dimensional linear

chains (Figure 1-4b) which, in turn, may be thought to be excised from larger two-dimensional Sb square nets (Figure 1-4c). The former can be found in the Zintl compound $\text{Li}_2\text{Sb}^{34}$ (Table 1-1) which contains Sb_2 dumbbells as well as infinitely long linear chains of Sb atoms, with Sb-Sb distances of 2.97 Å and 3.26 Å, respectively. The longer distance observed between adjacent chain atoms is consistent with a formal charge assignment of 2- for these atoms. Additionally, two-dimensional square nets represent a ubiquitous feature in antimonide structures,³⁵ as shown by the discovery of a growing number of structure types that feature this bonding motif, and exemplified by the Zintl compounds RESb_2^{36-39} ($RE = \text{La, Ce, Sm}$) (Table 1-1).¹⁴ Similar to the one-dimensional linear chains, the Sb-Sb interactions within the square nets are of the elongated variety (> 3.1 Å), consistent with the assignment of formal charge of -1 for these Sb atoms. These weaker Sb-Sb bonds have been modeled as one-electron bonds in some of these compounds.⁴⁰⁻⁴² The Zintl chemical notations for Li_2Sb and RESb_2 ($RE = \text{La, Ce, Sm}$) can be summarized as $(\text{Li}^+)_2[\text{Sb}^{2-}]$ and $(\text{RE}^{3+})[(\text{Sb}^{2-})(\text{Sb}^{1-})]$, respectively, the latter reflecting the presence of Sb pairs in addition to the square nets.

METHODS OF PROCEDURE

SYNTHESIS^{1,2,43}

Unlike molecular chemistry and its “rational” approach to synthesis, solid state reactions often proceed with such unpredictability and uncertainty that some practitioners have called this aspect of the field an “art”,¹ or perhaps disdainfully as “black magic” by the less appreciative chemical *hoi polloi!* One can attribute the difference to the

bewildering array of bonding interactions present in solids which consist of a complex mixture of covalent, ionic, metallic, as well as weaker van der Waals and partial bonds. Currently, the nature of chemical bonding in solids is not easily reduced to simple concepts. This is in stark contrast to molecules whose structures are mainly dominated by *localized* covalent bonding, albeit with varying degrees of polarity. Furthermore, molecular reactions are governed by specific rules based upon empirical or theoretical grounds, and they often occur with sufficient consistency to allow workers to predict and exploit their behaviour. Ultimate testimony comes from the fact that extremely complex natural products have been synthesized in the laboratory using established organic chemical principles. Unfortunately, these same rules are not accessible to the solid state chemist who must develop truly novel ways to overcome the challenges specific to the solid state.

The difficulties inherent in solid state syntheses originate from huge kinetic barriers produced by reactants usually having high melting points and therefore remaining as solids at the time of reaction. The product initially forms at the interfaces (“grain boundaries”) between reactant particles, where atoms free themselves from the parent structure to recondense to form the initial seed (nucleation) of the new product. Further growth of the crystal depends on the availability of the reacting elements at the product surfaces. One can imagine, then, the greater challenge of synthesizing quaternary phases compared to binary ones, given the lower probabilities of finding all four components simultaneously present! Consequently, reaction rates are highly dependent on the slow rates of diffusion of the participating atoms through the solid matrices towards the reactant-product interfaces.

Several techniques are available for enhancing the rate of diffusion of the reactants. A common strategy in solid state syntheses is to use extremely harsh conditions, such as high temperatures or pressures, to induce nucleation and improve diffusion of the reacting atoms. Typically, stoichiometric amounts of the elements, in the form of very fine powder for increased surface area, are directly mixed together thoroughly and then placed in a reaction vessel to be annealed in a high-temperature furnace at 800–1200 °C for several days. Greater purity can be afforded by further intermediate grinding and reannealing. The vessels used here are fused-silica ampoules, in which the chosen elements are sealed under vacuum, or metal (Nb or Ta) tubes since the desired products are non-oxides. The metal tubes offer the advantage of protecting the reaction mixture from attacking the quartz tubes. For reactions requiring even higher temperatures than the range mentioned, an arc-furnace may be employed which offers instant temperature conditions in excess of 2000 °C. The latter technique can also be used as a “quick and dirty” method for synthesizing certain solid state compounds but has the disadvantage of not always affording well-crystallized pure products as a result of the rapid cooling condition. Finally, techniques utilizing milder synthetic conditions (< 500 °C) have been developed by the French (“chimie douce” or soft chemistry) for preparing oxides and chalcogenides, some of which are not attainable under higher temperature conditions.

Numerous techniques are available for growing suitable crystals for single-crystal X-ray studies. The most direct method involves using a slow cooling procedure after reaching the maximum reaction temperature in a heating program. Additionally, several types of fluxes may be employed, such as elemental Sn used in the present research, to

induce crystallization. Fluxes are low-melting materials that provide a liquid medium for promoting nucleation of the reactants. They must be relatively inert to the reacting components and easy to remove after the reaction is finished. Sn fluxes can be readily dissolved and removed by treatment with HCl. Alternatively, one may use chemical vapour transport as a method for growing single crystals.⁴⁴ This technique also provides a good way to synthesize new materials or for purifying compounds. Briefly, the method involves adding a gaseous transport agent, such as I₂, to a reactant or product mixture which is normally not volatile under the reaction conditions. The reaction of the gaseous substance with the mixture to form a volatile intermediate promotes migration over a thermochemical potential gradient and subsequent redeposition of the mixture at a different part of the closed reaction vessel.

As shown, the unique nature of solid state reactions lies in the inability of the investigator to control or predict their compositional or structural outcome. Much of the blame can be placed on our lack of understanding of the reaction mechanisms. Recent attempts to study this challenging aspect of solid state chemistry have resulted in significant progress.^{45,46} However, we are far from being able to design new structures and then attempt to synthesize them in the laboratory (notwithstanding hyped claims to the contrary!) Considering the significant element of serendipity in solid state syntheses, it is not surprising that combinatorial methods⁴⁷ have now been developed for synthesizing new solid state materials. Curiously, the parallel screening of more than 25000 members prepared by automated thin-film synthesis resulted in the discovery of the unusual luminescent inorganic material Sr₂CeO₄.⁴⁷ Given the lack of rational

synthetic techniques, perhaps this represents the most efficient technique for discovering new solid state compounds given a certain composition.

CHARACTERIZATION

Spectroscopic methods such as NMR and IR represent important structural tools in organic and inorganic chemistry but these play a lesser role in solid state chemistry. Although some of the characterization techniques employed here overlap strongly with other disciplines of chemistry, such as single-crystal X-ray diffraction, the complementary use of all the following methods is unique to the study of solids.

X-ray diffraction remains the single most important tool for the structural study of solid state materials owing to the periodic arrangement of atoms in most of these compounds. For efficient screening of reaction products in exploratory solid state chemistry, X-ray powder diffraction is the method most commonly used. Since every crystalline material exhibits a characteristic powder X-ray diffraction pattern, one can compare an unknown powder pattern of a reaction product mixture against pure "fingerprints" of suspected product phases to assess the relative purity of that reaction, in addition to confirming the presence of possible new compounds. Accurate unit cell parameters can be obtained by indexing the powder patterns, an important exercise for assessing the substitutional range of certain compounds or solid solutions.

If suitable single crystals of a compound are available, their approximate elemental compositions can be determined by the technique of X-ray microanalysis on a scanning electron microscope (SEM). This powerful technique for elemental analysis of microvolumes is based on the fact that when a sample is placed in the SEM and

bombarded with high energy electrons, characteristic X-ray emission spectra of the elements present in the sample are generated. Thus, it is possible to identify the elements present in the sample by analyzing the emitted X-rays using either an energy dispersive spectrometer, which operates by discriminating X-ray energies (EDX), or a crystal spectrometer, which uses a diffracting crystal to scan the desired wavelength (wavelength dispersive, WD). Quantitative elemental analysis may then be obtained by using a suitable calibration procedure.²

Next, it is desirable to perform preliminary photographic work to determine possible space groups, obtain approximate cell parameters, as well as assessing the crystals' quality before data collection on a diffractometer. Single-crystal X-ray diffraction represents the most important structural determination technique. With the advent of area detectors in CCD diffractometers, data can be obtained quickly and accurately, even on crystals once considered to be of marginal quality.

PHYSICAL PROPERTIES²

It is important to study how the physical properties of solids are related to the atomic arrangements in their crystal structures. Formulating structure-property relationships for a material is a challenging task, often requiring a thorough knowledge of its electronic band structure as well as its atomic structure, but can lead to the ultimate goal of being able to optimize that property for useful applications through designing new compounds with specific structures. Although there are many properties of solids that are available for measuring, ranging from magnetic and optical to mechanical, this discussion will only focus on one relevant aspect of a material's electronic properties – its

resistivity. As shown earlier, the electronic properties of Zintl compounds reside at the interesting border between *insulating* ionic compounds and *metallic* intermetallic compounds. Therefore, it is worthwhile to investigate the electronic properties of this large class of compounds to determine the source of its conductivity, or lack thereof.

Solid state materials are frequently classified according to how their electrical resistivity (ρ) behaviour changes as a function of temperature (T). Briefly, the electronic conductivity (σ), or the ability of a material to convey an electrical current, is given by the expression

$$\sigma = \frac{1}{\rho} = n Z e \mu$$

where n is the number of charge carriers, $Z e$ their charge, and μ their mobility. For electronic conductors, the value $Z e$ is thus constant and independent of temperature and μ decreases slightly with increasing temperature as a result of increased interference by lattice vibrations (*i.e.*, phonons). Therefore, materials may be distinguished by the magnitude of n and their temperature dependence.

For *metals*, which are good conductors ($\sigma \sim 10^4 - 10^6 \Omega^{-1} \text{ cm}^{-1}$),² the number of carriers is large and remains nearly constant with temperature. Thus, the conductivity of metals is determined by μ which decreases gradually with increasing temperature as there are more scattering of the mobile electrons by the phonons. The relatively high conductivity of metals is attributed to partially filled bands, giving rise to a density of states at the Fermi level. In essence, the ability of the metal to move the carriers along its length is enhanced.

For *insulators* ($\sigma < 10^{-15} \Omega^{-1} \text{ cm}^{-1}$)² and *semiconductors* ($\sigma \sim 10^{-5} - 10^3 \Omega^{-1} \text{ cm}^{-1}$),² the concentration of carriers (n) usually increases exponentially with temperature. This can be easily understood by realizing that these materials possess a completely filled valence band and an empty conduction band, resulting in a measurable band gap between the two. It is possible to promote electrons from the filled valence band to the conduction band, thereby increasing the number of carriers and thus conductivity, by increasing the temperature. The lopsided competition between the exponentially increasing number of carriers and the increased deleterious effects of lattice vibrations results in the observation of increasing conductivity with increasing temperature for semiconductors. The difference in magnitude of the band gap between insulators and semiconductors effectively distinguishes these two classes of materials. It is possible to observe semiconducting behaviour in insulators, whose band gaps are greater than 3 eV, if high enough temperatures are reached.

Experimentally, the resistivity of a rod-like material (*i.e.*, needle-like crystals) may be measured using a four-probe approach.^{43,48} In this type of setup, four probes are attached along the length of the needle. By driving a current through the two outer leads, the voltage drop between the two middle leads can be simultaneously determined using a high-impedance voltmeter. Thus, one is able to obtain the absolute *resistance*, through Ohm's law, as a function of temperature. The *resistivity* of the material is then given by the relationship

$$\rho = \frac{RA}{l}$$

where ρ is the resistivity, R is the measured resistance, and A and l represent the cross-sectional area of the needle crystal and the distance between the two middle contacts, respectively.

Finally, to understand the nature of bonding and the origins of the physical properties of the materials presented in this thesis, electronic band structure calculations have been performed. These semi-empirical calculations⁴⁹ represent the electronic wavefunctions of solids as linear combinations of valence atomic orbitals using the extended Hückel method. Although these theoretical calculations do not predict the optimum structure of a crystal since the basis sets representing the atomic orbitals are taken from published electronic structure calculations of atoms, they provide an invaluable tool for solid state chemists wishing to develop structure-property relationships in solids. Analysis of the band structure of a material, as well as numerous other useful results that may be extracted from these calculations such as orbital interactions or density of states, can provide great insight into its physical properties.

Table 1–1. Common Geometries of Sb Anionic Networks in Selected ZintlCompounds¹⁴

Compound	Structure Type	Structural Features	
		Classical	Nonclassical
Ba_5Sb_4	Sm_5Ge_4	atoms, dumbbells	
$Ca_{11}Sb_{10}$	$Ho_{11}Ge_{10}$	atoms, dumbbells, squares	
A_2Sb_3 ($A = Sr, Ba, Eu$)	Sr_2Sb_3	Sb_6 zigzag segments	
KSb	$LiAs$	1D helical chains	
ASb_2 ($A = Ca, Eu$)	$CaSb_2$	1D zigzag chains	
$BaSb_3$	BaP_3	2D 2,3-connected nets	
$Ca_{14}AlSb_{11}$	$Ca_{14}AlSb_{11}$	atoms	linear Sb_3 units
Li_2Sb	Li_2Sb	Sb_2 dumbbells	1D linear chains
$RESb_2$ ($RE = La, Ce, Sm$)	$SmSb_2$	Sb_2 dumbbells	2D square sheets

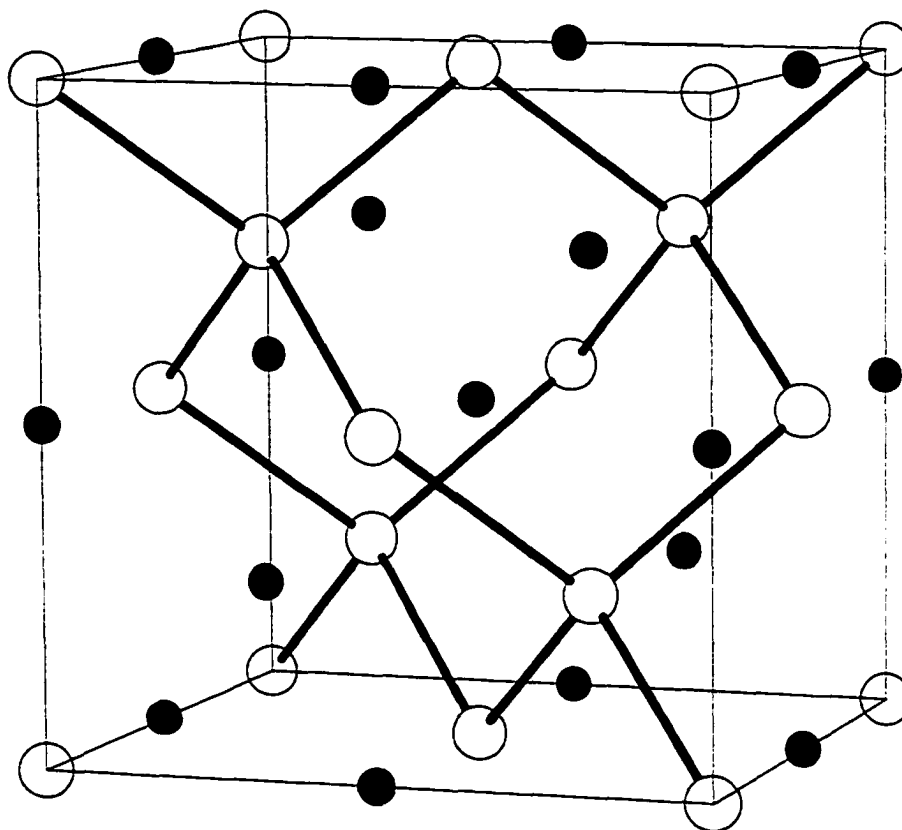


Figure 1-1. Diamond-like lattice of tetrahedrally connected Tl atoms in the structure of NaTl that inspired Eduard Zintl to formulate a set of valence rules to account for the bonding in many polar intermetallic compounds. These rules later became known as the *Zintl concept*. The large open circles are Tl⁻ anions and the small dark circles are Na⁺ cations.

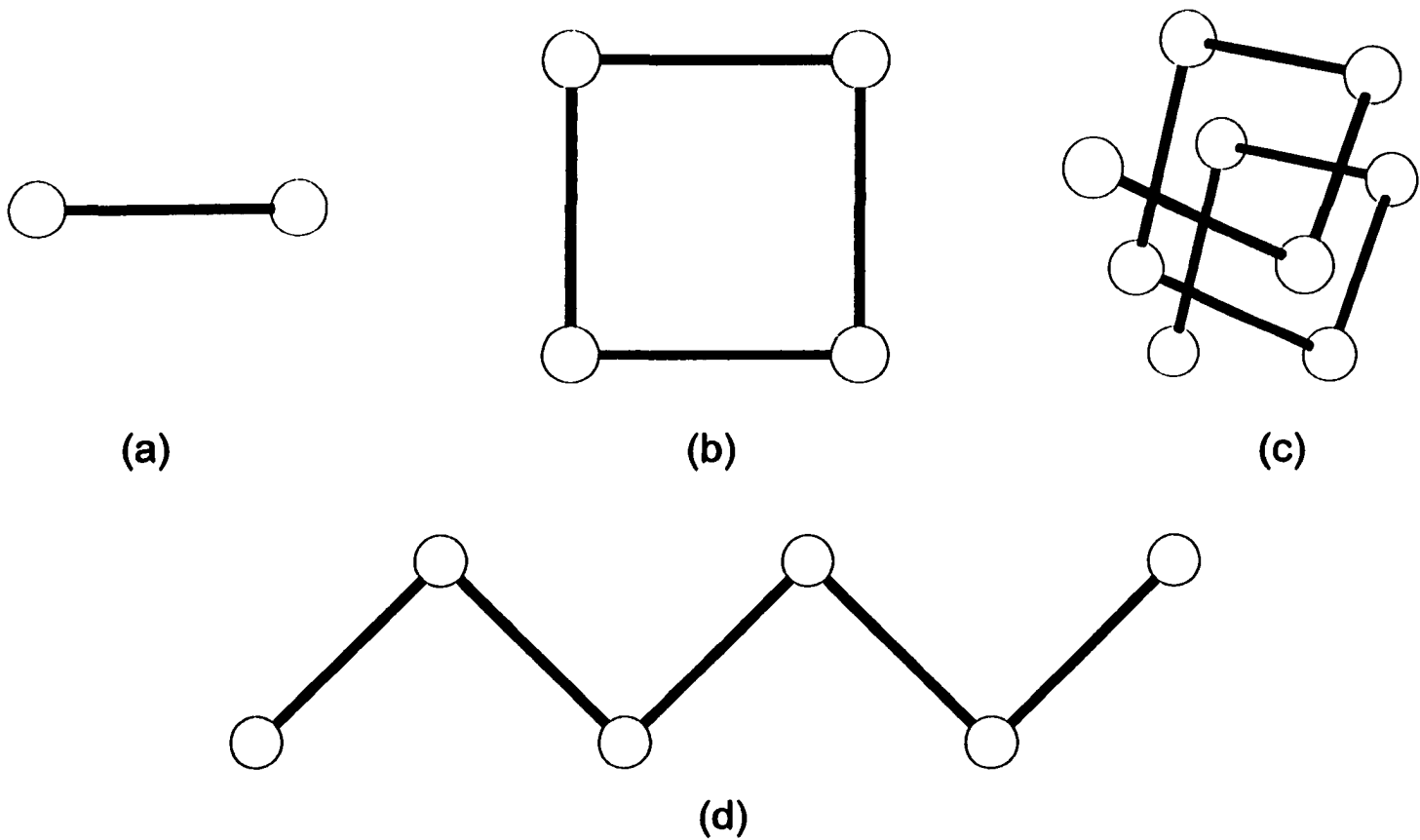
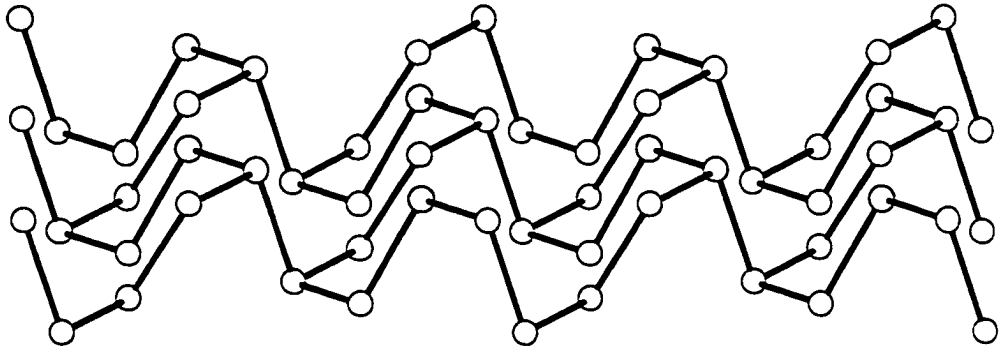


Figure 1–2. Examples of zero- and one-dimensional “classical” geometries adopted by Sb: (a) Sb_2 dumbbell; (b) Sb_4 square; (c) helical chain; and (d) planar zigzag chain.

(a)



(b)

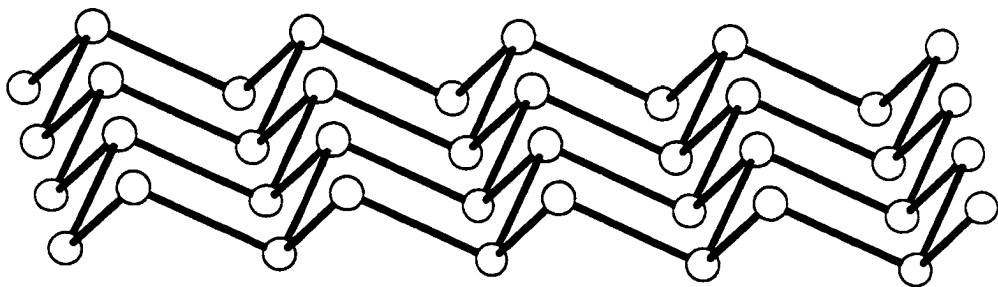


Figure 1–3. Examples of two-dimensional “classical” Sb networks in (a) BaSb_3 and (b) elemental Sb.

(a)



(b)



(c)

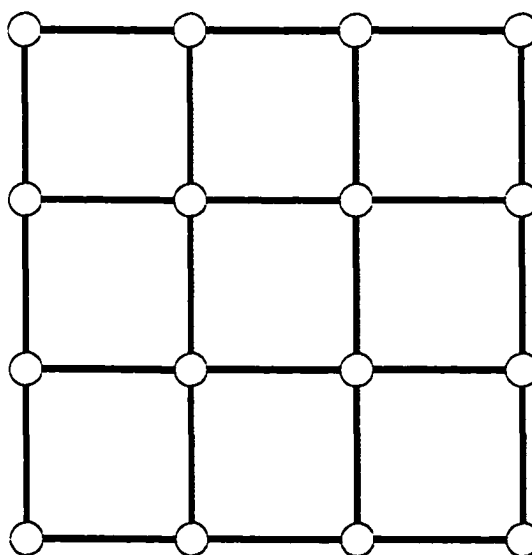


Figure 1-4. “Nonclassical” structural features in anionic Sb networks: (a) linear Sb_3 segment; (b) one-dimensional linear chain; and (c) two-dimensional square sheet.

REFERENCES

- (1) DiSalvo, F. J. *Science* **1990**, *247*, 649.
- (2) West, A. R. *Solid State Chemistry and its Applications*; John Wiley & Sons, Inc.: New York, 1995.
- (3) Westbrook, J. H., Ed. *Intermetallic Compounds*; Wiley: New York, 1967.
- (4) DiSalvo, F. J. *Solid State Commun.* **1997**, *102*, 79.
- (5) Cheetham, A. K.; Day, P., Eds. *Solid State Chemistry: Compounds*; Clarendon Press: Oxford, 1992.
- (6) Chan, J. Y.; Kauzlarich, S. M.; Klavins, P.; Shelton, R. N.; Webb, D. J. *Chem. Mater.* **1997**, *9*, 3132.
- (7) Chan, J. Y.; Kauzlarich, S. M.; Klavins, P.; Shelton, R. N.; Webb, D. J. *Phys. Rev. B: Condens. Matter* **1998**, *57*, R8103.
- (8) Webb, D. J.; Cohen, R.; Klavins, P.; Shelton, R. N.; Chan, J. Y.; Kauzlarich, S. M. *J. Appl. Phys.* **1998**, *83*, 7192.
- (9) Müller, R.; Shelton, R. N.; Richardson, J. W.; Jacobson, R. A. *J. Less-Common Met.* **1983**, *92*, 177.
- (10) Meisner, G. P. *Physica* **1981**, *108b*, 763.
- (11) Nolas, G. S.; Morelli, D. T.; Tritt, T. M. *Annu. Rev. Mater. Sci.* **1999**, *29*, 89.
- (12) Muro, Y.; Takeda, N.; Ishikawa, M. *J. Alloys Compd.* **1997**, *257*, 23.
- (13) Kauzlarich, S. M., Ed. *Chemistry, Structure, and Bonding of Zintl Phases and Ions*; VCH Publishers: New York, 1996.
- (14) Papoian, G. A.; Hoffmann, R. *Angew. Chem. Int. Ed.* **2000**, *39*, 2408.
- (15) Schäfer, H. *Annu. Rev. Mater. Sci.* **1985**, *15*, 1.

- (16) Corbett, J. D. *Chem. Rev.* **1985**, *85*, 383.
- (17) von Schnering, H. G. *Angew. Chem., Int. Ed. Engl.* **1981**, *20*, 33.
- (18) Kauzlarich, S. M. *Comments Inorg. Chem.* **1990**, *10*, 75.
- (19) Schäfer, H.; Eisenmann, B.; Müller, W. *Angew. Chem., Int. Ed. Engl.* **1973**, *12*, 694.
- (20) Nesper, R. *Angew. Chem., Int. Ed. Engl.* **1991**, *30*, 789.
- (21) Schäfer, H.; Eisenmann, B. *Rev. Inorg. Chem.* **1981**, *3*, 29.
- (22) Lam, R.; Zhang, J.; Mar, A. *J. Solid State Chem.* **2000**, *150*, 371.
- (23) Zhao, J.-T.; Corbett, J. D. *Inorg. Chem.* **1995**, *34*, 378.
- (24) Brechtel, E.; Cordier, G.; Schäfer, H. *Z. Naturforsch., B: Anorg. Chem., Org. Chem.* **1981**, *36*, 1341.
- (25) Deller, K.; Eisenmann, B. *Z. Naturforsch., B: Anorg. Chem., Org. Chem.* **1976**, *31*, 29.
- (26) Eisenmann, B.; Jordan, H.; Schäfer, H. *Z. Naturforsch., B: Anorg. Chem., Org. Chem.* **1985**, *40*, 1603.
- (27) Chapius, G.; Hulliger, F.; Schmelczer, R. *J. Solid State Chem.* **1980**, *31*, 59.
- (28) Eisenmann, B. *Z. Naturforsch., B: Anorg. Chem., Org. Chem.* **1979**, *34*, 1162.
- (29) Hulliger, F.; Schmelczer, R. *J. Solid State Chem.* **1978**, *26*, 389.
- (30) Deller, K.; Eisenmann, B. *Z. Anorg. Allg. Chem.* **1976**, *425*, 104.
- (31) Höhle, W.; von Schnering, H. G. *Z. Kristallogr.* **1981**, *155*, 307.
- (32) Deller, K.; Eisenmann, B. *Z. Naturforsch., B: Anorg. Chem., Org. Chem.* **1978**, *33*, 676.
- (33) Cordier, G.; Schäfer, H.; Stelter, M. *Z. Anorg. Allg. Chem.* **1984**, *519*, 183.

- (34) Müller, W. *Z. Naturforsch., B: Anorg. Chem., Org. Chem.* **1977**, *32*, 357.
- (35) Tremel, W.; Hoffmann, R. *J. Am. Chem. Soc.* **1987**, *109*, 124.
- (36) Canfield, P. C.; Thompson, J. D.; Fisk, Z. *J. Appl. Phys.* **1991**, *70*, 5992.
- (37) Wang, B. R.; Steinfink, H. *Inorg. Chem.* **1967**, *6*, 1685.
- (38) Eatough, N. L.; Hall, T. *Inorg. Chem.* **1969**, *8*, 1439.
- (39) Abdusalyamova, M. N. *J. Alloys Compd.* **1993**, *202*, 15.
- (40) Brylak, M.; Jeitschko, W. *Z. Naturforsch. B: Chem. Sci.* **1994**, *49*, 747.
- (41) Brylak, M.; Jeitschko, W. *Z. Naturforsch. B: Chem. Sci.* **1995**, *50*, 899.
- (42) Brylak, M.; Möller, M. H.; Jeitschko, W. *J. Solid State Chem.* **1995**, *115*, 305.
- (43) Cheetham, A. K.; Day, P., Eds. *Solid State Chemistry: Techniques*; Clarendon Press: Oxford, 1987.
- (44) For a recent review, see: Gruehn, R.; Glaum, R. *Angew. Chem., Int. Ed. Engl.* **2000**, *39*, 692.
- (45) Oyelaran, O.; Novet, T.; Johnson, C. D.; Johnson, D. C. *J. Am. Chem. Soc.* **1996**, *118*, 2422.
- (46) Parkinson, B. *Science* **1995**, *270*, 1157.
- (47) Danielson, E.; Devenney, M.; Giaquinta, D. M.; Golden, J. H.; Haushalter, R. C.; McFarland, E. W.; Poojary, D. M.; Reaves, C. M.; Weinberg, W. H.; Wu, X. D. *Science* **1998**, *279*, 837.
- (48) Wieder, H. H. *Laboratory Notes on Electrical and Galvanomagnetic Measurements*; Elsevier Scientific Publishing Company: Amsterdam, 1979.
- (49) Hoffmann, R. *Solids and Surfaces: A Chemist's View of Bonding in Extended Structures*; VCH Publishers: New York, 1988.

CHAPTER 2

Synthesis and Structure of $\text{Ba}_2\text{Sn}_3\text{Sb}_6$, a Zintl Phase Containing Channels and Chains[†]

INTRODUCTION

The Zintl concept continues to serve as a powerful unifying principle to explain the bonding in many solids classified as polar intermetallic compounds.¹⁻³ The compositions of these Zintl phases can be complex and their structures display a beautiful diversity of clusters, chains, nets, rings, and other polyanionic frameworks. They can be rationalized in terms of an ionic model whereby the strongly electropositive elements lose their valence electrons to the electronegative semimetals, which respond if necessary through the formation of bonds (to complete their octets) in the anionic substructure.

Numerous examples of ternary antimony-containing Zintl phases in the systems $A/M/Sb$, where A is an alkali metal or an alkaline earth and M is a triel (group 13) or tetrel (group 14), have been uncovered in recent years.⁴⁻¹⁸ As part of an ongoing investigation of new low-dimensional antimonides in our laboratory, we have extended our search to such systems. While many alkali metal or alkaline earth *triel* antimonides are now

[†] A version of this chapter has been published. Lam, R.; Mar, A. *Inorg. Chem.* 1996, 35, 6959. Copyright 1996 American Chemical Society.

known,^{4,5} we were surprised to discover that there were relatively meagre reports of alkali metal *tetrel* antimonides ($A_8\text{SnSb}_4$ ($A = \text{Na, K}$),^{6,7} $A_5\text{SnSb}_3$ ($A = \text{Na, K}$),^{7,8} KSnSb ,⁹⁻¹¹ NaSn_2Sb_2 ,¹² and Rb_4SnSb_6 ¹³), and only disordered or poorly structurally characterized examples of alkaline earth *tetrel* antimonides (Mg/Si/Sb ,^{14,15} Mg/Sn/Sb ,^{16,17} and Mg/Pb/Sb ¹⁸ phase studies). We report here the synthesis and structure of $\text{Ba}_2\text{Sn}_3\text{Sb}_6$, the first example, to our knowledge, of an alkaline earth *tetrel* antimonide with an ordered structure. It is a Zintl phase that adopts a novel structure type presenting a delightful assortment of chains and channels in an arrangement that has not been encountered previously in related $A/M/X$ ($A =$ alkali metal or alkaline earth; $M =$ triel or tetrel; $X = \text{P, As, Sb, Bi}$) systems. We will also demonstrate that application of the Zintl concept leads to the implication that $\text{Ba}_2\text{Sn}_3\text{Sb}_6$ is a mixed-valence compound containing tin(II) and tin(IV).

EXPERIMENTAL SECTION

SYNTHESIS

$\text{Ba}_2\text{Sn}_3\text{Sb}_6$ was first isolated as a minor phase from the reaction of a 0.25-g mixture of BaO, La, and Sb in a 1:1:1 ratio to which a large excess of Sn was added (BaO, 93 mg, 0.60 mmol, Fisher; La, 84 mg, 0.60 mmol, 99.9%, Cerac; Sb, 74 mg, 0.60 mmol, 99.999%, Cerac; Sn, 358 mg, 3.02 mmol, 99.8%, Cerac). The reactants were loaded into a quartz tube (8-cm length, 10-mm i.d.) that was then evacuated and sealed. The mixture was heated at 600 °C for 1 day, 900 °C for 2 days, cooled to 500 °C over 1 day, and then cooled to room temperature over 5 hours. After the excess Sn was

dissolved with concentrated HCl, thin silver needle-shaped crystals were found in the product. Windowless EDX (energy-dispersive X-ray analysis) on a JEOL JSM-6301FXV field-emission scanning electron microscope showed that Ba, Sn, and Sb were present in these crystals, but that La and, more importantly, O were *not* present. Anal. (mol %) Calcd for Ba₂Sn₃Sb₆: Ba, 18; Sn, 27; Sb, 55. Found (average of 4 analyses): Ba, 15(2); Sn, 28(2); Sb, 57(3). The crystals obtained from this reaction, which is reproducible, were used for the single-crystal structure determination. The compound Ba₂Sn₃Sb₆ can also be prepared through a more rational route, by reaction of the elements in their stoichiometric proportions with the same heating profile as above. This procedure results in nearly phase-pure Ba₂Sn₃Sb₆, as revealed by the X-ray powder pattern obtained on an Enraf-Nonius FR552 Guinier camera (CuKα₁ radiation; Si standard). The cell parameters of this sample were refined from the powder diffraction data with the use of the program POLSQ.¹⁹ Table A-1 lists observed and calculated interplanar distances as well as the intensities calculated with the use of the program LAZY-PULVERIX²⁰ from the single-crystal structure.

STRUCTURE DETERMINATION

Preliminary cell parameters were determined from Weissenberg photographs, which revealed Laue symmetry *mmm* and systematic extinctions (*0kl*: $k + l = 2n + 1$; *hk0*: $h = 2n + 1$) consistent with the orthorhombic space groups $D_{2h}^{16} - Pnma$ and $C_{2v}^9 - Pn2_1a$. Final cell parameters were determined from a least-squares analysis of the setting angles of 24 reflections in the range $20^\circ \leq 2\theta(\text{MoK}\alpha) \leq 32^\circ$ centred on an Enraf-Nonius CAD4 diffractometer. Intensity data were collected at -50°C with the θ - 2θ scan

technique in the range $3^\circ \leq 2\theta(\text{MoK}\alpha) \leq 50^\circ$. Crystal data and further details of the data collection are given in Table 2–1.

Calculations were carried out with the use of the SHELXTL (Version 5.0) package.^{21,22} Conventional atomic scattering factors and anomalous dispersion corrections were used.²³ Intensity data were processed, and face-indexed Gaussian-type absorption corrections were applied with the use of the program XPREP. Based on the intensity statistics, the satisfactory averaging, and the successful structure solution, the centrosymmetric space group *Pnma* was chosen. Initial atomic positions of all atoms were found by direct methods with the program XS. Given the similarity of their X-ray scattering factors, discrimination between Sn and Sb atoms is not possible. However, we believe that our proposed model is acceptable based on several observations. First, the Sn and Sb atoms are distributed among the nine crystallographically inequivalent sites (Table 2–2), each at a Wyckoff position *4c*, such that the proportion of Sb to Sn sites agrees with that of the elemental analysis (2:1). Any other distribution results in a calculated elemental composition that is beyond that which can be accounted for by the actual chemical analysis. Second, and perhaps more convincingly, one can appeal to the chemical reasonableness of the structure, in terms of the similarity of coordination geometries and metrical details to those of related structures as well as its consistency with the proposed oxidation state formulation. These chemical arguments will be discussed in detail later.

Refinements were performed by least-squares methods with the program XL. Refinements in which the occupancies of successive atoms were allowed to vary (while the isotropic displacement parameters were fixed) resulted in values of 100.5(6)% for

Ba(1), 100.3(6)% for Ba(2), 100.6(7)% for Sn(1), 99.9(7)% for Sn(2), 99.4(7)% for Sn(3), 99.6(7)% for Sb(1), 100.2(7)% for Sb(2), 99.4(7)% for Sb(3), 100.6(7)% for Sb(4), 99.5(7)% for Sb(5), and 99.6(7)% for Sb(6). The values of the displacement parameters are unexceptional, and the difference electron density map is featureless ($\Delta\rho_{\max} = 3.24$; $\Delta\rho_{\min} = -2.39 \text{ e}^- \text{ \AA}^{-3}$), ruling out the possibility that interstitial oxygen atoms might be present. We thus accept the ordered, stoichiometric model $\text{Ba}_2\text{Sn}_3\text{Sb}_6$. The atomic positions were standardized with the use of the program STRUCTURE TIDY.²⁴ The final cycle of least-squares refinement on F_o^2 of 68 variables (including anisotropic displacement parameters and an isotropic extinction parameter) and 1443 averaged reflections (including those having $F_o^2 < 0$) converged to residuals of $R_w(F_o^2)$ of 0.105 and $R(F)$ (for $F_o^2 > 2\sigma(F_o^2)$) of 0.056. Final values of the positional and displacement parameters are given in Table 2–2. Anisotropic displacement parameters are given in Table A–2.

RESULTS AND DISCUSSION

DESCRIPTION OF THE STRUCTURE

A view of the structure of $\text{Ba}_2\text{Sn}_3\text{Sb}_6$ down the short b axis is shown in Figure 2–1. Selected interatomic distances and angles are given in Table 2–3. Gross features that can be readily discerned from this view are the large lozenge-shaped channels running along $[010]$, zigzag Sb–Sb chains aligned within and parallel to these channels, and the isolated Ba^{2+} cations.

The large channels are defined by 30-membered rings and are constructed from an anionic framework intricately connected together by Sn and Sb atoms that display an interesting palette of coordination geometries. Figure 2–2 shows a more detailed view of part of this framework. The Sn atoms reside in two kinds of coordination environments. The Sn(1) and Sn(3) atoms are each bonded to three Sb atoms in a trigonal pyramidal fashion, while the Sn(2) atom is bonded to four Sb atoms in a tetrahedral fashion. The “vertical” sides of the lozenge shape of the channel (*i.e.*, parallel to the *ab* plane) are formed by sharing corners of these Sn-centred coordination polyhedra in the order: tetrahedron–trigonal pyramid–tetrahedron–trigonal pyramid–tetrahedron. The other two sides (*i.e.*, parallel to the $(10\bar{1})$ or (101) planes) are formed in a similar fashion, except that an intervening zigzag Sb–Sb chain takes the place of the middle tetrahedron. The four Sn-centred tetrahedra at the corners of the lozenge serve as links to adjoining lozenges to extend the framework along the *a* direction, while the two other tetrahedra at the middle of the “vertical” sides extend the framework along the *c* direction (Figure 2–1). Corner-sharing of the coordination polyhedra along the *b* direction completes the three-dimensional extension of this framework. It is amusing to note the chair conformation adopted by the Sn(2)–Sb(3)–Sn(1)–Sb(4)–Sn(1)–Sb(3) atoms, and the boat conformation adopted by the Sn(1)–Sb(4)–Sn(2)–Sb(3)–Sn(2)–Sb(4) atoms (Figure 2–2).

Within each channel reside two zigzag chains of Sb(1)–Sb(2) atoms, extending infinitely along the *b* direction. These chains are to be considered as isolated and separate from the channel framework, as the nearest distance to the framework atoms is greater than 3.6 Å.

The Ba^{2+} cations are positioned within the cavities of the channel, and are coordinated by Sb atoms of the anionic framework as well as those of the isolated zigzag chains. The Ba(1) atom is coordinated in a highly irregular fashion by eight Sb atoms at distances of 3.478(3) to 3.628(2) Å, as shown in Figure 2–3(a). The distance of 3.857(3) Å to a ninth Sb atom is probably too long to be important. However, the Ba(1)–Sn(1) distance of 3.629(3) Å cannot be ignored, and indeed lies along a direction that would seem to indicate an interaction to a stereochemically active lone pair on Sn(1). The coordination around the Ba(2) atom is a little more regular, with distances of 3.513(2) to 3.580(2) Å to six Sb atoms in a trigonal prismatic environment, as shown in Figure 2–3(b). The next nearest Ba(2)–Sb distances of 3.804(3) and 3.913(3) Å are probably unimportant. Again, the Ba(2)–Sn(3) distance of 3.659(3) Å may bear some significance.

STRUCTURAL RELATIONSHIPS AND BONDING

In its overall form, $\text{Ba}_2\text{Sn}_3\text{Sb}_6$ resembles the structure of KMSb_4 ($M = \text{Al}, \text{Ga}$) in that they also possess channels defined by smaller 22-membered rings formed by MSb_4 tetrahedra.^{40,p} Fragments of the $\text{Ba}_2\text{Sn}_3\text{Sb}_6$ structure are reminiscent of features found in related antimonides. The tetrahedral Sn(2)Sb₄ unit in $\text{Ba}_2\text{Sn}_3\text{Sb}_6$ has Sn–Sb distances of 2.793(3) to 2.840(2) Å; these distances are comparable to those found in the isolated tetrahedra in Na_8SnSb_4 (2.843(1) Å)⁶ and K_8SnSb_4 (2.898(1) Å),⁷ the edge-sharing tetrahedral dimers in K_5SnSb_3 (2.818(1) to 2.886(1) Å),⁸ and the infinite corner-sharing tetrahedral chains in Na_5SnSb_3 (2.805(1) to 2.945(1) Å).⁷ The Sb–Sn(2)–Sb angles in the Sn(2)Sb₄ tetrahedron range from 101.89(10)° to 116.11(7)°, slightly distorted from the ideal tetrahedral angle. The trigonal pyramidal Sn(1)Sb₃ and Sn(3)Sb₃ units in $\text{Ba}_2\text{Sn}_3\text{Sb}_6$

have Sn–Sb distances of 2.894(3)–2.901(2) Å and 2.876(3)–2.913(2) Å, respectively. These are similar to the 2.883(2) Å distances found in the SnSb₃ trigonal pyramids in KSnSb.⁹ The Sb–Sn(1)–Sb and Sb–Sn(3)–Sb angles are considerably reduced (93.10(7)°–98.96(10)° and 94.14(7)°–98.40(9)°, respectively) from the ideal tetrahedral angles, consistent with the greater *p* character of the Sn–Sb bonds in such units. All of these Sn–Sb distances are close to 2.81 Å, the sum of the Pauling covalent radii of Sn and Sb atoms.²⁵

Two kinds of zigzag Sb–Sb chains are present in the structure of Ba₂Sn₃Sb₆. One kind forms part of the channel framework, and has Sb(5)–Sb(5) distances of 2.902(3) Å and angles of 98.9(1)°. The other is isolated on its own, and has Sb(1)–Sb(2) distances of 2.924(2) Å and angles of 97.87(10)°. Isolated zigzag Sb–Sb chains also occur, for instance, as the anionic part of the Zintl phases CaSb₂ and SrSb₂; these chains have Sb–Sb distances of 2.915(1)–2.939(1) Å and 2.895(2)–2.919(2) Å, respectively.^{26,27} These values are close to the 2.908 Å distance found in elemental antimony.²⁸

We are now in a position to propose a bonding model for Ba₂Sn₃Sb₆. Applying the Zintl concept results in the partial formulation (Ba²⁺)₂[Sn₃Sb₆]⁴⁻. If we assume that full two-electron single Sb–Sb bonds occur in the isolated zigzag chains, the oxidation states Sb(1)^{-I} and Sb(2)^{-I} can be assigned for these two-bonded Sb atoms. The three-coordinate Sb atoms forming part of the channel framework are assigned all of the electrons in their octets, being the more electronegative partners of the Sn–Sb bonds, resulting in Sb(3)^{-III}, Sb(4)^{-III}, and Sb(6)^{-III}. The Sb(5) atom also forms two single Sb–Sb bonds to symmetry-equivalents of itself, and are assigned as Sb(5)^{-I}. The assignment of Sb^{-I} in the zigzag chains is consistent with that of Sr^{II}(Sb^{-I})₂,²⁷ for instance. Proceeding

to the Sn atoms, we conclude that those in the trigonal pyramidal coordination must be Sn(1)^{II} and Sn(3)^{II}, while that in the tetrahedral coordination must be Sn(2)^{IV}. Again, this is consistent with the assignment of trigonal pyramidal⁹ Sn^{II} in K^ISn^{II}Sb^{-III} and tetrahedral Sn^{IV} in (K^I)₈(Sn^{IV})(Sb^{-III})₄ or (Na^I)₅(Sn^{IV})(Sb^{-III})₃.⁷ Note also the slightly longer Sn–Sb distances in the trigonal pyramids (Table 2–3), in agreement with the larger size expected for Sn^{II}. The presence of a stereochemically active lone pair on the Sn^{II} atoms is evident, given that it points inside the channel in an orientation that allows it to interact with the Ba²⁺ cations. Thus, Ba₂Sn₃Sb₆ is also interesting in being a *mixed-valence* compound. It is convenient to give the crystal chemical formulation as: (Ba²⁺)₂ ⋯₃ [(Sn^{II})₂(Sn^{IV})(Sb^{-III})₃(Sb^{-I})]²⁻ ⋯₁ [(Sb^{-I})₂]²⁻, in which the separate anionic substructures of the channel framework and the isolated zigzag chains are explicitly indicated.

The bonding model above was based on the assignment of *oxidation states*, a useful notion that helps to rationalize the coordination geometries of the Sn atoms in the structure. However, given the similar electronegativities of Sn and Sb, it should not be thought that the actual charge distribution resembles as extreme a situation as implied by the oxidation state assignment, which is, after all, a formalism. Rather, the Sn–Sb bonds are expected to be highly covalent. The alternative but equivalent approach based on *formal charges* leads to the assignment of 3-bonded Sn¹⁻, 4-bonded Sn⁰, 2-bonded Sb¹⁻, and 3-bonded Sb⁰. When different isosteric combinations are considered for the anionic substructure,¹ the same conclusion is reached for the distribution of Sn and Sb atoms as before.

In conclusion, the preceding arguments strongly support an ordered, stoichiometric model for the structure of the novel compound Ba₂Sn₃Sb₆, which provides

a good example of the structural diversity that Zintl phases can adopt. The anionic framework is remarkable for its combination of heteroatomic associations (Sn–Sb) with homoatomic ones (Sb–Sb). It will be interesting to see if the same structure is retained upon substitution of the alkaline earth. Mössbauer spectroscopy would be helpful in confirming the mixed-valent nature of the Sn atoms, as the chemical isomer shifts of trigonal pyramidal and tetrahedral Sn atoms should be resolvable.¹² We envisage measuring the physical properties and attempting to formulate a more quantitative description of the bonding through electronic band structure calculations.

Table 2–1. Crystallographic Data for Ba₂Sn₃Sb₆

Formula	Ba ₂ Sn ₃ Sb ₆
Formula mass, amu	1361.25
Space group	$D_{2h}^{16} - Pnma$ (No. 62)
a , Å	13.351(1) ^a
b , Å	4.4100(5) ^a
c , Å	24.449(3) ^a
V , Å ³	1439.5(3)
Z	4
T , °C	–50
Diffractometer	Enraf-Nonius CAD4
ρ_{calc} , g cm ^{–3}	6.281
Crystal dimensions, mm	Silver needle, 0.012 × 0.488 × 0.016
Radiation	Graphite-monochromated MoK α , $\lambda = 0.71073$ Å
$\mu(\text{MoK}\alpha)$, cm ^{–1}	214.9
Transmission factors ^b	0.666–0.780
Scan type	θ – 2θ
Scan speed, deg. min ^{–1}	2.0
Scan range, deg.	$0.8 + 0.344 \tan \theta$
2θ limits	$3^\circ \leq 2\theta(\text{MoK}\alpha) \leq 50^\circ$
Data collected	$-21 \leq h \leq 21, -7 \leq k \leq 7, 0 \leq l \leq 39$
No. of data collected	4949
No. of unique data, including $F_o^2 < 0$	1443 ($R_{\text{int}} = 0.191$)

Table 2–1. Crystallographic Data for Ba₂Sn₃Sb₆ (continued)

No. of unique data, with $F_o^2 > 2\sigma(F_o^2)$	977
No. of variables	68
Extinction coefficient ^c	0.00003(4)
$R(F)$ for $F_o^2 > 2\sigma(F_o^2)$ ^d	0.056
$R_w(F_o^2)$ ^e	0.105
Goodness of fit ^f	1.02
$(\Delta\rho)_{\max}, (\Delta\rho)_{\min}, e^{-\text{\AA}^{-3}}$	3.2, -2.4

^a Obtained from a refinement constrained so that $\alpha = \beta = \gamma = 90^\circ$.

^b A Gaussian-type absorption correction was applied, with the use of programs in the SHELXTL package (Sheldrick, G. M. SHELXTL Version 5.0, Siemens Analytical X-Ray Instruments, Inc., Madison, WI, 1994).

^c An extinction parameter x was refined, where F_c is multiplied by: $k[1 + 0.001 * x * F_c^2 * \lambda^3 / \sin(2\theta)]^{-1/4}$.

$$^d R(F) = \frac{\sum ||F_o| - |F_c||}{\sum |F_o|}$$

$$^e R_w(F_o^2) = \frac{[\sum [w(F_o^2 - F_c^2)^2]]^{1/2}}{[\sum wF_o^4]^{1/2}}; w^{-1} = [\sigma^2(F_o^2) + (0.0042P)^2 + 0.00P] \text{ where } P = [\max(F_o^2, 0) + 2F_c^2]/3.$$

$$^f \text{GooF} = S = \left[\frac{\sum [w(F_o^2 - F_c^2)^2]}{(n - p)} \right]^{1/2} \text{ where } n \text{ is the number of reflections and } p \text{ is the total number of parameters refined.}$$

Table 2–2. Atomic Coordinates, Occupancies, and Equivalent Isotropic DisplacementParameters (\AA^2) for $\text{Ba}_2\text{Sn}_3\text{Sb}_6$

Atom	Wyckoff position, site symmetry	<i>x</i>	<i>y</i>	<i>z</i>	Occupancy	U_{eq}^a
Ba(1)	4 <i>c</i> . <i>m</i> .	0.1312(1)	¼	0.10924(8)	1	0.0104(5)
Ba(2)	4 <i>c</i> . <i>m</i> .	0.0484(2)	¼	0.42043(8)	1	0.0113(5)
Sn(1)	4 <i>c</i> . <i>m</i> .	0.0417(2)	¼	0.24939(9)	1	0.0104(5)
Sn(2)	4 <i>c</i> . <i>m</i> .	0.1948(2)	¼	0.76595(9)	1	0.0109(5)
Sn(3)	4 <i>c</i> . <i>m</i> .	0.3205(2)	¼	0.40239(10)	1	0.0135(5)
Sb(1)	4 <i>c</i> . <i>m</i> .	0.1609(2)	¼	0.57758(9)	1	0.0123(5)
Sb(2)	4 <i>c</i> . <i>m</i> .	0.3017(2)	¼	0.00171(9)	1	0.0132(5)
Sb(3)	4 <i>c</i> . <i>m</i> .	0.3487(2)	¼	0.19674(9)	1	0.0120(5)
Sb(4)	4 <i>c</i> . <i>m</i> .	0.3838(2)	¼	0.81486(9)	1	0.0119(5)
Sb(5)	4 <i>c</i> . <i>m</i> .	0.4297(2)	¼	0.50378(9)	1	0.0124(5)
Sb(6)	4 <i>c</i> . <i>m</i> .	0.5653(2)	¼	0.64425(9)	1	0.0116(5)

^a U_{eq} is defined as one-third of the trace of the orthogonalized U_{ij} tensor.

Table 2-3. Selected Interatomic Distances (Å) and Angles (°) for Ba₂Sn₃Sb₆

Sn(1)–Sb(3)	2.894(3)	Ba(1)–Sb(2)	3.478(3)
Sn(1)–Sb(4)	2.901(2) (2x)	Ba(1)–Sb(5)	3.489(2) (2x)
Sn(2)–Sb(4)	2.793(3)	Ba(1)–Sb(6)	3.533(2) (2x)
Sn(2)–Sb(6)	2.794(3)	Ba(1)–Sb(3)	3.607(3)
Sn(2)–Sb(3)	2.840(2) (2x)	Ba(1)–Sb(1)	3.628(2) (2x)
Sn(3)–Sb(5)	2.876(3)	Ba(1)–Sb(5)	3.857(3)
Sn(3)–Sb(6)	2.913(2) (2x)	Ba(1)–Sn(1)	3.629(3)
Sb(1)–Sb(2)	2.924(2) (2x)	Ba(2)–Sb(4)	3.513(2) (2x)
Sb(5)–Sb(5)	2.902(3) (2x)	Ba(2)–Sb(1)	3.560(2) (2x)
Ba(1)–Ba(1)	4.4100(5) (2x)	Ba(2)–Sb(2)	3.580(2) (2x)
Ba(2)–Ba(2)	4.4100(5) (2x)	Ba(2)–Sb(2)	3.804(3)
		Ba(2)–Sb(3)	3.913(3)
		Ba(2)–Sn(3)	3.659(3)
Sb(3)–Sn(1)–Sb(4)	93.10(7) (2x)	Sb(2)–Sb(1)–Sb(2)	97.87(10)
Sb(4)–Sn(1)–Sb(4)	98.96(10)	Sb(1)–Sb(2)–Sb(1)	97.87(10)
Sb(3)–Sn(2)–Sb(3)	101.89(10)	Sn(2)–Sb(3)–Sn(2)	101.89(10)
Sb(4)–Sn(2)–Sb(3)	116.11(7) (2x)	Sn(2)–Sb(3)–Sn(1)	84.89(7) (2x)
Sb(6)–Sn(2)–Sb(3)	109.99(7) (2x)	Sn(2)–Sb(4)–Sn(1)	94.21(7) (2x)
Sb(4)–Sn(2)–Sb(6)	102.85(10)	Sn(1)–Sb(4)–Sn(1)	98.96(10)
Sb(5)–Sn(3)–Sb(6)	94.14(7) (2x)	Sn(3)–Sb(5)–Sb(5)	105.85(10) (2x)
Sb(6)–Sn(3)–Sb(6)	98.40(9)	Sb(5)–Sb(5)–Sb(5)	98.9(1)
		Sn(2)–Sb(6)–Sn(3)	89.08(7) (2x)
		Sn(3)–Sb(6)–Sn(3)	98.40(9)

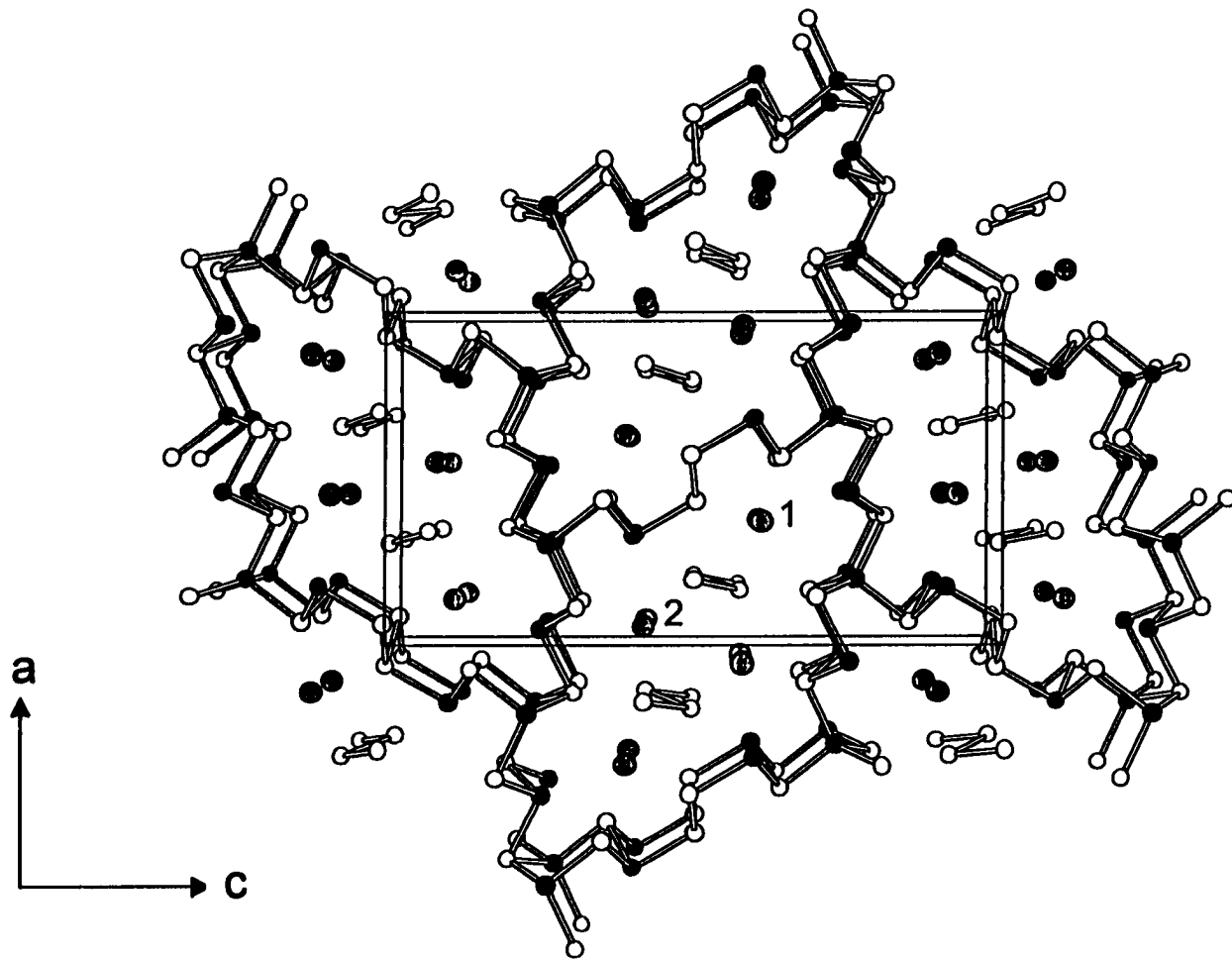


Figure 2-1. View down the b axis of $Ba_2Sn_3Sb_6$, with the unit cell outlined. The large lightly shaded circles are Ba atoms, the solid circles are Sn atoms, and the open circles are Sb atoms. The two types of Ba atoms are labeled.

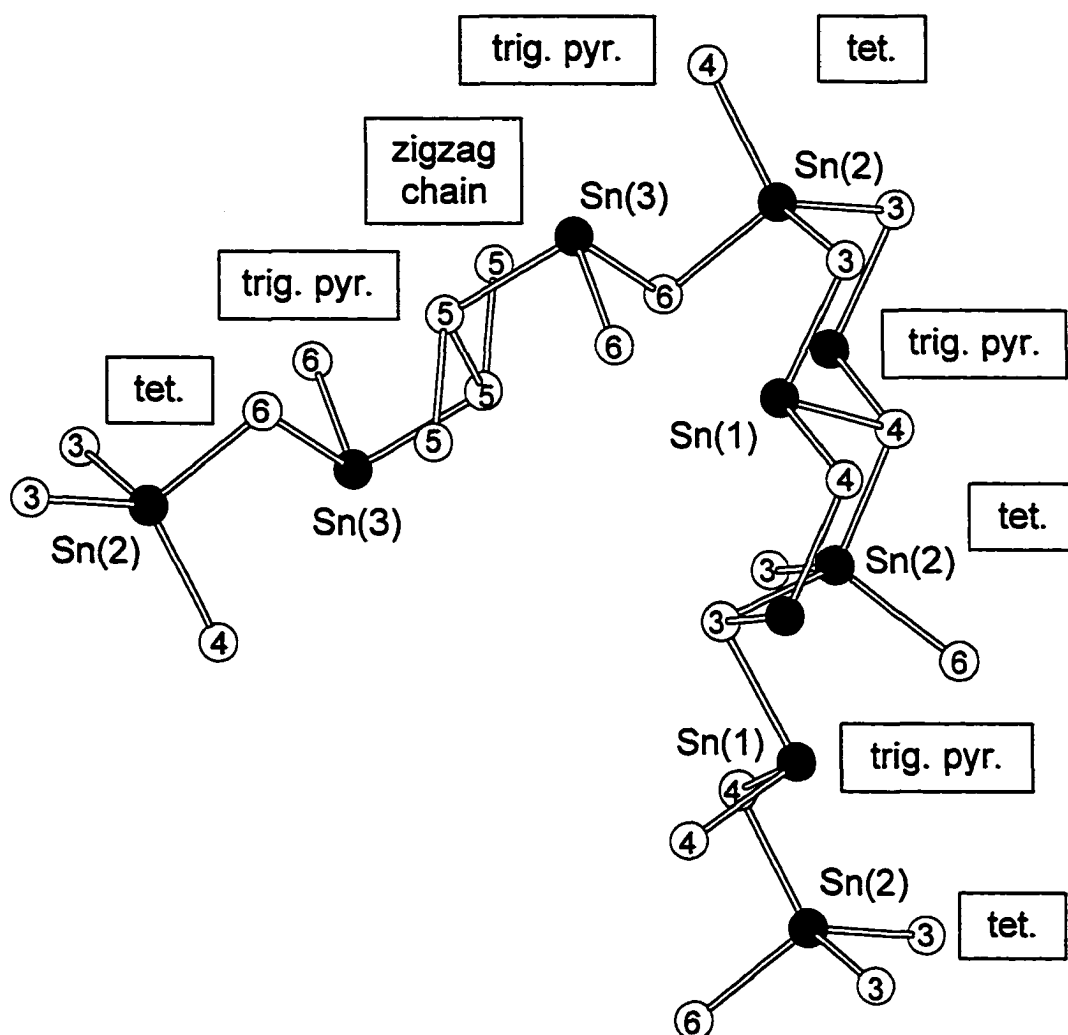


Figure 2-2. Detailed view of part of the anionic framework of $\text{Ba}_2\text{Sn}_3\text{Sb}_6$, showing the labeling of the Sn and Sb atoms. For clarity, only two sides making up the four-sided lozenge-shaped channels in Figure 2-1 are shown.

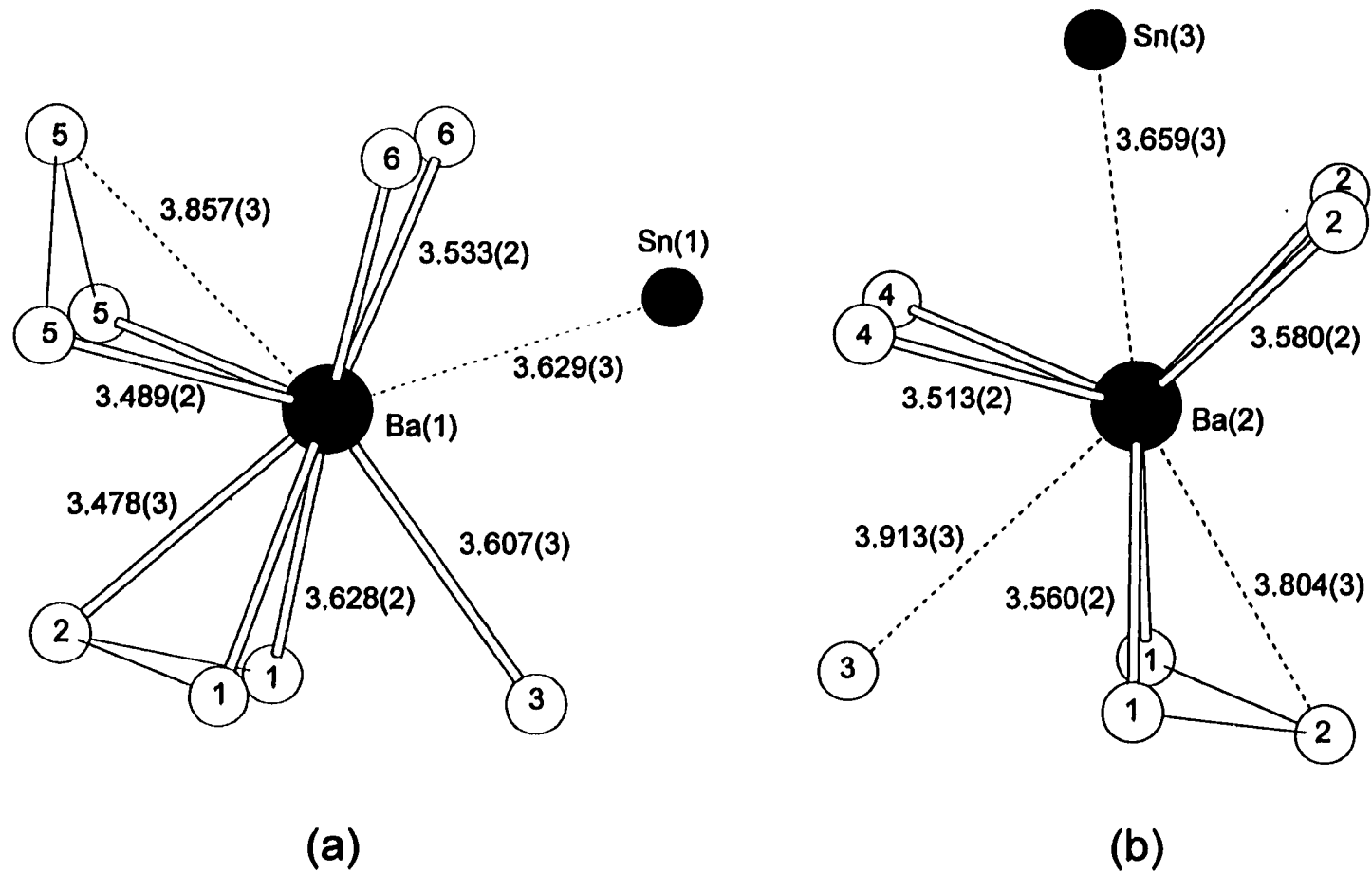


Figure 2–3. Coordination of the (a) Ba(1) and (b) Ba(2) atoms in $\text{Ba}_2\text{Sn}_3\text{Sb}_6$. Relevant interatomic distances (Å) are shown.

REFERENCES

- (1) Schäfer, H. *Annu. Rev. Mater. Sci.* **1985**, *15*, 1.
- (2) Corbett, J. D. *Chem. Rev.* **1985**, *85*, 383.
- (3) von Schnering, H. G. *Angew. Chem., Int. Ed. Engl.* **1981**, *20*, 33.
- (4) (a) $K_9In_9GeSb_{22}$: Schreeve-Keyer, J. L.; Haushalter, R. C.; Seo, D.-K.; Whangbo, M.-H. *J. Solid State Chem.* **1996**, *122*, 239. (b) $Na_3K_6Sb(AlSb_3)$: Somer, M.; Carillo-Cabrera, W.; Peters, E.-M.; Peters, K.; von Schnering, H. G. *Z. Kristallogr.* **1995**, *210*, 527. (c) $Na_3K_6Sb(GaSb_3)$: Somer, M.; Carillo-Cabrera, W.; Peters, E.-M.; Peters, K.; von Schnering, H. G. *Z. Kristallogr.* **1995**, *210*, 143. (d) $K_{10}In_5Sb_9$: Blase, W.; Cordier, G.; Somer, M. *Z. Kristallogr.* **1993**, *203*, 146. (e) $K_2Na(InSb_2)$: Carillo-Cabrera, W.; Caroca-Canales, N.; von Schnering, H. G. *Z. Anorg. Allg. Chem.* **1993**, *619*, 1717. (f) Rb_6AlSb_3 : Blase, W.; Cordier, G.; Somer, M. *Z. Kristallogr.* **1992**, *199*, 279. (g) Cs_6GaSb_3 : Blase, W.; Cordier, G.; Somer, M. *Z. Kristallogr.* **1992**, *199*, 277. (h) $KGaSb_2$: Cordier, G.; Ochmann, H. *Z. Kristallogr.* **1991**, *197*, 297. (i) $K_2In_2Sb_3$: Cordier, G.; Ochmann, H. *Z. Kristallogr.* **1991**, *197*, 291. (j) $K_2Ga_2Sb_3$: Cordier, G.; Ochmann, H. *Z. Kristallogr.* **1991**, *197*, 289. (k) $Na_2In_2Sb_3$: Cordier, G.; Ochmann, H. *Z. Kristallogr.* **1991**, *197*, 281. (l) $Cs_{3.31}K_{2.25}Rb_{1.44}Ga_2Sb_5$: Somer, M.; Peters, K.; von Schnering, H. G. *Z. Kristallogr.* **1991**, *197*, 249. (m) $K_3Cs_6Sb(AlSb_3)$: Somer, M.; Peters, K.; von Schnering, H. G. *Z. Kristallogr.* **1991**, *195*, 316. (n) Cs_2GaSb_2 : Cordier, G.; Ochmann, H. *Z. Kristallogr.* **1991**, *195*, 310. (o) $KAlSb_4$: Cordier, G.; Ochmann, H. *Z. Kristallogr.* **1991**, *195*, 308. (p) $KGaSb_4$: Cordier, G.; Ochmann, H. *Z. Kristallogr.* **1991**, *195*, 306. (q)

- Rb₂GaSb₂: Cordier, G.; Ochmann, H. *Z. Kristallogr.* **1991**, *195*, 125. (r)
- Na₃InSb₂: Cordier, G.; Ochmann, H. *Z. Kristallogr.* **1991**, *195*, 107. (s)
- K₃Cs₆Sb(GaSb₃): Somer, M.; Peters, K.; von Schnering, H. G. *Z. Kristallogr.* **1991**, *195*, 101. (t) K₄In₄Sb₆: Birdwhistell, T. L. T.; Klein, C. L.; Jeffries, T.; Stevens, E. D.; O'Connor, C. J. *J. Mater. Chem.* **1991**, *1*, 555. (u)
- Cs₆K₃Sb(AlSb₃), Cs₆K₃Sb(GaSb₃): Somer, M.; Peters, K.; Popp, T.; von Schnering, H. G. *Z. Anorg. Allg. Chem.* **1991**, *597*, 201. (v) Cs₆AlSb₃: von Schnering, H. G.; Somer, M.; Peters, K.; Blase, W.; Cordier, G. *Z. Kristallogr.* **1990**, *193*, 283. (w) K₂₀Ga₆Sb_{12.66}: Cordier, G.; Ochmann, H. *Z. Naturforsch. B: Chem. Sci.* **1990**, *45*, 277. (x) Na₂Ga₃Sb₃: Cordier, G.; Ochmann, H.; Schäfer, H. *Mater. Res. Bull.* **1986**, *21*, 331. (y) K₂GaSb₂: Cordier, G.; Ochmann, H.; Schäfer, H. *J. Less-Common Met.* **1986**, *119*, 291. (z) Na₇Al₂Sb₅: Cordier, G.; Ochmann, H.; Schäfer, H. *Z. Anorg. Allg. Chem.* **1984**, *517*, 118. (aa) K₂Al₂Sb₃, Na₂Al₂Sb₃: Cordier, G.; Ochmann, H.; Schäfer, H. *Rev. Chim. Miner.* **1984**, *21*, 282.
- (5) (a) Ca₁₁MSb₉ (M = Al, Ga, In): Young, D. M.; Kauzlarich, S. M. *Chem. Mater.* **1995**, *7*, 206. (b) A₁₄AlSb₁₁ (A = Ca, Sr, Ba): Brock, S. L.; Weston, L. J.; Olmstead, M. M.; Kauzlarich, S. M. *J. Solid State Chem.* **1993**, *107*, 513. (c) Sr₅Al₂Sb₆, Ba₅In₂Sb₆: Cordier, G.; Stelter, M. *Z. Naturforsch. B: Chem. Sci.* **1988**, *43*, 463. (d) Sr₃GaSb₃: Cordier, G.; Schäfer, H.; Stelter, M. *Z. Naturforsch. B: Chem. Sci.* **1987**, *42*, 1268. (e) Ba₇Ga₄Sb₉: Cordier, G.; Schäfer, H.; Stelter, M. *Z. Anorg. Allg. Chem.* **1986**, *534*, 137. (f) Ba₃GaSb₃: Cordier, G.; Schäfer, H.; Stelter, M. *Z. Naturforsch. B: Anorg. Chem., Org.*

- Chem.* 1985, 40, 1100. (g) $\text{Ca}_{11}\text{InSb}_9$: Cordier, G.; Schäfer, H.; Stelter, M. *Z. Naturforsch. B: Anorg. Chem., Org. Chem.* 1985, 40, 868. (h) $\text{Ca}_5\text{Ga}_2\text{Sb}_6$, $\text{Ca}_5\text{In}_2\text{Sb}_6$, $\text{Sr}_5\text{In}_2\text{Sb}_6$: Cordier, G.; Schäfer, H.; Stelter, M. *Z. Naturforsch. B: Anorg. Chem., Org. Chem.* 1985, 40, 5. (i) $\text{Ca}_{14}\text{AlSb}_{11}$: Cordier, G.; Schäfer, H.; Stelter, M. *Z. Anorg. Allg. Chem.* 1984, 519, 183. (j) Ca_3AlSb_3 : Cordier, G.; Schäfer, H.; Stelter, M. *Z. Naturforsch. B: Anorg. Chem., Org. Chem.* 1984, 39, 727. (k) Sr_3AlSb_3 : Cordier, G.; Stelter, M.; Schäfer, H. *J. Less-Common Met.* 1984, 98, 285. (l) Ba_3AlSb_3 : Cordier, G.; Savelsberg, G.; Schäfer, H. *Z. Naturforsch. B: Anorg. Chem., Org. Chem.* 1982, 37, 975. (m) $\text{Ca}_5\text{Al}_2\text{Sb}_6$: Cordier, G.; Czech, E.; Jakowski, M.; Schäfer, H. *Rev. Chim. Miner.* 1981, 18, 9.
- (6) Eisenmann, B.; Klein, J. *Z. Naturforsch. B: Chem. Sci.* 1988, 43, 69.
- (7) Eisenmann, B.; Klein, J. *Z. Naturforsch. B: Chem. Sci.* 1988, 43, 1156.
- (8) Eisenmann, B.; Klein, J. *Z. Kristallogr.* 1991, 196, 213.
- (9) Eisenmann, B.; Klein, J. *Z. Anorg. Allg. Chem.* 1991, 598/599, 93.
- (10) Lii, K.-H.; Haushalter, R. C. *J. Solid State Chem.* 1987, 67, 374.
- (11) Schmidt, P. C.; Stahl, D.; Eisenmann, B.; Kniep, R.; Eyert, V.; Kübler, J. *J. Solid State Chem.* 1992, 97, 93.
- (12) Asbrand, M.; Berry, F. J.; Eisenmann, B.; Kniep, R.; Smart, L. E.; Thied, R. C. *J. Solid State Chem.* 1995, 118, 397.
- (13) Asbrand, M.; Eisenmann, B. *Z. Kristallogr.* 1992, 198, 309.
- (14) Bol'shakov, K. A.; Bul'onkov, N. A.; Yakovenko, A. G.; Sakharov, V. V.; Nedev, S. K.; Il'in, E. G. *Inorg. Mater. (Engl. Transl.)* 1968, 4, 1051.

- (15) Bol'shakov, K. A.; Bul'onkov, N. A.; Rastorguev, L. N.; Tsirlin, M. S. *Russ. J. Inorg. Chem. (Engl. Transl.)* **1963**, *8*, 1418.
- (16) Bol'shakov, K. A.; Bul'onkov, N. A.; Rastorguev, L. N.; Umanskii, Ya. S.; Tsirlin, M. S. *Russ. J. Inorg. Chem. (Engl. Transl.)* **1963**, *8*, 1421.
- (17) Jönsson, B.; Ågren, J. *Z. Metallkd.* **1987**, *78*, 810.
- (18) Abel, E.; Redlich, O.; Spausta, F. *Z. Anorg. Allg. Chem.* **1930**, *194*, 79.
- (19) POLSQ: Program for least-squares unit cell refinement. Modified by D. Cahen and D. Keszler, Northwestern University, 1983.
- (20) Yvon, K.; Jeitschko, W.; Parthé, E. *J. Appl. Crystallogr.* **1977**, *10*, 73.
- (21) Sheldrick, G. M. SHELXTL Version 5.0, Siemens Analytical X-ray Instruments, Inc., Madison, WI, 1994.
- (22) Sheldrick, G. M. *J. Appl. Crystallogr.*, in press.
- (23) *International Tables for X-ray Crystallography*; Wilson, A. J. C., Ed.; Kluwer: Dordrecht, 1992; Vol. C.
- (24) Gelato, L. M.; Parthé, E. *J. Appl. Crystallogr.* **1987**, *20*, 139.
- (25) Pauling, L. *The Nature of the Chemical Bond*, 3rd ed.; Cornell University Press: Ithaca, NY, 1960.
- (26) Deller, K.; Eisenmann, B. *Z. Anorg. Allg. Chem.* **1976**, *425*, 104.
- (27) Deller, K.; Eisenmann, B. *Z. Naturforsch. B: Anorg. Chem., Org. Chem.* **1976**, *31*, 1146.
- (28) Donohue, J. *The Structures of the Elements*; Wiley: New York, 1974.

CHAPTER 3

Ternary Antimonide EuSn_3Sb_4 and Related Metallic Zintl

Phases[†]

INTRODUCTION

The Zintl concept provides a convenient approach to rationalizing the structure and bonding of many solid-state compounds consisting of an electropositive (alkali metal, alkaline-earth, or rare-earth elements) and an electronegative component (*p*-block elements).¹⁻⁴ The diversity of structures that can be explained by this set of rules, which prescribes that the electronegative atoms attain an octet through formation of covalent bonds or presence of lone pairs, is evidence of the ubiquity of this scheme. Since an energy gap is usually expected between occupied (bonding and nonbonding) and unoccupied (antibonding) states in the electronic structure of closed-shell systems, the assumption that Zintl compounds should be semiconductors, in general, may have discouraged the actual measurement of their electronic properties. Especially with the heavier main-group elements, metallic behaviour can arise through increased band overlap, diminished band gaps, or partial electron transfer from cations to the anionic

[†] A version of this chapter has been published. Lam, R.; Zhang, J.; Mar, A. *J. Solid State Chem.* 2000, 150, 371. Copyright 2000 Academic Press.

network.⁵ Some of these metallic Zintl phases include La_3In_5 ⁶ and the CMR materials $A_{14}\text{Mn}Pn_{11}$ ($A = \text{Eu, Sr}; Pn = \text{Sb, Bi}$).⁷⁻⁹

Previously we prepared two new ternary alkaline-earth tetrel antimonides, SrSn_3Sb_4 ¹⁰ and $\text{Ba}_2\text{Sn}_3\text{Sb}_6$,¹¹ which adopt related structures containing large channels made up of 30-membered rings. We now report here the preparation of another member, EuSn_3Sb_4 , and the resistivity measurements of the entire series. These are metallic Zintl phases whose electronic structures are analyzed through extended Hückel calculations.

EXPERIMENTAL SECTION

SYNTHESIS

Single crystals of EuSn_3Sb_4 used in the structure determination were obtained from a reaction of a 0.25-g mixture of Eu_2O_3 , Nb, and Sb in a 1:2:3 ratio (in an attempt to prepare a pnictide oxide), with an excess of Sn added (Eu_2O_3 , 97 mg, 0.28 mmol, 99.99%, donated from Changchun Institute of Applied Chemistry; Nb, 51 mg, 0.55 mmol, 99.8%, Cerac; Sb, 101 mg, 0.83 mmol, 99.995%, Aldrich; Sn, 0.50 g, 4.2 mmol, 99.8%, Cerac). The reactants were loaded into a sealed and evacuated fused-silica tube (8-cm length; 10-mm i.d.) which was heated at 600 °C for 5 h and 900 °C for 6 days, and then cooled to room temperature over 24 h. Some needle-shaped crystals were obtained after the excess Sn was dissolved with concentrated HCl. Windowless EDX (energy-dispersive X-ray) analysis of these crystals on a Hitachi S-2700 scanning electron microscope confirmed the presence of Eu, Sn, and Sb but more significantly showed the absence of Nb and O. Anal. Calcd. (mol %) for EuSn_3Sb_4 : Eu, 12; Sn, 38; Sb, 50.

Found (average of 10 analyses): Eu, 11(2); Sn, 36(2); Sb, 53(3). EuSn_3Sb_4 can be prepared rationally, albeit in low yield (~10% as gauged by powder X-ray diffraction), through the direct reaction of the elements at 1000 °C for 2 days in an evacuated fused-silica tube. The major competing phases are the binary antimonides SnSb and EuSb_2 . Arc-melting reactions on pressed pellets of mixtures of the elements result in only these binary antimonides. One member of the solid solution $\text{Sr}_{1-x}\text{Eu}_x\text{Sn}_3\text{Sb}_4$ ($x = 0.5$) could also be prepared by direct reaction of the elements at 950 °C for 2 days, although we have not elaborated the entire series.

STRUCTURE DETERMINATION

Weissenberg photography revealed Laue symmetry mmm and systematic extinctions ($0kl: k + l = 2n + 1; hk0: h = 2n + 1$) consistent with the orthorhombic space groups $D_{2h}^{16} - Pnma$ and $C_{2v}^9 - Pn2_1a$. Final cell parameters were determined from a least-squares analysis of the setting angles of 24 reflections in the range $20^\circ \leq 2\theta(\text{MoK}\alpha) \leq 38^\circ$ centred on an Enraf-Nonius CAD4 diffractometer. Crystal data and further details of the data collection are given in Table 3-1.

Calculations were carried out with the use of programs in the SHELXTL (Version 5.0) package.¹² Conventional atomic scattering factors and anomalous dispersion corrections were used.¹³ Intensity data were processed, and face-indexed Gaussian-type absorption corrections were applied. On the basis of similar intensity patterns, the centrosymmetric space group $Pnma$ was chosen and the initial atomic positions for EuSn_3Sb_4 were taken from those of SrSn_3Sb_4 .¹⁰ In particular, although Sn and Sb have similar scattering factors, we propose the same ordered model for EuSn_3Sb_4 as for

SrSn_3Sb_4 for reasons discussed previously.¹⁰ Refinements were performed by least-squares methods. Since refinements of occupancies lead to values ranging from 98(4) to 102(4)% for all atoms, we accept a fully stoichiometric model. The atomic positions were standardized using STRUCTURE TIDY.¹⁴ The final cycle of least-squares refinement on F_o^2 of 50 variables (including anisotropic displacement parameters and an isotropic extinction parameter) and 982 averaged reflections (including those having $F_o^2 < 0$) converged to residuals of $R_w(F_o^2)$ of 0.067 and $R(F)$ (for $F_o^2 > 2\sigma(F_o^2)$) of 0.028. Final values of the positional and isotropic displacement parameters are in Table 3–2, selected interatomic distances and angles are in Table 3–3. Anisotropic displacement parameters are given in Table A–3.

ELECTRICAL RESISTIVITY

Two single crystals of each of EuSn_3Sb_4 , SrSn_3Sb_4 , and $\text{Ba}_2\text{Sn}_3\text{Sb}_6$ (0.5 to 0.9 mm in length), confirmed by EDX measurements to be the ternary compounds, were mounted with Ag paint on Au wires with graphite extensions. Four-probe ac electrical resistivity measurements were made along the needle axis b of all crystals between 25 and 290 K. The measurements are reproducible between the two samples of each compound.

BAND STRUCTURE

One-electron band structure calculations on the anionic channel frameworks $[\text{Sn}_3\text{Sb}_4]^{2-}$ (in EuSn_3Sb_4 or SrSn_3Sb_4) and $[\text{Sn}_3\text{Sb}_6]^{4-}$ (in $\text{Ba}_2\text{Sn}_3\text{Sb}_6$) were performed using the EHMACC suite of programs.^{15,16} Extended Hückel parameters used for Sn ($H_{ii}(\text{eV})$: -16.16 (5s), -8.32 (5p); ζ_I : 2.12 (5s), 1.82 (5p)) and Sb ($H_{ii}(\text{eV})$: -18.8 (5s),

-11.7 (5p); ζ_1 : 2.323 (5s), 1.999 (5p)) were taken from literature values.^{17,18} Properties were extracted from the band structure using 80 k -points in the irreducible portion of the Brillouin zone.¹⁹

RESULTS AND DISCUSSION

DESCRIPTION OF THE STRUCTURE

In structures of Zintl compounds, the cations play an important role in influencing the shape of the anionic substructure through ionic interactions. Given the values of ionic radii of divalent cations (Eu²⁺, 1.25; Sr²⁺, 1.26; Ba²⁺, 1.42 Å for CN8),²⁰ it is not surprising that EuSn₃Sb₄ and SrSn₃Sb₄ are isostructural, while Ba₂Sn₃Sb₆ is different. Detailed descriptions of these two structure types, shown down their short b axis in Figure 3–1, have been given before,^{10,11} but it is instructive to review the major features for the purposes of later discussion of the band structures. Both structures possess channels defined by an anionic framework $\text{[Sn}_3\text{Sb}_4\text{]}^{2-}$, made up of 30-membered rings, and constructed from SnSb₄ tetrahedra, SnSb₃ trigonal pyramids, and Sb–Sb zigzag chains connected in the same sequence but in different conformations. The larger channels in Ba₂Sn₃Sb₆ accommodate additional Ba²⁺ cations and isolated Sb–Sb zigzag chains $\text{[Sb}_2\text{]}^{2-}$ (isosteric with neutral chains of two-bonded chalcogen atoms) to give an overall anionic network $\text{[Sn}_3\text{Sb}_6\text{]}^{4-}$. A comparison of metrical details (Table 3–4) reveals the relative constancy of the SnSb₄ tetrahedra and SnSb₃ trigonal pyramids in the three structures, with consistently longer Sn–Sb bonds in the trigonal pyramids reflecting the lower valency of the Sn atoms possessing a lone pair. The Sn–Sb anionic frameworks

in EuSn_3Sb_4 and SrSn_3Sb_4 are practically identical, so any differences in the properties of these two compounds would have to originate with the divalent cation.

RESISTIVITY

Figure 3–2 shows the electrical resistivities of $A\text{Sn}_3\text{Sb}_4$ ($A = \text{Eu}, \text{Sr}$) and $\text{Ba}_2\text{Sn}_3\text{Sb}_6$ measured along b , the direction along which the channels run. All three compounds are poorly metallic. EuSn_3Sb_4 and SrSn_3Sb_4 show nearly identical behaviour ($\rho_{290} = 3.4 \times 10^{-3} \Omega \text{ cm}$, $\rho_{25} = 2.2 \times 10^{-3} \Omega \text{ cm}$, $\rho_{290}/\rho_{25} = 1.5$), and are both poorer conductors by an order of magnitude than $\text{Ba}_2\text{Sn}_3\text{Sb}_6$ ($\rho_{290} = 3.3 \times 10^{-4} \Omega \text{ cm}$, $\rho_{25} = 3.9 \times 10^{-5} \Omega \text{ cm}$, $\rho_{290}/\rho_{25} = 8.5$).

BAND STRUCTURE

To probe the origin of metallic conductivity and to analyze the bonding more fully in $A\text{Sn}_3\text{Sb}_4$ ($A = \text{Eu}, \text{Sr}$) and $\text{Ba}_2\text{Sn}_3\text{Sb}_6$, the band structures of their anionic frameworks were calculated. Isolating a single channel from the ${}^3[\text{Sn}_3\text{Sb}_4]^{2-}$ framework common to both structure types results in ${}^1[\text{Sn}_{14}\text{Sb}_{22}]$, where the coordination of Sb atoms has been completed around all tetrahedral Sn atoms which serve to link neighbouring channels together. As shown in Figure 3–3(a) and (b), the density of states (DOS) curves for such isolated channels in $A\text{Sn}_3\text{Sb}_4$ ($A = \text{Eu}, \text{Sr}$) and $\text{Ba}_2\text{Sn}_3\text{Sb}_6$ are grossly similar, which is expected since they are constructed from the same composition and sequence of building units. Although there are two manifolds of states, the lower energy one originating largely from more electronegative Sb and the higher energy one from less electronegative Sn, there is substantial mixing of Sn and Sb states, indicative of

the strong covalent character of the bonding within these networks. There is a small band gap (<1 eV) located near -6.5 eV in both cases. If the octets were completed on all atoms making up these isolated channels $\frac{1}{2}[\text{Sn}_{14}\text{Sb}_{22}]$, the charge on this formula unit would be $18-$. Such an electron count would indeed just fill up all the lower energy states, leaving a band gap and implying semiconducting behaviour. Inclusion of the isolated Sb–Sb zigzag chains within the channels in $\text{Ba}_2\text{Sn}_3\text{Sb}_6$ introduces additional Sb–Sb bonding and antibonding levels which narrows, but does not completely remove the energy gap (Figure 3–3(c)).

Of course, these channels do not exist in isolation in the real structures but are linked up to neighbouring channels through each of the SnSb_4 tetrahedra. Figure 3–4(a) shows how a portion of one channel in the $A\text{Sn}_3\text{Sb}_4$ ($A = \text{Eu}, \text{Sr}$) structure is connected to a neighbouring channel (reference should be made to Figure 3–1(a) to compare with the complete structure). The electron count described above leaves lone pairs on all terminal Sb atoms of the SnSb_4 tetrahedra. Two of these pairs reside in orbitals oriented to form additional Sn–Sb bonds (Figure 3–4(b)), but to avoid repulsive $2c-4e^-$ interactions, loss of e^- must occur. Effectively, this lowers the Fermi level, so that in the DOS curves of the full three-dimensional structures of the anionic frameworks in $A\text{Sn}_3\text{Sb}_4$ ($A = \text{Eu}, \text{Sr}$) and $\text{Ba}_2\text{Sn}_3\text{Sb}_6$ (Figure 3–5), the Fermi level lies just below the top edge of the lower energy manifold in a region of low DOS, leading to the observed metallic behaviour. Interestingly, the additional interactions arising from linking the channels in the a and c directions are sufficient in themselves to induce further band broadening so that no energy gap is present (Figure 3–5).

Figure 3–6 shows the band dispersion curves along the special directions in the Brillouin zone parallel to the crystallographic axes. In both ASn_3Sb_4 ($A = \text{Eu}, \text{Sr}$) and $Ba_2Sn_3Sb_6$, the Fermi level crosses bands of significant dispersion only along ΓY , parallel to the direction along which the channels run. The metallic conductivity is thus predicted to be highly anisotropic, although the small dimensions of the crystals along the other directions have precluded further measurements. The bands crossed by the Fermi level are dispersed over the range -10 to -6 eV in both structure types along ΓY . The better conduction observed in $Ba_2Sn_3Sb_6$ is probably attributable to the greater number of bands crossed (six) than in ASn_3Sb_4 ($A = \text{Eu}, \text{Sr}$) (four) along ΓY . Analysis of the orbital composition of bands crossed by the Fermi level shows primarily p character belonging to atoms comprising the $SnSb_4$ tetrahedra and $SnSb_3$ trigonal pyramids (but not the Sb–Sb zigzag chains).

The crystal orbital overlap population (COOP) curves shown in Figure 3–7 confirm that predominantly Sn–Sb and Sb–Sb bonding levels are occupied up to the Fermi level. The states from -10 to -6 eV can be associated with contributions from Sn–Sb nonbonding levels, originating from lone pairs on Sn atoms. The cumulated overlap populations are large (Sn–Sb, 0.59; Sb–Sb, 0.55) for these ~ 2.9 Å interactions, implying full single bonds.

The metallic compounds ASn_3Sb_4 ($A = \text{Eu}, \text{Sr}$) and $Ba_2Sn_3Sb_6$ may be compared to the series of layered compounds $KSnPn$ ($Pn = \text{As}, \text{Sb}$) (21, 22) and $SrSn_2As_2$,²³ which consist of single or double As-like sheets, respectively, of corner-sharing $SnPn_3$ trigonal pyramids. Calculations suggest that the already small band gap in $KSnPn$ diminishes even further on going to $SrSn_2As_2$ because of increased interactions between the

sheets.^{5,24} In a sense, the walls of the channels in ASn_3Sb_4 ($A = \text{Eu, Sr}$) and $Ba_2Sn_3Sb_6$ may be regarded as As-like sheets of $SnSb_3$ trigonal pyramids that are warped and folded back on themselves. Additional bonding interactions through the formation of $SnSb_4$ tetrahedra when neighbouring channels are adjoined serve as a source of band broadening that leads eventually to the disappearance of the band gap.

Table 3–1. Crystallographic Data for EuSn_3Sb_4

Formula	EuSn_3Sb_4
Formula mass, amu	995.03
Space group	$D_{2h}^{16} - Pnma$ (No. 62)
a , Å	9.954(2) ^a
b , Å	4.3516(7) ^a
c , Å	22.650(4) ^a
V , Å ³	981.2(3)
Z	4
T , °C	22
Diffractometer	Enraf-Nonius CAD4
ρ_{calc} , g cm ⁻³	6.736
Crystal dimensions, mm	0.41 × 0.03 × 0.03
Radiation	Graphite-monochromated $\text{MoK}\alpha$, $\lambda = 0.71073$ Å
$\mu(\text{MoK}\alpha)$, cm ⁻¹	245
Transmission factors ^b	0.274–0.564
Scan type	θ – 2θ
Scan speed, deg. min ⁻¹	1.7
Scan range, deg.	$1.0 + 0.344 \tan \theta$
2θ limits	$3^\circ \leq 2\theta(\text{MoK}\alpha) \leq 50^\circ$
Data collected	$-11 \leq h \leq 11, -5 \leq k \leq 5, 0 \leq l \leq 26$
No. of data collected	3382
No. of unique data, including $F_o^2 < 0$	982 ($R_{\text{int}} = 0.053$)

Table 3–1. Crystallographic Data for EuSn_3Sb_4 (continued)

No. of unique data, with $F_o^2 > 2\sigma(F_o^2)$	834
No. of variables	50
Extinction coefficient ^c	0.00041(8)
$R(F)$ for $F_o^2 > 2\sigma(F_o^2)$ ^d	0.028
$R_w(F_o^2)$ ^e	0.067
Goodness of fit ^f	1.09
$(\Delta\rho)_{\text{max}}, (\Delta\rho)_{\text{min}}, \text{e}^{-\text{\AA}^{-3}}$	1.8, -2.2

^a Obtained from a refinement constrained so that $\alpha = \beta = \gamma = 90^\circ$.

^b A Gaussian-type absorption correction was applied, with the use of programs in the SHELXTL package (Sheldrick, G. M. SHELXTL Version 5.0, Siemens Analytical X-Ray Instruments, Inc., Madison, WI, 1994).

^c An extinction parameter x was refined, where F_c is multiplied by: $k[1 + 0.001 * x * F_c^2 * \lambda^3 / \sin(2\theta)]^{-1/4}$.

$$^d R(F) = \frac{\sum ||F_o| - |F_c||}{\sum |F_o|}$$

$$^e R_w(F_o^2) = \frac{[\sum [w(F_o^2 - F_c^2)^2]]^{1/2}}{[\sum wF_o^4]^{1/2}}; w^{-1} = [\sigma^2(F_o^2) + (0.0367P)^2 + 0.00P] \text{ where } P = [\max(F_o^2, 0) + 2F_c^2]/3.$$

$$^f \text{Goof} = S = \left[\frac{\sum [w(F_o^2 - F_c^2)^2]}{(n - p)} \right]^{1/2} \text{ where } n \text{ is the number of reflections and } p \text{ is the total number of parameters refined.}$$

Table 3–2. Atomic Coordinates, Occupancies, and Equivalent Isotropic DisplacementParameters (\AA^2) for EuSn_3Sb_4

Atom	Wyckoff position, site symmetry	x	y	z	Occupancy	U_{eq}^a
Eu	4c .m.	0.06055(7)	¼	0.12946(3)	1	0.0159(2)
Sn(1)	4c .m.	0.27824(10)	¼	0.24954(4)	1	0.0192(2)
Sn(2)	4c .m.	0.35009(10)	¼	0.01098(4)	1	0.0232(2)
Sn(3)	4c .m.	0.45533(9)	¼	0.85038(4)	1	0.0169(2)
Sb(1)	4c .m.	0.03089(9)	¼	0.76859(3)	1	0.0171(2)
Sb(2)	4c .m.	0.20417(9)	¼	0.59370(4)	1	0.0182(2)
Sb(3)	4c .m.	0.21417(9)	¼	0.37625(4)	1	0.0180(2)
Sb(4)	4c .m.	0.57001(9)	¼	0.52978(4)	1	0.0194(2)

^a U_{eq} is defined as one-third of the trace of the orthogonalized U_{ij} tensor.

Table 3–3. Selected Interatomic Distances (Å) and Angles (°) for EuSn₃Sb₄

Sn(1)–Sb(1)	2.921(1) (2×)	Eu–Sb(2)	3.2978(9) (2×)
Sn(1)–Sb(3)	2.940(1)	Eu–Sb(1)	3.3007(8) (2×)
Sn(2)–Sb(2)	2.9217(9) (2×)	Eu–Sb(4)	3.3943(8) (2×)
Sn(2)–Sb(4)	2.937(2)	Eu–Sb(3)	3.450(1)
Sn(3)–Sb(2)	2.782(1)	Eu–Sb(4)	3.608(1)
Sn(3)–Sb(1)	2.798(1)	Eu–Sn(1)	3.478(1)
Sn(3)–Sb(3)	2.8150(9) (2×)	Eu–Sn(1)	3.925(1)
Sb(4)–Sb(4)	2.915(1) (2×)	Eu–Sn(2)	3.938(1)
Sb(1)–Sn(1)–Sb(1)	96.31(4)	Sn(3)–Sb(1)–Sn(1)	91.87(3) (2×)
Sb(1)–Sn(1)–Sb(3)	89.82(3) (2×)	Sn(1)–Sb(1)–Sn(1)	96.31(4)
Sb(2)–Sn(2)–Sb(2)	96.27(4)	Sn(3)–Sb(2)–Sn(2)	97.32(3) (2×)
Sb(2)–Sn(2)–Sb(4)	91.49(3) (2×)	Sn(2)–Sb(2)–Sn(2)	96.27(4)
Sb(2)–Sn(3)–Sb(1)	101.49(4)	Sn(3)–Sb(3)–Sn(3)	101.23(4)
Sb(2)–Sn(3)–Sb(3)	116.03(3) (2×)	Sn(3)–Sb(3)–Sn(1)	85.80(3) (2×)
Sb(1)–Sn(3)–Sb(3)	111.20(3) (2×)	Sb(4)–Sb(4)–Sb(4)	96.57(6)
Sb(3)–Sn(3)–Sb(3)	101.23(4)	Sb(4)–Sb(4)–Sn(2)	107.97(4) (2×)

Table 3-4. Comparison of Distances (Å) and Angles (°) in SnSb₄ Tetrahedra, SnSb₃ Trigonal Pyramids, and Sb-Sb Zigzag Chains in A₂Sn₃Sb₆ (A = Eu, Sr) and Ba₂Sn₃Sb₆

	EuSn ₃ Sb ₄	SrSn ₃ Sb ₄	Ba ₂ Sn ₃ Sb ₆
<i>d</i> (Sn-Sb) tet.	2.782(1)–2.8150(9)	2.788(2)–2.821(1)	2.793(3)–2.840(2)
<i>d</i> (Sn-Sb) trig. pyr.	2.921(1)–2.940(1)	2.920(1)–2.952(2)	2.876(3)–2.913(2)
<i>d</i> (Sb-Sb) zigzag	2.915(1)	2.920(2)	2.902(3)–2.924(2)
<(Sb-Sn-Sb) tet.	101.23(4)– 116.03(3)	101.24(6)– 115.65(4)	101.89(1)– 116.11(7)
<(Sb-Sn-Sb) trig. pyr.	89.82(3)–96.31(4)	90.91(5)–96.64(5)	93.10(7)–98.96(10)
<(Sb-Sb-Sb) zigzag	96.57(6)	96.61(9)	97.9(1)–98.9(1)

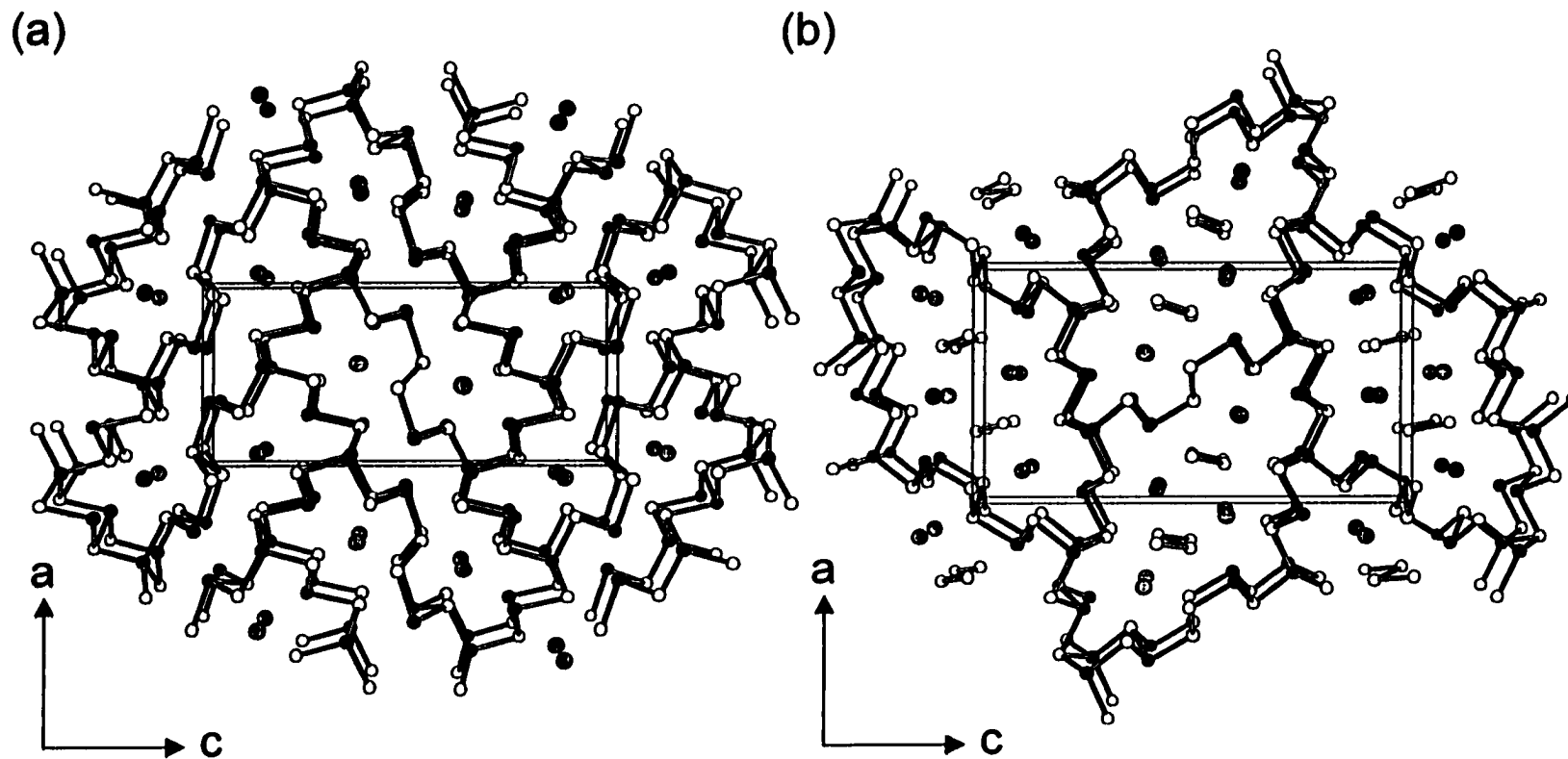


Figure 3-1. View down the *b* axis of the structures of (a) ASn_3Sb_4 ($A = \text{Eu, Sr}$) and (b) $Ba_2Sn_3Sb_6$, with the unit cells outlined. The large lightly-shaded circles are Eu, Sr, or Ba atoms, the solid circles are Sn atoms, and the open circles are Sb atoms.

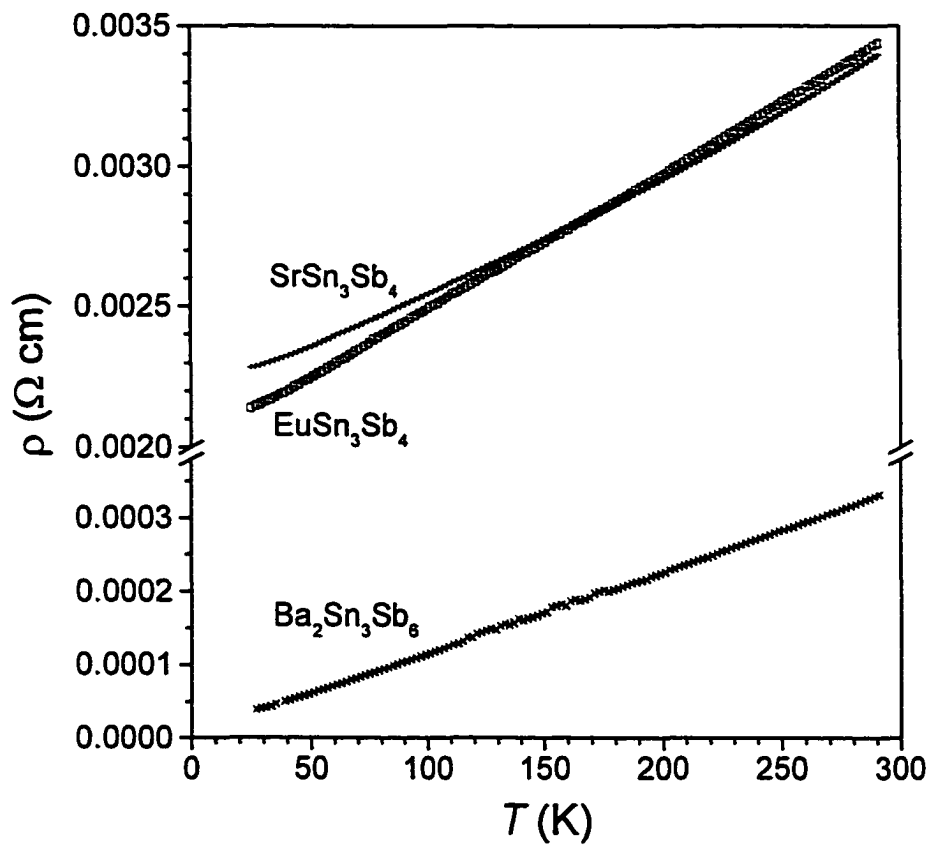


Figure 3–2. Plot of resistivity vs. temperature for $A\text{Sn}_3\text{Sb}_4$ ($A = \text{Eu}, \text{Sr}$) and $\text{Ba}_2\text{Sn}_3\text{Sb}_6$. The resistivity is measured along the needle axis b . Note the axis break.

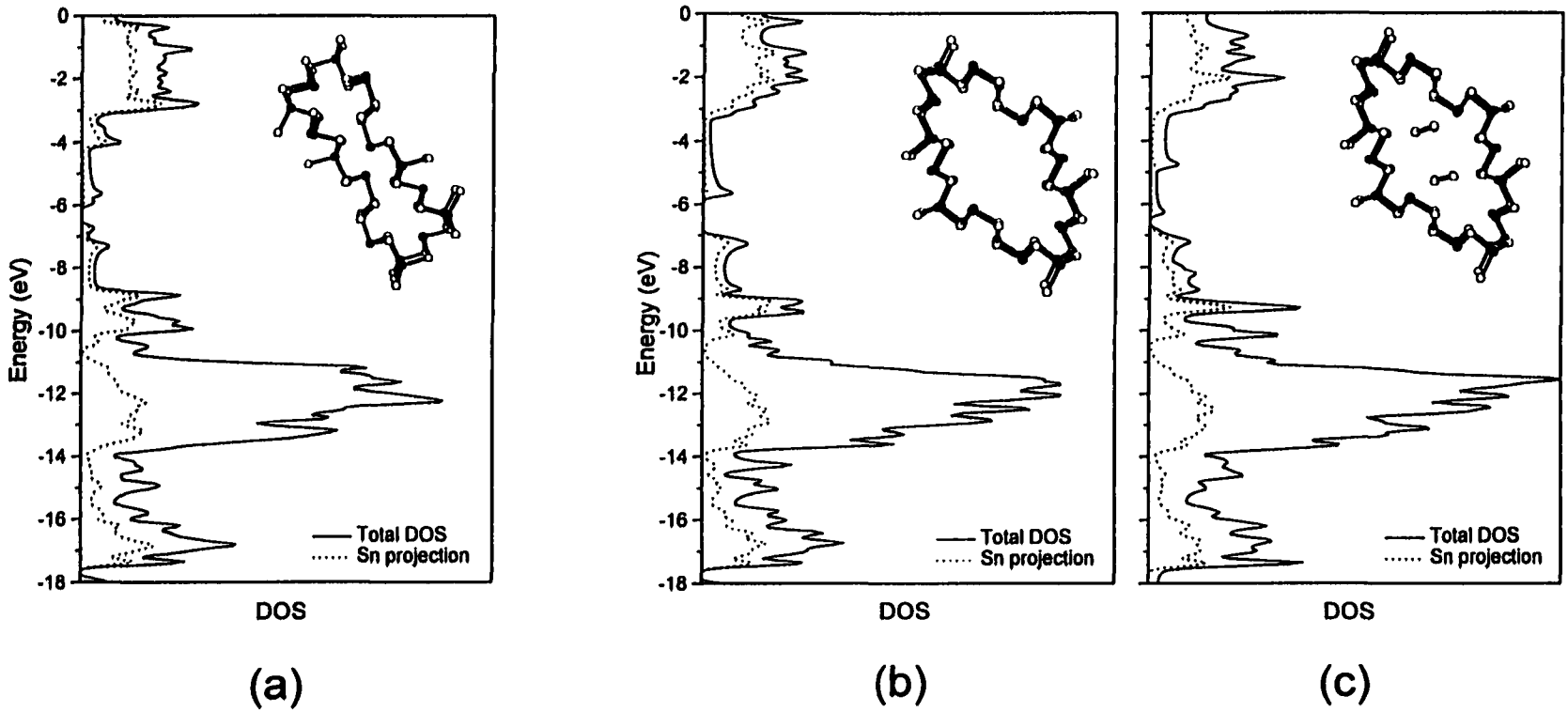


Figure 3-3. Density of states (DOS) for isolated one-dimensional channels ${}^1[Sn_{14}Sb_{22}]$ in (a) ASn_3Sb_4 ($A = Eu, Sr$) and (b) $Ba_2Sn_3Sb_6$ without and (c) with internal ${}^1[Sb_2]$ zigzag chains included. The Sn projection is shown by the dotted line; what remains of the total DOS is the Sb projection.

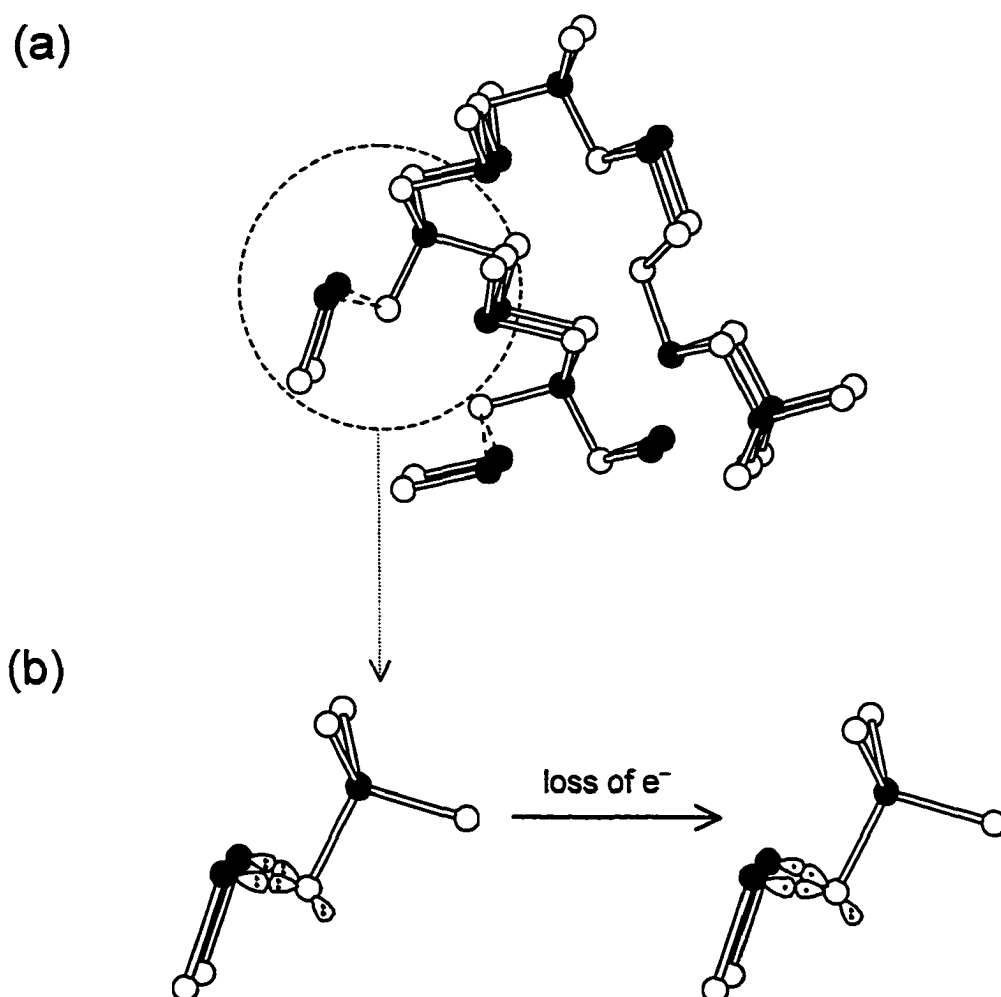


Figure 3-4. (a) Portion of the one-dimensional channel in ASn_3Sb_4 ($A = \text{Eu, Sr}$) being connected to a neighbouring channel through formation of Sn-Sb bonds (dashed lines). (b) A terminal Sb atom in one of the $SnSb_4$ tetrahedra loses electrons in the formation of Sn-Sb bonds to avoid repulsive interactions.

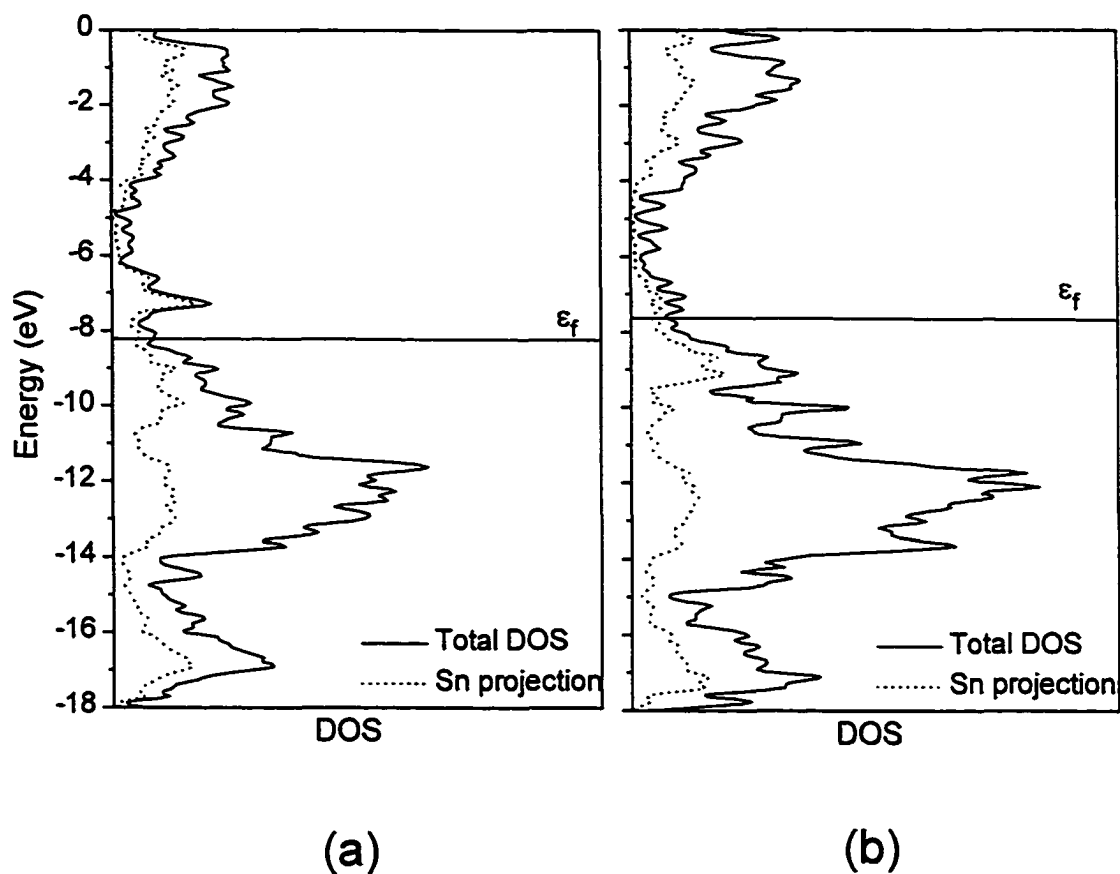
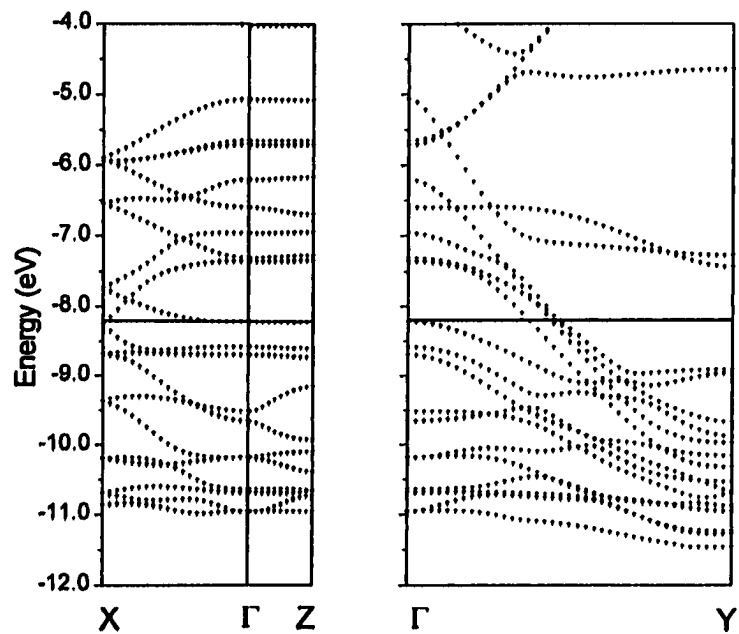
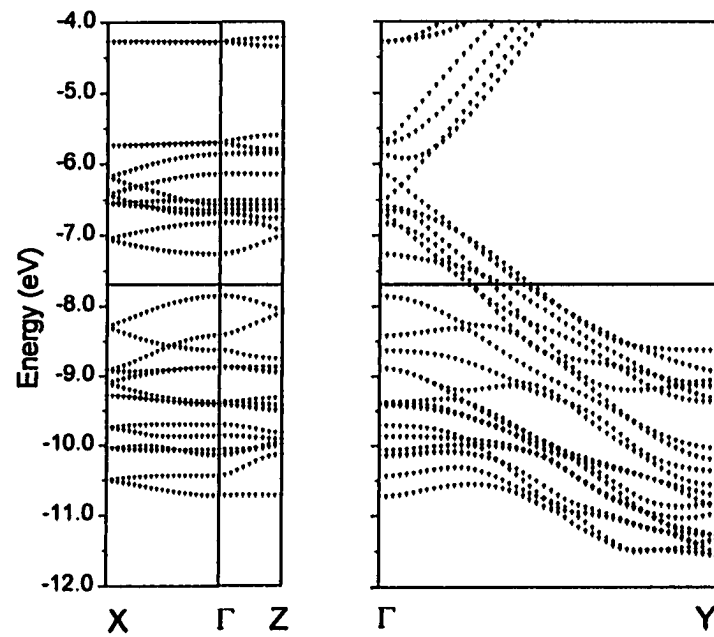


Figure 3–5. Total density of states (DOS) for the full three-dimensional anionic substructure of (a) ASn_3Sb_4 ($A = \text{Eu, Sr}$) and (b) $Ba_2Sn_3Sb_6$. The Fermi level (ϵ_f) is at -8.21 eV for ASn_3Sb_4 and -7.67 eV for $Ba_2Sn_3Sb_6$. The Sn projection is shown by the dotted line; what remains of the total DOS is the Sb projection.



(a) ${}^3[\text{Sn}_3\text{Sb}_4]^{2-}$ in $A\text{Sn}_3\text{Sb}_4$ ($A = \text{Eu}, \text{Sr}$)



(b) ${}^3[\text{Sn}_3\text{Sb}_6]^+$ in $\text{Ba}_2\text{Sn}_3\text{Sb}_6$

Figure 3–6. Band dispersion curves along special symmetry directions for the full three-dimensional anionic substructure of (a) $A\text{Sn}_3\text{Sb}_4$ ($A = \text{Eu}, \text{Sr}$) and (b) $\text{Ba}_2\text{Sn}_3\text{Sb}_6$. The Fermi level is shown by the horizontal line.

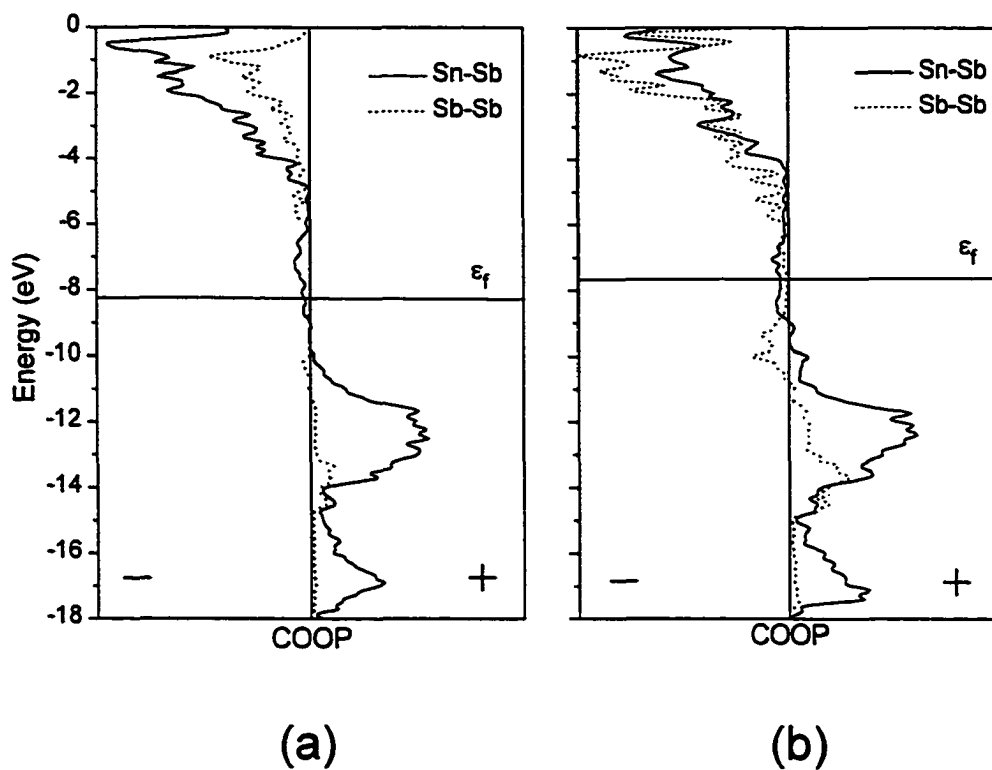


Figure 3–7. Crystal orbital overlap population (COOP) curves for ~ 2.9 Å Sn–Sb (solid line) and Sb–Sb (dashed line) interactions in the full three-dimensional anionic substructure of (a) ASn_3Sb_4 ($A = \text{Eu, Sr}$) and (b) $Ba_2Sn_3Sb_6$. The Fermi level is shown by the horizontal line.

REFERENCES

- (1) Schäfer, H. *Annu. Rev. Mater. Sci.* **1985**, *15*, 1.
- (2) Corbett, J. D. *Chem. Rev.* **1985**, *85*, 383.
- (3) von Schnering, H. G. *Angew. Chem., Int. Ed. Engl.* **1981**, *20*, 33.
- (4) Kauzlarich, S. M., Ed. *Chemistry, Structure, and Bonding of Zintl Phases and Ions*; VCH Publishers: New York, 1996 (and references therein).
- (5) Burdett, J. K. *Chemical Bonding in Solids*; Oxford University Press: New York, 1995.
- (6) Zhao, J.-T.; Corbett, J. D. *Inorg. Chem.* **1995**, *34*, 378.
- (7) Chan, J. Y.; Kauzlarich, S. M.; Klavins, P.; Shelton, R. N.; Webb, D. J. *Chem. Mater.* **1997**, *9*, 3132.
- (8) Chan, J. Y.; Kauzlarich, S. M.; Klavins, P.; Shelton, R. N.; Webb, D. J. *Phys. Rev. B: Condens. Matter* **1998**, *57*, R8103.
- (9) Webb, D. J.; Cohen, R.; Klavins, P.; Shelton, R. N.; Chan, J. Y.; Kauzlarich, S. M. *J. Appl. Phys.* **1998**, *83*, 7192.
- (10) Chow, D. T.; McDonald, R.; Mar, A. *Inorg. Chem.* **1997**, *36*, 3750.
- (11) Lam, R.; Mar, A. *Inorg. Chem.* **1996**, *35*, 6959.
- (12) Sheldrick, G. M. *SHELXTL Version 5.0*; Siemens Analytical X-ray Instruments, Inc.: Madison, WI, 1994.
- (13) *International Tables for X-ray Crystallography*; Wilson, A. J. C., Ed.; Kluwer: Dordrecht, 1992, Vol. C.
- (14) Gelato L. M.; Parthé, E. *J. Appl. Crystallogr.* **1987**, *20*, 139.
- (15) Whangbo, M.-H.; Hoffmann, R. *J. Am. Chem. Soc.* **1978**, *100*, 6093.

- (16) Hoffmann, R. *Solids and Surfaces: A Chemist's View of Bonding in Extended Structures*; VCH Publishers: New York, 1988.
- (17) Li, J.; Hoffmann, R. *Z. Naturforsch., B: Anorg. Chem., Org. Chem.* **1986**, *41*, 1399.
- (18) Alemany, P.; Alvarez, S.; Hoffmann, R. *Inorg. Chem.* **1990**, *29*, 3070.
- (19) Ramírez, R.; Böhm, M. C. *Int. J. Quantum Chem.* **1986**, *30*, 391.
- (20) Shannon, R. D. *Acta Crystallogr. Sect. A: Cryst. Phys., Diff., Theor. Gen. Crystallogr.* **1976**, *32*, 751.
- (21) Lii, K.-H.; Haushalter, R. C. *J. Solid State Chem.* **1987**, *67*, 374.
- (22) Klein, J.; Eisenmann, B. *Mater. Res. Bull.* **1988**, *23*, 587.
- (23) Eisenmann, B.; Klein, J. *Z. Anorg. Allg. Chem.* **1991**, *598/599*, 93.
- (24) Schmidt, P. C.; Stahl, D.; Eisenmann, B.; Kniep, R.; Eyert, V.; Kübler, J. *J. Solid State Chem.* **1992**, *97*, 93.

CHAPTER 4

The Metallic Zintl Phase $\text{Ba}_3\text{Sn}_4\text{As}_6$ [†]

INTRODUCTION

There exists a large family of polar intermetallic compounds with general compositions M_xA_y or $M_xA_yB_z$ (M = alkali or alkaline-earth metal; A, B = main-group elements) whose structures and bonding can be readily understood in terms of the Zintl concept.¹⁻⁴ Assuming that each atom attains a closed-shell electron configuration, the electropositive elements (M) completely transfer their valence electrons to their electronegative main-group partners (A, B) which satisfy the octet rule by forming anion-anion bonds ($A-A, A-B$, or $B-B$) or lone pairs. The rational manner by which elements of the p -block condense in Zintl-type structures to form diverse polyanionic networks of wide-ranging dimensionality is a welcoming feature in the synthesis of new materials with desired properties, considering the inherent difficulty in predicting new solid-state structures given a certain composition. By controlling the electronegativity difference between cations and anions, size of cation, or number of electrons available to the anionic substructure through the use of different electropositive atoms, one hopes to be able to

[†] A version of this chapter has been submitted for publication. Lam, R.; Mar, A.

induce specific structural changes.^{5,6}

Traditionally, the properties of Zintl compounds were considered to be limited to semiconductivity, since the fulfillment of closed-shell configurations is expected to give rise to an energy gap between occupied and unoccupied states.¹ For the majority of Zintl compounds, this assumption is probably valid despite a lack of physical property measurements. The discovery of a number of Zintl compounds with metallic properties,⁵⁻¹¹ especially those involving the heavier main-group elements, should encourage the search for potentially useful properties in this large family of compounds. Moreover, rare-earth or transition metal substitutions for the alkali or alkaline earth atoms introduce a new level of complexity in Zintl compounds whose properties are expected to be interesting owing to the presence of f and d electrons. Such efforts have resulted in the discovery of CMR in the materials $A_{14}MnPn_{11}$ ($A = \text{Eu, Sr}$; $Pn = \text{Sb, Bi}$),⁹⁻¹¹ which are extensions of the main-group Zintl analogues $A_{14}AlSb_{11}$ ($A = \text{Ca, Sr, Ba}$),^{12,13} and promising thermoelectric properties in the classic Zintl compound $\text{Ba}_4\text{In}_8\text{Sb}_{16}$.¹⁴ We report here the preparation and resistivity measurements of a new metallic Zintl phase, $\text{Ba}_3\text{Sn}_4\text{As}_6$, which represents an intermediate structure type between the hypothetical limiting structures “ $\text{Ba}_4\text{Sn}_2\text{As}_6$,” containing one-dimensional corner-sharing chains of Sn-centered tetrahedra and “ $\text{Ba}_2\text{Sn}_6\text{As}_6$,” featuring two-dimensional corrugated layers with pentagonal channels.

EXPERIMENTAL SECTION

SYNTHESIS

Single crystals of $\text{Ba}_3\text{Sn}_4\text{As}_6$ used in the structure determination were isolated as a minor phase from the reaction of a 0.25-g mixture of Ba, Zr, and As in a 3:1:5 ratio in a tin flux (Ba, 117 mg, 0.85 mmol, 99.9%, Alfa-Aesar; Zr, 26 mg, 0.28 mmol, 99.7% Cerac; As, 107 mg, 1.42 mmol, 99.99%, Alfa-Aesar; Sn, 332 mg, 2.80 mmol, 99.8%, Cerac), originally intended for the preparation of the target compound “ Ba_3ZrAs_5 ”. The reactants were loaded into a sealed and evacuated fused-silica tube (7-cm length; 10-mm i.d.), which was heated at 600 °C for 1 day and 950 °C for 2 days, cooled to 600 °C over 1 day, and then cooled to room temperature over 10 h. Dissolving the excess Sn in concentrated HCl revealed a mixture of greyish brown powder containing the major phase ZrAs ,¹⁵ as well as hexagonal crystals of Sn_4As_3 ¹⁶ and dark grey needles of a Ba/Sn/As-containing phase. EDX (energy-dispersive X-ray) analysis of the latter on a Hitachi S-2700 scanning electron microscope showed that Ba, Sn, and As were present, exclusively, in these crystals (Anal. (mol %): Ba, 21(1); Sn, 29(5); As, 49(6) (average of six analyses)). The compound $\text{Ba}_3\text{Sn}_4\text{As}_6$ was subsequently prepared in a rational manner, by reaction of the elements in their stoichiometric proportions under the same reaction conditions as the original synthesis. The X-ray powder pattern, obtained on an Enraf-Nonius FR552 Guinier camera ($\text{Cu } K\alpha_1$ radiation; Si standard), revealed the presence of nearly phase-pure $\text{Ba}_3\text{Sn}_4\text{As}_6$. Attempts to substitute Sr for Ba were unsuccessful using the same procedures, yielding the known compounds SrSn_2As_2 ¹⁷ and SnAs ¹⁸ instead.

STRUCTURE DETERMINATION

A crystal confirmed by EDX analysis to be the ternary compound was analyzed by Weissenberg photography for singularity and suitability for data collection in addition to preliminary cell parameters. Final cell parameters were determined from least-squares analysis of the setting angles of 24 reflections centred on an Enraf-Nonius CAD4 diffractometer. Intensity data were collected at 22 °C with the θ - 2θ scan technique in the range $2^\circ \leq 2\theta(\text{MoK}\alpha) \leq 70^\circ$. Crystal data and further details of the data collection are given in Table 4-1. All calculations were carried out with the use of the SHELXTL (Version 5.1) package.¹⁹ Conventional atomic scattering factors and anomalous dispersion corrections were used.²⁰ The intensity data were processed and face-indexed numerical absorption corrections were applied in XPREP. Initial atomic positions were found by direct methods using XS followed by subsequent difference Fourier syntheses, and refinements were performed by least-squares methods using XL.

Weissenberg photographs of $\text{Ba}_3\text{Sn}_4\text{As}_6$ displayed apparently orthorhombic Laue symmetry mmm , giving approximate cell constants of 8.63 (needle axis), 9.68, and 18.39 Å. The initial stages of structure solution were hindered by ambiguity in space group determination owing to the presence of meaningless systematic absences, which were clearly shown in the zero- and upper-level photographs and later confirmed by inspection of the reciprocal space plots in XPREP of the diffractometer data. The apparent limiting conditions ($h0l$: $h + l = 2n$; $h00$: $h = 4n$; $0k0$: $k = 2n$; $00l$: $l = 2n$) did not correspond to any valid orthorhombic space groups. Additionally, the oscillation photograph about the needle axis revealed that layers of odd indices were notably weaker than those of even indices. The weakness of intensities also extended to the first-level Weissenberg

photograph. Aware that these unusual features of the X-ray diffraction pattern may be produced by twinning of monoclinic crystals to give pseudo-orthorhombic Laue symmetry,²¹⁻²³ we first wanted to investigate a possible solution in the orthorhombic system to confirm this. Under the assumption of orthorhombic symmetry, data were initially collected at room temperature for the octants hkl and $\bar{h}\bar{k}\bar{l}$, with refined cell parameters $a = 8.6354(9) \text{ \AA}$, $b = 9.7192(11) \text{ \AA}$, $c = 18.3541(15) \text{ \AA}$. The space group most consistent with the systematic absences discussed above, $Pmn2_1$, was chosen upon transforming the set of axes. A reasonable solution was found by direct methods which refined to $R(F)$ (for $F_o^2 > 2\sigma(F_o^2)$) of 0.15. Apart from the unsatisfactory agreement parameters and incorrect space group, other disturbing features in this model suggested more insidious problems with the original data. Specifically, structure refinements were beset by persistent difference Fourier peaks which occurred too close to existing atoms, presence of crystallographically distinguishable but chemically identical Sn/As layers, and poor agreement of the weak reflections. Moreover, an apparent 2_1 -screw axis along b (corresponding to the condition $0k0: k = 2n$, which is inconsistent with the $Pmn2_1$ space group) can be readily identified in the structure.

To resolve some of these ambiguities, intensity data were recollected at room temperature on the same crystal for all octants. The centrosymmetric monoclinic space group $P2_1/n$, which permits the simultaneous occurrence of an n -glide plane perpendicular to a two-fold screw axis, was chosen on the basis of intensity statistics and the successful structure solution. Once the positions of all atoms except Ba(1) and Ba(2) were found, a subsequent refinement revealed residual electron density at (0.11, 0.29, 0.44) and (0.63, 0.29, 0.44). Although these sites resided too close (1.215(9)–1.698(8) \AA)

to the Sn(1), Sn(2), Sn(5), and Sn(6) atoms, they were assigned to Ba(1) and Ba(2) on the basis of reasonable Ba–As distances. This model assumed a disorder between Ba(1) cations and Sn(1)–Sn(5) dumbbells as well as between Ba(2) cations and Sn(2)–Sn(6) dumbbells. A refinement based on the ideal formula “Ba₃Sn₄As₆,” in which the occupancies of Ba(1), Ba(2), Sn(1), Sn(2), Sn(5), and Sn(6) were set at 50%, revealed that the weak reflections were still poorly modeled and that the list of most disagreeable reflections showed F_o^2 to be consistently larger than F_c^2 , implying the existence of a twin component. To model a twin reflection plane perpendicular to the a axis, the twin law $[\bar{1}00, 010, 001]$ with two components was included in subsequent refinements. Given the high correlation between positions of related atoms, refinements on the occupancies of the atoms involved in the disorder between Ba and Sn–Sn dumbbells proceeded with the constraint that the sum of the occupancies of Ba(1) and Sn(1)–Sn(5) (and also Ba(2) and Sn(2)–Sn(6)) be 100% and with the restraint that the occupancies of the Sn atoms making up the dumbbells be equal, since we assume the Sn atoms must occur locally bonded as pairs. This resulted in occupancies of 11.5(3)% (Ba(1)) and 84.8(3)% (Sn(1) and Sn(5)); and 86.5(4)% (Ba(2)) and 12.8(2)% (Sn(2) and Sn(6)). This unequal distribution is the source of the lower monoclinic symmetry, notwithstanding the nearly 90° β -angle of the unit cell. The occupancies of all other atoms were essentially 100%. The displacement parameters for all atoms were reasonable. The BASF parameter converged to 0.417(3), implying an approximate 42:58 twin distribution. The final cycle of least-squares refinement on F_o^2 of 133 variables (including anisotropic displacement parameters and an isotropic extinction parameter) and 6727 averaged reflections (including those having $F_o^2 < 0$) converged to values of $R_w(F_o^2)$ of 0.177 and $R(F)$ (for

$F_o^2 > 2\sigma(F_o^2)$ of 0.063. The final difference electron density map is featureless ($\Delta\rho_{\max} = 5.8$, $\Delta\rho_{\min} = -5.1 \text{ e}^{-\text{\AA}^{-3}}$). The final refined formula, $\text{Ba}_3\text{Sn}_4\text{As}_6$ ($Z = 4$), is consistent with the chemical analysis determined independently (Anal. Calcd. (mol%): Ba 23, Sn 31, As 46). Furthermore, the weak reflections are now well modeled and an examination of the listing of structure factors shows that F_o^2 matches F_c^2 reasonably well. Final values of the positional and equivalent isotropic displacement parameters are given in Table 4–2. Anisotropic displacement parameters are given in Table A–4.

A subcell ($\text{Ba}_3\text{Sn}_4\text{As}_6$; $Z = 2$; space group $Pnma$; $a = 9.7192(11) \text{ \AA}$, $b = 4.3177(5) \text{ \AA}$, $c = 18.3541(15) \text{ \AA}$) of the $P2_1/n$ solution can be obtained by halving the 8.6 \AA axis to 4.3 \AA , which effectively removes the set of unusual absences in the previous $hk0$ plane and generates an n -glide plane. The number of crystallographically distinguishable atoms is also reduced in half in the orthorhombic unit cell. The subcell represents the average structure, in which the planes of Ba and Sn–Sn dimers with alternating distributions of ~15%:85% and ~85%:15% are averaged out, refining to a 50:50 distribution. The subcell model will not be presented here but details are provided in the Appendix (Tables A–5 to A–7).

ELECTRICAL RESISTIVITY

A single crystal of dimensions $0.32 \times 0.02 \times 0.02 \text{ mm}$, verified to be $\text{Ba}_3\text{Sn}_4\text{As}_6$ by EDX analysis, was mounted in a four-probe configuration for an ac resistivity measurement between 20 and 290 K. This measurement gives the resistivity along the crystallographic a axis.

RESULTS AND DISCUSSION

DESCRIPTION OF THE STRUCTURE

A view of the structure of $\text{Ba}_3\text{Sn}_4\text{As}_6$ is shown in a projection down the short a axis in Figure 4-1, which also shows the labeling scheme. Selected interatomic distances and angles are listed in Table 4-3. At first glance, Figure 4-1 shows that the structure of $\text{Ba}_3\text{Sn}_4\text{As}_6$ consists of corrugated layers, built up of Sn and As atoms, parallel to the (010) plane, and are separated by $\text{Ba}(3)^{2+}$ and $\text{Ba}(4)^{2+}$ cations. However, closer inspection reveals that Sn-Sn dumbbells, namely Sn(1)-Sn(5) and Sn(2)-Sn(6), within the anionic $[\text{Sn}_3\text{As}_6]^{6-}$ sheets are disordered with Ba(1) and Ba(2) cations, respectively. As shown in Figure 4-2, a projection down the b axis featuring only the disordered sites, there appears to be an 85%:15% distribution of Ba and Sn-Sn in one plane parallel to (101), and the reversed (15%:85%) in the adjacent parallel planes. A similar disorder scheme can be seen in the intermetallic compound $\text{FeGe}_{1-x}\text{Sb}_x$ ($0 \leq x \leq 0.33$),²⁴ where the relative distribution of Ge atoms and Sb_2 pairs occupying the same sites is dependent on the loading compositions.

Given the disordered nature of the crystal structure, it will be instructive to propose two ordered models for the compound $\text{Ba}_3\text{Sn}_4\text{As}_6$ for the purpose of the following discussion. For clarity, one can envisage two limiting ordered structures (Figure 4-3) that can be derived from the intermediate parent compound by assuming full occupancy of either Ba cations (*Model A*) or Sn-Sn pairs (*Model B*) at their respective sites. Note that complete filling (100 %) of one component necessarily precludes the presence of the other (0 %).

In *Model A*, in which we assume complete removal of all Sn–Sn dumbbells in favour of full Ba(1) and Ba(2) occupancy, we arrive at the hypothetical composition “Ba₄Sn₂As₆” ($Z = 4$). As shown in Figure 4–3a, the structure consists of one-dimensional chains of SnAs₄ tetrahedra that are corner-sharing along the a direction and separated by Ba²⁺ cations. The Sn(3)- and Sn(4)-centred tetrahedral units have Sn–As distances of 2.586(2)–2.736(3) Å; these distances are comparable to those found in the edge-sharing tetrahedral dimers in Na₅SnAs₃ (2.598(2)–2.696(2) Å)²⁵ and Na₂K₃[SnAs₃] (2.634(1)–2.703(1) Å),²⁵ the infinite corner-sharing tetrahedral chains in Ca₅Sn₂As₆ (2.572(3)–2.638(3) Å),²⁶ and the three-dimensional corner-sharing tetrahedral networks in Na₂[SnAs₂] (2.588(3)–2.644(3) Å).²⁷ The As–Sn–As angles of 105.33(6)–114.28(9)° and 105.74(9)–113.94(10)° in Sn(3)As₄ and Sn(4)As₄, respectively, deviate only slightly from ideal tetrahedral angles. The tetrahedra are condensed via the As(1) and As(2) vertices to form infinite chains.

At the other extreme lies the ordered hypothetical structure “Ba₂Sn₆As₆” ($Z = 4$) (*Model B*), which is obtained by replacing all Ba(1) and Ba(2) atoms in the actual structure with Sn(1)–Sn(5) and Sn(2)–Sn(6) pairs, respectively. As shown in Figure 4–3b, completely “stuffing” the structure with Sn–Sn pairs results in additional Sn–As bonding and the formation of pentagonal channels running parallel to the a axis. The pentagonal tubes are connected together through Sn–As bonds to form two-dimensional corrugated layers parallel to (010) that are separated by Ba(3)²⁺ and Ba(4)²⁺ cations. The trigonal pyramidal Sn(1)(SnAs₂) and Sn(2)(SnAs₂) units have Sn–Sn distances of 2.881(2)–2.902(10) Å and Sn–As distances of 2.562(9)–2.752(3) Å. The latter are similar to the 2.700–2.784(1) Å distances found in the SnAs₃ trigonal pyramids in

KSnAs ,^{28,29} SrSn_2As_2 ,¹⁷ and $\text{K}_6\text{Sn}_3\text{As}_5$.²⁹ Furthermore, the bond angles around Sn(1) and Sn(2) ($97.2(3)$ – $106.8(3)^\circ$), resembling those around the three-bonded As atoms in the structure ($88.6(2)$ – $111.1(2)^\circ$), are significantly smaller than ideal tetrahedral angles, suggesting greater *p* character in the bonds of such trigonal pyramidal units. Examination of the interatomic distances in the Sn(5)(SnAs₃) and Sn(6)(SnAs₃) tetrahedral units shows that in addition to a Sn–Sn bond ($2.881(2)$ – $2.902(10)$ Å), Sn–As distances vary from $2.644(3)$ – $2.689(2)$ Å for Sn(5) to $2.482(10)$ – $2.941(8)$ Å for Sn(6). Comparisons can be made to similar Sn(SnAs₃)-based tetrahedra in the Zintl phase $\text{Ba}_3\text{Sn}_2\text{As}_4$,³⁰ where the Sn–Sn (2.795 Å) and Sn–As (2.593 – 2.691 Å) distances are close to the sums of Pauling covalent radii (Sn–Sn 2.80 Å; Sn–As 2.61 Å) for single bonds. Although the Sn(6)–As(2) ($2.941(8)$ Å) and Sn(6)–As(5) ($2.482(10)$ Å) values are slightly removed from these ranges, the As–Sn–As and As–Sn–Sn angles around Sn(5) ($100.83(7)$ – $120.54(6)^\circ$) and Sn(6) ($97.1(3)$ – $120.4(3)^\circ$) are comparable to the tetrahedral angles reported for $\text{Ba}_3\text{Sn}_2\text{As}_4$ (97.0 – 117.2°).³⁰ In spite of the unusually short Sn(6)–As(5) contacts, which may be an artifact of the crystallographic constraints and restraints used to model the distribution of Ba and Sn–Sn pairs in the superstructure or, more realistically, matrix effects exerted by the surrounding Ba^{2+} cations, Sn–As separations as short as $2.531(5)$ – $2.538(5)$ Å have been reported for the compounds $A_6[\text{SnAs}_3]\text{O}_{0.5}$ ($A = \text{Rb}, \text{Cs}$).³¹

The contributions of the electropositive Ba atoms, which separate the layers of Sn and As atoms in $\text{Ba}_3\text{Sn}_4\text{As}_6$, cannot be ignored. The importance of alkaline earth cations in Zintl compounds lies in their size, which can influence the shape of the anionic framework through ionic interactions,^{32,33} as well as donation of two valence electrons, leading to overall charge balance. As shown in Figure 4–4a and 4–4b, the coordination

around Ba(1) and Ba(2) can be described as monocapped trigonal prismatic, with six As atoms defining the trigonal prism and one additional As atom capping a rectangular face. The Ba(3) atom is coordinated in a more irregular fashion by the As and Sn atoms (Figure 4–4c), resembling a monocapped square antiprismatic geometry but two of the bonds to the basal square defined by As(5)–Sn(1)–As(4)–Sn(2) are elongated. The environment around Ba(4) is a square antiprism, with As(3)–Sn(1)–As(6)–Sn(2) outlining one square and As(1)–As(2)–As(3)–As(4) defining the other which is rotated 45° relative to the first. Significant Ba–As (3.233(2)–3.615(2) Å) and Ba–Sn (3.515(9)–3.588(2) Å) distances in Ba₃Sn₄As₆ are comparable to those in Ba₃Sn₂As₄ (Ba–As: 3.246(2)–3.510(2) Å),³⁰ Ba_{0.8}Hf_{1.2}As_{17.7} (Ba–As: 3.202(3)–3.461(5) Å),³⁴ Ba₆Sn₂P₆ (Ba–Sn: 3.503(1) Å),³⁵ and Ba₅Sn₃ (Ba–Sn: 3.585–3.613 Å).³⁶

Conventional wisdom suggests that compounds whose composition consists of an electropositive (alkali or alkaline earth metal) and an electronegative (*p*-block elements) component should adhere to the Zintl concept, which prescribes that the electronegative atoms attain an octet through formation of covalent bonds or presence of lone pairs. Examination of the systems *A*/Sn/*Pn* (*A* = Ca, Sr, Ba; *Pn* = P, As, Sb) reveals that all known phases (Sr₃Sn₂P₄,³⁷ Ba₃Sn₂P₄,³⁸ and Ba₆Sn₂P₆,³⁵ Ca₅Sn₂As₆,²⁶ SrSn₂As₂,¹⁷ and Ba₃Sn₂As₄,³⁰ SrSn₃Sb₄³³ and Ba₂Sn₃Sb₆³²) can be classified as Zintl compounds, their structures based on tetrahedral Sn*Pn*₄ or Sn(Sn*Pn*₃) and trigonal pyramidal Sn*Pn*₃ building blocks. Applying the Zintl concept to Ba₃Sn₄As₆ results in the formulation (Ba²⁺)₃[Sn₄As₆]⁶⁻, where the electropositive Ba atoms are assumed to transfer two valence electrons to the anionic substructure. However, assigning formal charges to the Sn and As atoms is not straightforward because of the disorder observed in the structure.

Instead, we examine the hypothetical ordered structures represented by the limiting extremes “Ba₄Sn₂As₆” (*Model A*) and “Ba₂Sn₆As₆” (*Model B*). Assuming a closed-shell configuration (octet) for the Sn and As atoms, formal charges are assigned to be 1– and 0 for three- and four-bonded Sn, respectively, while they are 2–, 1–, and 0 for one-, two-, and three-bonded As, respectively. Applying these formal charge assignments based on these structures (Figure 4–3) results in the formulations (Ba²⁺)₄[Sn₂As₆]^{10–} and (Ba²⁺)₂[Sn₆As₆]^{2–}. This means that the hypothetical structures of *Model A* and *Model B* carry net charges of 2– and 2+, respectively, and therefore cannot be considered Zintl compounds by themselves! However, a superposition consisting of an equal mixture of “[Ba₄Sn₂As₆]^{2–}” and “[Ba₂Sn₆As₆]²⁺” yields a charge-neutral structure. “[Ba₂Sn₆As₆]²⁺[Ba₄Sn₂As₆]^{2–}” or “Ba₃Sn₄As₆” which *does* adhere to the Zintl concept. Such an analysis thus provides a rational explanation for the inherent disorder observed in Ba₃Sn₄As₆.

ELECTRICAL RESISTIVITY

Although the assumption of semiconducting behavior is probably accurate for the vast majority of classical Zintl phases, a surprising number of exceptions^{5–11} exist which demonstrate that metallic behavior can result from increased band overlap, diminished band gaps, or partial electron transfer from the cations to the Zintl anions. These exceptions to the rule should not deter the application of the Zintl concept in providing a convenient and qualitative approach to rationalizing the structure and bonding of numerous solid state compounds but they should remind us of the limitations that the concept has in predicting the interactions among energy levels, a task for which it was not

originally intended. For quantitative results, more sophisticated calculations³⁹⁻⁴¹ should be employed.

Previously, we have begun to study the electronic properties of Zintl compounds of the heavier main-group elements,⁷ for which metallic conduction is more prevalent. The metallic Zintl compounds ASn_3Sb_4 ($A = Sr, Eu$)^{7,33} and $Ba_2Sn_3Sb_6$ ³² were found to exhibit such behavior through band broadening caused by bonding interactions between adjacent channels built up of the semimetals Sn and Sb. A representative plot of the electrical resistivity of $Ba_3Sn_4As_6$, measured along the needle axis a , as a function of temperature, is shown in Figure 4-5, which shows that it is weakly metallic ($\rho_{290} = 2.7 \times 10^{-4} \Omega \text{ cm}$, $\rho_{25} = 1.2 \times 10^{-4} \Omega \text{ cm}$, $\rho_{290}/\rho_{25} = 2.3$). The compound is expected to be an anisotropic conductor owing to the two-dimensional nature of the structure although this needs to be confirmed by band structure calculations or resistivity measurements along the remaining two axes. The latter was not possible owing to the small dimensions of the crystal perpendicular to the needle axes.

STRUCTURAL RELATIONSHIPS

It is not surprising that the limiting substructures “ $Ba_4Sn_2As_6$ ” (*Model A*) and “ $Ba_2Sn_6As_6$ ” (*Model B*) have not been reported since our exercise of assigning formal charges to the atoms revealed that there is a net nonzero charge for these proposed structures, therefore violating the Zintl concept. Curiously, there does exist a Zintl phase $Ca_5Sn_2As_6$ (*Pbam*),²⁶ whose structure resembles that of *Model A* in consisting of one-dimensional chains of corner-sharing tetrahedra separated by alkaline earth cations. This suggests that given the composition “ $Ba_4Sn_2As_6$ ”, a Zintl compound is not expected to

form but addition of a divalent cation into the formula may result in the charge-neutral phase “Ba₅Sn₂As₆,” although we have not detected it. Other factors besides charge balance, such as the size of cation, may play an important role in influencing the structure of Zintl compounds. One can postulate that the large Ba atoms in Ba₃Sn₄As₆ provide sufficient room to accommodate Sn–Sn dumbbells into the structure.

The other limiting structure “Ba₂Sn₆As₆” represents a stuffed version of *Model A* whereby Sn–Sn pairs replace all of the Ba(1) and Ba(2) cations, resulting in corrugated layers of Sn and As that are separated by alkaline earth atoms. Within the two-dimensional layers, tetrahedral and trigonal pyramidal Sn units share corners to form pentagonal channels extending along the *a* axis. This hypothetical structure “Ba₂Sn₆As₆” belongs to a larger family of low-dimensional structure types which also feature corrugated layers containing five-membered channels (Figure 4–6). The simplest structure in this group is the binary phase GeAs₂ (*Pbam*)⁴² (Figure 4–6a), whose structure consists of the corrugated layers stacked parallel to each other in the absence of any intervening cations. Insertion of alkaline earth atoms between the layers results in the structure of Ba₄In₈Sb₁₆ (*Pnma*)¹⁴ (Figure 4–6b). Note that heteroatomic “dumbbells” (Ge–As and In–Sb), analogous to the Sn–Sn pairs in Ba₃Sn₄As₆, constitute one side of the five-membered rings in the structures of GeAs₂ and Ba₄In₈Sb₁₆, accompanied by homoatomic bonding between the more electronegative main-group element (Sb–Sb and As–As). Consistent with the substitution pattern of the five-membered rings in Ba₃Sn₄As₆, the pentagonal channels in Ba₃Si₄P₆ (*P2₁/m*)⁴³ (Figure 4–6c) feature Si–Si pairs. However, the channels are joined through the Si–Si dimers to give infinite zigzag chains of Si atoms within the corrugated layers, resulting in a slightly different structure.

The discovery of $\text{Ba}_3\text{Sn}_4\text{As}_6$ provides another example of the relevance and effectiveness of the classical Zintl concept in rationalizing the structure and bonding of many solid state compounds containing a combination of electropositive (alkali and alkaline earth elements) and electronegative (groups 13–17) elements. The tendency for atoms to complete their octets according to the $8-N$ rule in Zintl phases lends a degree of rationality towards the structural investigation of this large class of materials that is not present in the study of other types of solid state compounds such as intermetallics. It is worthwhile to exploit the convenience of this scheme in the design of new materials, especially those with interesting features such as channels, cages, or low-dimensionality, which may lead to useful properties.

Table 4–1. Crystallographic Data for Ba₃Sn₄As₆

Formula	Ba ₃ Sn ₄ As ₆
Formula mass, amu	1336.30
Space group	$C_{2h}^5 - P2_1/n$ (No. 14)
a , Å	8.6374(10) ^a
b , Å	18.3536(13) ^a
c , Å	9.7209(11) ^a
β , deg.	90.05(2) ^a
V , Å ³	1541.0(3)
Z	4
T , °C	22
Diffractometer	Enraf-Nonius CAD4
ρ_{calc} , g cm ⁻³	5.760
Crystal dimensions, mm	Dark grey needle, 0.45 × 0.11 × 0.06
Radiation	Graphite monochromated MoK α $\lambda = 0.71073$ Å
$\mu(\text{MoK}\alpha)$, cm ⁻¹	266.6
Transmission factors ^b	0.158–0.300
Scan type	θ – 2θ
Scan speed, deg. min ⁻¹	1.7
Scan range, deg.	$0.5 + 0.344 \tan \theta$
2θ limits	$2^\circ \leq 2\theta(\text{MoK}\alpha) \leq 70^\circ$
Data collected	$-12 \leq h \leq 13, -29 \leq k \leq 29, -15 \leq l \leq 15$
No. of data collected	23058

Table 4–1. Crystallographic Data for Ba₃Sn₄As₆ (continued)

No. of unique data, including $F_o^2 < 0$	6727 ($R_{\text{int}} = 0.1079$)
No. of unique data, with $F_o^2 > 2\sigma(F_o^2)$	5016
No. of variables	133
Extinction coefficient ^c	0.00029(6)
$R(F)$ for $F_o^2 > 2\sigma(F_o^2)$ ^d	0.063
$R_w(F_o^2)$ ^e	0.177
Goodness of fit ^f	1.05
$(\Delta\rho)_{\text{max}}, (\Delta\rho)_{\text{min}}, e^{-\text{\AA}^{-3}}$	5.8, – 5.1

^a Obtained from a refinement constrained so that $\alpha = \gamma = 90^\circ$.

^b A Gaussian-type absorption correction was applied, with the use of programs in the SHELXTL package (Sheldrick, G. M. SHELXTL Version 5.0, Siemens Analytical X-Ray Instruments, Inc., Madison, WI, 1994).

^c An extinction parameter x was refined, where F_c is multiplied by: $k[1 + 0.001 * x * F_c^2 * \lambda^3 / \sin(2\theta)]^{-1/4}$.

$$^d R(F) = \frac{\sum ||F_o| - |F_c||}{\sum |F_o|}$$

$$^e R_w(F_o^2) = \left[\frac{\sum [w(F_o^2 - F_c^2)^2]}{\sum wF_o^4} \right]^{1/2}; \quad w^{-1} = [\sigma^2(F_o^2) + (0.0652P)^2 + 72.1812P]$$

where $P = [\max(F_o^2, 0) + 2F_c^2]/3$.

$$^f \text{GooF} = S = \left[\frac{\sum [w(F_o^2 - F_c^2)^2]}{(n - p)} \right]^{1/2}$$

where n is the number of reflections and p is the total number of parameters refined.

Table 4–2. Atomic Coordinates, Occupancies, and Equivalent Isotropic Displacement Parameters (\AA^2) for $\text{Ba}_3\text{Sn}_4\text{As}_6$

Atom	Wyckoff position, site symmetry		x	y	z	Occupancy	U_{eq}^a
Ba(1)	4e	1	0.1112(12)	0.2893(4)	0.4384(11)	0.115(3)	0.0121(2)
Ba(2)	4e	1	0.6259(2)	0.28756(5)	0.44216(14)	0.865(4)	0.0121(2)
Ba(3)	4e	1	0.1216(2)	0.54293(5)	0.23888(10)	1	0.0158(2)
Ba(4)	4e	1	0.6275(2)	0.54611(5)	0.24799(10)	1	0.0180(2)
Sn(1)	4e	1	0.1211(2)	0.37444(6)	0.50562(14)	0.848(3)	0.0106(2)
Sn(2)	4e	1	0.6100(11)	0.3746(4)	0.4996(10)	0.128(2)	0.0106(2)
Sn(3)	4e	1	0.3666(2)	0.35998(5)	0.15578(10)	1	0.0115(2)
Sn(4)	4e	1	0.8841(2)	0.36023(5)	0.15112(11)	1	0.0130(2)
Sn(5)	4e	1	0.1223(2)	0.23721(6)	0.36173(14)	0.848(3)	0.0101(2)
Sn(6)	4e	1	0.6088(11)	0.2372(4)	0.3518(10)	0.128(2)	0.0101(2)
As(1)	4e	1	0.1242(3)	0.11086(8)	0.5018(2)	1	0.0126(3)
As(2)	4e	1	0.6295(3)	0.09850(9)	0.5022(2)	1	0.0163(3)
As(3)	4e	1	0.3773(3)	0.43476(8)	0.38189(15)	1	0.0130(3)
As(4)	4e	1	0.8713(3)	0.43207(8)	0.37967(15)	1	0.0130(3)
As(5)	4e	1	0.3746(4)	0.22145(8)	0.2068(2)	1	0.0133(3)
As(6)	4e	1	0.8755(4)	0.22202(8)	0.2031(2)	1	0.0141(3)

^a U_{eq} is defined as one-third of the trace of the orthogonalized U_{ij} tensor.

Table 4–3. Selected Interatomic Distances (Å) and Angles (°) for Ba₃Sn₄As₆

Sn(1)–As(3)	2.752(3)	Ba(1)–Sn(4)	3.651(10)
Sn(1)–As(4)	2.696(3)	Ba(2)–As(2)	3.519(2)
Sn(1)–Sn(5)	2.8810(15)	Ba(2)–As(3)	3.500(3)
Sn(2)–As(3)	2.562(9)	Ba(2)–As(4)	3.450(3)
Sn(2)–As(4)	2.752(10)	Ba(2)–As(5)	3.354(3)
Sn(2)–Sn(6)	2.902(10)	Ba(2)–As(5)	3.378(3)
Sn(3)–As(1)	2.736(3)	Ba(2)–As(6)	3.340(3)
Sn(3)–As(2)	2.645(3)	Ba(2)–As(6)	3.392(3)
Sn(3)–As(3)	2.593(2)	Ba(2)–Sn(3)	3.811(2)
Sn(3)–As(5)	2.591(2)	Ba(2)–Sn(4)	3.843(2)
Sn(4)–As(1)	2.724(3)	Ba(3)–As(1)	3.443(2)
Sn(4)–As(2)	2.678(3)	Ba(3)–As(2)	3.351(2)
Sn(4)–As(4)	2.586(2)	Ba(3)–As(2)	3.469(2)
Sn(4)–As(6)	2.588(2)	Ba(3)–As(3)	3.278(2)
Sn(5)–As(1)	2.689(2)	Ba(3)–As(4)	3.270(3)
Sn(5)–As(5)	2.666(3)	Ba(3)–As(4)	3.737(2)
Sn(5)–As(6)	2.644(3)	Ba(3)–As(5)	3.319(2)
Sn(6)–As(2)	2.941(8)	Ba(3)–Sn(1)	3.588(2)
Sn(6)–As(5)	2.482(10)	Ba(3)–Sn(2)	3.757(9)
Sn(6)–As(6)	2.734(10)	Ba(4)–As(1)	3.468(2)
Ba(1)–As(1)	3.334(8)	Ba(4)–As(1)	3.745(2)
Ba(1)–As(3)	3.567(9)	Ba(4)–As(2)	3.355(3)
Ba(1)–As(4)	3.389(9)	Ba(4)–As(3)	3.247(3)

Table 4-3. Selected Interatomic Distances (Å) and Angles (°) for Ba₃Sn₄As₆ (continued)

Ba(1)–As(5)	3.322(11)	Ba(4)–As(3)	3.615(2)
Ba(1)–As(5)	3.435(10)	Ba(4)–As(4)	3.233(2)
Ba(1)–As(6)	3.300(10)	Ba(4)–As(6)	3.264(2)
Ba(1)–As(6)	3.445(11)	Ba(4)–Sn(1)	3.545(2)
Ba(1)–Sn(3)	3.756(10)	Ba(4)–Sn(2)	3.515(9)
As(3)–Sn(1)–As(4)	106.69(6)	Sn(3)–As(1)–Sn(4)	109.91(6)
As(3)–Sn(1)–Sn(5)	97.83(6)	Sn(3)–As(1)–Sn(5)	95.95(7)
As(4)–Sn(1)–Sn(5)	97.22(6)	Sn(4)–As(1)–Sn(5)	96.11(7)
As(3)–Sn(2)–As(4)	106.8(3)	Sn(3)–As(2)–Sn(4)	103.07(6)
As(3)–Sn(2)–Sn(6)	98.7(3)	Sn(3)–As(2)–Sn(6)	94.5(2)
As(4)–Sn(2)–Sn(6)	97.2(3)	Sn(4)–As(2)–Sn(6)	88.6(2)
As(1)–Sn(3)–As(2)	105.33(6)	Sn(1)–As(3)–Sn(2)	105.2(2)
As(1)–Sn(3)–As(3)	109.37(9)	Sn(1)–As(3)–Sn(3)	97.43(8)
As(1)–Sn(3)–As(5)	105.97(9)	Sn(2)–As(3)–Sn(3)	100.3(2)
As(2)–Sn(3)–As(3)	110.67(8)	Sn(1)–As(4)–Sn(2)	108.3(2)
As(2)–Sn(3)–As(5)	114.28(9)	Sn(1)–As(4)–Sn(4)	98.94(9)
As(3)–Sn(3)–As(5)	110.87(6)	Sn(2)–As(4)–Sn(4)	101.8(2)
As(1)–Sn(4)–As(2)	108.01(6)	Sn(3)–As(5)–Sn(5)	88.85(8)
As(1)–Sn(4)–As(4)	108.83(9)	Sn(3)–As(5)–Sn(6)	90.9(2)
As(1)–Sn(4)–As(6)	105.74(9)	Sn(5)–As(5)–Sn(6)	109.4(2)
As(2)–Sn(4)–As(4)	110.77(9)	Sn(4)–As(6)–Sn(5)	89.27(8)
As(2)–Sn(4)–As(6)	113.94(10)	Sn(4)–As(6)–Sn(6)	91.6(2)
As(4)–Sn(4)–As(6)	109.32(6)	Sn(5)–As(6)–Sn(6)	111.1(2)

Table 4-3. Selected Interatomic Distances (Å) and Angles (°) for Ba₃Sn₄As₆ (continued)

As(1)–Sn(5)–As(5)	100.83(7)
As(1)–Sn(5)–As(6)	102.05(7)
As(1)–Sn(5)–Sn(1)	120.54(6)
As(5)–Sn(5)–As(6)	108.54(7)
As(5)–Sn(5)–Sn(1)	111.87(7)
As(6)–Sn(5)–Sn(1)	111.84(7)
As(2)–Sn(6)–As(5)	103.3(3)
As(2)–Sn(6)–As(6)	97.1(3)
As(2)–Sn(6)–Sn(2)	120.4(3)
As(5)–Sn(6)–As(6)	112.0(3)
As(5)–Sn(6)–Sn(2)	112.6(4)
As(6)–Sn(6)–Sn(2)	110.3(3)

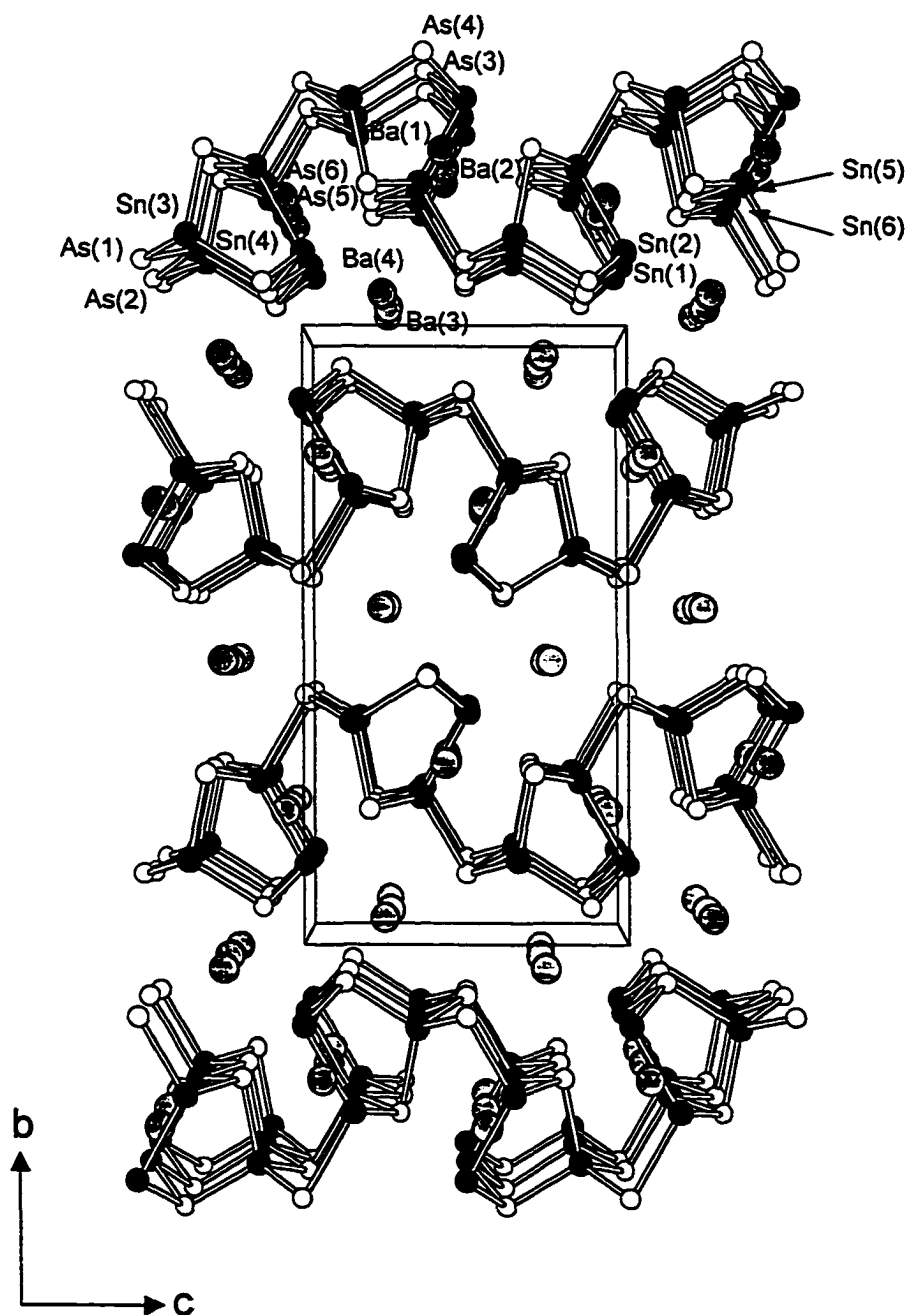


Figure 4-1. View of $\text{Ba}_3\text{Sn}_4\text{As}_6$ down the a axis with the unit cell outlined and the atoms labeled. The large lightly shaded circles are Ba atoms, the medium solid circles are Sn atoms, and the small open circles are As atoms.

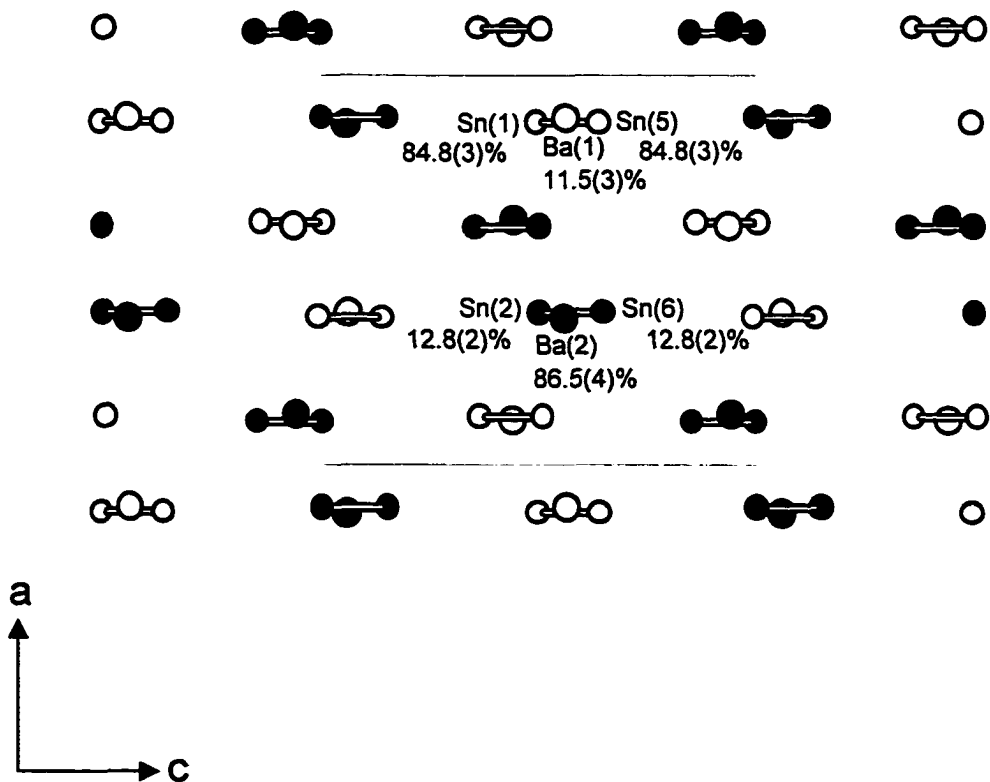


Figure 4-2. Projection down the b axis showing the relative distributions of Ba and Sn-Sn pairs. Large open and solid circles are Ba(1) and Ba(2) sites, respectively; small open and solid circles are Sn(1)-Sn(5) and Sn(2)-Sn(6) pairs, respectively.

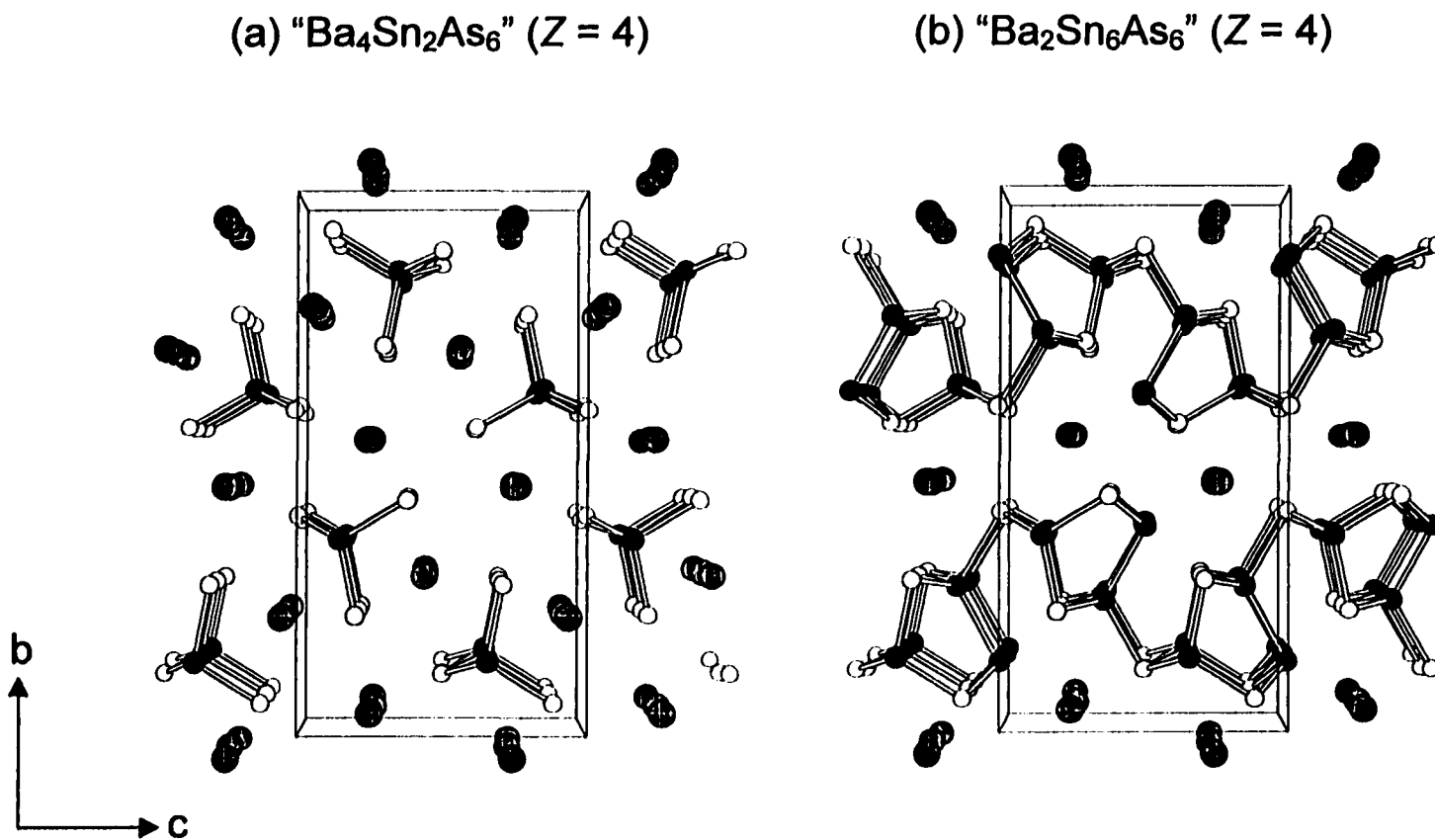


Figure 4-3. View of the proposed limiting structures (a) " $\text{Ba}_4\text{Sn}_2\text{As}_6$ " (*Model A*) and (b) " $\text{Ba}_2\text{Sn}_6\text{As}_6$ " (*Model B*), showing one-dimensional chains of corner-sharing tetrahedra and two-dimensional corrugated layers with pentagonal channels, respectively. The labelling scheme is the same as for Figure 4-1.

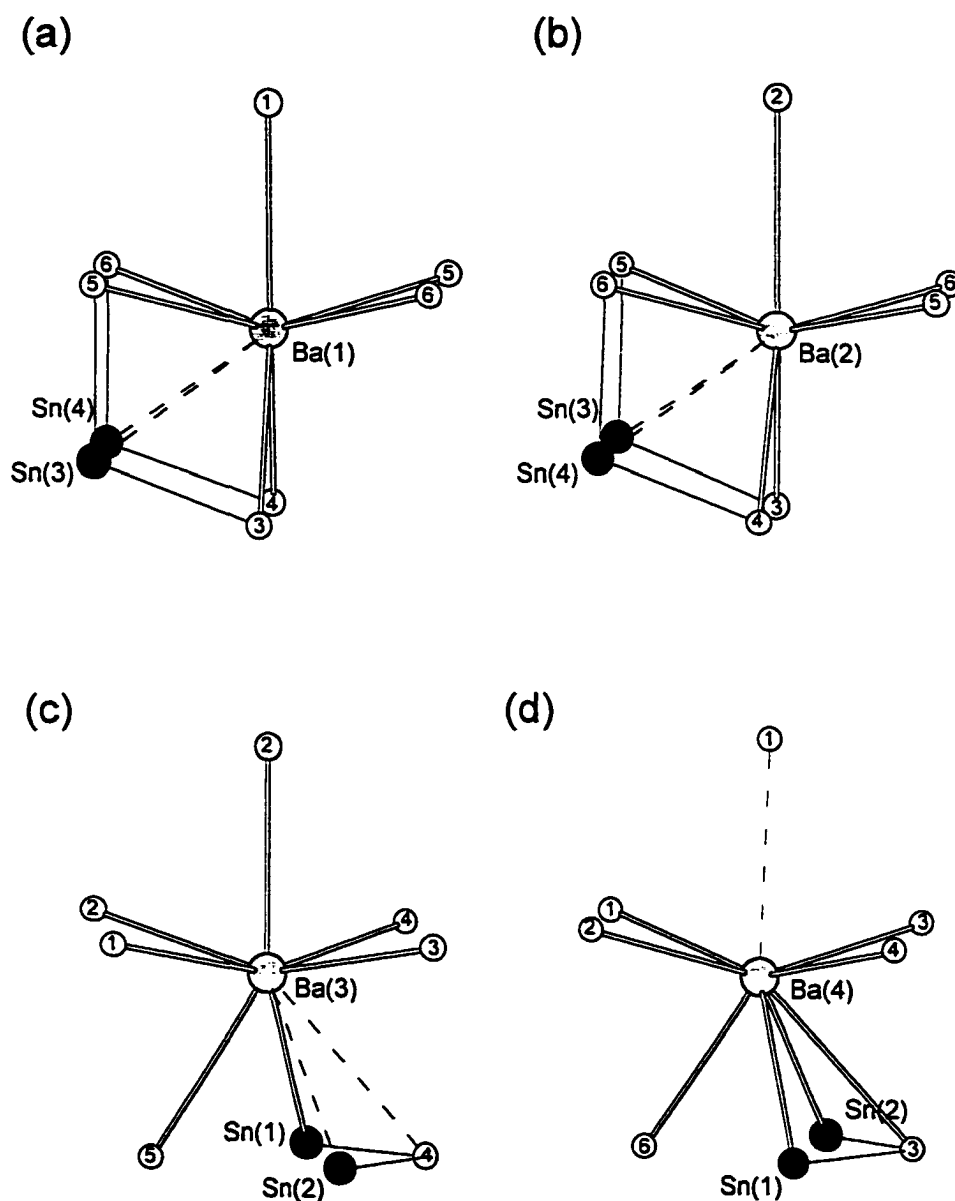


Figure 4-4. Coordination environments around Ba atoms in $Ba_3Sn_4As_6$. Solid lines represent normal Ba-As or Ba-Sn bond distances and dashed lines represent weaker interactions.

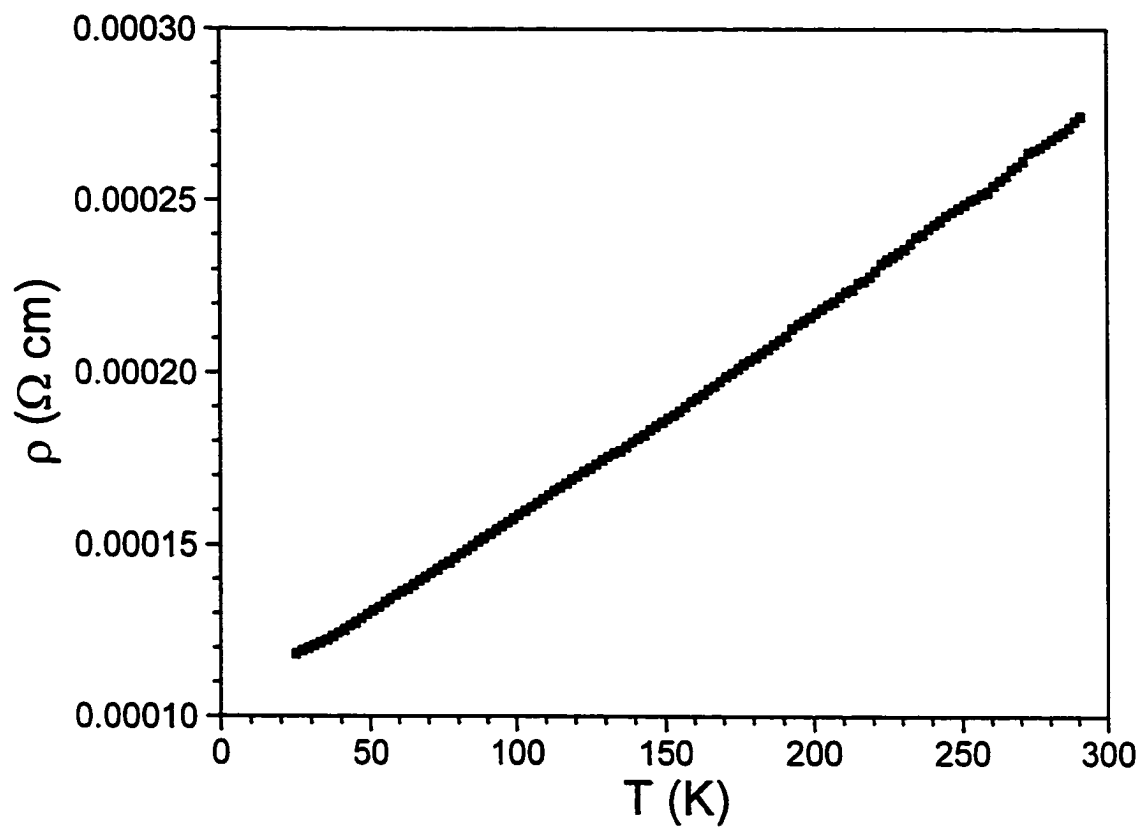
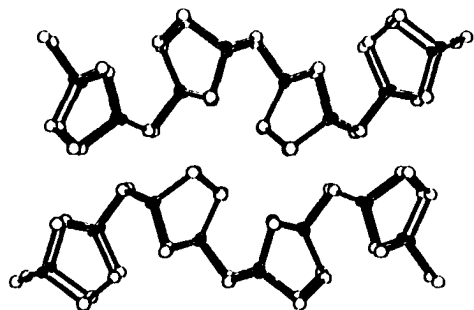
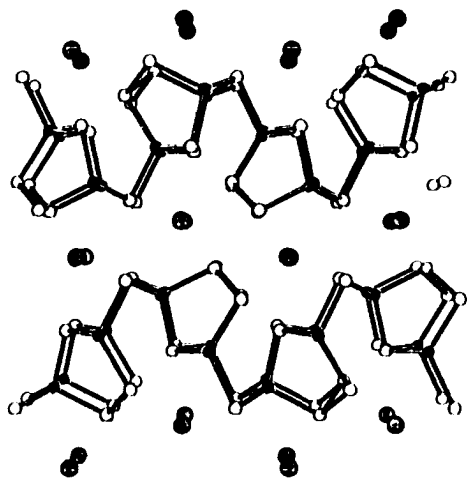


Figure 4-5. Plot of the electrical resistivity of Ba₃Sn₄As₆, measured along the needle axis *a*.

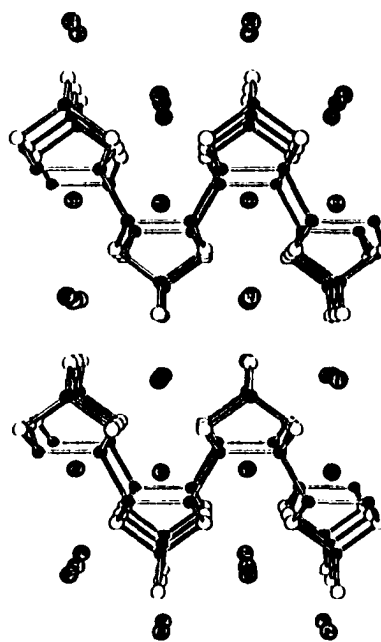
(a) GeAs_2 ($Pbam$)



(b) $\text{Ba}_4\text{In}_8\text{Sb}_{16}$ ($Pnma$)



(c) $\text{Ba}_3\text{Si}_4\text{P}_6$ ($P2_1/m$)



(d) $\text{Ba}_3\text{Sn}_4\text{As}_6$ ($P2_1/n$)

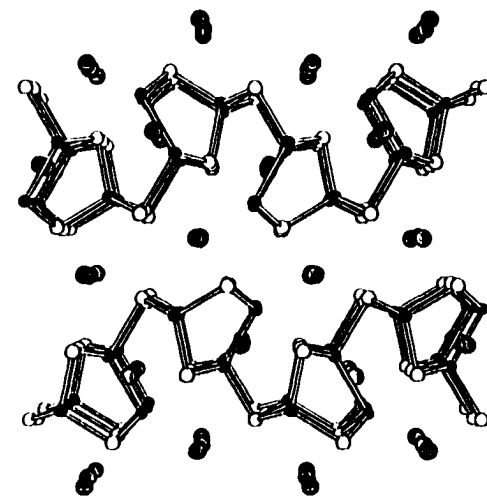


Figure 4-6. Comparison of the structures of (a) GeAs_2 , (b) $\text{Ba}_4\text{In}_8\text{Sb}_{16}$, (c) $\text{Ba}_3\text{Si}_4\text{P}_6$, and (d) $\text{Ba}_3\text{Sn}_4\text{As}_6$. The large lightly shaded circles are Ba atoms, the small solid circles are Ge, In, Si, or Sn atoms, and the medium open circles are P, As, or Sb atoms.

REFERENCES

- (1) *Chemistry, Structure, and Bonding of Zintl Phases and Ions*; Kauzlarich, S. M., Ed.; VCH Publishers: New York, 1996 (and references therein).
- (2) Schäfer, H. *Ann. Rev. Mater. Sci.* **1985**, *15*, 1.
- (3) Corbett, J. D. *Chem. Rev.* **1985**, *85*, 383.
- (4) von Schnering, H. G. *Angew. Chem. Int. Ed. Engl.* **1981**, *20*, 33.
- (5) Nesper, R.; Currao, A.; Wengert, S. *Chem. Eur. J.* **1998**, *4*, 2251.
- (6) Wengert, S.; Nesper, R. *Inorg. Chem.* **2000**, *39*, 2861.
- (7) Lam, R.; Zhang, J.; Mar, A. *J. Solid State Chem.* **2000**, *150*, 371.
- (8) Zhao, J.-T.; Corbett, J. D. *Inorg. Chem.* **1995**, *34*, 378.
- (9) Chan, J. Y.; Kauzlarich, S. M.; Klavins, P.; Shelton, R. N.; Webb, D. J. *Chem. Mater.* **1997**, *9*, 3132.
- (10) Chan, J. Y.; Kauzlarich, S. M.; Klavins, P.; Shelton, R. N.; Webb, D. J. *Phys. Rev. B: Condens. Matter* **1998**, *57*, R8103.
- (11) Webb, D. J.; Cohen, R.; Klavins, P.; Shelton, R. N.; Chan, J. Y.; Kauzlarich, S. M. *J. Appl. Phys.* **1998**, *83*, 7192.
- (12) Cordier, G.; Schäfer, H.; Stelter, M. *Z. Anorg. Allg. Chem.* **1984**, *519*, 183.
- (13) Brock, S. L.; Weston, L. J.; Olmstead, M. M.; Kauzlarich, S. M. *J. Solid State Chem.* **1993**, *107*, 513.
- (14) Kim, S.-J.; Hu, S.; Uher, C.; Kanatzidis, M. G. *Chem. Mater.* **1999**, *11*, 3154.
- (15) Trzebiatowski, W.; Wegłowski, S.; Lukaszewicz, K. *Rocz. Chem.* **1958**, *32*, 189.
- (16) Eckerlin, P.; Kischio, W. *Z. Anorg. Allg. Chem.* **1968**, *363*, 1.
- (17) Eisenmann, B.; Klein, J. *Z. Anorg. Allg. Chem.* **1991**, *598/599*, 93.

- (18) Vdovina, T. Z.; Medvedeva, Z. S. *Russ. J. Inorg. Chem. (Engl. Transl.)* **1974**, *19*, 1234.
- (19) Sheldrick, G. M. *SHELXTL* Version 5.1; Bruker Analytical X-ray Systems, Inc.: Madison, WI, 1997.
- (20) *International Tables for X-ray Crystallography*; Wilson, A. J. C., Ed.; Kluwer: Dordrecht, The Netherlands, 1992; Vol. C.
- (21) Dunitz, J. D. *Acta Crystallogr.* **1964**, *17*, 1299.
- (22) Herbstein, F. H. *Acta Crystallogr.* **1965**, *19*, 590.
- (23) Santoro, A. *Acta Crystallogr. Sect. A: Cryst. Phys., Diff., Theor. Gen. Crystallogr.* **1974**, *30*, 224.
- (24) Mills, A. M.; Mar, A. *J. Alloys Compd.* **2000**, *298*, 82.
- (25) Eisenmann, B.; Klein, J. *Z. Kristallogr.* **1991**, *196*, 213.
- (26) Eisenmann, B.; Jordan, H.; Schäfer, H. *Z. Anorg. Allg. Chem.* **1985**, *530*, 74.
- (27) Asbrand, M.; Eisenmann, B. *Z. Naturforsch., B: Chem. Sci.* **1993**, *48*, 452.
- (28) Lii, K.-H.; Haushalter, R. C. *J. Solid State Chem.* **1987**, *67*, 374.
- (29) Klein, J.; Eisenmann, B. *Mater. Res. Bull.* **1988**, *23*, 587.
- (30) Eisenmann, B.; Jordan, H.; Schäfer, H. *Z. Naturforsch., B: Anorg. Chem., Org. Chem.* **1984**, *39*, 1151.
- (31) Asbrand, M.; Eisenmann, B. *Z. Anorg. Allg. Chem.* **1994**, *620*, 1837.
- (32) Lam, R.; Mar, A. *Inorg. Chem.* **1996**, *35*, 6959.
- (33) Chow, D. T.; McDonald, R.; Mar, A. *Inorg. Chem.* **1997**, *36*, 3750.
- (34) Lam, R.; Mar, A. *Inorg. Chem.* **1998**, *37*, 5364.

- (35) Eisenmann, B.; Jordan, H.; Schäfer, H. *Z. Naturforsch., B: Anorg. Chem., Org. Chem.* **1983**, *38*, 404.
- (36) Dörrscheidt, W.; Widera, A.; Schäfer, H. *Z. Naturforsch., B: Anorg. Chem., Org. Chem.* **1977**, *32*, 1097.
- (37) Eisenmann, B.; Rössler, U. *Z. Anorg. Allg. Chem.* **1998**, *624*, 406.
- (38) Eisenmann, B.; Jordan, H.; Schäfer, H. *Z. Anorg. Allg. Chem.* **1986**, *532*, 73.
- (39) Hoffmann, R. *J. Chem. Phys.* **1963**, *39*, 1397.
- (40) Whangbo, M.-H.; Hoffmann, R. *J. Am. Chem. Soc.* **1978**, *100*, 6093.
- (41) Hoffmann, R. *Solids and Surfaces: A Chemist's View of Bonding in Extended Structures*; VCH Publishers: New York, 1988.
- (42) Bryden, J. H. *Acta Crystallogr.* **1962**, *15*, 167.
- (43) Eisenmann, B.; Jordan, H.; Schäfer, H. *Z. Naturforsch., B: Anorg. Chem., Org. Chem.* **1984**, *39*, 864.

CHAPTER 5

The Ternary Arsenide $\text{Ba}_{0.8}\text{Hf}_{12}\text{As}_{17.7}$, a Variant of the Cr_{12}P_7 Structure Type with Inserted Arsenic Ribbons[†]

INTRODUCTION

Ternary pnictides of the early transition metals provide fertile ground for discovering new classes of Zintl compounds.¹ The transition metal component introduces the potential for d electrons to participate in a variety of interesting electrical and magnetic phenomena, such as colossal magnetoresistance in $\text{Eu}_{14}\text{MnSb}_{11}$.² The restriction to the early transition metals rests on the expectation that phases isostructural to the main group analogues can be prepared. Thus, for instance, the $A_{14}\text{MnPn}_{11}$ ($A = \text{Ca}, \text{Sr}, \text{Ba}, \text{Eu}; \text{Pn} = \text{P}, \text{As}, \text{Sb}, \text{Bi}$) phases¹⁻⁴ adopt the $\text{Ca}_{14}\text{AlSb}_{11}$ structure type.⁵ There are few other ternary alkaline earth arsenides of the early transition metals known ($A_4\text{TiPn}_4$ ($A = \text{Sr}, \text{Ba}; \text{Pn} = \text{P}, \text{As}$)⁶ and $A\text{Cr}_2\text{As}_2$ ($A = \text{Ca}, \text{Sr}, \text{Ba}$)⁷), none of these exhibiting As-As bonding.

We report here the synthesis and structure of the nonstoichiometric ternary arsenide $\text{Ba}_{0.8}\text{Hf}_{12}\text{As}_{17.7}$. While an analogous main group compound is not expected

[†] A version of this chapter has been published. Lam, R.; Mar, A. *Inorg. Chem.* **1998**, *37*, 5364. Copyright 1998 American Chemical Society.

(because of the high CN of Hf), $\text{Ba}_{0.8}\text{Hf}_{12}\text{As}_{17.7}$ displays the unusual feature of As ribbons inserted between isolated columnar assemblies of Hf_6 trigonal prisms. These ribbons represent, to our knowledge, the first example of the stabilization of extended homoatomic bonding of the nonmetal (or metalloid) component within the large family of hexagonal structures based on the stacking of trigonal prisms.⁸ Extended Hückel band structure calculations are presented to lend insight into the nature of As–As bonding in $\text{Ba}_{0.8}\text{Hf}_{12}\text{As}_{17.7}$.

EXPERIMENTAL SECTION

SYNTHESIS

Single crystals of $\text{Ba}_{0.8}\text{Hf}_{12}\text{As}_{17.7}$ were obtained from reaction of a 0.25-g mixture of Ba, Hf, and As in a 3:1:5 ratio in a tin flux (Ba, 107 mg, 0.78 mmol, 99.9%, Alfa-Aesar; Hf, 46 mg, 0.26 mmol, 99.8%, Cerac; As, 97 mg, 1.30 mmol, 99.99%, Alfa-Aesar; Sn, 309 mg, 2.60 mmol, 99.8%, Cerac) loaded into a sealed and evacuated fused-silica tube (7 cm length, 10 mm i.d.). The mixture was heated at 600 °C for 1 day and 950 °C for 2 days, cooled to 600 °C over 1 day, and then cooled to room temperature over 10 hours. Dissolving the excess Sn in concentrated HCl afforded thin needles of the ternary compound, as well as the binary phases HfAs ⁹ and Sn_4As_3 ¹⁰ as byproducts. EDX (energy-dispersive X-ray) analysis of these crystals on a Hitachi S-2700 scanning electron microscope confirmed the presence of all three elements (Ba, 3(1); Hf, 44(1); As, 53(1) mol %; average of 8 analyses) and the absence of any residual Sn. The observed powder X-ray diffraction pattern of $\text{Ba}_{0.8}\text{Hf}_{12}\text{As}_{17.7}$, obtained on an Enraf-

Nonius FR552 Guinier camera (Cu $K_{\alpha 1}$ radiation; Si standard), agrees well with that calculated from the crystal structure by the program LAZY-PULVERIX¹¹ (Table A-8).

STRUCTURE DETERMINATION

Weissenberg photographs clearly revealed Laue symmetry $6/m$ and gave preliminary cell parameters. Final cell parameters were determined from a least-squares analysis of the setting angles of 38 reflections in the range $18^\circ \leq 2\theta(\text{MoK}\alpha) \leq 29^\circ$ centered on a Siemens P4RA diffractometer. Crystal data and further details of the data collection are given in Table 5-1.

Calculations were carried out with the use of programs in the SHELXTL (Version 5.0) package.¹² Conventional atomic scattering factors and anomalous dispersion corrections were used.¹³ Intensity data were processed, and face-indexed Gaussian-type absorption corrections were applied in XPREP. The systematic extinction ($00l: l = 2n + 1$) was noted, suggesting $C_6^6 - P6_3$ and $C_{6h}^2 - P6_3/m$ as possible space groups. The centrosymmetric space group $P6_3/m$ was chosen based on intensity statistics, satisfactory averaging, and the successful structure solution. The initial positions of the Hf and As atoms were found by direct methods, and the structure was refined by least-squares methods. Residual electron density at 0, 0, ~ 0.14 was assigned to Ba based on reasonable Ba-As distances. Note, however, that full occupation of Ba atoms at this site results in close contacts ($< 1 \text{ \AA}$) between symmetry-equivalent positions, as well as a very high value for the displacement parameter. The As(1) and As(4) sites also revealed anomalously large displacement parameters. When the occupancy parameters for these sites were refined, they converged to values of 20.9(6)% for Ba, 56(1)% for As(1), and

39(1)% for As(4), and the displacement parameters were now comparable to those of the other atoms. The occupancies of the Hf(1), Hf(2), As(2), and As(3) atoms were essentially 100%. The resulting formula, $\text{Ba}_{0.8}\text{Hf}_{12}\text{As}_{17.7}$, is consistent with the chemical analysis determined independently (*vide supra*). The atomic positions were standardized with the use of the program STRUCTURE TIDY.¹⁴ The final cycle of least-squares refinement on F_o^2 of 44 variables (including anisotropic displacement parameters and an isotropic extinction parameter) and 1148 averaged reflections (including those having $F_o^2 < 0$) converged to values of $R_w(F_o^2)$ of 0.118 and $R(F)$ (for $F_o^2 > 2\sigma(F_o^2)$) of 0.063. The final difference electron density map is featureless ($\Delta\rho_{\text{max}} = 5.58$; $\Delta\rho_{\text{min}} = -5.36 \text{ e}^- \text{ \AA}^{-3}$). Final values of the positional and equivalent isotropic displacement parameters are given in Table 5–2 and anisotropic displacement parameters are listed in Table A–9.

ELECTRICAL RESISTIVITY

Single crystals of ~0.5 mm length, verified to be $\text{Ba}_{0.8}\text{Hf}_{12}\text{As}_{17.7}$ by EDX analysis, were mounted with Ag paint on Au wires with graphite extensions. Four-probe ac electrical resistivity data were measured along the needle axis *c* of these crystals between 25 and 290 K.

BAND STRUCTURE

One-electron band structure calculations on the hypothetical fully-stoichiometric $[\text{Hf}_{12}\text{As}_{24}]$ substructure were performed by the tight-binding method with an extended Hückel-type Hamiltonian.^{15, 16} Extended Hückel parameters used^{17, 18} are listed in Table

5–3. Properties were extracted from the band structure using 50 k points in the irreducible portion of the Brillouin zone.¹⁹

RESULTS AND DISCUSSION

DESCRIPTION OF THE STRUCTURE

$\text{Ba}_{0.8}\text{Hf}_{12}\text{As}_{17.7}$ adopts a novel structure, shown in projection down the short c axis in Figure 5–1. Selected interatomic distances and angles are listed in Table 5–4. In order to draw structural relationships, it will be advantageous to view the structure of $\text{Ba}_{0.8}\text{Hf}_{12}\text{As}_{17.7}$ as comprising assemblies of As(3)-centered trigonal prisms whose vertices are the Hf(1) and Hf(2) atoms. Three AsHf_6 trigonal prisms are linked to give a larger triangular grouping, in turn generating a vacant site at $\frac{1}{3}, \frac{2}{3}, \frac{1}{4}$. The triangular faces of these trigonal prisms are then shared to give the columnar assemblies ${}^1_x[\text{As}_3\text{Hf}_6]$ running along [001]. Separating these columns are Ba cations and six-atom wide ribbons built up from As(1), As(2), and As(4). Figure 5–2 shows a view perpendicular to one of these As ribbons, which consists of alternating short (As(2)–As(4) 2.518(5) Å, As(1)–As(1) 2.495(6) Å) and long (As(1)–As(4) 2.599(5) Å) bonds. These distances are slightly longer than those for typical As–As single bonds (2.4–2.5 Å).^{20–25} The ribbons are nearly flat, with As–As–As bond angles of 86.2(2)–92.01(8)°. While the As(2) sites at the two edges of the ribbon are fully occupied, the inner As(1) and As(4) sites are deficient, with occupancies of 56(1)% and 39(1)%, respectively. These ribbons may be considered to be excised from infinite square nets, which form a common motif in the structures of many pnictides and chalcogenides.²⁶ In particular, square nets of partially-occupied (57.5%) As

sites, at comparable As–As distances of 2.563(7) Å, also occur in the compound $Zr_2As_{1.9}S$ (ZrSiS-type structure).²⁷ One interpretation for the As vacancies is that the ribbon is constructed locally from finite zigzag segments of As atoms, stitched together at irregular intervals. We have not detected any superstructure reflections that might suggest long-range order of these As vacancies.

Alternatively, the more conventional approach of viewing the structure as consisting of coordination polyhedra centered by the electropositive Hf and Ba atoms is also useful. The Hf atoms adopt two types of coordination geometries, as shown in Figure 5–3. The Hf(1) atoms are coordinated by nine As atoms at distances of 2.718(2)–2.842(3) Å in a monocapped square antiprism, the capping As atom being tilted to one side as is characteristically observed. The Hf(2) atoms are coordinated by eight As atoms at distances of 2.730(2)–2.839(7) Å in a more regular square antiprism. These Hf–As distances are comparable to those in the binary $HfAs_2$ (2.77(5)–2.92(2) Å), in which a similar Hf monocapped square antiprismatic coordination is found.⁹ The Ba atoms, at the sites $4e$ (0, 0, z , with $z = 0.137$), are located along the sixfold axes within channels outlined by the As(2) atoms. Each Ba atom is coordinated by nine As(2) atoms at distances of 3.202(3)–3.852(7) Å in a tricapped trigonal prism. As shown in Figure 5–4, the short 0.80(2) and 0.97(2) Å contacts preclude full occupancy of these sites. The refined partial occupancy of 20.9(6)% implies that approximately every fourth site contains a Ba atom, consistent with a reasonable minimum Ba–Ba separation equal to the c repeat (3.5526(4) Å). Perhaps the best interpretation of this disorder is that first proposed for the closely-related $V_{12}P_7$ structure:²⁸ while there may be local ordering of Ba atoms along a particular sixfold axis (*i.e.*, only one of the four possible sites 0, 0,

0.137; 0, 0, 0.363; 0, 0, 0.637; or 0, 0, 0.863 is occupied), it is the distribution of such axes that is either random or incommensurate with the unit cell repeats.

STRUCTURAL RELATIONSHIPS

The formula of the title compound may be represented as $Ba_{1-x}Hf_{12}As_{24-y}$, where there are deficiencies in both the Ba and As sites. Assuming exactly 25% occupancy of the Ba site (necessary to maintain sensible Ba–Ba separations) and 100% occupancy of all As sites, we will refer to the ideal formula as $BaHf_{12}As_{24}$ for the discussion that follows. This helps to draw attention to its close relation to a large family of hexagonal structure types with a metal/nonmetal ratio close to 2 and built up of linked trigonal prisms.⁸ However, there are some unique differences displayed by $BaHf_{12}As_{24}$ that make it a novel addition to this family. $BaHf_{12}As_{24}$ is best regarded as an intermediate structure type between the $Cr_{12}P_7$ (anti- Th_7S_{12})^{28–32} and $Ho_6Ni_{20}P_{13}$ types,^{33–37} as shown in Figure 5–5. All three structures share the feature of the large triangular assembly of linked trigonal prisms extended as columns along the threefold axes of the unit cell. From one point of view, $Cr_{12}P_7$ and $BaHf_{12}As_{24}$ are similar in having the nonmetal atoms centered in the outermost trigonal prisms whose vertices are the metal atoms; the central trigonal prism remains vacant. Then, insertion of ribbons of As atoms into tetrahedral (As(1), As(4)) and trigonal pyramidal (As(2)) sites between these triangular assemblies results in the $BaHf_{12}As_{24}$ structure. From another point of view, $BaHf_{12}As_{24}$ can be regarded as an antitype of the $Ho_6Ni_{20}P_{13}$ structure, in which the metal and nonmetal atoms are interchanged. Moreover, there is a triangular (planar) site at $\frac{1}{3}, \frac{2}{3}, \frac{1}{4}$ that is occupied by a Ni atom in $Ho_6Ni_{20}P_{13}$ but is vacant in $BaHf_{12}As_{24}$. The Ni atom closest to the

sixfold axis is disordered over two closely-spaced sites in $\text{Ho}_6\text{Ni}_{20}\text{P}_{13}$,³³ while the corresponding As atom is well-behaved in $\text{BaHf}_{12}\text{As}_{24}$. This occurs in association with the disorder of the atom occupying the channels along the sixfold axis $0, 0, z$. While it is at $z = 0$ or $z = \frac{1}{4}$ where a small nonmetal atom is located for most Cr_{12}P_7 - and $\text{Zr}_6\text{Ni}_{20}\text{P}_{13}$ -related structures, the large Ba atom achieves its high CN to surrounding As atoms by being situated at $z = 0.137$. The relationship between the Cr_{12}P_7 , $\text{BaHf}_{12}\text{As}_{24}$, and $\text{Ho}_6\text{Ni}_{20}\text{P}_{13}$ structures is summarized in Table 5-5, which shows the correspondence between the various atomic sites and their occupation.

ELECTRICAL RESISTIVITY

A representative plot of the electrical resistivity of $\text{Ba}_{0.8}\text{Hf}_{12}\text{As}_{17.7}$, measured along the needle axis c , as a function of temperature, is shown in Figure 5-6. It is poorly metallic with resistivity values ($\rho_{290} \approx 3 \times 10^{-4} \Omega \text{ cm}$, $\rho_{25} \approx 2 \times 10^{-4} \Omega \text{ cm}$, and $\rho_{290}/\rho_{25} \approx 0.63$) that are consistent among several samples. For the linear portion of the curve, the temperature coefficient is $4 \times 10^{-7} \Omega \text{ cm K}^{-1}$. The plateau at low temperature arises from impurity scattering.

BONDING

Whether one considers the idealized formula $\text{BaHf}_{12}\text{As}_{24}$ or the observed nonstoichiometric one $\text{Ba}_{0.8}\text{Hf}_{12}\text{As}_{17.7}$, a first approximation of the distribution of electrons via the Zintl scheme (metal atoms transferring their valence electrons to the nonmetal atoms) dictates that the As atoms cannot attain an octet without forming additional homoatomic bonds. For instance, the idealized formulation

$(\text{Ba}^{2+})[(\text{Hf}^{4+})_{12}(\text{As}^{2.1-})_{24}]$ implies that, on average, each As atom has only 7.1 valence electrons available to it, so that some As–As bonding must occur. For the observed nonstoichiometric composition and assuming As(3) to be As^{3-} , the more detailed formulation $(\text{Ba}^{2+})_{0.8}[(\text{Hf}^{4+})_{12}(\text{As}(3)^{3-})_6(\text{As}^{2.7-})_{11.7}]$ also implies that As is not fully reduced within the ribbons and that weak As–As bonding is present. This ionic extreme is not expected to be realistic, of course.

The band structure calculation on the ideal $[\text{Hf}_{12}\text{As}_{24}]$ framework confirms the presence of significant covalency in the Hf–As bonds. As shown in Figure 5–7, both Hf and As states have substantial contributions to the DOS in the region -16 to -10 eV. Equally important, the Hf and As bands are broad enough to overlap such that there is no energy gap. Assuming a rigid band model, the Fermi level in the actual compound (substoichiometric in As) falls in the valence band, consistent with the metallic behavior observed experimentally. Certainly, the presence of As vacancies will modify the details of orbital overlap in the true electronic structure, but limitations in the EHMO framework preclude a straightforward way of modeling vacancies. Particularly satisfying, nonetheless, is that even this simple band picture provides insight as to why As deficiencies occur in $\text{Ba}_{0.8}\text{Hf}_{12}\text{As}_{17.7}$. Figure 5–8 shows the COOP curves for the As–As contacts within the As ribbons in the structure. At the electron count corresponding to the observed stoichiometry, the Fermi level just separates the As–As bonding states from the As–As antibonding states; that is, the extent of As–As bonding is maximized at precisely this electron count. Within this ribbon (Figure 5–2), the average integrated As–As overlap population is 0.476, indicating fairly strong bonding interactions. The alternation of strong and weak As–As bonding (integrated overlap populations: As(2)–

As(4) 0.553, As(4)–As(1) 0.389, As(1)–As(1) 0.499) is reminiscent of a similar pattern observed in the ribbons of Sb atoms in β -ZrSb₂.³⁸ The depopulation of the As–As antibonding states occurs at the expense of Hf–As bonding. Figure 5–9 shows the COOP curve for the Hf–As bonds in the structure. The Fermi level is lowered to a point below which depletion of strongly Hf–As bonding levels would no longer be compensated by any further gain in As–As bonding within the ribbons.

Overall, the band structure is in good agreement with the qualitative picture expected for a compound displaying homoatomic bonding of only the nonmetal component.¹ The overlap of As p states with Hf d states that can accept electron density back from the higher-lying As–As antibonding states is in part responsible for the metallic conduction.

There is an immense structural diversity displayed by the hexagonal structures built up from trigonal prisms centered by metal atoms. Generally these compounds are metal-rich, and metal-metal bonding is a predominant feature. The identification of Ba_{0.8}Hf₁₂As_{17.7} is significant in that it implies the existence of an equally rich family of inversely-related structures in which nonmetal-nonmetal bonding plays the important stabilizing role.

Table 5–1. Crystallographic Data for Ba_{0.8}Hf₁₂As_{17.7}

Formula	Ba _{0.8} Hf ₁₂ As _{17.7}
Formula mass, amu	3577.85
Space group	$C_{6h}^2 - P6_3/m$ (No. 176)
a , Å	14.997(1) ^a
c , Å	3.5526(4) ^a
V , Å ³	692.0(1)
Z	1
T , °C	22
Diffractometer	Siemens P4RA
ρ_{calc} , g cm ⁻³	8.617
Crystal dimensions, mm	0.265 × 0.003 × 0.003
Radiation	Graphite-monochromated MoK α , $\lambda = 0.71073$ Å
$\mu(\text{MoK}\alpha)$, cm ⁻¹	670.6
Transmission factors ^b	0.763–0.849
Scan type	θ – 2θ
Scan speed, deg. min ⁻¹	5.0
Scan range, deg.	0.40 below K α_1 to 0.40 above K α_2
2θ limits	$2^\circ \leq 2\theta(\text{MoK}\alpha) \leq 70^\circ$
Data collected	$-15 \leq h \leq 23$, $-24 \leq k \leq 17$, $-5 \leq l \leq 5$
No. of data collected	7115
No. of unique data, including $F_o^2 < 0$	1148 ($R_{\text{int}} = 0.158$)
No. of unique data, with $F_o^2 > 2\sigma(F_o^2)$	654

Table 5–1. Crystallographic Data for Ba_{0.8}Hf₁₂As_{17.7} (continued)

No. of variables	44
Extinction coefficient ^c	0.0013(1)
$R(F)$ for $F_o^2 > 2\sigma(F_o^2)$ ^d	0.063
$R_w(F_o^2)$ ^e	0.118
Goodness of fit ^f	1.06
$(\Delta\rho)_{\max}, (\Delta\rho)_{\min}, e^{-\text{\AA}^{-3}}$	5.6, -5.4

^a Obtained from a refinement constrained so that $\alpha = \beta = 90^\circ$ and $\gamma = 120^\circ$.

^b A Gaussian-type absorption correction was applied, with the use of programs in the SHELXTL package (Sheldrick, G. M. SHELXTL Version 5.0, Siemens Analytical X-Ray Instruments, Inc., Madison, WI, 1994).

^c An extinction parameter x was refined, where F_c is multiplied by: $k[1 + 0.001 * x * F_c^2 * \lambda^3 / \sin(2\theta)]^{-1/4}$.

$$^d R(F) = \frac{\sum ||F_o| - |F_c||}{\sum |F_o|}$$

$$^e R_w(F_o^2) = \frac{[\sum [w(F_o^2 - F_c^2)^2]]^{1/2}}{[\sum wF_o^4]^{1/2}}; w^{-1} = [\sigma^2(F_o^2) + (0.0356P)^2 + 0.00P] \text{ where } P = [\max(F_o^2, 0) + 2F_c^2]/3.$$

$$^f \text{GooF} = S = \left[\frac{\sum [w(F_o^2 - F_c^2)^2]}{(n - p)} \right]^{1/2} \text{ where } n \text{ is the number of reflections and } p \text{ is the total number of parameters refined.}$$

Table 5-2. Atomic Coordinates, Occupancies, and Equivalent Isotropic DisplacementParameters (\AA^2) for $\text{Ba}_{0.8}\text{Hf}_{12}\text{As}_{17.7}$

Atom	Wyckoff position, site symmetry		x	y	z	Occupancy	U_{eq}^a
Ba	4e	3..	0	0	0.137(3)	0.209(6)	0.033(6)
Hf(1)	6h	$m..$	0.35495(7)	0.11892(7)	$\frac{1}{4}$	1	0.0042(2)
Hf(2)	6h	$m..$	0.61802(8)	0.17720(8)	$\frac{1}{4}$	1	0.0042(2)
As(1)	6h	$m..$	0.0142(3)	0.4500(3)	$\frac{1}{4}$	0.56(1)	0.006(1)
As(2)	6h	$m..$	0.0718(2)	0.2384(2)	$\frac{1}{4}$	1	0.0053(5)
As(3)	6h	$m..$	0.2850(2)	0.5099(2)	$\frac{1}{4}$	1	0.0027(4)
As(4)	6h	$m..$	0.3422(5)	0.2965(5)	$\frac{1}{4}$	0.39(1)	0.007(2)

^a U_{eq} is defined as one-third of the trace of the orthogonalized U_{ij} tensor.**Table 5-3.** Extended Hückel Parameters^{17, 18}

Atom	Orbital	H_{ii} (eV)	ζ_1	c_1	ζ_2	c_2
Hf	6s	-8.12	2.21			
	6p	-4.50	2.17			
	5d	-8.14	4.36	0.6967	1.709	0.5322
As	4s	-16.22	2.23			
	4p	-12.16	1.89			

Table 5-4. Selected Interatomic Distances (Å) and Angles (°) for Ba_{0.8}Hf₁₂As_{17.7}

Ba–As(2)	3.202(3) (x3)	Hf(2)–As(3)	2.730(2) (x2)
Ba–As(2)	3.461(5) (x3)	Hf(2)–As(3)	2.740(2) (x2)
Ba–As(2)	3.852(7) (x3)	Hf(2)–As(1)	2.794(3) (x2)
Hf(1)–As(3)	2.718(2) (x2)	Hf(2)–As(1)	2.805(4)
Hf(1)–As(4)	2.763(7)	Hf(2)–As(4)	2.839(7)
Hf(1)–As(4)	2.803(5) (x2)	As(1)–As(1)	2.495(6) (x2)
Hf(1)–As(1)	2.806(4)	As(1)–As(4)	2.599(5) (x2)
Hf(1)–As(2)	2.823(2) (x2)	As(2)–As(4)	2.518(5) (x2)
Hf(1)–As(2)	2.842(3)		
As(2)–Ba–As(2)	118.45(9) (x3)	As(1)–As(1)–As(1)	90.8(3)
As(2)–Ba–As(2)	163.8(4) (x3)	As(1)–As(1)–As(4)	91.5(1) (x2)
As(2)–Ba–As(2)	105.3(2) (x3)	As(4)–As(1)–As(4)	86.2(2)
As(2)–Ba–As(2)	66.08(4) (x6)	As(4)–As(2)–As(4)	89.7(2)
		As(2)–As(4)–As(2)	89.7(2)
		As(2)–As(4)–As(1)	92.01(8) (x2)
		As(1)–As(4)–As(1)	86.2(2)

Table 5-5. Comparison of Site Occupation²⁸⁻³⁷

Sites	Cr ₁₂ P ₇	BaHf ₁₂ As ₂₄ ^a	Ho ₆ Ni ₂₀ P ₁₃
trigonal prisms	6 P	6 As	6 Ho
tetrahedra and pyramids	—	18 As	18 Ni
triangles	—	—	2 Ni
vertices of trigonal prisms	12 Cr	12 Hf	12 P
disordered sites along 0, 0, z	1 P	1 Ba	1 P

^a Ideal formula assuming 25% Ba and 100% As occupancies.

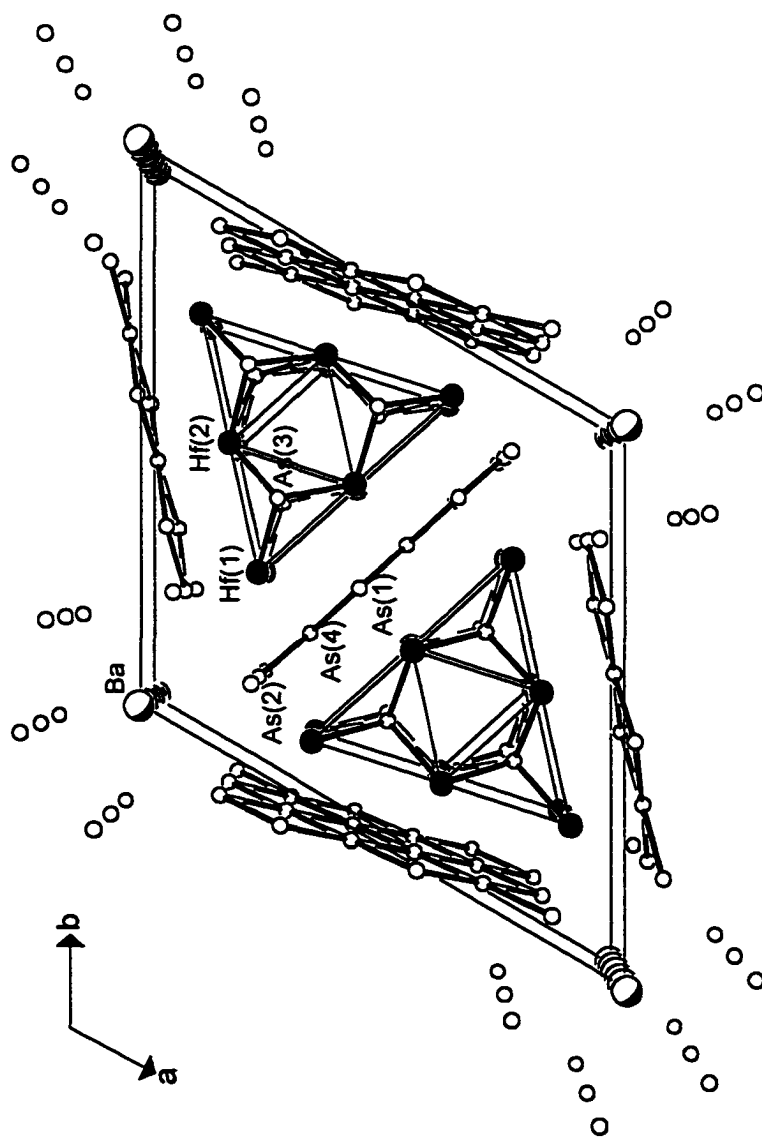


Figure 5-1. View of $\text{Ba}_{0.8}\text{Hf}_{1.2}\text{As}_{17.7}$ down the c axis with the unit cell outlined and the atoms labeled. The large partly-shaded circles are Ba atoms, the medium solid circles are Hf atoms, and the small open circles are As atoms.

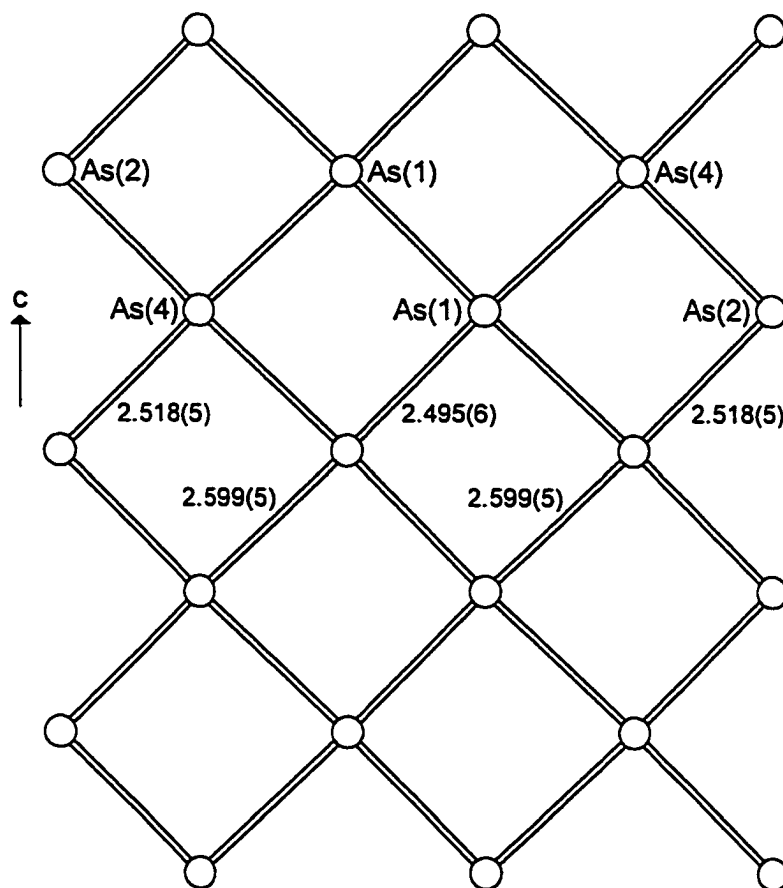


Figure 5–2. View of the As ribbon in $\text{Ba}_{0.8}\text{Hf}_{12}\text{As}_{17.7}$ running along c and built up from As(2), As(4), and As(1).

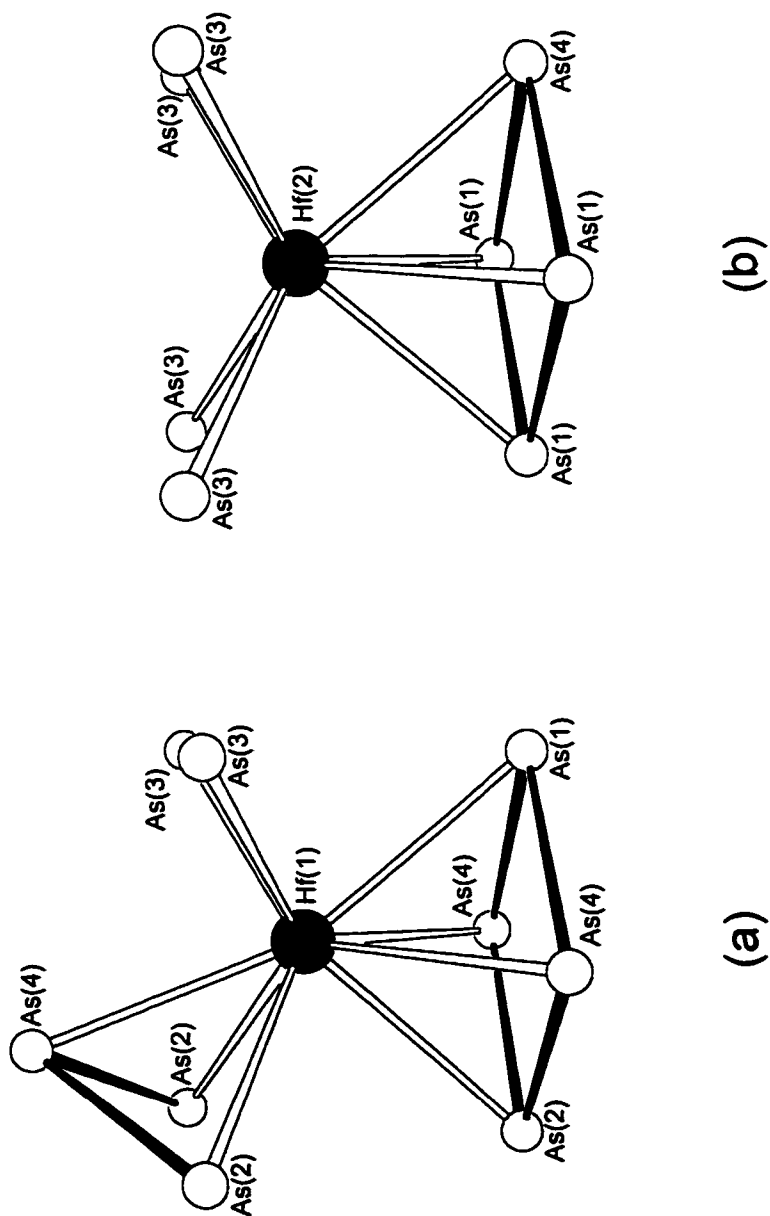


Figure 5-3. Coordination environment around (a) monocoordinated square antiprismatic Hf(1), and (b) square antiprismatic Hf(2) in $\text{Ba}_{0.8}\text{Hf}_{12}\text{As}_{17.7}$.

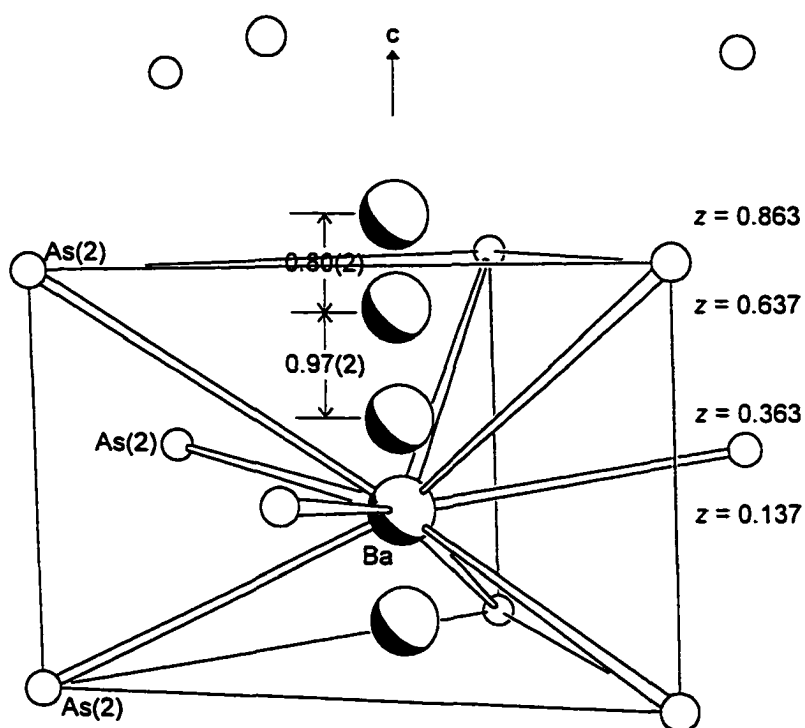


Figure 5-4. Coordination environment around Ba atom (at 0, 0, 0.137) in $\text{Ba}_{0.8}\text{Hf}_{12}\text{As}_{17.7}$, disordered among symmetry-equivalent sites along the sixfold axis (0, 0, z at the z coordinates shown).

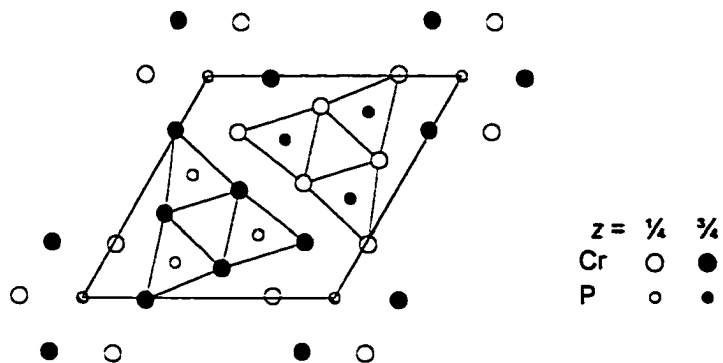
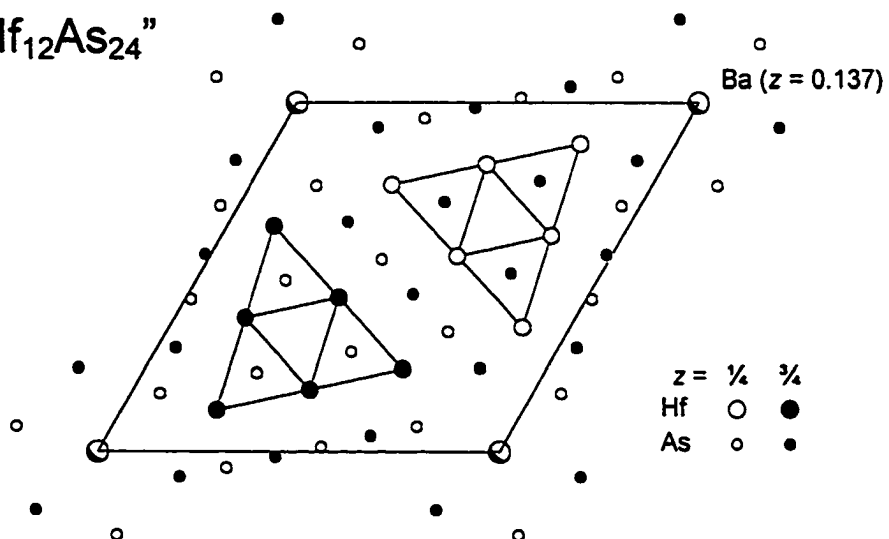
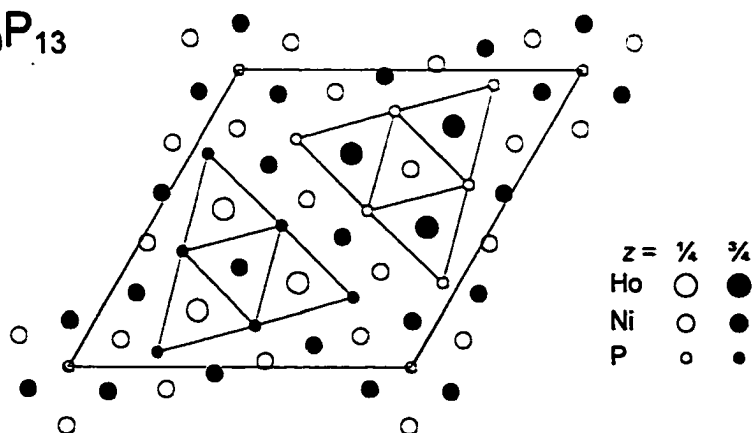
(a) Cr_{12}P_7 (b) "BaHf₁₂As₂₄"(c) $\text{Ho}_6\text{Ni}_{20}\text{P}_{13}$ 

Figure 5-5. Comparison of the structures of (a) Cr_{12}P_7 ,³⁰ (b) "BaHf₁₂As₂₄" (idealized formula), and (c) $\text{Ho}_6\text{Ni}_{20}\text{P}_{13}$,³⁴ shown in projection down the hexagonal c axis.

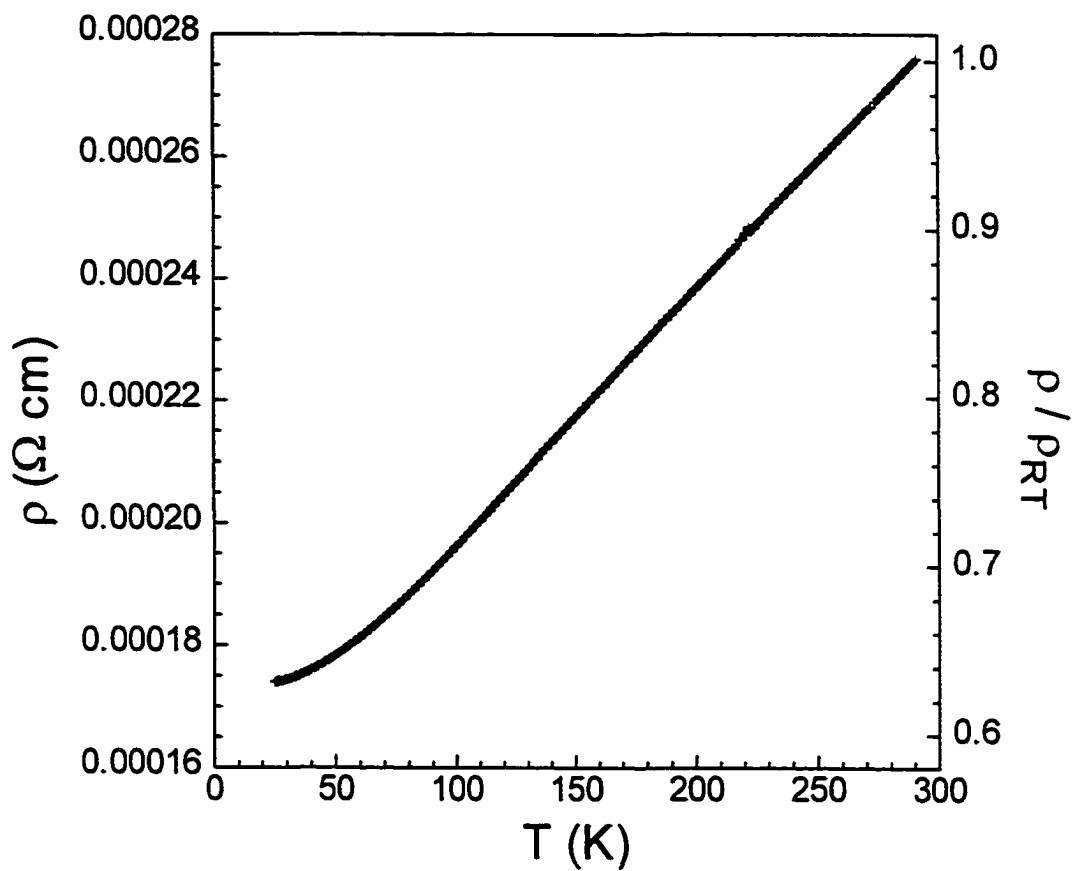


Figure 5-6. Plot of the electrical resistivity of $\text{Ba}_{0.8}\text{Hf}_{12}\text{As}_{17.7}$, measured along the needle axis c .

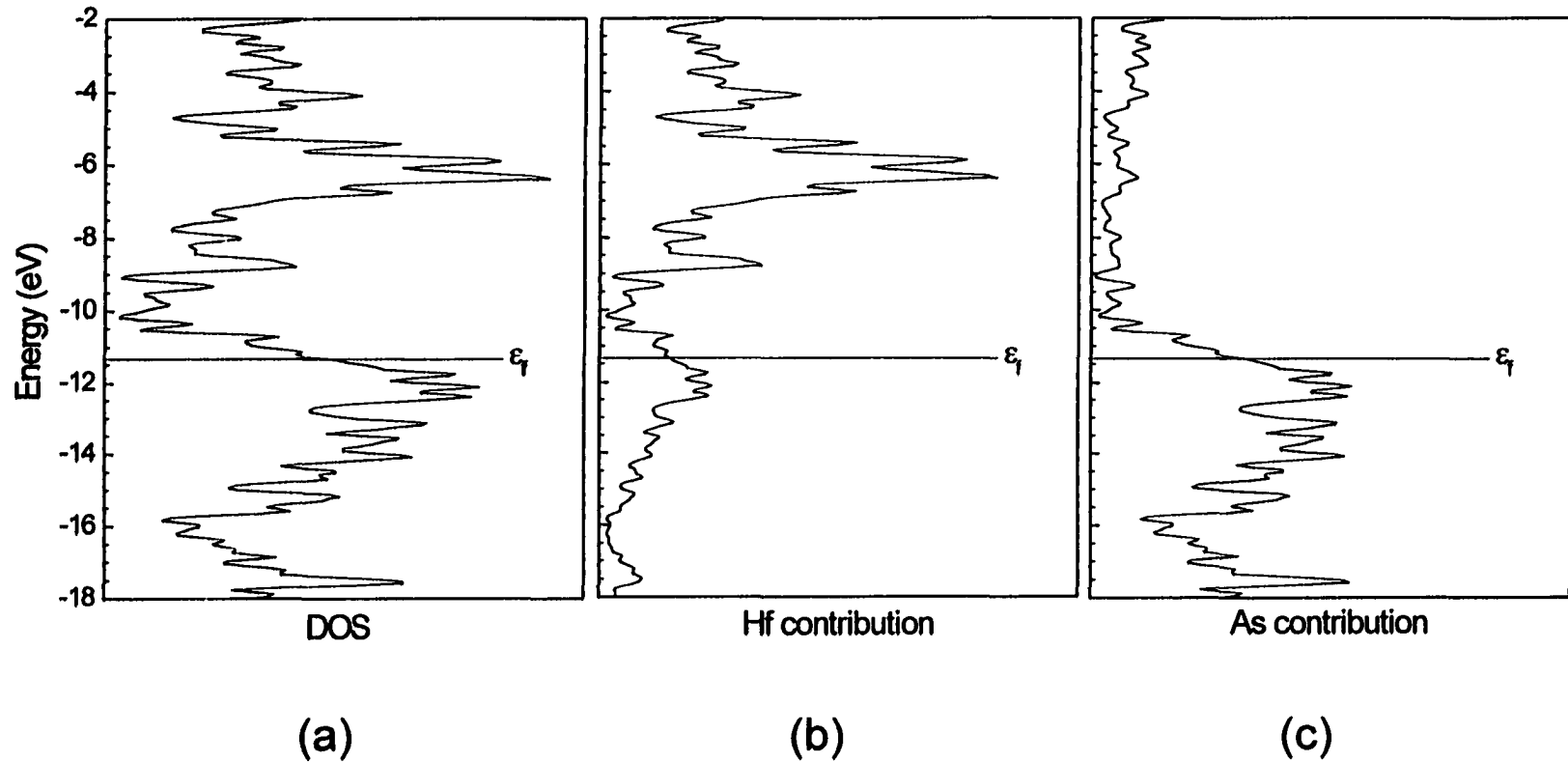


Figure 5-7. Density of states curve (and its Hf and As projections) for the $[\text{Hf}_{12}\text{As}_{24}]$ framework in idealized “ $\text{BaHf}_{12}\text{As}_{24}$.” The Fermi level ($\epsilon_f = -11.4$ eV) corresponding to substoichiometric $\text{Ba}_{0.8}\text{Hf}_{12}\text{As}_{17.7}$ is shown (assuming rigid band model).

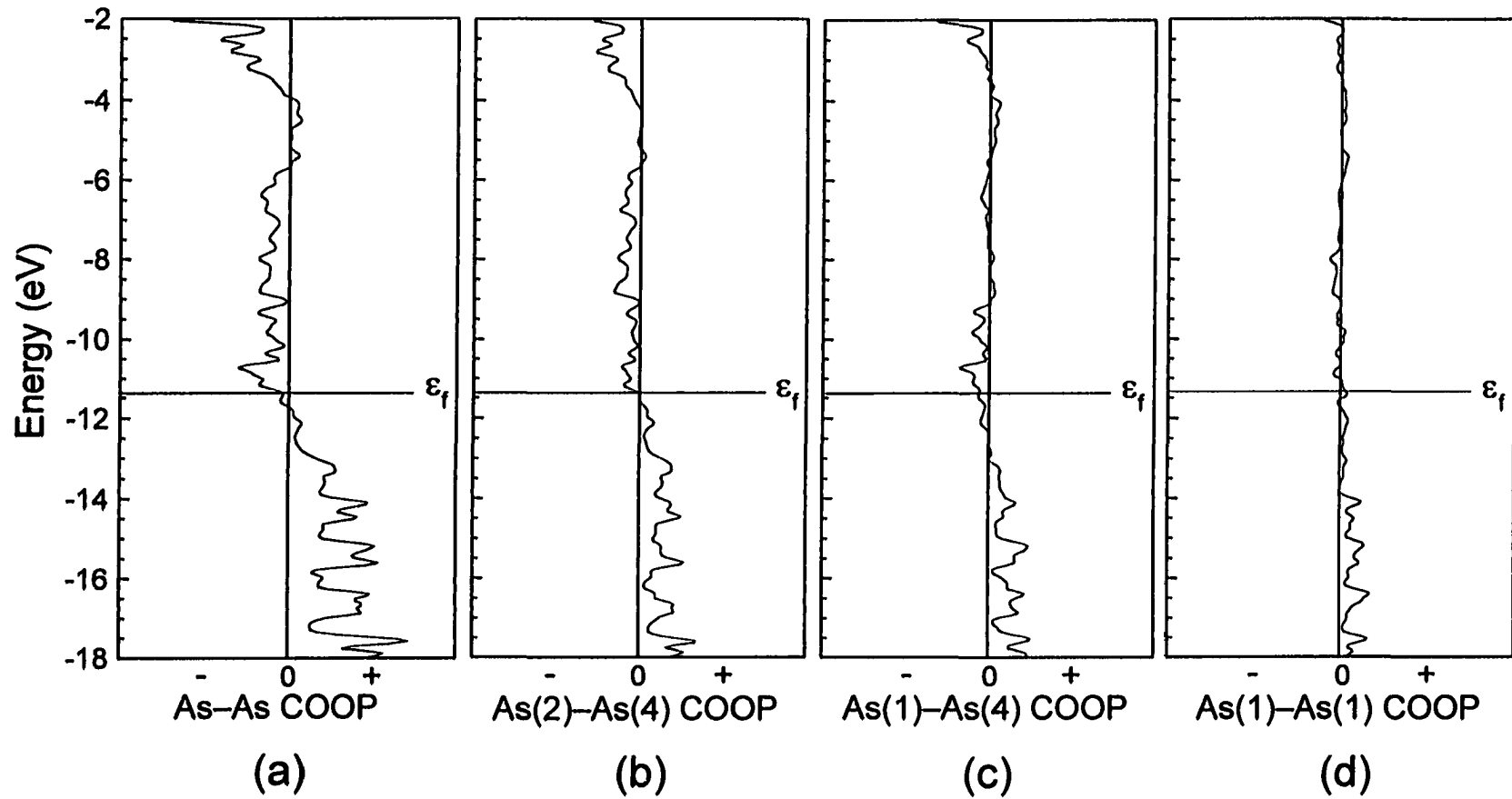


Figure 5-8. Crystal orbital overlap population curves for ((a) all; (b), (c), (d) specific) As-As contacts within the As ribbon of the $[\text{Hf}_{12}\text{As}_{24}]$ framework. The Fermi level corresponding to substoichiometric $\text{Ba}_{0.8}\text{Hf}_{12}\text{As}_{17.7}$ is shown.

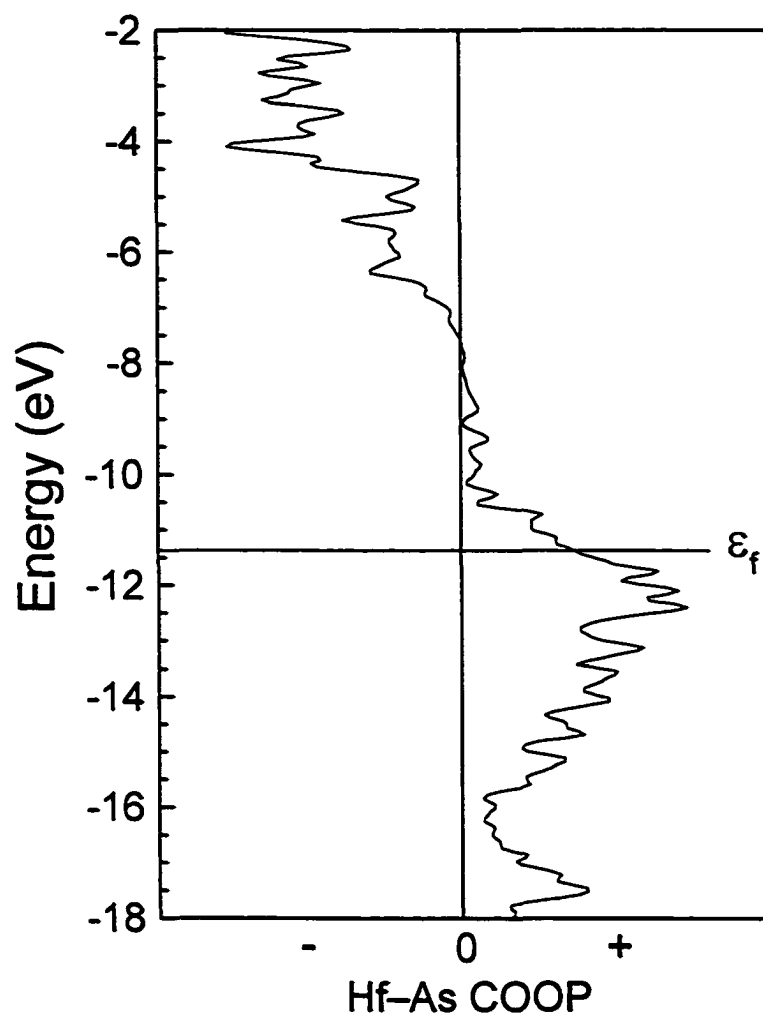


Figure 5–9. Crystal orbital overlap population curve for Hf–As contacts in the $[\text{Hf}_{12}\text{As}_{24}]$ framework. The Fermi level corresponding to $\text{Ba}_{0.8}\text{Hf}_{12}\text{As}_{17.7}$ is shown.

REFERENCES

- (1) Kauzlarich, S. M., Ed. *Chemistry, Structure, and Bonding of Zintl Phases and Ions*; VCH Publishers: New York, 1996.
- (2) Chan, J. Y.; Kauzlarich, S. M.; Klavins, P.; Shelton, R. N.; Webb, D. J. *Chem. Mater.* **1997**, *9*, 3132.
- (3) Rehr, A.; Kuromoto, T. Y.; Kauzlarich, S. M.; Del Castillo, J.; Webb, D. J. *Chem. Mater.* **1994**, *6*, 93.
- (4) Chan, J. Y.; Wang, M. E.; Rehr, A.; Kauzlarich, S. M.; Webb, D. J. *Chem. Mater.* **1997**, *9*, 2131 (and references therein).
- (5) Cordier, G.; Schäfer, H.; Stelter, M. *Z. Anorg. Allg. Chem.* **1984**, *519*, 183.
- (6) Nuss, J.; Höhle, W.; Peters, K.; von Schnering, H. G. *Z. Anorg. Allg. Chem.* **1996**, *622*, 1879.
- (7) Pfisterer, M.; Nagorsen, G. *Z. Naturforsch., B: Anorg. Chem., Org. Chem.* **1980**, *35*, 703.
- (8) Pivan, J.-Y.; Guérin, R.; Sergent, M. *J. Solid State Chem.* **1987**, *68*, 11.
- (9) Jeitschko, W.; Nowotny, H. *Monatsh. Chem.* **1962**, *93*, 1284.
- (10) Eckerlin, P.; Kischio, W. *Z. Anorg. Allg. Chem.* **1968**, *363*, 1.
- (11) Yvon, K.; Jeitschko, W.; Parthé, E. *J. Appl. Crystallogr.* **1977**, *10*, 73.
- (12) Sheldrick, G. M. *SHELXTL Version 5.0*, Siemens Analytical X-ray Instruments. Inc., Madison, WI, 1994.
- (13) *International Tables for X-ray Crystallography*; Wilson, A. J. C., Ed.; Kluwer: Dordrecht, The Netherlands, 1992; Vol. C.
- (14) Gelato, L. M.; Parthé, E. *J. Appl. Crystallogr.* **1987**, *20*, 139.

- (15) Whangbo, M.-H.; Hoffmann, R. *J. Am. Chem. Soc.* **1978**, *100*, 6093.
- (16) Hoffmann, R. *Solids and Surfaces: A Chemist's View of Bonding in Extended Structures*; VCH Publishers: New York, 1988.
- (17) Kleinke, H.; Franzen, H. F. *J. Alloys Compd.* **1997**, *225*, 110.
- (18) Johrendt, D.; Mewis, A. *Z. Naturforsch., B: Chem. Sci.* **1996**, *51*, 655.
- (19) Ramírez, R.; Böhm, M. C. *Int. J. Quantum Chem.* **1986**, *30*, 391.
- (20) Somer, M.; Carillo-Cabrera, W.; Peters, K.; von Schnering, H. G. *Z. Kristallogr.* **1995**, *210*, 876.
- (21) Höhle, W.; Lin, J.; Hartweg, M.; von Schnering, H. G. *J. Solid State Chem.* **1992**, *97*, 1.
- (22) Bauhofer, W.; Wittmann, M.; von Schnering, H. G. *J. Phys. Chem. Solids* **1981**, *42*, 687.
- (23) Deller, K.; Eisenmann, B. *Z. Naturforsch., B: Anorg. Chem., Org. Chem.* **1977**, *32*, 1368.
- (24) Iandelli, A.; Franceschi, E. *J. Less-Common Met.* **1973**, *30*, 211.
- (25) Schmettow, W.; von Schnering, H. G. *Angew. Chem. Int. Ed. Engl.* **1977**, *16*, 857.
- (26) Tremel, W.; Hoffmann, R. *J. Am. Chem. Soc.* **1987**, *109*, 124.
- (27) Barthelat, J. C.; Jeannin, Y. *J. Less-Common Met.* **1972**, *26*, 273.
- (28) V₁₂P₇: Olofsson, O.; Ganglberger, E. *Acta Chem. Scand.* **1970**, *24*, 2389.
- (29) Cr₁₂P₇: Chun, H. K.; Carpenter, G. B. *Acta Crystallogr., Sect. B: Struct. Crystallogr. Cryst. Chem.* **1979**, *35*, 30.
- (30) Th₇S₁₂: Zachariasen, W. H. *Acta Crystallogr.* **1949**, *2*, 288.

- (31) $\text{Rh}_{12}\text{As}_7$: Pivan, J.-Y.; Guérin, R.; Sergent, M. *J. Less-Common Met.* **1985**, *107*, 249.
- (32) $\text{Rh}_{12}\text{As}_7$: Lambert-Andron, B.; Dhahri, E.; Chaudouët, P.; Madar, R. *J. Less-Common Met.* **1985**, *108*, 353.
- (33) $\text{Ho}_6\text{Ni}_{20}\text{P}_{13}$: Pivan, J.-Y.; Guérin, R.; Padiou, J.; Sergent, M. *J. Less-Common Met.* **1986**, *118*, 191.
- (34) $\text{Zr}_6\text{Ni}_{20}\text{P}_{13}$: Guérin, R.; El Ghadraoui, E. H.; Pivan, J.-Y.; Padiou, J.; Sergent, M. *Mater. Res. Bull.* **1984**, *19*, 1257.
- (35) $\text{U}_6\text{Ni}_{20}\text{P}_{13}$, $\text{U}_6\text{Ni}_{20}\text{As}_{13}$: Troc, R.; Kaczorowski, D.; Noël, H.; Le Bihan, T. *J. Alloys Compd.* **1992**, *184*, L27.
- (36) $\text{Tl}_6\text{Ag}_{20-x}\text{Se}_{1+y}$: Klepp, K. O. *J. Less-Common Met.* **1987**, *128*, 131.
- (37) $\text{Ho}_6\text{Ni}_{20}\text{P}_{13}$ ($P6_3/m$)³⁴ is essentially isotypic to $\text{Zr}_6\text{Ni}_{20}\text{P}_{13}$ ($P\bar{6}$)³⁵. We have chosen the former designation for the basis of comparison to “ $\text{BaHf}_{12}\text{As}_{24}$,” which also crystallizes in $P6_3/m$. The space group problem is discussed in: Jeitschko, W.; Jakubowski-Ripke, U. *Z. Kristallogr.* **1993**, *207*, 69.
- (38) Garcia, E.; Corbett, J. D. *J. Solid State Chem.* **1988**, *73*, 452.

CHAPTER 6

Rare-Earth Germanium Antimonides $RE_6Ge_{5-x}Sb_{11+x}$ ($RE =$ La–Nd, Sm, Gd–Dy): Syntheses and Structures[†]

INTRODUCTION

Our continuing exploration of the ternary rare-earth main-group-element antimonide systems $RE_xA_ySb_z$ ($A = Al, Ga, In, Si, Ge, Sn$) has revealed a strikingly rich and structurally diverse crystal chemistry, reinforced by recent discoveries of the novel compounds $La_{13}Ga_8Sb_{21}$,¹ $RE_{12}Ga_4Sb_{23}$ ($RE = La-Nd, Sm$),¹ $REIn_{1-x}Sb_2$ ($RE = La-Nd$),² $RESn_xSb_2$ ($RE = La-Nd, Sm$),³ and $EuSn_3Sb_4$.⁴ In all of these systems, the Zintl concept⁵⁻⁸ is invoked as a tool to rationalize the complex networks formed by the electronegative main-group atoms and characterized by extensive homoatomic (Ga–Ga, In–In, Sn–Sn, Sb–Sb) bonding. Historically, the Zintl concept has served as a successful paradigm for explaining the bonding in valence compounds of the form M_xA_y or $M_xA_yB_z$ ($M =$ alkali or alkaline-earth metal; $A, B =$ main-group elements), where the assumption of complete transfer of valence electrons from the electropositive elements (M) to the electronegative main-group atoms (A, B), which use them to satisfy the octet rule, is

[†] A version of this chapter has been submitted for publication. Lam, R.; McDonald, R; Mar, A.

tenable. However, the presence of “non-classical” structural features such as one-dimensional Sb ribbons or two-dimensional Sb square sheets, weak homoatomic bonding of the main-group elements, and partial covalent character in bonds between rare-earth and main-group elements in the aforementioned ternary compounds, poses challenging problems which test the limits of this important concept.⁹ The exception is the compound EuSn_3Sb_4 , whose structure is constructed from “classical” building blocks of trigonal pyramids of Sn and Sb and Sn-centred tetrahedra, for which the Zintl concept is applied in a straightforward manner.⁴

A recent investigation of the Ce–Ge–Sb ternary phase diagram¹⁰ has revealed a potentially rich system, yielding three new ternary compounds: Ce_2GeSb_3 (superstructure of ThGe_2 -type), “ $\text{Ce}_5\text{Ge}_3\text{Sb}_2$ ” (unknown structure), and Ce_3GeSb (La_3GeIn -type). We report here the syntheses and transport behaviour of a new series of ternary rare-earth germanium antimonides, $\text{RE}_6\text{Ge}_{5-x}\text{Sb}_{11+x}$ ($\text{RE} = \text{La–Nd, Sm, Gd–Dy}$), and the structures of the representative members $\text{La}_6\text{Ge}_{2.8(1)}\text{Sb}_{13.2(1)}$, $\text{Nd}_6\text{Ge}_{3.6(1)}\text{Sb}_{12.4(1)}$, and $\text{Gd}_6\text{Ge}_{4.3(1)}\text{Sb}_{11.7(1)}$. Their complex structures feature columns of face-sharing trigonal prisms of rare-earth atoms, separated by interconnecting walls defined by Ge and Sb atoms. Interest in ternary rare-earth-containing compounds is derived from the presence of *f* electrons which may give rise to useful magnetic and electronic properties, while interactions among three elemental components introduce a level of complexity not accessible in binary systems. The magnetic properties of these materials are detailed separately.¹¹

EXPERIMENTAL SECTION

SYNTHESIS

Reactions of powders of the elements (La–Nd, 99.9%, Alfa-Aesar; Sm, Gd–Dy, 99.9%, Cerac; Ge, 99.999%, Cerac; Sb, 99.995%, Aldrich) were carried out on a 0.25-g scale in evacuated fused-silica tubes (8-cm length; 10-mm i.d.). Elemental compositions of selected crystals were determined by EDX (energy-dispersive X-ray) analysis on a Hitachi S-2700 scanning electron microscope (Table 6–1). X-ray powder patterns were obtained on an Enraf-Nonius FR552 Guinier camera (Cu $K\alpha_1$ radiation; Si standard) and analyzed with the FilmScan and Jade 3.1 software packages.¹²

Single crystals of $\text{La}_6\text{Ge}_{2.8(1)}\text{Sb}_{13.2(1)}$, $\text{Nd}_6\text{Ge}_{3.6(1)}\text{Sb}_{12.4(1)}$, and $\text{Gd}_6\text{Ge}_{4.3(1)}\text{Sb}_{11.7(1)}$ used in the structure determination were obtained from reactions of the corresponding rare-earth element, Ge, and Sb in the ratio 6:5:11. The samples were heated at 570 °C for 1 day and then at 950 °C for 2 days, cooled to 500 °C over 1 day, and finally cooled to 20 °C over 5 hours. The extent of rare-earth substitution was investigated and in total, eight members in this series $\text{RE}_6\text{Ge}_{5-x}\text{Sb}_{11+x}$ ($\text{RE} = \text{La–Nd, Sm, Gd–Dy}$) could be successfully prepared. The products typically consisted of aggregates of shiny grey bulky needle-shaped crystals of $\text{RE}_6\text{Ge}_{5-x}\text{Sb}_{11+x}$ and grey powder, containing mostly the ternary compound and unreacted Ge. Unlike the other reactions which produced large quantities of single crystals, the Dy–Ge–Sb reaction resulted in only few tiny needle-shaped crystals of the ternary compound or the binary phase DySb^{13} and reddish brown powder consisting of DySb (major phase), $\text{Dy}_6\text{Ge}_{5-x}\text{Sb}_{11+x}$, as well as unreacted Ge. Attempts to substitute other trivalent rare-earth metals beyond Dy were unsuccessful, resulting instead in a mixture of the binary phase RESb (major phase), unreacted Ge, and other

unidentified phases. Substitutions involving the divalent Eu and Yb metals resulted predominantly in the binary phases EuSb_2 ¹⁴ and YbSb_2 ,¹⁵ respectively, in addition to unreacted Ge and other unidentified phases. The powder patterns of the entire series, $\text{RE}_6\text{Ge}_{5-x}\text{Sb}_{11+x}$ ($\text{RE} = \text{La-Nd, Sm, Gd-Dy}$), were indexed, and the cell parameters refined by least-squares fits with the use of the program POLSQ¹⁶ are given in Table 6-2. The observed and calculated interplanar distances, as well as intensities determined using the program LAZY-PULVERIX,¹⁷ are listed in Tables A-10 to A-17.

STRUCTURE DETERMINATION

X-ray structure determinations were performed on representative members in the series $\text{RE}_6\text{Ge}_{5-x}\text{Sb}_{11+x}$ ($\text{RE} = \text{La-Nd, Sm, Gd-Dy}$), one each for the early, middle, and late rare-earth substitutions. Preliminary cell parameters for $\text{La}_6\text{Ge}_{2.8(1)}\text{Sb}_{13.2(1)}$, $\text{Nd}_6\text{Ge}_{3.6(1)}\text{Sb}_{12.4(1)}$, and $\text{Gd}_6\text{Ge}_{4.3(1)}\text{Sb}_{11.7(1)}$ were determined from Weissenberg photographs, which revealed Laue symmetry mmm and systematic extinctions ($hkl: h + k + l = 2n + 1$) consistent with the orthorhombic space groups $Immm$, $Imm2$, $I222$, and $I2_12_12_1$. Final cell parameters for all three compounds were obtained from least-squares analyses of the setting angles of 24 reflections centred on an Enraf-Nonius CAD4 diffractometer. Intensity data were collected at 22 °C with the θ - 2θ scan technique in the range $3^\circ \leq 2\theta(\text{Mo } K_\alpha) \leq 70^\circ$. Crystal data and further details of the data collection are given in Table 6-3. All calculations were carried out with the use of the SHELXTL (Version 5.1) package.¹⁸ Conventional atomic scattering factors and anomalous dispersion corrections were used.¹⁹ The intensity data were processed and corrected for absorption by a semi-empirical method based on psi-scans in XPREP. Initial atomic

positions were found by direct methods using XS followed by subsequent difference Fourier syntheses, and refinements were performed by least-squares methods using XL.

For $\text{La}_6\text{Ge}_{2.8(1)}\text{Sb}_{13.2(1)}$, the centrosymmetric space group *Immm* was chosen on the basis of intensity statistics and the successful structure solution. Once all atomic positions were found, a refinement based on the formula “ $\text{La}_6\text{Ge}_5\text{Sb}_{11}$ ” revealed considerable electron density ($\Delta\rho_{\text{max}} = 73.91$, $\Delta\rho_{\text{min}} = -23.36 \text{ e}^- \text{ \AA}^{-3}$) at the site (~ 0.40 , $\frac{1}{2}$, 0), located 0.44 Å from Sb(4) ($\frac{1}{2}$, $\frac{1}{2}$, 0). Reminiscent of the “sliding distortion” observed for the central atom of similar Sb ribbons previously encountered in the related compound $\text{La}_6\text{MnSb}_{15}$,^{20,21} Sb(4) was subsequently reassigned exclusively to the new site (~ 0.40 , $\frac{1}{2}$, 0). Shifting Sb(4) off the $\frac{1}{2} \times y$ mirror plane resulted in significantly improved agreement factors but more importantly, the original site ($\frac{1}{2}$, $\frac{1}{2}$, 0) did not reappear in the difference Fourier map in later refinements. However, close Sb(4)–Sb(4) contacts (0.60 Å) required the occupancy of Sb(4) to be fixed at the theoretical maximum of 50% (51.4(3)% if allowed to refine). The sites at (0, ~ 0.12 , ~ 0.15) (*M*(1)) and (0, ~ 0.04 , 0) (*M*(2)) were next assumed to be occupied only by Ge, since reasonable Ge–Ge and Ge–Sb distances are obtained. This ordered model corresponds to the ideal formulation “ $\text{La}_6\text{Ge}_5\text{Sb}_{11}$ ” (Anal. Calcd. (mol%): La 27, Ge 23, Sb 50). However, given the consistently higher percentage of Sb and lower percentage of Ge observed in the EDX analyses (Table 6–1) relative to the current formula, the possibility that the sites *M*(1) and *M*(2) are occupied by a mixture of Ge and Sb was explored. The presence of residual electron density near these two sites, their relatively low displacement parameters, as well as chemical arguments to be presented later provided convincing evidence in favour of a disordered model. The occupancy of *M*(1) was assumed to be 100% (121(1)% when

refined with $M(1) = \text{Ge}$ and that for $M(2)$ was assumed to be 50% (65(1)% when refined with $M(2) = \text{Ge}$) owing to close $M(2)$ – $M(2)$ contacts (0.85 Å) as a result of the $x = 0$ z mirror plane. Successive refinements in which the sites $M(1)$ and $M(2)$ were constrained to be fully and half occupied, respectively, by a mixture of Ge and Sb resulted in occupancies of 61(3)% Ge(1) and 39(2)% Sb(6) in the site (0, \sim 0.12, \sim 0.15) and 19(2)% Ge(2) and 31(1)% Sb(7) in the site (0, \sim 0.04, 0). These refinements also led to reasonable values for the anisotropic displacement parameters, a featureless difference electron density map ($\Delta\rho_{\text{max}} = 4.82$, $\Delta\rho_{\text{min}} = -5.36 \text{ e}^- \text{ \AA}^{-3}$), and overall improvements in the agreement factors. A series of refinements allowing the occupancies of successive atoms to vary freely revealed full occupancies (99.4(4) – 100.1(4)%) for all other atoms. The final refined formula, $\text{La}_6\text{Ge}_{2.8(1)}\text{Sb}_{13.2(1)}$ ($Z = 2$) (Anal. Calcd. (mol%): La 27, Ge 13, Sb 60), is in excellent agreement with the elemental analysis.

The treatment of $\text{Nd}_6\text{Ge}_{3.6(1)}\text{Sb}_{12.4(1)}$ and $\text{Gd}_6\text{Ge}_{4.3(1)}\text{Sb}_{11.7(1)}$ proceeded similarly given the resemblance of their intensity patterns to that of $\text{La}_6\text{Ge}_{2.8(1)}\text{Sb}_{13.2(1)}$. In both cases, the chosen space group *Immm* was further supported by the intensity statistics and the successful structure solutions. Atomic assignments were made using the structure of $\text{La}_6\text{Ge}_{2.8(1)}\text{Sb}_{13.2(1)}$ as an initial model. For $\text{Nd}_6\text{Ge}_{3.6(1)}\text{Sb}_{12.4(1)}$, moving Sb(4) off the $\frac{1}{2}xy$ mirror plane to the position (\sim 0.44, $\frac{1}{2}$, 0) alleviated the problem of an elongated anisotropic displacement parameter ($U_{11} = 0.124(4)$) and resulted in the same solution as $\text{La}_6\text{Ge}_{2.8(1)}\text{Sb}_{13.2(1)}$. Analogous to the latter, occupancies of the $M(2)$ (0, \sim 0.04, 0) and Sb(4) sites were assumed to be at the maximum allowed limit of 50% given the close distances to their crystallographic equivalents ($M(2)$ – $M(2)$ 0.82 Å; Sb(4)–Sb(4) 0.53 Å). Applying the Ge/Sb disorder model resulted in occupancies of 72(3)% Ge(1) and 28(2)%

Sb(6) (*M*(1) site) and 36(2)% Ge(2) and 14(1)% Sb(7) (*M*(2) site). More importantly, however, these refinements also led to reasonable values for the anisotropic displacement parameters, a featureless difference electron density map ($\Delta\rho_{\max} = 2.22$, $\Delta\rho_{\min} = -2.62 \text{ e}^- \text{ \AA}^{-3}$), and substantial improvements in the agreement factors. For $\text{Gd}_6\text{Ge}_{4.3(1)}\text{Sb}_{11.7(1)}$, structure refinements proceeded accordingly with only a few exceptions. Sb(4) was not displaced from the $\frac{1}{2} x y$ mirror plane but successfully refined at the site $(\frac{1}{2}, \frac{1}{2}, 0)$. The thermal ellipsoid of this site is slightly elongated along *a*, suggesting that a similar but less pronounced “sliding distortion” of the central Sb(4) atom may also be occurring in $\text{Gd}_6\text{Ge}_{4.3(1)}\text{Sb}_{11.7(1)}$, randomly displacing the atom slightly above and below the mirror plane but not sufficiently to render a split site. The other possible split site $(0, \sim 0.02, 0)$, analogous to position “*M*(2)” in the other compounds, remained situated away from the *x* $0 z$ mirror plane and also resulted in extremely short contacts (0.48 Å). Allowing the site to be occupied (50%) by a mixture of Ge and Sb revealed that the site was exclusively occupied by Ge. On the other hand, disorder still exists for the *M*(1) site with atomic distributions of 83(3)% Ge(1) and 17(2)% Sb(6). The final difference electron density map is featureless ($\Delta\rho_{\max} = 3.74$, $\Delta\rho_{\min} = -4.93 \text{ e}^- \text{ \AA}^{-3}$). The occupancies of all other atoms in $\text{Nd}_6\text{Ge}_{3.6(1)}\text{Sb}_{12.4(1)}$, and $\text{Gd}_6\text{Ge}_{4.3(1)}\text{Sb}_{11.7(1)}$ were confirmed to be essentially 100% (95.7(6) – 101.2(9)%) through independent refinements of their occupancies. Final refinements resulted in the formulations $\text{Nd}_6\text{Ge}_{3.6(1)}\text{Sb}_{12.4(1)}$ (*Z* = 2) (Anal. Calcd. (mol%): Nd 27, Ge 16, Sb 56) and $\text{Gd}_6\text{Ge}_{4.3(1)}\text{Sb}_{11.7(1)}$ (*Z* = 2) (Anal. Calcd. (mol%): Gd 27, Ge 20, Sb 53), which are in exceptionally good agreement with EDX analyses (Table 6–1).

There was initial concern over the chosen space group *Immm* because the related structure $\text{La}_6\text{MnSb}_{15}$ was successfully solved in the lower symmetry space group *Imm2*

by removal of the mirror plane perpendicular to the c axis.²⁰ This had the effect of splitting the position $4j$ occupied by Sb(6) in that structure into two independent sites, $2a$ and $2b$, of which only one was occupied, thereby eliminating the occurrence of extremely short Sb(6)–Sb(6) distances arising from the operation of the $x\ y\ 0$ mirror plane in the higher symmetry space group $Immm$. Two such positions, $4f(x, \frac{1}{2}, 0)$ and $4g(0, y, 0)$, exist in $RE_6Ge_{5-x}Sb_{11+x}$ ($Immm$) which also give rise to short interatomic contacts. Attempted solution of the structure in $I2mm$ (removing $\frac{1}{2}\ x\ y$ mirror plane), $Im2m$ (removing $x\ 0\ z$ mirror plane), or $I222$ (removing all mirror planes) was unsuccessful as electron density was found in the two emerging split sites. The resulting Flack parameter²² did not suggest the presence of an absolute structure and further analysis of the final refined structure by ADDSYM²³ in the PLATON suite of programs,²⁴ which indicated the presence of mirror planes perpendicular to all twofold axes in the lower symmetry space groups, confirmed the positional disorder at these two sites. In the absence of a detectable superstructure, we opted for the higher symmetry space group $Immm$ for the title compounds.

The atomic positions of $La_6Ge_{2.8(1)}Sb_{13.2(1)}$, $Nd_6Ge_{3.6(1)}Sb_{12.4(1)}$, and $Gd_6Ge_{4.3(1)}Sb_{11.7(1)}$ were standardized with the program STRUCTURE TIDY.²⁵ The final cycle of least-squares refinement on F_o^2 included anisotropic displacement parameters for all atoms and an isotropic extinction parameter. Final values of the positional and displacement parameters are given in Table 6–4 and selected interatomic distances are listed in Table 6–5. Anisotropic displacement parameters are listed in Table A–18.

TRANSPORT MEASUREMENTS

Electrical resistivities of single crystals (needles typically 0.02–0.05 mm wide and 0.5–2.0 mm long) were measured with the current parallel to the needle axis (crystallographic a -axis) by standard four-probe technique on a Quantum Design PPMS system using an AC-transport controller (Model 7100). A current of 0.05 mA and a frequency of 16 Hz were used.

RESULTS AND DISCUSSION

TRENDS

Elemental analyses on selected crystals of $RE_6Ge_{5-x}Sb_{11+x}$ ($RE = La-Nd, Sm, Gd-Dy$) (Table 6–1) show a gradual trend (mol%), as substitution proceeds across the series from La to Dy, of increasing Ge content coupled with a corresponding decrease in Sb while the amount of the RE component remains relatively constant. Although the quality of the elemental analyses greatly depends on the accuracy of the calibration standards of the elements, chemical arguments and results of the crystal structures of the early, intermediate, and late members also support the inverse proportionality of the Ge and Sb content in this series of compounds. Consistent with the lanthanide contraction and an oxidation state assignment of +3 for all RE atoms, the cell parameters (Figure 6–1, Table 6–2) show a monotonic decrease in all unit cell axes as expected given the three-dimensional nature of the structure.

DESCRIPTION OF THE STRUCTURES

A view of the structure of $\text{La}_6\text{Ge}_{2.8(1)}\text{Sb}_{13.2(1)}$ down the a axis is given in Figure 6–2, which shows the labeling scheme. Positions $M(1)$ and $M(2)$ represent disordered sites containing 61(3)% Ge(1), 39(2)% Sb(6) and 19(2)% Ge(2), 31(1)% Sb(7), respectively. (The remaining 50% in $M(2)$ represent vacancies.) $\text{Nd}_6\text{Ge}_{3.6(1)}\text{Sb}_{12.4(1)}$ and $\text{Gd}_6\text{Ge}_{4.3(1)}\text{Sb}_{11.7(1)}$ are isostructural to $\text{La}_6\text{Ge}_{2.8(1)}\text{Sb}_{13.2(1)}$, differing only in the proportions of Ge and Sb at these two sites. As indicated previously, the Ge:Sb ratio increases as size of RE decreases, resulting in distributions of $M(1) = 72(3)\%$ Ge(1), 28(2)% Sb(6) and $M(2) = 36(2)\%$ Ge(2), 14(1)% Sb(7) for $\text{Nd}_6\text{Ge}_{3.6(1)}\text{Sb}_{12.4(1)}$; and $M(1) = 83(3)\%$ Ge(1), 17(2)% Sb(6) and $M(2) = 50\%$ Ge(2) for $\text{Gd}_6\text{Ge}_{4.3(1)}\text{Sb}_{11.7(1)}$. $RE_6\text{Ge}_{5-x}\text{Sb}_{11+x}$ adopts a new structure type, conveniently described as comprising Sb(1)-centered trigonal prisms, whose vertices are the $RE(1)$ and $RE(2)$ atoms, which share triangular faces to form columns running along [100]. These columns are separated from each other by an intricate network of interconnecting walls defined by Ge and Sb atoms.

Although the structure is three-dimensional in character, it will be instructive to employ a “retrotheoretical” approach²¹ to decompose it into lower dimensional subunits which can then be discussed more coherently. By reassembling the individual components in an *aufbau* fashion later, insight can be gained on the overall complex structure. We begin by removing the electropositive RE atoms, revealing the underlying three-dimensional metalloid framework (Figure 6–3a). For clarity, position $M(1)$ will be momentarily considered to be filled exclusively by Sb atoms. Next, the closely-spaced disordered position $M(2)$ is removed to generate a collection of three separated constituents (Figure 6–3b): linear arrays of essentially isolated Sb(1) atoms (0-D), three-

atom wide Sb ribbons (1-D), and kinked Sb square sheets (2-D). The latter may be imagined to be derived from an idealized flat Sb square net by a process of folding at every fifth atom (Sb(5)).²¹ The extracted components are represented schematically in Figure 6–3c.

A view of the one-dimensional three-atom wide Sb ribbons (Sb(3)–Sb(4)–Sb(3)) which extend along [100] is shown in Figure 6–4 for the $\text{Gd}_6\text{Ge}_{4.3(1)}\text{Sb}_{11.7(1)}$ and $\text{La}_6\text{Ge}_{2.8(1)}\text{Sb}_{13.2(1)}$ members. In $\text{Gd}_6\text{Ge}_{4.3(1)}\text{Sb}_{11.7(1)}$, the symmetrically organized strips consist of Sb(4) atoms that reside at the center ($\frac{1}{2}, \frac{1}{2}, 0$) of the squares outlined by Sb(3) atoms, yielding four equivalent Sb(3)–Sb(4) distances of 3.0780(8) Å (Figure 6–4a). These Sb–Sb distances have been postulated to correspond to one-electron half-bonds^{2,3,26–29} which are ubiquitous in Sb square sheets, such as those observed in LaSb_2 (3.087–3.157 Å),³⁰ $\text{LaIn}_{0.8}\text{Sb}_2$ (3.119(3)–3.142(3) Å)² or $\text{LaZn}_{0.52}\text{Sb}_2$ (3.097(2) Å).³¹ A useful interpretation of these ribbons is to consider them to be excised from infinite square nets.³² Using this analogy, one can envisage Sb ribbons or strips of varying atom widths (n) ranging from linear skewers ($n = 1$) and zigzag chains ($n = 2$) to increasingly wider ribbons ($n = 6$ or greater); we have now identified many structures containing these ribbons.^{1,26,32–34} In $\text{La}_6\text{Ge}_{2.8(1)}\text{Sb}_{13.2(1)}$, the central Sb(4) atoms in the ribbons are located asymmetrically off-center ($-0.40, \frac{1}{2}, 0$), creating two closely-spaced symmetry-equivalent sites about a mirror plane, only one of which can be occupied locally. One way to view such a picture is in terms of an energetically favorable second-order Peierls-type sliding distortion of the symmetrical ribbon as observed in the related alloy $\text{La}_{12}\text{Mn}_2\text{Sb}_{30}$.²⁰ A distortion along a , such as that shown in Figure 6–4b, necessarily results in alternating short (2.918(1) Å) and long (3.333(1) Å) Sb(3)–Sb(4) distances. For

comparison, intralayer Sb–Sb single bond lengths of 2.908 Å and weaker interlayer interactions of 3.355 Å are observed in elemental Sb.³⁵ A similar situation exists for the three-atom wide ribbons in Nd₆Ge_{3.6(1)}Sb_{12.4(1)}, where the short and long Sb(3)–Sb(4) distances are 2.9175(9) and 3.279(1) Å, respectively. One can rationalize that the distortion should occur more prominently in structures containing the largest RE components, viz., La₆Ge_{2.8(1)}Sb_{13.2(1)}, because the cell expansion would force a symmetrical ribbon to have four longer and therefore weaker Sb–Sb bonds. The asymmetric distortion optimizes stability by allowing two full Sb–Sb single bonds to form at the expense of the two weakened Sb–Sb interactions within a Sb(4)–Sb(3)–Sb(4)–Sb(3) square. This is consistent with the similarity in the short Sb(3)–Sb(4) distances in the La and Nd compounds, despite the significant reduction in cell volume due to lanthanide contraction. The reduced cell volume of the Gd compound favours a more symmetrical ribbon by formation of four half-bonds as opposed to the proposed alternative configuration.

The decomposed view (Figure 6–3b) of the structure also reveals kinked sheets parallel to *b*, derived from folding an idealized square net at every fifth atom. The resulting folded sheets consist of six-atom wide sections (Sb(5)–Sb(6)–Sb(2)–Sb(2)–Sb(6)–Sb(5)) which are approximately parallel to (011) and (0 $\bar{1}$ 1). A consequence of the acute angles (~48°), subtended by Sb(6)–Sb(5)–Sb(6), which form at the corners of the bends is short distances (2.547(2)–2.615(2) Å) between Sb(6) atoms from adjacent sections, unreasonably short to be Sb–Sb bonds but ideal for Ge–Sb or Ge–Ge bonds. These distances may be compared to Ge–Ge single bond distances in the clathrate Cs₈Na₁₆Ge₁₃₆ (2.4859(7)–2.5033(9) Å)³⁶ or elemental Ge (2.4497(1) Å).³⁵ Somewhat

more rare are clear examples of Ge–Sb bond distances in the literature. If we accept values of 2.62 Å, the bond valence parameter for a Ge–Sb single bond,³⁷ or 2.66(2)–2.68(2) Å, observed in the disordered clathrate $\text{Ge}_{14}(\text{GaSb})_{12}\text{Sb}_8\text{I}_8$,³⁸ as reasonable Ge–Sb single bond distances, then a possible explanation for the inherent disorder actually observed at this site is that Sb–Sb repulsions are eliminated in favour of reasonable Ge–Sb and Ge–Ge bonding interactions through incorporation of Ge into this site. In $\text{La}_6\text{Ge}_{2.8(1)}\text{Sb}_{13.2(1)}$, the $M(1)$ – $M(1)$ distance of 2.615(2) Å represents an ideal Ge–Sb single bond distance. The observed Ge(1):Sb(6) ratio of 61(3)%:39(2)% is consistent with a hypothesized local environment of mostly Ge–Sb single bonds, with weaker Ge–Ge contacts substituted occasionally. Substituting La with smaller *RE* atoms results in reduced $M(1)$ – $M(1)$ distances of 2.588(1) Å (*RE* = Nd) and 2.547(2) Å (*RE* = Gd). These values become increasingly too short for Ge–Sb bonds but converge to ideal Ge–Ge single bond distances. Thus, consistent with the predicted trend of increasing number of Ge–Ge bonds as the $M(1)$ – $M(1)$ distance decreases are the observed larger amounts of Ge(1) relative to Sb(6) for $\text{Nd}_6\text{Ge}_{3.6(1)}\text{Sb}_{12.4(1)}$ (72(3)%) and $\text{Gd}_6\text{Ge}_{4.3(1)}\text{Sb}_{11.7(1)}$ (83(3)%). The implication of some unusually short Ge–Sb contacts (2.547(2)–2.588(1) Å), randomly distributed throughout the extended network, is intriguing.

A view perpendicular to one of the six-atom wide sections making up the kinked sheets is shown in Figure 6–5. A pattern of long-short-long-short-long for the interatomic distances is apparent in the square nets. For the Gd compound, in which the $M(1)$ site contains mostly Ge, the section is best viewed (Figure 6–5a) as four-atom wide ribbons, where the Ge–Sb and Sb–Sb bonds within are fractional in bond order. In the structure of the La compound, in which the $M(1)$ site consists of almost equal proportions

of Ge and Sb, the square net (Figure 6–5b) is best interpreted as weakly associating zigzag chains.

The overall structure of $RE_6Ge_{5-x}Sb_{11+x}$ can now be appreciated by recondensing these artificially separated subunits to form the real structure. Stacking the kinked sheets along [001] with the Sb(5) corners approaching each other sees the emergence of large channels defined by the six-atom wide ribbons discussed earlier. By reintroducing into each channel two columns of Sb(1)-centered trigonal prisms of RE atoms and a three-atom wide Sb ribbon, a “hole” centering on position (0, 0, 0) is generated at the junction. The actual three-dimensional structure can now be obtained by filling sites (0, -0, 0) ($M(2)$) residing slightly off-center with Ge(2) and Sb(7) atoms which link together the kinked sheets and ribbons to form an overall extended network.

Since $M(2)$ is less than 1 Å away from a symmetry-equivalent position across a mirror plane in the three crystal structures, the maximum occupancy is 50%, or put another way, only one of these can be occupied locally. The Ge(2) content at this disordered site increases dramatically from the La (19(2)%) to the Nd (36(2)%) compound. In $Gd_6Ge_{4.3(1)}Sb_{11.7(1)}$, this site is no longer disordered, being occupied (at 50%) instead exclusively by Ge(2). The increase in Ge content at $M(2)$ may be explained by examining the distances to neighbouring atoms. The coordination geometry of the $M(2)$ position is a square pyramid, as outlined by four Sb(5) atoms defining the square base and one Sb(3) atom forming the apex. In $La_6Ge_{2.8(1)}Sb_{13.2(1)}$, the distances from $M(2)$ to Sb(5) (2.9320(8) Å) and Sb(3) (2.743(3) Å) represent ideal separations for Sb–Sb bonds. Despite the fact that the latter distance ($M(2)$ –Sb(3)) also falls within favourable Ge–Sb bonding interactions, the stronger Sb–Sb orbital overlaps may be the reason for

the relatively higher proportion of Sb(7) compared to Ge(2) observed for this site. In $\text{Gd}_6\text{Ge}_{4.3(1)}\text{Sb}_{11.7(1)}$, both distances are notably reduced, yielding Ge(2)–Sb(5) and Ge(2)–Sb(3) separations of 2.781(1) and 2.709(5), respectively. Although unusually short Sb–Sb single bond distances have been reported for the compounds $[\text{C}_{18}\text{H}_{36}\text{N}_2\text{O}_6\cdot\text{Na}]_3[\text{Sb}_7]$ (2.693(4) Å),³⁹ NdPdSb (2.709(1) Å),⁴⁰ NbSb_2 (2.711 Å),^{41,42} $[\text{K}(2,2,2\text{-crypt})]_3[\text{Sb}_7]$ (2.717(2) Å),⁴³ and $[\text{Na}(2,2,2\text{-crypt})]_3[\text{Sb}_{11}]$ (2.716(4) Å)⁴⁴ with values around 2.75 Å more common in other examples,^{45–47} the relatively high coordination number surrounding this site in the Gd compound would be sterically unfavourable for any Sb occupancy. Interestingly, the middle member $\text{Nd}_6\text{Ge}_{3.6(1)}\text{Sb}_{12.4(1)}$ exhibits values of 2.8434(6) and 2.653(2) Å for distances to the basal and apical atoms, respectively. Despite the short $M(2)$ –Sb(3) separation, Sb is still present at this site at 14(1)% occupancy. Comparison may be made to the organometallic complexes $[\text{Sb}\{\text{C}_6\text{H}_2[\text{CH}(\text{SiMe}_3)_2]_{3-2,4,6}\}]_2$,⁴⁸ $[\text{Sb}(\text{C}_6\text{H}_3\text{Mes}_{2-2,6})_2]$ (Mes = $\text{C}_6\text{H}_2\text{-}2,4,6\text{-Me}_3$),⁴⁹ and $[\text{Sb}(\text{C}_6\text{H}_3\text{Trip}_{2-2,6})_2]$ (Trip = $\text{C}_6\text{H}_2\text{-}2,4,6\text{-}^i\text{Pr}_3$)⁴⁹ where multiple bond character^{50,51} has been invoked to explain the short Sb–Sb separations (2.642(1) – 2.668(2) Å). Caution should be exercised here, however, because the observed $M(2)$ –Sb(3) distance of 2.653(2) Å may be artificially shortened by the disorder modeling in structure refinements. It should be expected that the equilibrium positions of Ge(2) and Sb(7) will be independently achieved locally in the structure. The nonspherical directional parameters for this site in all three compounds are supportive of this fact.

As shown in Figure 6–6, the coordination environments around $RE(1)$ (CN 8) and $RE(2)$ (CN 9) are representative of a bicapped trigonal prism and a monocapped square antiprism, respectively. In the first type of arrangement, two Sb(1) and four Sb(2) atoms

define the trigonal prism. Additional Sb(2) atoms then cap two of the rectangular faces to form the bicapped trigonal prism. If the two nearby $M(1)$ atoms, at much longer distances away, are considered then the geometry may be described as a bicapped square antiprism where one $M(1)$ atom caps a trigonal face while an Sb(2) atom caps a square face. The second environment, adopted by $RE(2)$, is more reminiscent of the type of coordination geometry observed for the rare-earth atoms in other solid state compounds of the main-group elements,^{2,3} where two-dimensional square nets are common. The monocapped square antiprism adopted by $RE(2)$ is outlined by a basal square consisting of the combination Sb(5)– $M(1)$ –Sb(2)– $M(1)$, another square, twisted 45° relative to the first, defined by two each of Sb(1) and Sb(3) atoms, and a capping Sb(4) atom. The RE –Sb and RE –Ge distances (Table 6–5) in the three structures are comparable to those found in binary rare-earth antimonide and germanide compounds.

STRUCTURAL RELATIONSHIPS

There exists a large family of structures based on the stacking of trigonal prisms whose vertices are metal atoms. If attention is drawn to the columns of face-sharing trigonal prisms of RE atoms in $RE_6Ge_{5-x}Sb_{11+x}$, then a structural connection can be made to the compound La_6MnSb_{15} ,²⁰ as shown in Figure 6–7. For purposes of comparison, the two structures are best viewed in terms of the six-sided large channels which are clearly outlined in La_6MnSb_{15} by two- and six-atom wide segments of Sb atoms, together making up the 22-membered circumference. If each channel shares its six sides with adjacent channels to create a perfect fit, then the structure of La_6MnSb_{15} is obtained. In $RE_6Ge_{5-x}Sb_{11+x}$, each channel shares only four atoms from the six-atom sections with

adjacent channels, resulting in a non-ideal packing of the channels. The corners where the six-atom sections meet necessarily must cross with those from neighbouring channels using this mode of packing, creating the short $M(2)$ – $M(2)$ distances.

TRANSPORT PROPERTIES

All $RE_6Ge_{5-x}Sb_{11+x}$ members are metallic, as indicated by their resistivity curves (Figure 6–8 and Figure 6–9), with the members containing RE other than La displaying kinks in their resistivity vs. temperature curves. For $RE = Ce$ – Nd , Sm , Gd , the change in slope of the resistivity at low temperatures (insets of Figures 6–8(a) and (b)) is attributed to the loss in spin-disorder scattering upon establishment of long-range magnetic ordering. These members all exhibit residual resistivity ratios ($\rho_{300\text{ K}}/\rho_{2\text{ K}}$) close to 2.0 (Table 6–6).

For $RE = Tb$ and Dy , the resistivity does not decrease continuously with decreasing temperature, but rather shows strikingly different behaviour from the other members, attaining pronounced minima in their curves at 10 and 150 K, respectively (Figures 6–9(a) and (b)). Not only does the resistivity minimum for the Dy member occur at much higher temperatures than for the Tb member, but the resistivity is also greater at low temperatures than at room temperature ($\rho_{2\text{ K}} > \rho_{300\text{ K}}$) and it becomes temperature independent below 10 K, reaching a constant value of $\sim 200\ \mu\Omega\text{ cm}$. These two resistivity minima are reminiscent of Kondo-like behaviour, in which interactions between the localized f electrons and the conduction electrons lead to a compensation of the RE moments.⁵² Such resistivity minima have also been observed in compounds that additionally display colossal magnetoresistance.^{53,54} The absence of a further decrease in

resistivity at very low temperatures suggests that long-range magnetic ordering does not occur in this temperature range. The magnetic measurements of the entire series are reported elsewhere.¹¹

In conclusion, a new series of rare-earth germanium antimonides was synthesized and structurally characterized. The novel structure illustrates the importance of contributions of strong as well as weak homoatomic bonding between the main-group elements towards the overall stability of extended structures. Interesting properties may be expected to arise from the triangular arrangements of the *RE* atoms forming columns of trigonal prisms.

Table 6–1. Elemental (EDX) Analyses for Compounds $RE_6Ge_{5-x}Sb_{11+x}$ ($RE = La-Nd$,
Sm, Gd–Dy)

compound	RE (mol%)	Ge (mol%)	Sb (mol%)	no. of samples
$La_6Ge_{2.8(1)}Sb_{13.2(1)}$ ^a	28.7(1)	11.7(2)	59.5(3)	2
(Calcd. ^a	27	13	60)
$Ce_6Ge_{5-x}Sb_{11+x}$	29.2(6)	16(1)	54.6(6)	5
$Pr_6Ge_{5-x}Sb_{11+x}$	30.6(6)	16.6(8)	52.8(4)	5
$Nd_6Ge_{3.6(1)}Sb_{12.4(1)}$ ^a	27.6(6)	16(1)	55.9(4)	3
(Calcd. ^a	27	16	56)
$Sm_6Ge_{5-x}Sb_{11+x}$	29.1(1)	17.3(6)	53.6(5)	2
$Gd_6Ge_{4.3(1)}Sb_{11.7(1)}$ ^a	27.7(6)	19.7(1)	52.6(5)	2
(Calcd. ^a	27	20	53)
$Tb_6Ge_{5-x}Sb_{11+x}$	32.2(2)	20.8(8)	47.0(6)	4
$Dy_6Ge_{5-x}Sb_{11+x}$	29.3(4)	16.8(6)	53.9(5)	6

^a These formulas represent compositions deduced from refinements of the crystal structures.

Table 6–2. Cell Parameters for Compounds $RE_6Ge_{5-x}Sb_{11+x}$ ($RE = La-Nd, Sm, Gd-Dy$)

compound	a (Å)	b (Å)	c (Å)	V (Å ³)
$La_6Ge_{2.8(1)}Sb_{13.2(1)}$	4.3289(7)	10.857(1)	27.076(3)	1272.6(2)
$Ce_6Ge_{5-x}Sb_{11+x}$	4.2972(7)	10.740(1)	26.791(4)	1236.4(2)
$Pr_6Ge_{5-x}Sb_{11+x}$	4.2674(9)	10.677(2)	26.626(5)	1213.1(3)
$Nd_6Ge_{3.6(1)}Sb_{12.4(1)}$	4.2412(8)	10.637(2)	26.552(4)	1197.8(3)
$Sm_6Ge_{5-x}Sb_{11+x}$	4.1942(7)	10.537(1)	26.350(3)	1164.5(2)
$Gd_6Ge_{4.3(1)}Sb_{11.7(1)}$	4.1511(6)	10.440(1)	26.228(3)	1136.7(2)
$Tb_6Ge_{5-x}Sb_{11+x}$	4.1305(8)	10.393(2)	26.139(4)	1122.1(2)
$Dy_6Ge_{5-x}Sb_{11+x}$	4.1032(10)	10.345(2)	26.014(5)	1104.2(3)

Table 6–3. Crystallographic Data for $\text{La}_6\text{Ge}_{2.8(1)}\text{Sb}_{13.2(1)}$, $\text{Nd}_6\text{Ge}_{3.6(1)}\text{Sb}_{12.4(1)}$, and $\text{Gd}_6\text{Ge}_{4.3(1)}\text{Sb}_{11.7(1)}$

Formula	$\text{La}_6\text{Ge}_{2.8(1)}\text{Sb}_{13.2(1)}$	$\text{Nd}_6\text{Ge}_{3.6(1)}\text{Sb}_{12.4(1)}$	$\text{Gd}_6\text{Ge}_{4.3(1)}\text{Sb}_{11.7(1)}$
Formula mass, amu	2643.81	2636.46	2678.27
Space group	$D_{2h}^{25} - Immm$ (No. 71)	$D_{2h}^{25} - Immm$ (No. 71)	$D_{2h}^{25} - Immm$ (No. 71)
a , Å	4.3034(8) ^a	4.2310(3) ^a	4.1509(3) ^a
b , Å	10.851(3) ^a	10.6362(7) ^a	10.4438(7) ^a
c , Å	27.073(7) ^a	26.526(2) ^a	26.2400(18) ^a
V , Å ³	1264.2(5)	1193.73(15)	1137.53(14)
Z	2	2	2
T , °C	22	22	22
Diffractometer	Enraf-Nonius CAD4		
ρ_{calc} , g cm ⁻³	6.945	7.335	7.819
Crystal dimensions, mm	Silver needle, 0.43 × 0.03 × 0.02	Silver needle, 0.25 × 0.04 × 0.02	Silver needle, 0.20 × 0.02 × 0.02
Radiation	Graphite monochromated $\text{MoK}\alpha$, $\lambda = 0.71073$ Å		
$\mu(\text{MoK}\alpha)$, cm ⁻¹	269.6	309.7	363.9

Table 6–3. Crystallographic Data for $\text{La}_6\text{Ge}_{2.8(1)}\text{Sb}_{13.2(1)}$, $\text{Nd}_6\text{Ge}_{3.6(1)}\text{Sb}_{12.4(1)}$, and $\text{Gd}_6\text{Ge}_{4.3(1)}\text{Sb}_{11.7(1)}$ (continued)

Transmission factors ^b	0.049–0.110	0.049–0.094	0.062–0.113
Scan type	0–20	0–20	0–20
Scan speed, deg. min ⁻¹	1.7	1.7	1.7
Scan range, deg.	$0.8 + 0.344 \tan\theta$	$0.6 + 0.344 \tan\theta$	$0.6 + 0.344 \tan\theta$
2 θ limits	$3^\circ \leq 2\theta(\text{MoK}\alpha) \leq 70^\circ$	$3^\circ \leq 2\theta(\text{MoK}\alpha) \leq 70^\circ$	$3^\circ \leq 2\theta(\text{MoK}\alpha) \leq 70^\circ$
Data collected	$-6 \leq h \leq 6, -17 \leq k \leq 17,$ $-43 \leq l \leq 43$	$-6 \leq h \leq 6, -17 \leq k \leq 17,$ $-42 \leq l \leq 42$	$-6 \leq h \leq 6, -16 \leq k \leq 16,$ $-42 \leq l \leq 42$
No. of data collected	17185	10453	9969
No. of unique data, including $F_o^2 < 0$	1625 ($R_{\text{int}} = 0.108$)	1538 ($R_{\text{int}} = 0.072$)	1472 ($R_{\text{int}} = 0.102$)
No. of unique data, with $F_o^2 > 2\sigma(F_o^2)$	1415	1292	1203
No. of variables	48	48	45
Extinction coefficient ^c	0.00156(10)	0.00136(6)	0.00236(11)
$R(F)$ for $F_o^2 > 2\sigma(F_o^2)$ ^d	0.041	0.031	0.042
$R_w(F_o^2)$ ^e	0.098	0.068	0.101
Goodness of fit ^f	1.17	1.10	1.11

Table 6–3. Crystallographic Data for La₆Ge_{2.8(1)}Sb_{13.2(1)}, Nd₆Ge_{3.6(1)}Sb_{12.4(1)}, and Gd₆Ge_{4.3(1)}Sb_{11.7(1)} (continued)

$(\Delta\rho)_{\max}, (\Delta\rho)_{\min}, \text{e}^{-\text{\AA}^{-3}}$	4.8, – 5.4	2.2, – 2.6	3.7, – 4.9
---	------------	------------	------------

^a Obtained from a refinement constrained so that $\alpha = \beta = \gamma = 90^\circ$.

^b A semi-empirical psi-scan absorption correction was applied in all cases, with the use of programs in the SHELXTL package (Sheldrick, G. M. SHELXTL Version 5.1, Bruker Analytical X-Ray Instruments, Inc., Madison, WI, 1997).

^c An extinction parameter x was refined, where F_c is multiplied by: $k[1 + 0.001 * x * F_c^2 * \lambda^3 / \sin(2\theta)]^{-1/4}$.

$$^d R(F) = \sum \left| |F_o| - |F_c| \right| / \sum |F_o|.$$

^e $R_w(F_o^2) = [\sum [w(F_o^2 - F_c^2)^2] / \sum wF_o^4]^{1/2}$; $w^{-1} = [\sigma^2(F_o^2) + (AP)^2 + BP]$ where $P = [\max(F_o^2, 0) + 2F_c^2] / 3$, $A = 0.0513, 0.0298$, and 0.0471 , and $B = 3.3625, 1.2302$, and 0 for La₆Ge_{2.8(1)}Sb_{13.2(1)}, Nd₆Ge_{3.6(1)}Sb_{12.4(1)}, and Gd₆Ge_{4.3(1)}Sb_{11.7(1)}, respectively.

^f $Goof = S = [\sum [w(F_o^2 - F_c^2)^2] / (n - p)]^{1/2}$ where n is the number of reflections and p is the total number of parameters refined.

Table 6-4. Atomic Coordinates, Occupancies, and Equivalent Isotropic Displacement Parameters (\AA^2) for $RE_6\text{Ge}_{5-x}\text{Sb}_{11+x}$ ($RE = \text{La, Nd, Gd}$)

Atom	Wyckoff position, site symmetry	x	y	z	Occupancy	U_{eq}^a
$\text{La}_6\text{Ge}_{2.8(1)}\text{Sb}_{13.2(1)}$						
La(1)	4i $m m 2$	0	0	0.26676(2)	1	0.01330(12)
La(2)	8l $m . .$	0	0.19435(3)	0.405447(15)	1	0.01409(11)
Sb(1)	4j $m m 2$	$\frac{1}{2}$	0	0.35768(2)	1	0.01454(14)
Sb(2)	8l $m . .$	0	0.30555(4)	0.28863(2)	1	0.01691(12)
Sb(3)	4g $m 2 m$	0	0.29207(7)	0	1	0.01696(14)
Sb(4)	4f $2 m m$	0.4300(3)	$\frac{1}{2}$	0	0.5	0.0162(3)
Sb(5)	4j $m m 2$	$\frac{1}{2}$	0	0.07187(3)	1	0.0248(2)
$M(1)^b$	8l $m . .$	0	0.12051(7)	0.14765(2)	1	0.0194(2)
$M(2)^c$	4g $m 2 m$	0	0.0393(2)	0	0.5	0.0216(5)
$\text{Nd}_6\text{Ge}_{3.6(1)}\text{Sb}_{12.4(1)}$						
Nd(1)	4i $m m 2$	0	0	0.26593(2)	1	0.01241(10)
Nd(2)	8l $m . .$	0	0.19331(3)	0.405129(14)	1	0.01321(9)
Sb(1)	4j $m m 2$	$\frac{1}{2}$	0	0.35698(2)	1	0.01363(12)
Sb(2)	8l $m . .$	0	0.30521(4)	0.28910(2)	1	0.01542(10)
Sb(3)	4g $m 2 m$	0	0.28797(7)	0	1	0.01682(13)
Sb(4)	4f $2 m m$	0.4375(3)	$\frac{1}{2}$	0	0.5	0.0154(3)
Sb(5)	4j $m m 2$	$\frac{1}{2}$	0	0.06994(3)	1	0.02311(15)
$M(1)^b$	8l $m . .$	0	0.12165(6)	0.14609(3)	1	0.0169(2)
$M(2)^c$	4g $m 2 m$	0	0.0385(2)	0	0.5	0.0219(6)

Table 6-4. Atomic Coordinates, Occupancies, and Equivalent Isotropic Displacement Parameters (\AA^2) for $RE_6\text{Ge}_{5-x}\text{Sb}_{11+x}$ ($RE = \text{La, Nd, Gd}$) (continued)

$\text{Gd}_6\text{Ge}_{4.3(1)}\text{Sb}_{11.7(1)}$							
Gd(1)	4i	<i>m m 2</i>	0	0	0.26538(3)	1	0.01210(15)
Gd(2)	8l	<i>m . .</i>	0	0.19247(5)	0.40424(2)	1	0.01323(13)
Sb(1)	4j	<i>m m 2</i>	½	0	0.35643(4)	1	0.01287(19)
Sb(2)	8l	<i>m . .</i>	0	0.30521(7)	0.28967(3)	1	0.01412(15)
Sb(3)	4g	<i>m 2 m</i>	0	0.28235(11)	0	1	0.0154(2)
Sb(4)	2c	<i>m m m</i>	½	½	0	1	0.0232(3)
Sb(5)	4j	<i>m m 2</i>	½	0	0.06994(5)	1	0.0231(2)
<i>M</i> (1) ^b	8l	<i>m . .</i>	0	0.12196(11)	0.14510(4)	1	0.0159(4)
Ge(2)	4g	<i>m 2 m</i>	0	0.0230(5)	0	0.5	0.0247(14)

^a U_{eq} is defined as one-third of the trace of the orthogonalized U_{ij} tensor.

^b Site *M*(1) contains 61(3)% Ge(1), 39(2)% Sb(6) in $\text{La}_6\text{Ge}_{2.8(1)}\text{Sb}_{13.2(1)}$; 72(3)% Ge(1), 28(2)% Sb(6) in $\text{Nd}_6\text{Ge}_{3.6(1)}\text{Sb}_{12.4(1)}$; and 83(3)% Ge(1), 17(2)% Sb(6) in $\text{Gd}_6\text{Ge}_{4.3(1)}\text{Sb}_{11.7(1)}$.

^c Site *M*(2) contains 19(2)% Ge(2), 31(1)% Sb(7) in $\text{La}_6\text{Ge}_{2.8(1)}\text{Sb}_{13.2(1)}$ and 36(2)% Ge(2), 14(1)% Sb(7) in $\text{Nd}_6\text{Ge}_{3.6(1)}\text{Sb}_{12.4(1)}$; and 50% Ge(2) in $\text{Gd}_6\text{Ge}_{4.3(1)}\text{Sb}_{11.7(1)}$. The remaining 50% represent vacancies.

Table 6–5. Selected Interatomic Distances (Å) in $RE_6Ge_{5-x}Sb_{11+x}$ ($RE = La, Nd, Gd$)

	$La_6Ge_{2.8(1)}Sb_{13.2(1)}$	$Nd_6Ge_{3.6(1)}Sb_{12.4(1)}$	$Gd_6Ge_{4.3(1)}Sb_{11.7(1)}$
$RE(1)-RE(2)$ (×2)	4.3064(9)	4.2263(6)	4.1614(8)
$RE(2)-RE(2)$	4.2178(9)	4.1122(6)	4.0202(8)
$RE(1)-Sb(1)$ (×2)	3.2694(8)	3.2107(6)	3.1647(9)
$RE(1)-Sb(2)$ (×2)	3.3680(10)	3.3039(5)	3.2507(7)
$RE(1)-Sb(2)$ (×4)	3.3661(6)	3.3012(4)	3.2455(6)
$RE(1)-M(1)^a$ (×2)	3.4797(11)	3.4321(9)	3.4035(13)
$RE(2)-Sb(1)$ (×2)	3.2787(6)	3.2147(4)	3.1498(6)
$RE(2)-Sb(2)$	3.3850(10)	3.3000(6)	3.2285(9)
$RE(2)-Sb(3)$ (×2)	3.3473(6)	3.2936(3)	3.2697(4)
$RE(2)-Sb(4)$	3.3303(7)	3.2605(4)	3.2179(5)
$RE(2)-Sb(5)$	3.3730(9)	3.3283(4)	3.2826(6)
$RE(2)-M(1)^a$ (×2)	3.2759(7)	3.1929(6)	3.1209(9)
$Sb(2)-Sb(2)$ (×2)	3.2339(9)	3.1870(7)	3.1579(11)
$Sb(2)-M(1)^a$ (×2)	2.8722(7)	2.8348(6)	2.7956(9)
$Sb(3)-Sb(4)$	2.9179(11)	2.9175(9)	} 3.0780(8)
$Sb(3)-Sb(4)$	3.3328(11)	3.2788(10)	
$Sb(3)-M(2)^b$	2.743(2)	2.653(2)	—
$Sb(3)-Ge(2)^b$	—	—	2.709(5)
$Sb(5)-M(1)^a$ (×4)	3.2480(9)	3.1985(7)	3.1337(12)
$Sb(5)-M(2)^b$ (×2)	2.9320(8)	2.8434(6)	—
$Sb(5)-Ge(2)^b$ (×2)	—	—	2.7808(10)
$M(1)-M(1)^a$	2.6154(16)	2.5879(14)	2.547(2)

Table 6–5. Selected Interatomic Distances (Å) in $RE_6Ge_{5-x}Sb_{11+x}$ ($RE = La, Nd, Gd$)

(continued)

- ^a Site $M(1)$ contains 61(3)% Ge(1), 39(2)% Sb(6) in $La_6Ge_{2.8(1)}Sb_{13.2(1)}$; 72(3)% Ge(1), 28(2)% Sb(6) in $Nd_6Ge_{3.6(1)}Sb_{12.4(1)}$; and 83(3)% Ge(1), 17(2)% Sb(6) in $Gd_6Ge_{4.3(1)}Sb_{11.7(1)}$.
- ^b Site $M(2)$ contains 19(2)% Ge(2), 31(1)% Sb(7) in $La_6Ge_{2.8(1)}Sb_{13.2(1)}$; 36(2)% Ge(2), 14(1)% Sb(7) in $Nd_6Ge_{3.6(1)}Sb_{12.4(1)}$; and 50% Ge(2) in $Gd_6Ge_{4.3(1)}Sb_{11.7(1)}$. *The remaining 50% represent vacancies.*

Table 6–6. Summary of Residual Resistivity Ratios ($\rho_{300\text{ K}}/\rho_{2\text{ K}}$) for $RE_6Ge_{5-x}Sb_{11+x}$

compound	$\rho_{300\text{ K}}/\rho_{2\text{ K}}$
$La_6Ge_{5-x}Sb_{11+x}$	2.18
$Ce_6Ge_{5-x}Sb_{11+x}$	2.23
$Pr_6Ge_{5-x}Sb_{11+x}$	2.03
$Nd_6Ge_{5-x}Sb_{11+x}$	1.70
$Sm_6Ge_{5-x}Sb_{11+x}$	2.05
$Gd_6Ge_{5-x}Sb_{11+x}$	1.77
$Tb_6Ge_{5-x}Sb_{11+x}$	1.46
$Dy_6Ge_{5-x}Sb_{11+x}$	0.92

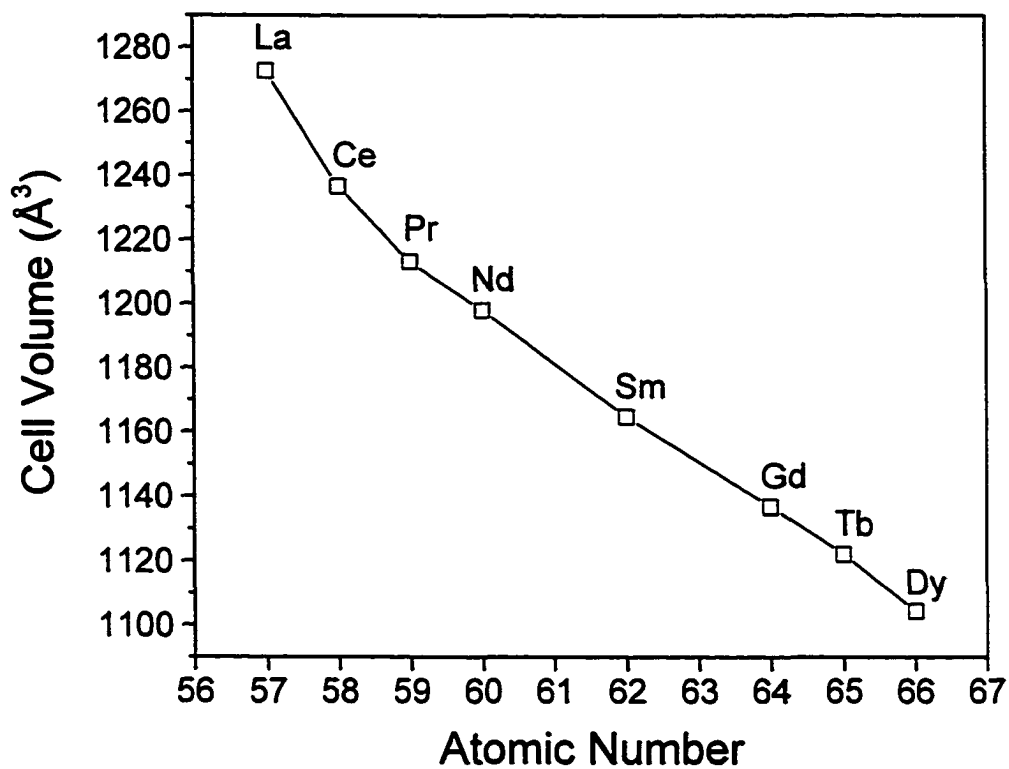


Figure 6-1. Plot of unit cell volume for $RE_6Ge_{5-x}Sb_{11+x}$ compounds. The lines are drawn only for guidance.

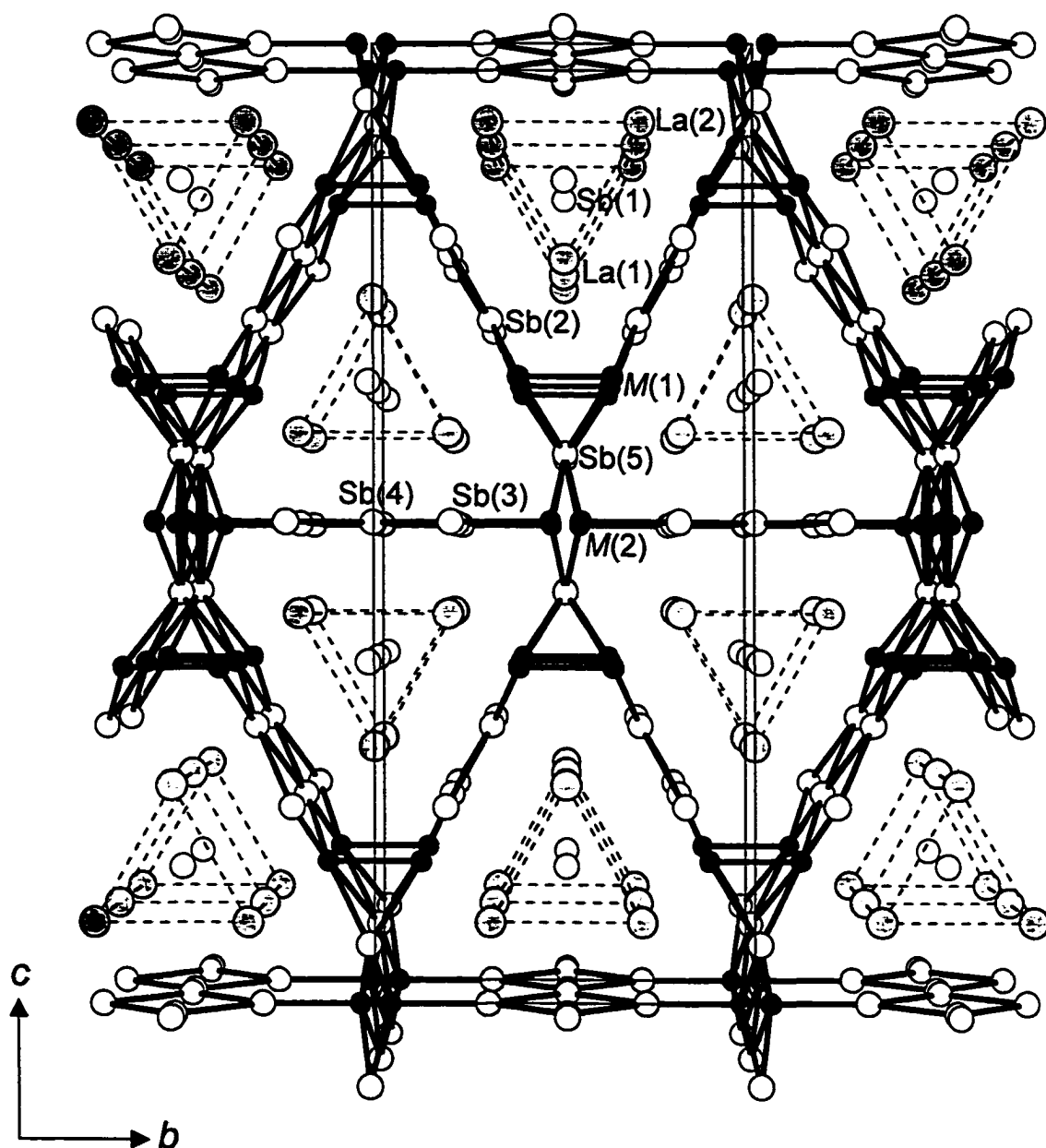
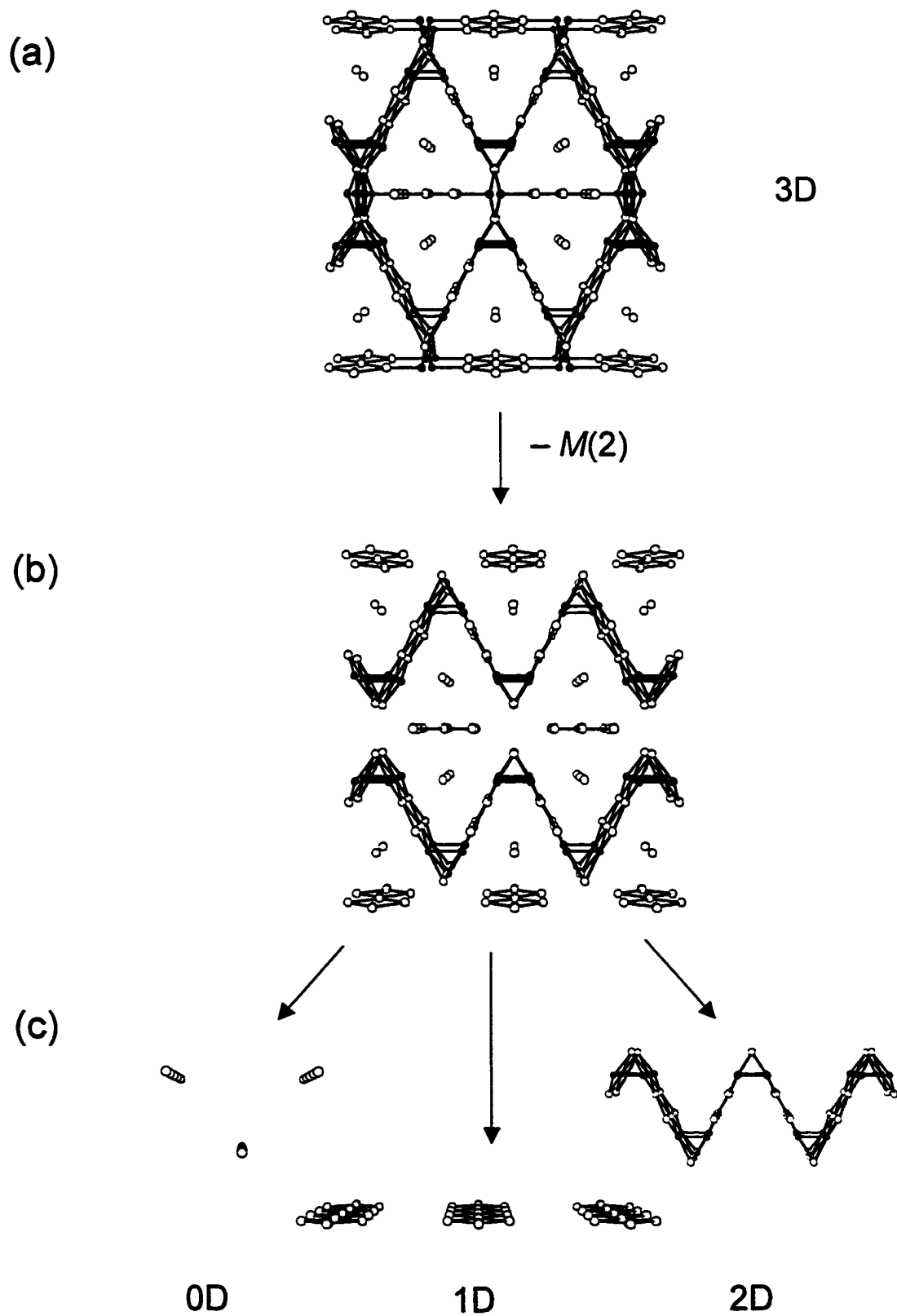


Figure 6-2. View of $\text{La}_6\text{Ge}_{2.8(1)}\text{Sb}_{13.2(1)}$ down the a axis showing the unit cell outline and the labeling scheme. The large lightly shaded circles are La atoms, the small solid circles are disordered sites ($M(1)$ and $M(2)$) containing Ge and Sb, and the medium open circles are Sb atoms. The dashed lines merely outline the assemblies of La_6 trigonal prisms.

Figure 6–3. A schematic diagram illustrating the process of “retrotheoretical analysis” of the $RE_6Ge_{5-x}Sb_{11+x}$ structure, an artificial decomposition of (a) the complex three-dimensional anionic network, by means of (b) removing the $M(2)$ atoms, into (c) discrete subunits of lower dimensionality (isolated Sb atoms, three-atom wide Sb ribbons, and kinked Sb square sheets).



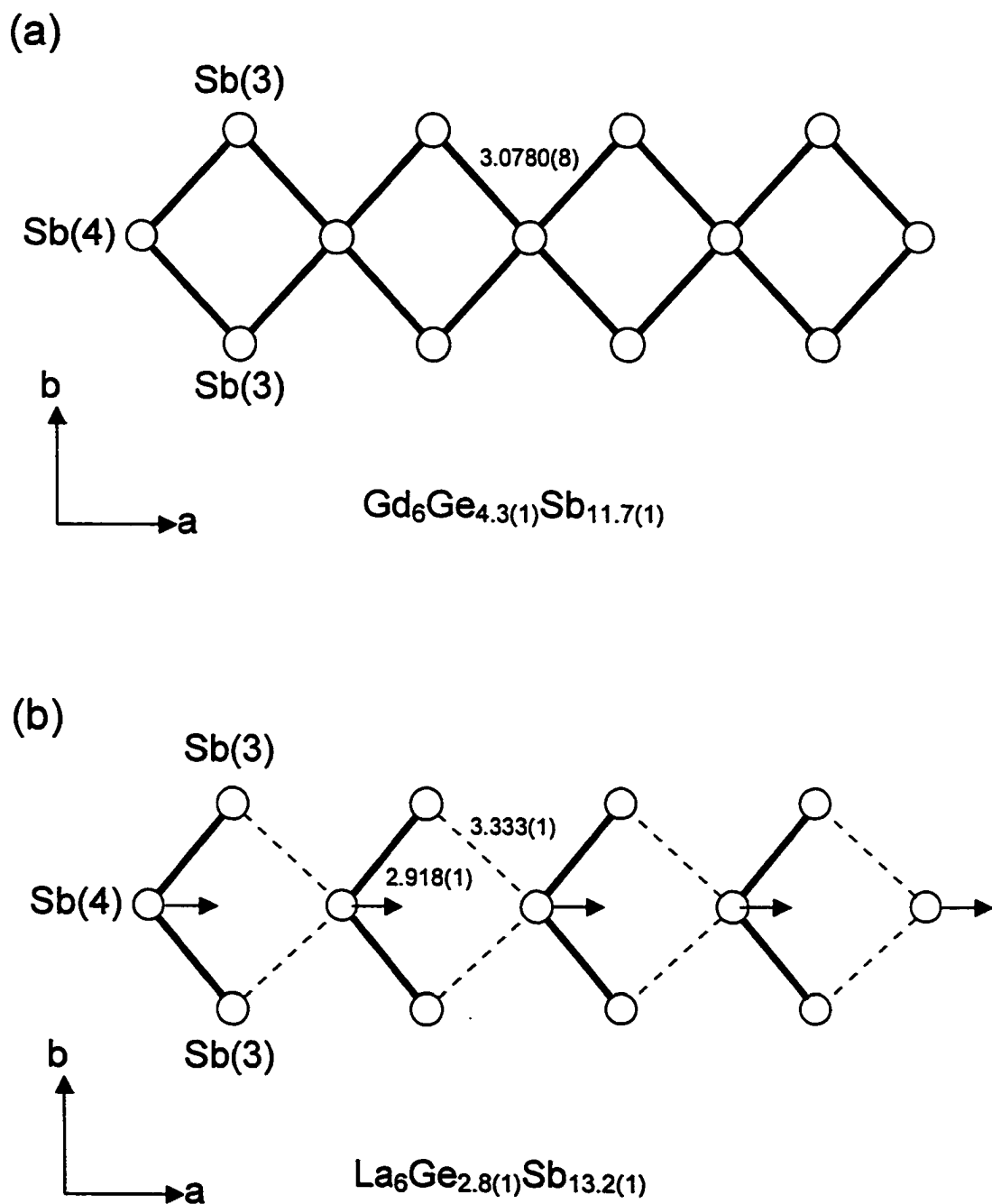


Figure 6-4. Comparison of the symmetrical and asymmetrical three-atom wide Sb ribbons, built up of Sb(3) and Sb(4), in (a) $\text{Gd}_6\text{Ge}_{4.3(1)}\text{Sb}_{11.7(1)}$ and (b) $\text{La}_6\text{Ge}_{2.8(1)}\text{Sb}_{13.2(1)}$, respectively, as viewed perpendicular to the plane of the strips.

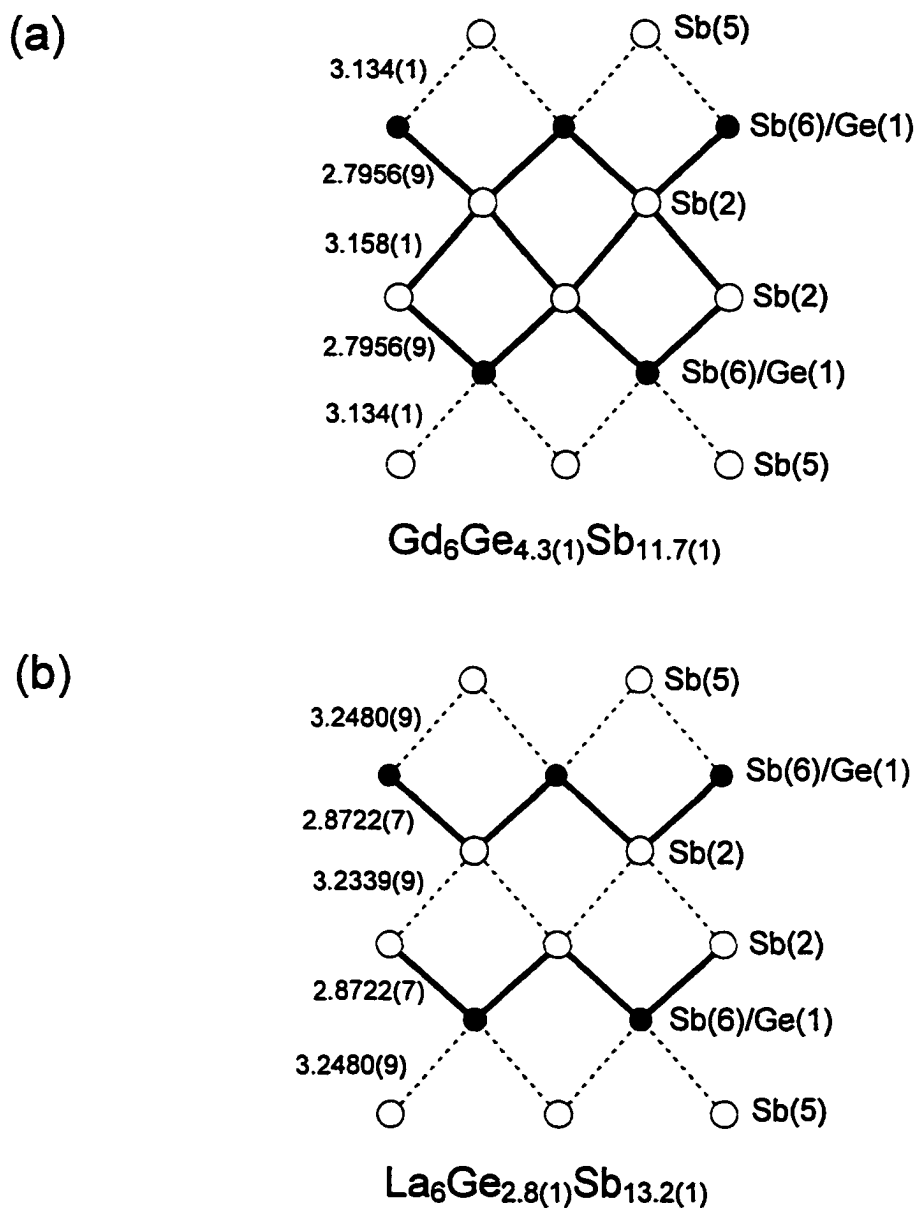


Figure 6–5. Comparison of the six-atom wide sections making up the kinked sheets in (a) $\text{Gd}_6\text{Ge}_{4.3(1)}\text{Sb}_{11.7(1)}$ and (b) $\text{La}_6\text{Ge}_{2.8(1)}\text{Sb}_{13.2(1)}$, respectively, as viewed perpendicular to the plane of the atoms. On the basis of bond distances and atomic distributions in the $M(1)$ site, local interpretations of four-atom wide ribbons ($RE = \text{Gd}$) and zigzag chains ($RE = \text{La}$) are emphasized for the six-atom wide sections. Thick lines represent bond orders greater than 0.5 and dashed lines represent weak bonding interactions.

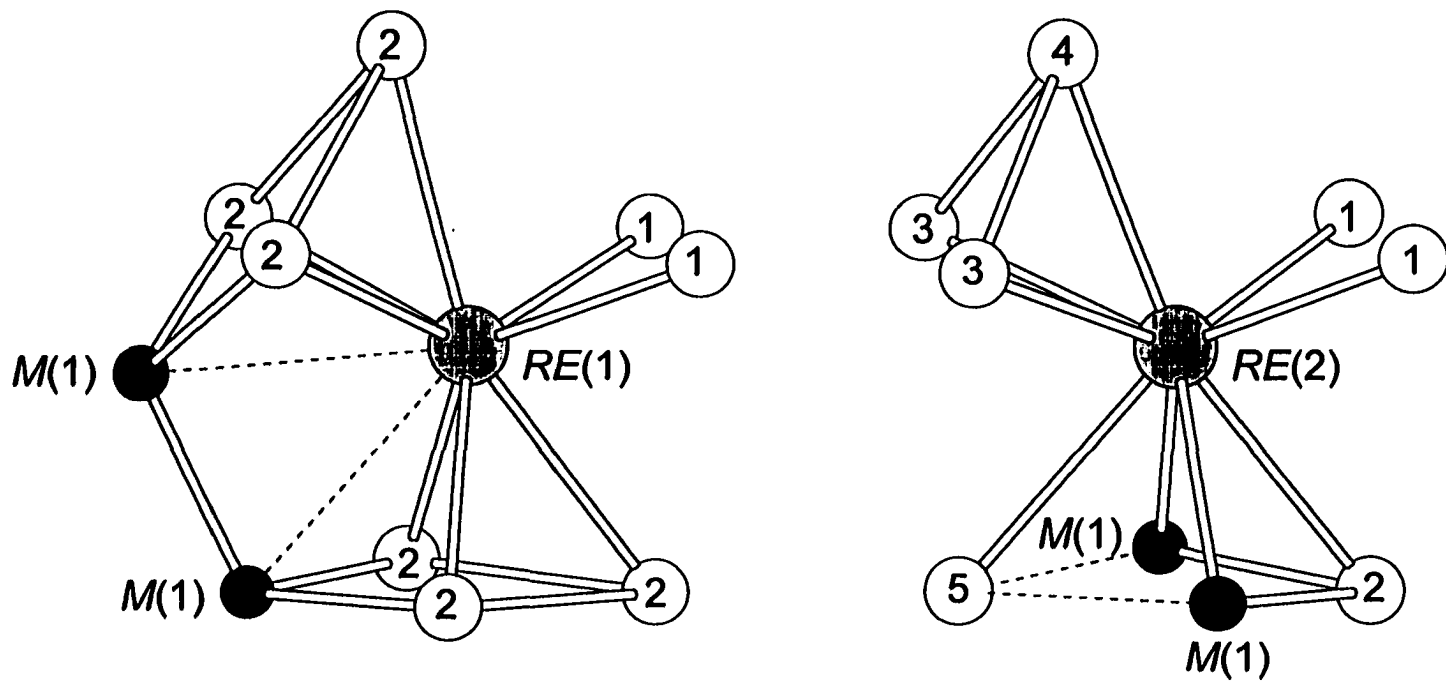


Figure 6-6. Coordination environments around $RE(1)$ and $RE(2)$ atoms, showing bicapped trigonal prism and monocapped square antiprism geometries, respectively. Alternatively, the coordination of $RE(1)$ may be described as a bicapped square antiprism if the two $M(1)$ atoms, situated further away as shown by the dashed lines, are considered.

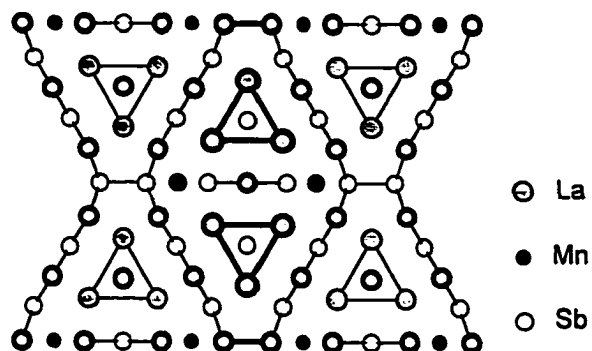
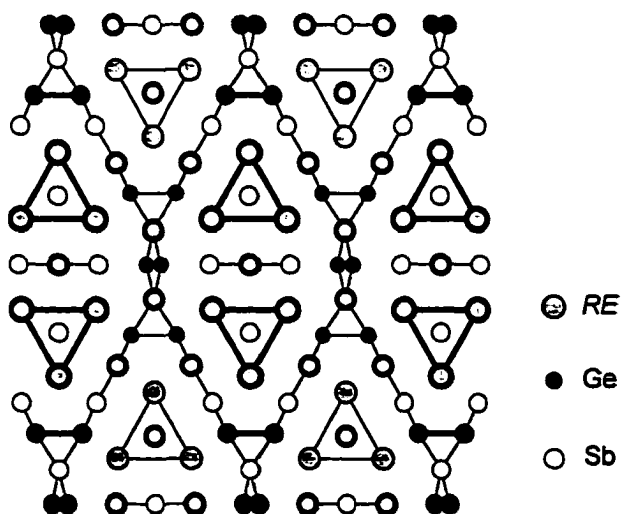
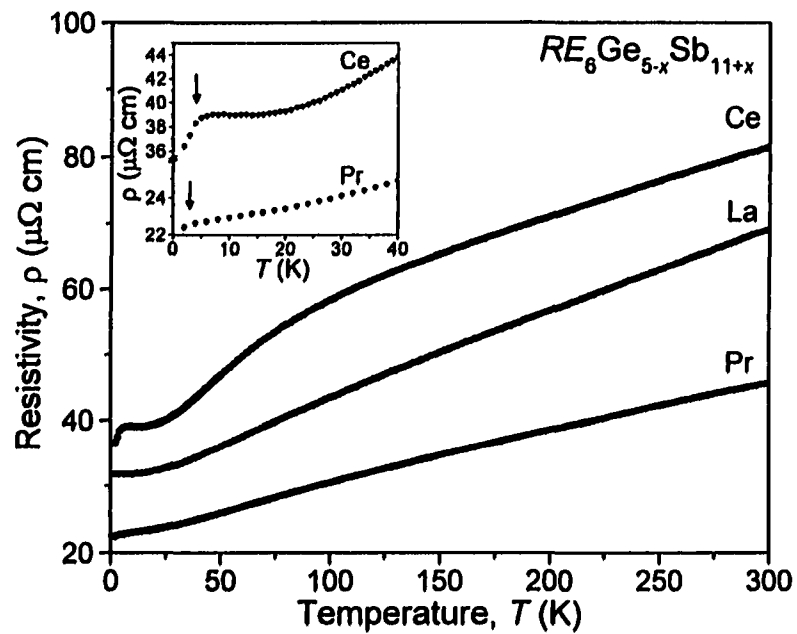
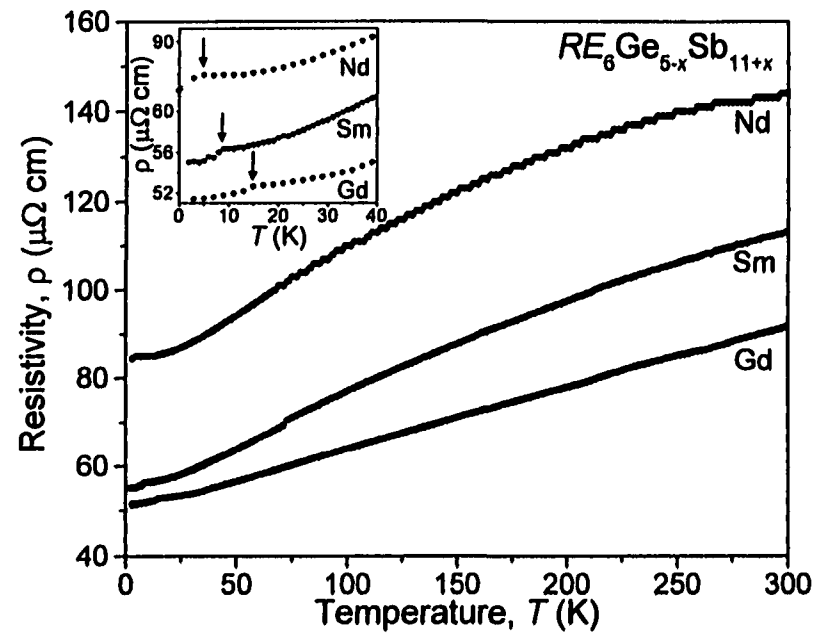
(a) $\text{La}_6\text{MnSb}_{15}$ (b) $\text{RE}_6\text{Ge}_{5-x}\text{Sb}_{11+x}$ 

Figure 6–7. Comparison of the structures of (a) $\text{La}_6\text{MnSb}_{15}$ and (b) $\text{RE}_6\text{Ge}_{5-x}\text{Sb}_{11+x}$ shown in projection down the shortest axis. Circles with thicker rims are atoms residing in planes displaced by $\frac{1}{2}$ the short axis parameter.

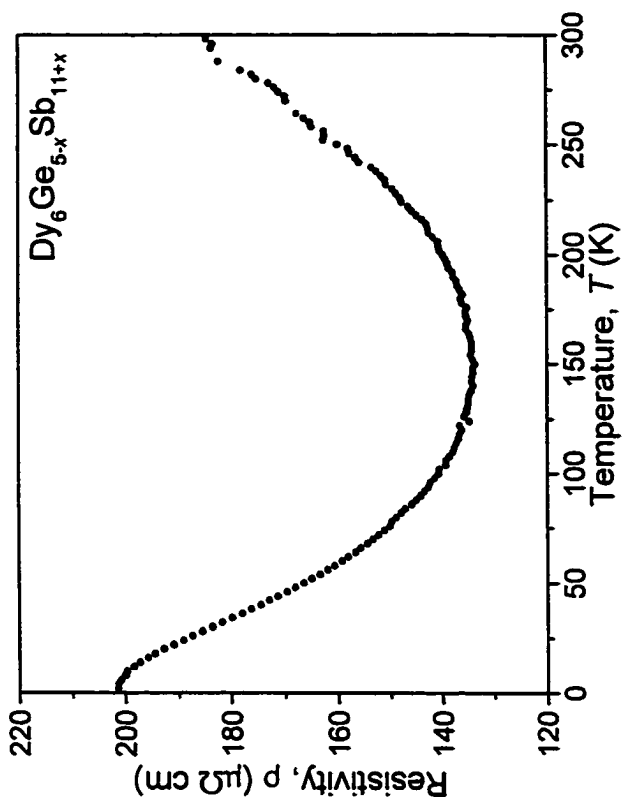


(a)

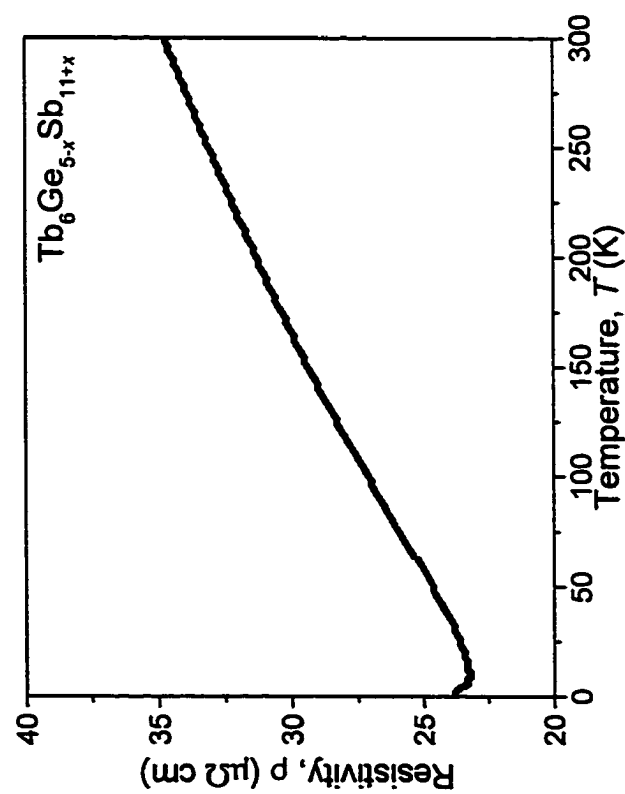


(b)

Figure 6–8. Electrical resistivity of single crystals of $RE_6Ge_{5-x}Sb_{11+x}$ measured along the a axis between 2 and 300 K. (a) $RE =$ La, Ce, Pr; (b) $RE =$ Nd, Sm, Gd. Insets show low-temperature behavior, the arrows indicating changes in slope arising from magnetic ordering.



(a)



(b)

Figure 6–8. Electrical resistivity of single crystals of $RE_6\text{Ge}_{5-x}\text{Sb}_{11+x}$ measured along the a axis between 2 and 300 K. (a) $RE = \text{Tb}$; (b) $RE = \text{Dy}$.

REFERENCES

- (1) Mills, A. M.; Mar, A. *Inorg. Chem.* In press.
- (2) Ferguson, M. J.; Ellenwood, R. E.; Mar, A. *Inorg. Chem.* **1999**, *38*, 4503.
- (3) Ferguson, M. J.; Hushagen, R. W.; Mar, A. *Inorg. Chem.* **1996**, *35*, 4505.
- (4) Lam, R.; Zhang, J.; Mar, A. *J. Solid State Chem.* **2000**, *150*, 371.
- (5) *Chemistry, Structure, and Bonding of Zintl Phases and Ions*; Kauzlarich, S. M., Ed.; VCH Publishers: New York, 1996 (and references therein).
- (6) Schäfer, H. *Annu. Rev. Mater. Sci.* **1985**, *15*, 1.
- (7) Corbett, J. D. *Chem. Rev.* **1985**, *85*, 383.
- (8) von Schnering, H. G. *Angew. Chem., Int. Ed. Engl.* **1981**, *20*, 33.
- (9) Papoian, G. A.; Hoffmann, R. *Angew. Chem., Int. Ed. Engl.* **2000**, *39*, 2408.
- (10) Steskiv, A. O.; Pavlyuk, V. V.; Bodak, O. I. *Pol. J. Chem.* **1998**, *72*, 956.
- (11) Deakin, L.; Lam, R.; Mar, A. *Inorg. Chem.* Submitted.
- (12) FilmScan and Jade 3.1; Materials Data Inc.: Livermore, CA, 1996.
- (13) Lévy, F. *Phys. Kondens. Mater.* **1969**, *10*, 85.
- (14) Hulliger, F.; Schmelczer, R. *J. Solid State Chem.* **1978**, *26*, 389.
- (15) Wang, R.; Bodnar, R.; Steinfink, H. *Inorg. Chem.* **1966**, *5*, 1468.
- (16) POLSQ: Program for least-squares unit cell refinement. Modified by D. Cahen and D. Keszler, Northwestern University, 1983.
- (17) Yvon, K.; Jeitschko, W.; Parthé, E. *J. Appl. Crystallogr.* **1977**, *10*, 73.
- (18) Sheldrick, G. M. *SHELXTL* Version 5.1; Bruker Analytical X-ray Systems, Inc.: Madison, WI, 1997.

- (19) *International Tables for X-ray Crystallography*, Wilson, A. J. C., Ed.; Kluwer: Dordrecht, The Netherlands, 1992; Vol. C.
- (20) Sologub, O.; Vybornov, M.; Rogl, P.; Hiebl, K.; Cordier, G.; Woll, P. *J. Solid State Chem.* **1996**, *122*, 266.
- (21) Papoian, G.; Hoffmann, R. *J. Solid State Chem.* **1998**, *139*, 8.
- (22) Flack, H. D. *Acta Crystallogr., Sect. A: Found. Crystallogr.* **1983**, *39*, 876.
- (23) Le Page, Y. *J. Appl. Crystallogr.* **1988**, *21*, 983.
- (24) Spek, A. L. *PLATON* Version 281097; Utrecht University: The Netherlands, 1997.
- (25) Gelato, L. M.; Parthé, E. *J. Appl. Crystallogr.* **1987**, *20*, 139.
- (26) Ferguson, M. J.; Hushagen, R. W.; Mar, A. *J. Alloys Compd.* **1997**, *249*, 191.
- (27) Brylak, M.; Möller, M. H.; Jeitschko, W. *J. Solid State Chem.* **1995**, *115*, 305.
- (28) Brylak, M.; Jeitschko, W. *Z. Naturforsch. B: Chem. Sci.* **1994**, *49*, 747.
- (29) Nesper, R. *Prog. Solid State Chem.* **1990**, *20*, 1.
- (30) Wang, R.; Steinfink, H. *Inorg. Chem.* **1967**, *6*, 1685.
- (31) Cordier, G.; Schäfer, H.; Woll, P. *Z. Naturforsch. B: Anorg. Chem., Org. Chem.* **1985**, *40*, 1097.
- (32) Lam, R.; Mar, A. *Inorg. Chem.* **1998**, *37*, 5364.
- (33) Lam, R.; Mar, A. *Inorg. Chem.* **1996**, *35*, 6959.
- (34) Bolloré, G.; Ferguson, M. J.; Hushagen, R. W.; Mar, A. *Chem. Mater.* **1995**, *7*, 2229.
- (35) Donohue, J. *The Structures of the Elements*; Wiley: New York, 1974.
- (36) Bobev, S.; Sevov, S. C. *J. Am. Chem. Soc.* **1999**, *121*, 3795.

- (37) O'Keeffe, M.; Brese, N. E. *Acta Crystallogr., Sect. B: Struct. Sci.* **1992**, *48*, 152.
- (38) von Schnering, H. G.; Menke, H. *Z. Anorg. Allg. Chem.* **1976**, *424*, 108.
- (39) Adolphson, D. G.; Corbett, J. D.; Merryman, D. J. *J. Am. Chem. Soc.* **1976**, *98*, 7234.
- (40) Mehta, A.; Malik, S. K.; Yelon, W. B. *J. Magn. Magn. Mater.* **1995**, *147*, 309.
- (41) Furuseth, S.; Kjekshus, A. *Nature* **1964**, *203*, 512.
- (42) Furuseth, S.; Kjekshus, A. *Acta Crystallogr.* **1965**, *18*, 320.
- (43) Critchlow, S. C.; Corbett, J. D. *Inorg. Chem.* **1984**, *23*, 770.
- (44) Bolle, U.; Tremel, W. *J. Chem. Soc., Chem. Commun.* **1992**, 91.
- (45) Cordier, G.; Ochmann, H. *Z. Kristallogr.* **1991**, *197*, 297.
- (46) Shreeve-Keyer, J. L.; Haushalter, R. C.; Seo, D.-K.; Whangbo, M.-H. *J. Solid State Chem.* **1996**, *122*, 239.
- (47) Asbrand, M.; Eisenmann, B. *Z. Kristallogr.* **1992**, *198*, 309.
- (48) Tokitoh, N.; Arai, Y.; Sasamori, T.; Okazaki, R.; Nagase, S.; Uekusa, H.; Ohashi, Y. *J. Am. Chem. Soc.* **1998**, *120*, 433.
- (49) Tramley, B.; Sofield, C. D.; Olmstead, M. M.; Power, P. P. *J. Am. Chem. Soc.* **1999**, *121*, 3357.
- (50) Power, P. P. *J. Chem. Soc., Dalton Trans.* **1998**, 2939.
- (51) Power, P. P. *Chem. Rev.* **1999**, *99*, 3463.
- (52) Hewson, A. C. *The Kondo Problem to Heavy Fermions*; Cambridge University Press: Cambridge, U. K., 1997.
- (53) Shimakawa, Y.; Kubo, Y.; Manako, T. *Nature* **1996**, *379*, 53.

- (54) Subramanian, M. A.; Toby, B. H.; Ramirez, A. P.; Marshall, W. J.; Sleight, A. W.; Kwei, G. H. *Science* **1996**, *273*, 81.

CHAPTER 7

New Ternary Zirconium Antimonides: $ZrSi_{0.7}Sb_{1.3}$, $ZrGeSb$, and $ZrSn_{0.4}Sb_{1.6}$. A Family Containing $ZrSiS$ -Type and β - $ZrSb_2$ -Type Compounds[†]

INTRODUCTION

The PbFCl structure type, along with its relatives $ZrSiS$, $BiOCl$, Cu_2Sb , and Fe_2As , is a ubiquitous one with more than 200 members possessing diverse properties ranging from insulating–semiconducting to metallic.^{1,2} Historically, despite significant differences among the “synonymous” structure types, all labels have been used interchangeably. The differences lie mainly in the degree of anion–anion bonding in the structure. For example, $PbFCl$ itself is a “normal valence” compound consisting essentially of discrete F^- and Cl^- anions and is thus nonmetallic, whereas $ZrSiS$ is deficient in electrons for the anions to satisfy the simple $8-n$ rule, so that fractional covalent anion–anion bonds or metallic properties must result.³ Traditionally, “PbFCl” has been the label of choice in referring to members possessing this or its closely related

[†] A version of this chapter has been published. Lam, R.; Mar, A. *J. Solid State Chem.* 1997, 134, 388. Copyright 1997 Academic Press.

structures. For clarity, we prefer the more accurate description, “ZrSiS-type,” for the compounds $\text{ZrSi}_{0.7}\text{Sb}_{1.3}$ and ZrGeSb described herein, owing to the presence of anion-anion bonding, and reserve the label “PbFCl-type” for cases in which no such bonding occurs.

Collectively, the PbFCl- or ZrSiS-type compounds may be designated as MAB (M = transition metal; A , B = main group elements). The tetragonal structure consists of square nets of each of M , A , and B , stacked in the sequence $[-A-M-B-B-M-A-]$, with the A net being twice as dense as M or B nets. The layers are held together by $M-A$ and $M-B$ bonds to produce an overall structure that, in most cases, is three-dimensional. As a consequence, the M atoms are surrounded by nine A or B atoms in a monocapped square antiprismatic geometry (Figure 7-1a). These units are arranged in an alternating head-to-head and tail-to-tail fashion along the c axis (Figure 7-2).

A useful way to systematize members of the MAB family is to compare their c/a ratios, which separate two-dimensional from three-dimensional structures,² and their valence electron counts, which measure the degree of anion-anion bonding. In normal valence compounds such as PbFCl, there is no deficiency of electrons ($\Delta = 0$) with respect to the simple $8-n$ rule.⁴ In polyanionic compounds, the greatest deficiency observed has been $\Delta = 2$, as in $\text{ZrSiS}^{5,6}$ or NbSiAs ,⁷ so that Si-Si half-bonds have to be invoked. Table 7-1 shows selected members with the PbFCl or ZrSiS structure type classified according to these two indicators. We report here two new compounds, $\text{ZrSi}_{0.7}\text{Sb}_{1.3}$ and ZrGeSb , that have three-dimensional ZrSiS-type structures and that have the most pronounced deficiency Δ yet observed in this family. In an attempt to synthesize the tin analogue, we show that the compound $\text{ZrSn}_{0.4}\text{Sb}_{1.6}$ reverts to a

disordered variant of the binary compound β -ZrSb₂.¹¹ Possible reasons for the adoption of these structure types are presented.

EXPERIMENTAL SECTION

SYNTHESIS

Reagents were elemental powders obtained from Cerac, Alfa-Aesar, or Aldrich, with >99.9% purity (except for Zr, which was 99.7% pure). Reactions were carried out on a 0.250 g scale in evacuated fused silica tubes (8-cm length; 10-mm i.d.). Elemental compositions (EDX analysis) of selected crystals were determined with the use of a Hitachi S-2700 scanning electron microscope (ZrSi_{0.7}Sb_{1.3} and ZrSn_{0.4}Sb_{1.6}) or a JEOL JSM-6301FXV field-emission scanning electron microscope (ZrGeSb and ZrSn_{0.4}Sb_{1.6}). X-ray powder patterns were obtained on an Enraf-Nonius FR552 Guinier camera (CuK α ₁ radiation; Si standard).

ZrSi_{0.7}Sb_{1.3} was first identified in a reaction of La, Zr, and Sb in a 8:13:30 ratio (intended for the preparation of La₃ZrSb₅¹²). The mixture was heated at 600 °C for 2 days and 1000 °C for 2 days, and cooled to 600 °C over 2 days and to 20 °C over 12 hours. Shiny square plates were found at the walls of the partially-attacked silica tube. Anal. (mol %): Zr, 31(1); Si, 22(1); Sb, 46(1) (average of 3 analyses). ZrSi_{0.7}Sb_{1.3} can also be prepared more rationally by reaction of the elements. It can be formed from diverse loading compositions, except those that are Si-rich, in which case ZrSi₂^{13,14} prevails as the major phase. For example, heating Zr, Si, and Sb in a 2:1:2 ratio at 1000 °C for 2 days and then cooling to 500 °C over 5 days and to 20 °C over 12 hours results

in a mixture of binary impurities ZrSi^{14} and $\text{ZrSi}_2^{13,14}$ (minor) as well as shiny square plates of the ternary compound. Anal. (mol %) Zr, 31(1); Si, 25(2); Sb, 44(3) (average of 3 analyses).

ZrGeSb resulted from a reaction of Zr, Ge, and Sb in a 1:1:3 ratio, heated at 570 °C for 1 day, 950 °C for 4 days, cooled to 500 °C over 4 days, and then cooled to 20 °C over 12 hours. The product consisted of square block-shaped crystals of ZrGeSb and microcrystalline powder, containing the ternary compound as the major phase and unreacted Ge. Anal. (mol %): Zr, 32(1); Ge, 30(2); Sb, 38(1) (average of 4 analyses). ZrGeSb can be obtained from reactions with diverse loading compositions except those that are Ge-rich, in which case ZrGe_2^{15} is the major phase.

$\text{ZrSn}_{0.4}\text{Sb}_{1.6}$ was originally obtained as a byproduct from a reaction of La, Zr, Cu, and Sb in a 1:1:1:4 ratio to which a 10-fold excess of Sn was added. The mixture was heated at 600 °C for 1 day, 900 °C for 2 days, cooled to 600 °C over 1 day, and then cooled to 20 °C over 10 hours. Dissolving the Sn with concentrated HCl afforded a grey powder and black block-shaped crystals of $\text{ZrSn}_{0.4}\text{Sb}_{1.6}$, which were used in the structure determination. Except for compositions where Zr is in excess, reaction of the elements in various ratios at 1000 °C for 2 days also results in $\text{ZrSn}_{0.4}\text{Sb}_{1.6}$. The ratio 2:1:2 produced the best yield of $\text{ZrSn}_{0.4}\text{Sb}_{1.6}$ (~ 50%) as well as unreacted Sn and an unidentified minor phase.

The cell parameters of selected samples were refined from the powder diffraction data with the use of the program POLSQ.¹⁶ The observed and calculated interplanar distances, as well as intensities determined using the program LAZY-PULVERIX,¹⁷ are listed in Tables A-19 to A-21.

STRUCTURE DETERMINATION

Two crystals of $\text{ZrSi}_{0.7}\text{Sb}_{1.3}$, one from the original synthesis and one from the rational synthesis, as well as one each of ZrGeSb and $\text{ZrSn}_{0.4}\text{Sb}_{1.6}$, were selected. As the two $\text{ZrSi}_{0.7}\text{Sb}_{1.3}$ crystals gave essentially identical results (the refined compositions were $\text{ZrSi}_{0.68(1)}\text{Sb}_{1.32(1)}$ and $\text{ZrSi}_{0.74(2)}\text{Sb}_{1.26(1)}$ with similar metrical details), we report only the more accurate determination. Preliminary cell parameters were determined from Weissenberg photographs, which revealed Laue symmetry $4/mmm$ and systematic extinctions ($0kl: k + l = 2n + 1$) consistent with the tetragonal space groups $D_{4h}^7 - P4/nmm$ and $D_{4h}^3 - P4/n$ for $\text{ZrSi}_{0.7}\text{Sb}_{1.3}$ and ZrGeSb , and Laue symmetry mmm and systematic extinctions ($0kl: k + l = 2n + 1$; $hk0: h = 2n + 1$) consistent with the orthorhombic space groups $D_{2h}^{16} - Pnma$ and $C_{2v}^9 - Pn2_1a$ for $\text{ZrSn}_{0.4}\text{Sb}_{1.6}$. Final cell parameters were determined from a least-squares analysis of the setting angles of 24 reflections centred on an Enraf-Nonius CAD4 diffractometer in the range $10^\circ \leq 2\theta(\text{MoK}\alpha) \leq 20^\circ$ for $\text{ZrSi}_{0.7}\text{Sb}_{1.3}$, $20^\circ \leq 2\theta(\text{MoK}\alpha) \leq 50^\circ$ for ZrGeSb , and $20^\circ \leq 2\theta(\text{MoK}\alpha) \leq 39^\circ$ for $\text{ZrSn}_{0.4}\text{Sb}_{1.6}$. Intensity data were collected at -50°C with the θ - 2θ scan technique in the range $4^\circ \leq 2\theta(\text{MoK}\alpha) \leq 70^\circ$. All calculations were carried out with the use of the SHELXTL (Version 5.0) package.^{18,19} Conventional atomic scattering factors and anomalous dispersion corrections were used.²⁰ Intensity data were reduced and averaged, and face-indexed Gaussian-type absorption corrections were applied in XPREP. Initial atomic positions were found by direct methods in XS, and least-squares refinements were performed in XL.

For $\text{ZrSi}_{0.7}\text{Sb}_{1.3}$, the centrosymmetric space group $P4/nmm$ was chosen based on the intensity statistics and on the similarity of the intensity pattern to that of ZrSiS . An

initial refinement assuming the formula ZrSiSb resulted in reasonable displacement parameters for all sites except the one at $\frac{3}{4}, \frac{1}{4}, 0$, for which the displacement parameter was anomalously low. Since disordering of the nonmetal atoms in this site has been previously observed,² a refinement was performed in which the two possible nonmetal sites were allowed to be fully occupied by a mixture of Si and Sb, with no constraint placed on the overall Si:Sb ratio. This resulted in occupancies of 98(1)% Sb and 2(2)% Si in the site $\frac{1}{4}, \frac{1}{4}, 0.61$ and 74(2)% Si and 26(1)% Sb in the site $\frac{3}{4}, \frac{1}{4}, 0$. The final refined formula, assuming the former site is fully occupied by Sb, is $\text{ZrSi}_{0.74(2)}\text{Sb}_{1.26(1)}$, which agrees well with the EDX analysis. Disorder appears to be inherent property in this compound, and we shall accept the formulation $\text{Zr}(\text{Si}_{0.7}\text{Sb}_{0.3})\text{Sb}$ or $\text{ZrSi}_{0.7}\text{Sb}_{1.3}$.

For ZrGeSb , the space group $P4/nmm$ was chosen based on the similarity of the intensity pattern with that of $\text{ZrSi}_{0.7}\text{Sb}_{1.3}$, despite a high R_{int} index for averaging (which we attribute to the difficulty in performing a good absorption correction). Refinements in which the occupancies of successive atoms were allowed to vary (while the isotropic displacement parameters were fixed) resulted in values of 99.4(7)% for Zr, 102.5(6)% for Ge, and 98.7(6)% for Sb. A refinement performed allowing the nonmetal sites to be disordered resulted in occupancies of 90(4)% Ge in one site and 98(3)% Sb in the other site. Thus, in contrast to $\text{ZrSi}_{0.7}\text{Sb}_{1.3}$, we accept the ordered model for ZrGeSb .

$\text{ZrSn}_{0.4}\text{Sb}_{1.6}$ was recognized to be isotypic to $\beta\text{-ZrSb}_2$.¹¹ Because of their similar scattering factors, it is not possible to distinguish between Sn and Sb from the X-ray data alone. In other ternary compounds containing Sn and Sb,²¹ an ordered model can be invoked because of their very different coordination geometries. In this case, however, there is no compelling reason to do so because the environments of the two anion sites

$X(1)$ and $X(2)$ are chemically indistinguishable: both sites together complete the monocapped square antiprismatic coordination around the Zr atom. Refinements in which these sites were occupied completely either by Sn or Sb produced identical results. Independent refinements of the site occupation factors of $X(1)$ and $X(2)$ (whether they were filled by Sn or Sb), as well as the Zr site, confirmed essentially 100% occupancy. Since the cell constants of $\text{ZrSn}_{0.4}\text{Sb}_{1.6}$ ($a = 7.3187(6)$, $b = 3.9618(4)$, $c = 9.7076(7)$ Å, $V = 281.47(4)$ Å³; $T = -50$ °C) deviate significantly from those of $\beta\text{-ZrSb}_2$ ($a = 7.393(1)$, $b = 3.9870(7)$, $c = 9.581(1)$ Å, $V = 282.42(7)$ Å³; $T = 25$ °C)¹¹ (more than can be accounted for even by the difference in temperature), partial substitution of larger Sn atoms for Sb atoms must have occurred. Ultimate composition was established from EDX analyses on two scanning electron microscopes. Averaging 8 analyses resulted in atomic percentages of 29(2)% Zr, 13(1)% Sn, and 58(2)% Sb (JEOL JSM-6301FXV), while averaging 5 resulted in 36(4)% Zr, 11(1)% Sn, and 53(3)% Sb (Hitachi S-2700). The discrepancies arise from use of different calibration standards. These analyses are consistent with a formula “ $\text{ZrSn}_{0.4}\text{Sb}_{1.6}$ ” (33% Zr, 13% Sn, 53% Sb). Sites $X(1)$ and $X(2)$ were thus occupied by a mixture of 20% Sn and 80% Sb in the final refinement.

The displacement parameters are unexceptional, and difference electron density maps are featureless ($\text{ZrSi}_{0.7}\text{Sb}_{1.3}$: $\Delta\rho_{\text{max}} = 1.00$, $\Delta\rho_{\text{min}} = -1.72$; ZrGeSb : $\Delta\rho_{\text{max}} = 5.81$, $\Delta\rho_{\text{min}} = -11.30$; $\text{ZrSn}_{0.4}\text{Sb}_{1.6}$: $\Delta\rho_{\text{max}} = 4.44$; $\Delta\rho_{\text{min}} = -4.95$ e⁻ Å⁻³). Crystal data and further details of the data collection are given in Tables 7–2. Final values of the positional and displacement parameters are given in Table 7–3. Selected interatomic distances and angles are given in Table 7–4 ($\text{ZrSi}_{0.7}\text{Sb}_{1.3}$ and ZrGeSb) and Table 7–5 ($\text{ZrSn}_{0.4}\text{Sb}_{1.6}$). Anisotropic displacement parameters are given in Table A–22.

RESULTS AND DISCUSSION

SYNTHESIS

The use of silica tubes in high-temperature solid-state reactions sometimes leads to materials incorporating Si or SiO₂,^{2,6,22} as was the case in the original synthesis of ZrSi_{0.7}Sb_{1.3}. This compound can be also formed by direct reaction of the elements at most compositions except those that are Si-rich, in which case formation of the binary ZrSi₂ predominates. The preferred formation of ZrSi₂ in ternary phase reactions has been documented.⁵ Similarly, in the ZrGeSb system, the thermodynamically more stable phase, ZrGe₂, was the major product in all Ge-rich reactions. Related observations have been noted in the syntheses of ternary zirconium silicon/germanium chalcogenides, whose thermal stability decreases with increasing formula weight.⁵ Since the most convenient temperatures for crystal growth of the ternary compounds are also precariously close to their decomposition region, it is difficult to obtain them in pure form. The non-existence of a “ZrSnSb” phase with the ZrSiS-type structure may be attributed to this trend in decreasing thermal stability, but other, structural reasons may be important.

The cell parameters refined from X-ray powder patterns resulting from compositionally diverse preparations of ZrSi_{0.7}Sb_{1.3}, ZrGeSb, and ZrSn_{0.4}Sb_{1.6} do not vary significantly. In particular, the cell volume remains relatively constant in different preparations of ZrSi_{0.7}Sb_{1.3}. Moreover, in the case of ZrSi_{0.7}Sb_{1.3}, the two crystals examined were obtained under very different synthetic conditions, but their compositions refined from the X-ray data are essentially identical. The degree of nonhomogeneity in these compounds is probably slight, if any.

STRUCTURE OF $\text{ZrSi}_{0.7}\text{Sb}_{1.3}$ AND ZrGeSb

The structure of $\text{ZrSi}_{0.7}\text{Sb}_{1.3}$ and ZrGeSb viewed down the b axis is shown in Figure 7–2, with the labeling scheme showing the stacking sequence. These adopt the ZrSiS -type structure,^{1–7} which may be described in terms of the connectivity of Zr-centered polyhedra, the smallest building units. Briefly, the Zr atoms reside in a monocapped square antiprismatic environment (CN 9) (Figure 1a). Four A atoms form the basal square plane ($A = \text{Si}$ and $\text{Sb}(1)$ in $\text{ZrSi}_{0.7}\text{Sb}_{1.3}$, or Ge atoms in ZrGeSb), four $\text{Sb}(2)$ atoms form a larger square twisted 45° relative to the first one, and a fifth $\text{Sb}(2)$ atom caps this square. If the capping Sb atom is designated as the “head” of the polyhedron, then the structure can be described as an arrangement of monocapped square antiprisms oriented head-to-head and tail-to-tail along the c axis.

Examination of Table 7–4 shows that most bonds are lengthened on going from $\text{ZrSi}_{0.7}\text{Sb}_{1.3}$ to ZrGeSb , consistent with substitution of Si by the larger Ge atom, although the increase may not be as pronounced as expected. In fact, the bond from Zr to the capping Sb atom is shorter in ZrGeSb (3.094(2) Å) than in $\text{ZrSi}_{0.7}\text{Sb}_{1.3}$ (3.1085(7) Å). This results from relief of steric crowding of the Sb atoms within the Sb squares and the presence of longer Ge–Ge bonds, thus allowing the capping Sb atom to better interact with the Zr center.²

The structure of $\text{ZrSi}_{0.7}\text{Sb}_{1.3}$ and ZrGeSb is derived from a three-dimensional layering of square nets. The Sb–Sb separations (>3.3 Å) within the less dense square net are too long to be bonding. Within the denser square net of A atoms, the A – A distances are 2.6934(1) Å for $\text{ZrSi}_{0.7}\text{Sb}_{1.3}$ and 2.7189(5) Å for ZrGeSb . These distances fall outside of the range normally considered for a full Si–Si or Ge–Ge single bond. For example,

such bonds are found in many ternary main-group pnictides $A_xM_yPn_z$ (A = alkali metal or alkaline earth; M = tetrel; Pn = P, As, Sb, Bi), where Si–Si^{23–27} and Ge–Ge^{23,24,28,29} single bond distances are ~2.3–2.4 Å and ~2.4–2.5 Å, respectively. The corresponding distances in ZrSi_{0.7}Sb_{1.3} and ZrGeSb are about 10–15% longer, suggesting that these bonds are of fractional order. The large number of MAB compounds may be organized along a continuum in which at one extreme lie PbFCl-type members that are non-metallic or “normal valence” compounds.^{4,30,31} For example, the formulation for UOTe may be represented as $U^{4+}(O^{2-})(Te^{2-})$. More importantly, the M cation provides sufficient electrons to the A and B atoms to satisfy the octet rule, so formation of anion–anion bonds in the square A net is excluded and the structure consists of discrete ions. Representatives of nonmetallic PbFCl-type compounds include the oxyhalides PuOX (X = Cl, Br, I)⁴ and oxychalcogenides UOY (Y = S, Se, Te).⁴ At the other extreme are found the more metallic phases in which the M cation provides insufficient electrons to saturate the valence requirements of A and B . These ZrSiS-type compounds necessarily contain A – A bonds of fractional order which have now been quantified by band structure calculations.¹ The degree of anion–anion interaction within the square nets of A atoms depends on the size of the cation as well as the anion.⁴ Examples of these metallic phases are provided by the ternary main-group chalcogenides given in Table 7–1.

The dimensionality of ZrSiS-type structures has also been studied previously.² The transition from a three-dimensional to a true layered structure depends on the distance from M to the capping B atom and is signalled by an anomalously high c/a ratio. In the series Zr AB (A = Si, Ge, Sn; B = S, Se, Te), ZrSiTe is shown to be a layered compound as indicated by its high c/a ratio (2.572) compared to normal values of 2.0–2.3

for three-dimensional structures (Table 7–1).^{1,2,5,6} This ratio also provides a useful division between metallic and nonmetallic phases, as values for the former do not fall below 2.0.⁴

We can now classify $\text{ZrSi}_{0.7}\text{Sb}_{1.3}$ and ZrGeSb according to electron count, ionic-metallic distinction, and dimensionality. As shown in Table 7–1, most ZrSiS-type compounds have electron counts that correspond to a deficiency Δ of 2 electrons required for the *A* and *B* atoms to satisfy the $8-n$ rule. Consequently, the *A*–*A* bonds within the denser square net are often portrayed as half-bonds, or one-electron bonds. $\text{ZrSi}_{0.7}\text{Sb}_{1.3}$ and ZrGeSb are noteworthy in having the largest value of $\Delta = 3$ while retaining the ZrSiS-type structure. Interestingly, the Ge–Ge distance in ZrGeSb (2.7189(5) Å) is not significantly different from that in ZrGeTe (2.734(1) Å).⁶ Presumably, other factors, such as the complex interplay of Zr–*A* and Zr–*B* bonds as well as steric effects, are important in controlling the stability of this structure type. A thorough band structure study is needed to unravel these complexities. In terms of bonding character, $\text{ZrSi}_{0.7}\text{Sb}_{1.3}$ and ZrGeSb belong to the more metallic phases containing fractional anion–anion bonds. Examination of the Zr–Sb(capping) distances in $\text{ZrSi}_{0.7}\text{Sb}_{1.3}$ (3.1085(7) Å) and ZrGeSb (3.094(2) Å) indicates that these are three-dimensional structures, as confirmed by their *c/a* ratios (2.266 and 2.245, respectively).

A reasonable explanation for nonstoichiometry in $\text{ZrSi}_{0.7}\text{Sb}_{1.3}$ and its absence in ZrGeSb may be attributed to the size difference between Si and Ge. Note that the anion–anion (*A*–*A*) distance remains fairly constant as one substitutes Si with Ge (~ 2.7 Å). This suggests that bond distances within the square net of smaller *A* atoms are already *fixed* by the constraint imposed by the presence of the larger Sb atoms in the less dense

square B net. Placing only Si atoms in the geometrically fixed sites in the square A net would result in an unstable compound because the A - A distances are too far for even fractional Si-Si bonding to be strong enough to provide sufficient bonding energy. Thus, $\text{ZrSi}_{0.7}\text{Sb}_{1.3}$ requires replacement of approximately every fourth Si atom with the larger Sb atom in the square net in order to achieve sufficient anion-anion bonding to stabilize the compound. Furthermore, we would not expect much variability in the nonstoichiometric formula for $\text{ZrSi}_{0.7}\text{Sb}_{1.3}$ since the degree of disorder is defined by the structurally constrained anion-anion distances. In contrast, for ZrGeSb , the insertion of the larger Ge atoms into site $2a$ results in sufficient anion-anion bonding to satisfy the electronic demands of the structure, thus giving rise to the stoichiometric and ordered formula ZrGeSb . Examples exist in which the size of the anionic square net does not remain constant in related series of compounds. For instance, the compounds $\text{Zr}A\text{Te}$ ($A = \text{Si, Ge, Sn}$)^{2,5,6} show that as the size of the A atoms in the square net increases, the A - A bond distance increases significantly from 2.61 to 2.87 Å (Table 7-1). However, other systems such as $\text{U}AS$ ($A = \text{Si, Ge}$),³⁰ $\text{U}A\text{Te}$ ($A = \text{Sn, Sb}$),³⁰ $\text{Zr}AS$ ($A = \text{Si, Ge}$),⁵ $\text{Hf}AS$ ($A = \text{Si, Ge}$),⁵ and $\text{Hf}A\text{Se}$ ($A = \text{Si, Ge}$)⁵ do support the trend that the square nets of A atoms remain relatively unperturbed by the effects of substitution.

STRUCTURE OF $\text{ZrSn}_{0.4}\text{Sb}_{1.6}$

A view of the b axis of the structure of $\text{ZrSn}_{0.4}\text{Sb}_{1.6}$ is shown in Figure 7-3. As part of our substitutional study of MAB compounds, we attempted to synthesize “ ZrSnSb ” to see if it would adopt the ZrSiS -type structure as well. Instead, we obtained the compound $\text{ZrSn}_{0.4}\text{Sb}_{1.6}$, a disordered variant of β - ZrSb_2 which is of the PbCl_2 -type.

The structure of β -ZrSb₂ has been described in detail before.¹¹ In ZrSn_{0.4}Sb_{1.6}, the two anion sites $X(1)$ and $X(2)$ are disordered, containing a mixture of 20% Sn and 80% Sb. Bond distances and angles are generally similar to the parent compound, with some irregular variations. The structure of ZrSn_{0.4}Sb_{1.6} is related to the ZrSiS-type structures of ZrSi_{0.7}Sb_{1.3} and ZrGeSb in that they are based on Zr-centered monocapped square antiprisms. As shown in Figure 7-1a, these units are undistorted in ZrSi_{0.7}Sb_{1.3} and ZrGeSb since the Zr atom is equidistant to the basal square of A atoms as well as the larger square of Sb atoms. Furthermore, the capping Sb atom is situated directly above the Zr atom. In ZrSn_{0.4}Sb_{1.6}, the monocapped square antiprism is distorted (Figure 7-1b), displaying irregular squares and a tilted capping atom. For example, three symmetry-equivalent sites ($X(1)$), at distances of 2.9902(6) (2x) and 3.0808(9) Å, and another site ($X(2)$), at a distance of 3.2588(8) Å, define the basal square. Four $X(2)$ sites at distances of 3.0186(6) (2x) and 3.0342(6) (2x) Å (2x) form a larger square twisted 45° relative to the first square. A ninth site ($X(1)$) completes the unit by “capping” the larger square at a distance of 2.9389(8) Å. It is noteworthy that the capping atom is tilted in ZrSn_{0.4}Sb_{1.6} but is directly above the metal in ZrSi_{0.7}Sb_{1.3} and ZrGeSb. The capping atom in such units can often be found with varying tilt angles.³² If the “capping” atom is again designated as the “head”, then the structure of ZrSn_{0.4}Sb_{1.6} can be built up from these units, aligned in a head-to-tail fashion along the c axis.

The displacement of the capping atom in ZrSn_{0.4}Sb_{1.6} affects the manner in which the building units are connected and accounts for the differences between the two structures. When undistorted capped square antiprisms are connected together, parallel square nets are aligned in ZrSi_{0.7}Sb_{1.3} and ZrGeSb. Figure 7-4a illustrates the

connectivity about a plane of *A* atoms in $\text{ZrSi}_{0.7}\text{Sb}_{1.3}$ and ZrGeSb , showing the tail-to-tail orientation of the building units. The “head” of the building units points in either direction along the *c* axis. In contrast, the tilting of the capping atom in the square antiprisms in $\text{ZrSn}_{0.4}\text{Sb}_{1.6}$ reduces the symmetry to an orthorhombic structure. As shown in Figure 7–4b, the building units are connected in a head-to-tail fashion, and they no longer point along the *c* axis but in several directions. The structure no longer consists of parallel square nets, but rather staggered “ribbons” that are four atoms wide (Figure 7–3).

IMPLICATIONS

The discontinuity of structure type upon substitution of Sn may be rationalized by the size differences of the Group 14 atoms. Haneveld and Jellinek provided a useful index for predicting the occurrence of the PbFCI structure type in *MAB* compounds, based on the ratio of the radii of the metal *M* and the elements *A* and *B*.³⁰ As shown in Table 7–1, the *M–4B* distances are always larger than the *A–A* distances and in instances in which this is not true, the resulting compound either does not exist or adopts a different structure type. When the condition is met, the resulting compound adopts either the PbFCI/ ZrSiS structure type (in most cases) or the closely related tetragonal (*I4/mmm*) UGeTe structure type.³⁰ In the present case, if we accept that *most* regular Sn–Sn single bond distances in the solid state lie in the range 2.804–2.891 Å,^{33–35} with a few examples of slightly longer distances such as 2.984 Å,³⁶ then it is reasonable that $\text{ZrSn}_{0.4}\text{Sb}_{1.6}$ prefers not to crystallize in the space group *P4/nmm* since the Zr–4Sb distances for a hypothetical ZrSiS -type compound “ ZrSnSb ” are expected to be at least 2.96 Å. Thus, $\text{ZrSn}_{0.4}\text{Sb}_{1.6}$ appears to be at the limit for the formation of the *MAB* structure type. The

fact that similarities can be drawn between the two structure types (ZrSiS and $\beta\text{-ZrSb}_2$) is probably an indication that $\text{ZrSn}_{0.4}\text{Sb}_{1.6}$ lies at the border between the two types. It is interesting to note that if Sb is substituted by Te, which has a similar atomic radius, the *MAB* member ZrSnTe_2 exists with Zr–Te and Sn–Sn distances of 3.038(1) Å and 2.867(1) Å, respectively. We believe Haneveld and Jellinek's model accounts for most observations but is not applicable in all cases.

The preparation of this series of compounds illustrates the great versatility of the PbFCI or ZrSiS structure type. The physical properties of these compounds, which are expected to be metallic conductors,^{2,4,31,37} are being investigated. A band structure calculation will help clarify the factors involved in their stability. It would be interesting to see if ZrSiS -type “ TiSnSb ” or “ HfSnSb ” compounds can be made, if “ ZrSnSb ” has not. The transition metal and main group elements can also be substituted to probe the limits of this diverse structural class.

Table 7–1. Representative Ternary Compounds That Adopt the ZrSiS-Type (or PbFCl-Type) Structure

<i>MAB</i>	<i>c/a</i>	<i>M–4B</i> (Å)	<i>M–B</i> (Å)	<i>A–A</i> (Å)	Δ^a	Reference
UOTe	1.871	3.20	3.42	2.83	0	4
ZrAs _{1.15} Se _{0.575}	2.17	2.81(1)	2.886(5)	2.647(4)	0.6	8
LaTe ₂	2.025	3.293(7)	3.260(7)	3.187(4)	1	9
ZrSiSe	2.30	2.76	3.01	2.57	2	5
ZrSiTe	2.572 ^b	2.918(1)	3.957(1)	2.614(1)	2	5, 10
ZrGeTe	2.224	2.93(1)	3.26(4)	2.734(1)	2	6
ZrSnTe	2.148	3.038(1)	3.086(1)	2.868(1)	2	2
NbSiAs	2.263	2.681(1)	2.811(1)	2.468(1)	2	7
ZrSi _{0.7} Sb _{1.3}	2.266	2.9460(3)	3.1085(7)	2.6934(1)	2.7	this work
ZrGeSb	2.245	2.9595(9)	3.094(2)	2.7189(5)	3	this work

^a Δ is defined as the deficiency of electrons available to the anions *A* and *B* with respect to satisfying the 8–*n* rule.[†] For normal valence compounds, $\Delta = 0$. For ZrGeSb, a polyanionic compound, $\Delta = ((8-4) + (8-5)) - 4 = 3$.

^b High values of *c/a* (~ 2.6) correspond to layered compounds.^{1,2,5,6}

Table 7-2. Crystallographic Data for ZrSi_{0.7}Sb_{1.3}, ZrGeSb, and ZrSn_{0.4}Sb_{1.6}

Formula	ZrSi _{0.74(2)} Sb _{1.26(1)}	ZrGeSb	ZrSn _{0.4} Sb _{1.6}
Formula mass, amu	264.80	285.56	330.50
Space group	$D_{4h}^7 - P4/nmm$ (No. 129)	$D_{4h}^7 - P4/nmm$ (No. 129)	$D_{2h}^{16} - Pnma$ (No. 62)
<i>a</i> , Å	3.8091(2) ^a	3.8451(7) ^a	7.3187(6) ^b
<i>b</i> , Å	—	—	3.9618(4) ^b
<i>c</i> , Å	8.630(1) ^a	8.634(2) ^a	9.7076(7) ^b
<i>V</i> , Å ³	125.22(2)	127.66(4)	281.47(4)
<i>Z</i>	2	2	4
<i>T</i> , °C	-50	-50	-50
Diffractometer		Enraf-Nonius CAD4	
ρ_{calc} , g cm ⁻³	7.023	7.429	7.870
Crystal dimensions, mm	0.17 × 0.14 × 0.05	0.14 × 0.12 × 0.05	0.07 × 0.24 × 0.06
Radiation	Graphite-monochromated MoK α , $\lambda = 0.71073$ Å		
$\mu(\text{MoK}\alpha)$, cm ⁻¹	175.8	258.0	220.4
Transmission factors ^c	0.122–0.408	0.080–0.301	0.194–0.308
Scan type	θ – 2θ	θ – 2θ	θ – 2θ
Scan speed, deg. min ⁻¹	1.7–6.7	2.0–6.7	1.5–6.7
Scan range, deg.	$0.8 + 0.344 \tan \theta$	$0.8 + 0.344 \tan \theta$	$0.6 + 0.344 \tan \theta$
2θ limits	$4^\circ \leq 2\theta(\text{MoK}\alpha) \leq 70^\circ$	$4^\circ \leq 2\theta(\text{MoK}\alpha) \leq 70^\circ$	$6^\circ \leq 2\theta(\text{MoK}\alpha) \leq 70^\circ$
Data collected	$-6 \leq h \leq 6,$ $-6 \leq k \leq 6,$ $-13 \leq l \leq 13$	$-6 \leq h \leq 6,$ $-6 \leq k \leq 6,$ $-13 \leq l \leq 13$	$-11 \leq h \leq 10,$ $-6 \leq k \leq 6,$ $-13 \leq l \leq 15$

Table 7–2. Crystallographic Data for ZrSi_{0.7}Sb_{1.3}, ZrGeSb, and ZrSn_{0.4}Sb_{1.6} (continued)

No. of data collected	2138	2158	2484
No. of unique data, including $F_o^2 < 0$	203 ($R_{\text{int}} = 0.068$)	203 ($R_{\text{int}} = 0.269$)	690 ($R_{\text{int}} = 0.127$)
No. of unique data, with $F_o^2 > 2\sigma(F_o^2)$	202	197	663
No. of variables	12	10	20
Extinction coefficient ^d	0.122(6)	0.10(2)	0.038(3)
$R(F)$ for $F_o^2 > 2\sigma(F_o^2)$ ^e	0.015	0.062	0.048
$R_w(F_o^2)$ ^f	0.039	0.144	0.107
Goodness of fit ^g	1.38	1.25	1.16
$(\Delta\rho)_{\text{max}}, (\Delta\rho)_{\text{min}}, \text{e}^{-\text{\AA}^{-3}}$	1.0, -1.7	5.8, -11.3	4.4, -4.9

^a Obtained from a refinement constrained so that $a = b$ and $\alpha = \beta = \gamma = 90^\circ$.

^b Obtained from a refinement constrained so that $\alpha = \beta = \gamma = 90^\circ$.

^c A Gaussian-type absorption correction was applied, with the use of programs in the SHELXTL package (Sheldrick, G. M. SHELXTL Version 5.0, Siemens Analytical X-Ray Instruments, Inc., Madison, WI, 1994).

^d An extinction parameter x was refined, where F_c is multiplied by: $k[1 + 0.001 * x * F_c^2 * \lambda^3 / \sin(2\theta)]^{-1/4}$.

$$^e R(F) = \frac{\sum ||F_o| - |F_c||}{\sum |F_o|}$$

$$^f R_w(F_o^2) = \frac{[\sum [w(F_o^2 - F_c^2)^2]]^{1/2}}{[\sum wF_o^4]^{1/2}}; w^{-1} = [\sigma^2(F_o^2) + (AP)^2 + BP] \text{ where}$$

$P = [\max(F_o^2, 0) + 2F_c^2]/3$, $A = 0.0029, 0.0601, 0.0600$, and $B = 0.34, 2.36, 1.71$ for ZrSi_{0.7}Sb_{1.3}, ZrGeSb, and ZrSn_{0.4}Sb_{1.6}, respectively.

^g $GooF = S = \left[\sum [w(F_o^2 - F_c^2)^2] / (n - p) \right]^{1/2}$ where n is the number of reflections and p is the total number of parameters refined.

Table 7-3. Atomic Coordinates, Occupancies, and Equivalent Isotropic DisplacementParameters (\AA^2) for $\text{ZrSi}_{0.7}\text{Sb}_{1.3}$, ZrGeSb , and $\text{ZrSn}_{0.4}\text{Sb}_{1.6}$

Atom	Wyckoff position, site symmetry		x	y	z	Occupancy	U_{eq}^a
$\text{ZrSi}_{0.7}\text{Sb}_{1.3}$							
Zr	2c	4 $m m$	$\frac{1}{4}$	$\frac{1}{4}$	0.25076(6)	1	0.0054(2)
A^b	2a	$\bar{4} m 2$	$\frac{3}{4}$	$\frac{1}{4}$	0	1	0.0080(3)
Sb(2)	2c	4 $m m$	$\frac{1}{4}$	$\frac{1}{4}$	0.61095(4)	1	0.0056(2)
ZrGeSb							
Zr	2c	4 $m m$	$\frac{1}{4}$	$\frac{1}{4}$	0.2532(2)	1	0.0049(6)
Ge	2a	$\bar{4} m 2$	$\frac{3}{4}$	$\frac{1}{4}$	0	1	0.0052(5)
Sb	2c	4 $m m$	$\frac{1}{4}$	$\frac{1}{4}$	0.6115(1)	1	0.0051(5)
$\text{ZrSn}_{0.4}\text{Sb}_{1.6}$							
Zr	4c	. m .	0.26110(9)	$\frac{1}{4}$	0.16278(6)	1	0.0047(2)
$X(1)^c$	4c	. m .	0.86981(6)	$\frac{1}{4}$	0.04578(4)	1	0.0057(2)
$X(2)^c$	4c	. m .	0.92828(6)	$\frac{1}{4}$	0.64836(4)	1	0.0053(2)

^a U_{eq} is defined as one-third of the trace of the orthogonalized U_{ij} tensor.^b A contains 74(2)% Si and 26(1)% Sb(1).^c Each site is occupied by 20% Sn and 80% Sb.

Table 7-4. Selected Interatomic Distances (Å) and Angles (°) in ZrSi_{0.74}Sb_{1.3} and ZrGeSb

	ZrSi _{0.74(2)} Sb _{1.26(1)}	ZrGeSb
Zr-Sb(2)	2.9460(3) (x4)	2.9595(9) (x4)
Zr-Sb(2)	3.1085(7)	3.094(2)
Zr-A	2.8829(4) (x4)	2.911(1) (x4)
A-A	2.6934(1) (x4)	2.7189(5) (x4)
Sb(2)-Sb(2)	3.3049(4) (x4)	3.331(1) (x4)
<i>A-Zr-A</i>	55.699(9)	55.68(3)
<i>A-Zr-A</i>	82.70(2)	82.66(4)
<i>A-Zr-Sb(2)</i>	136.99(1)	136.52(3)
<i>A-Zr-Sb(2)</i>	82.936(8)	82.39(2)
<i>Sb(2)-Zr-Sb(2)</i>	80.554(8)	81.03(2)
<i>Sb(2)-Zr-Sb(2)</i>	132.20(2)	133.48(7)
<i>Sb(2)-Zr-A</i>	138.651(7)	138.67(2)
<i>Sb(2)-Zr-Sb(2)</i>	66.10(1)	66.74(3)
<i>Zr-Sb(2)-Zr</i>	132.20(2)	133.48(7)
<i>Zr-Sb(2)-Zr</i>	80.554(8)	81.03(2)
<i>Zr-Sb(2)-Zr</i>	113.90(1)	113.26(3)
<i>A-A-Zr</i>	117.849(4)	117.84(1)
<i>A-A-Zr</i>	62.151(4)	62.16(1)
<i>Zr-A-Zr</i>	124.301(9)	124.32(3)
<i>Zr-A-Zr</i>	82.70(2)	82.66(4)

Table 7-5. Selected Interatomic Distances (Å) and Angles (°) in $\text{ZrSn}_{0.4}\text{Sb}_{1.6}$

Zr-X(1)	2.9389(8)	X(1)-X(1)	2.8888(7) (2x)
Zr-X(1)	2.9902(6) (2x)	X(1)-X(2)	3.1105(5) (2x)
Zr-X(2)	3.0186(6) (2x)		
Zr-X(2)	3.0342(6) (2x)		
Zr-X(1)	3.0808(9)		
Zr-X(2)	3.2588(8)		
X(1)-Zr-X(1)	137.61(1)	X(1)-X(1)-X(1)	86.58(3)
X(1)-Zr-X(1)	82.98(2)	X(1)-X(1)-X(2)	176.25(2)
X(1)-Zr-X(2)	80.84(2)	X(1)-X(1)-X(2)	97.15(1)
X(1)-Zr-X(2)	130.14(3)	X(2)-X(1)-X(2)	79.11(2)
X(1)-Zr-X(2)	77.01(1)	X(1)-X(2)-X(1)	79.11(2)
X(2)-Zr-X(2)	82.03(2)		
X(1)-Zr-X(2)	62.74(2)		
X(1)-Zr-X(2)	134.05(3)		
X(1)-Zr-X(2)	80.23(1)		
X(2)-Zr-X(2)	86.77(1)		
X(2)-Zr-X(2)	143.18(2)		

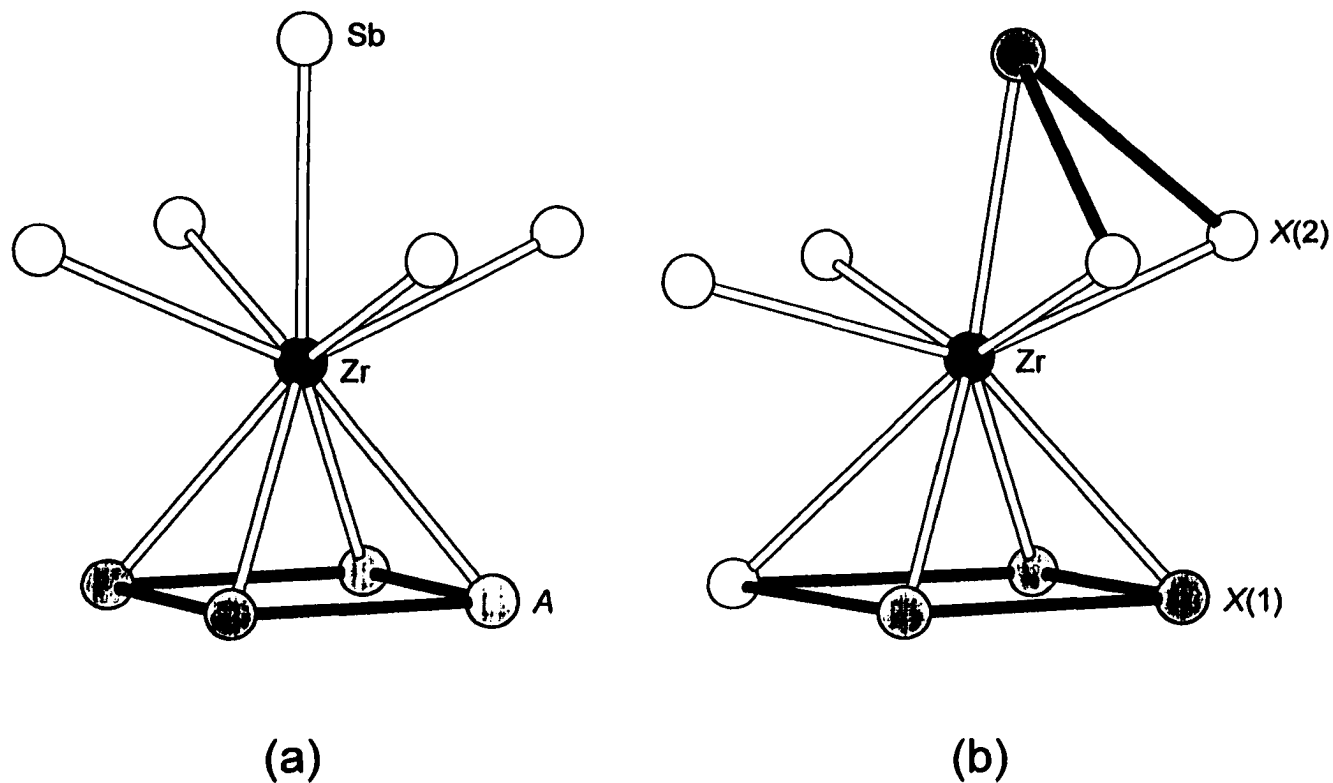


Figure 7-1. Coordination of Zr atoms in (a) $\text{ZrSi}_{0.7}\text{Sb}_{1.3}$ and ZrGeSb and (b) $\text{ZrSn}_{0.4}\text{Sb}_{1.6}$, showing the monocapped square antiprismatic geometry. The darkened bonds represent planes of bonding atoms within the structures. Site *A* contains 74(2)% Si and 26(1)% Sb(1) in $\text{ZrSi}_{0.7}\text{Sb}_{1.3}$ and 100% Ge atoms in ZrGeSb . Sites *X*(1) and *X*(2) are occupied by 20% Sn and 80% Sb in $\text{ZrSn}_{0.4}\text{Sb}_{1.6}$.

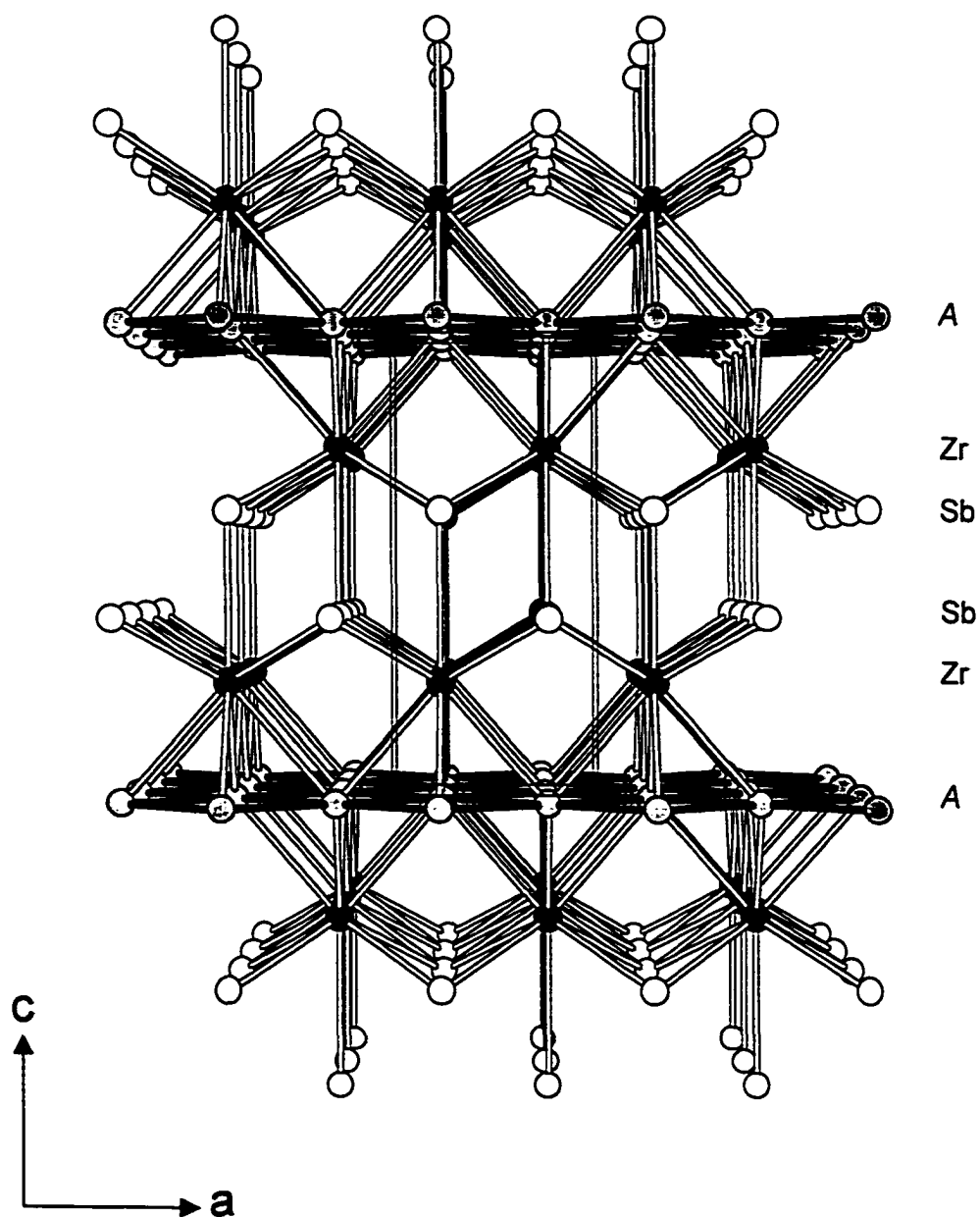


Figure 7-2. ZrSiS-type structure of $\text{ZrSi}_{0.7}\text{Sb}_{1.3}$ and ZrGeSb , as viewed down the b axis, with the unit cell outlined. Note the stacking order of the different layers of atoms. Site A is disordered for $\text{ZrSi}_{0.7}\text{Sb}_{1.3}$, containing a mixture of 74(2)% Si and 26(1)% Sb(1), and ordered for ZrGeSb , containing only Ge atoms.

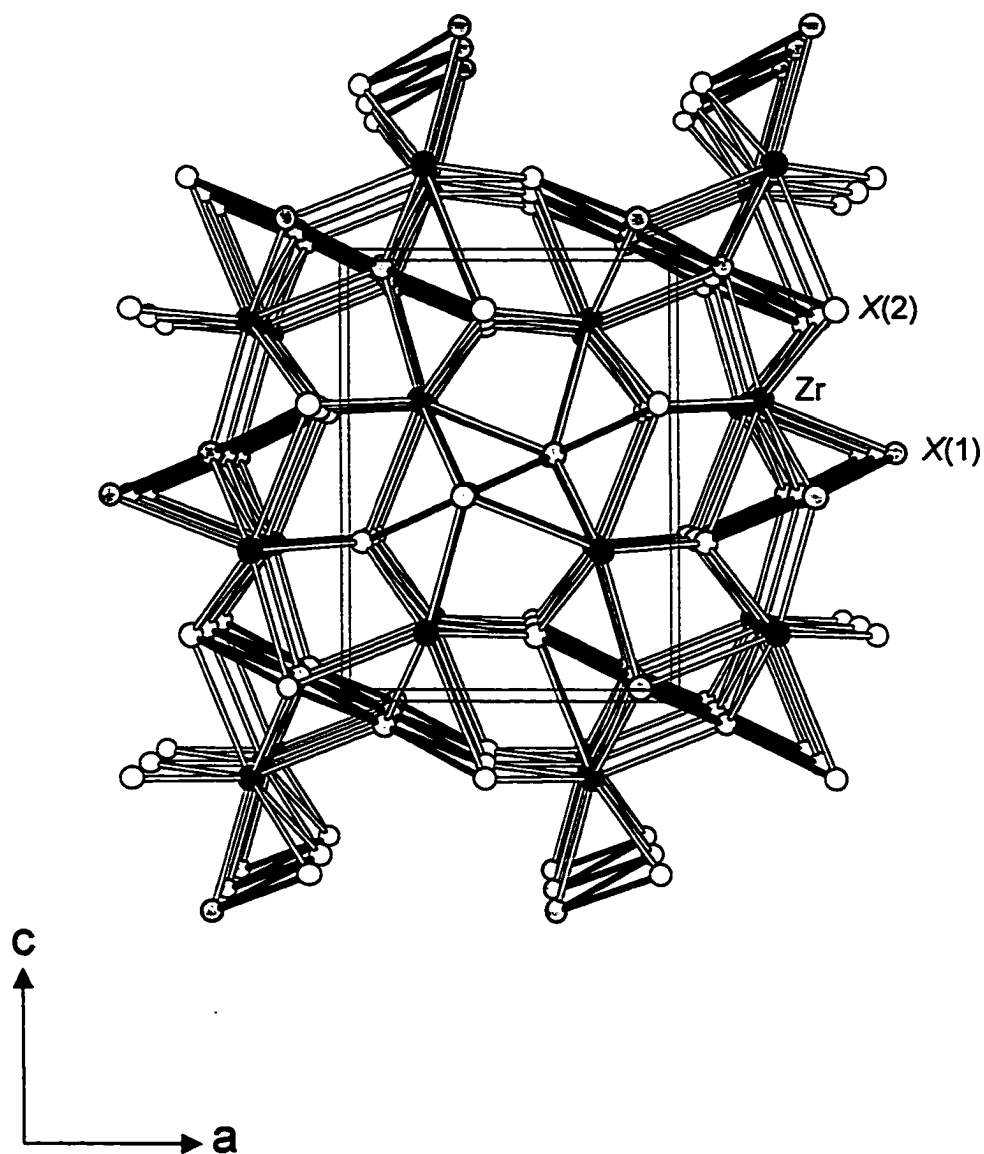


Figure 7-3. View down the b axis of $\text{ZrSn}_{0.4}\text{Sb}_{1.6}$ with the unit cell outlined. The solid circles are Zr atoms, while the two disordered sites are represented by the open ($X(2)$) and lightly shaded ($X(1)$) circles, each occupied by 20% Sn and 80% Sb.

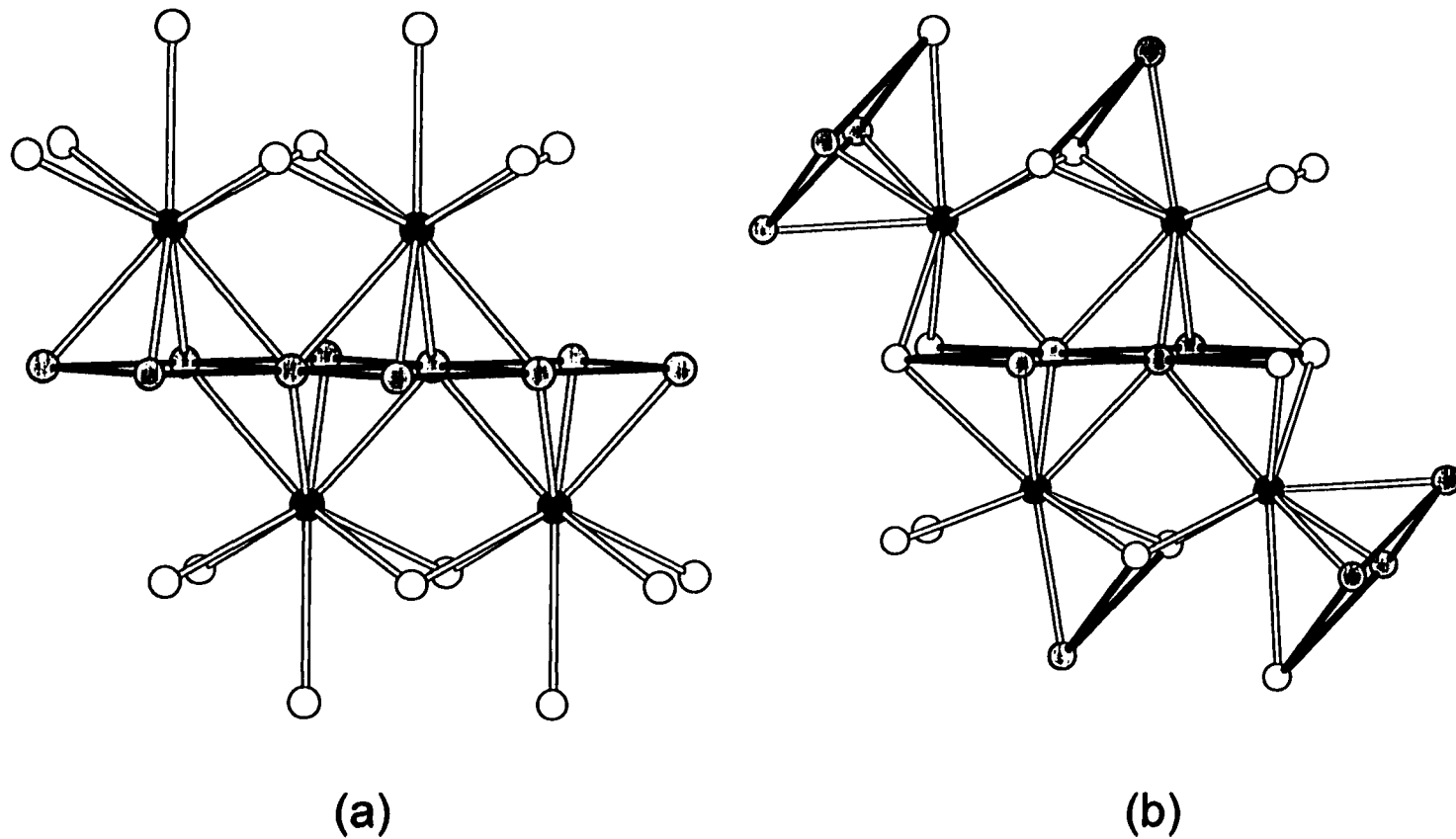


Figure 7-4. Connectivity of monocapped square antiprismatic building blocks in (a) $\text{ZrSi}_{0.7}\text{Sb}_{1.3}$ and ZrGeSb and (b) $\text{ZrSn}_{0.4}\text{Sb}_{1.6}$. Note the tail-to-tail (and head-to-head) orientation of the building units in the Si and Ge compounds in contrast to the head-to-tail orientation in the Sn compound.

REFERENCES

- (1) Tremel, W.; Hoffmann, R. *J. Am. Chem. Soc.* **1987**, *109*, 124.
- (2) Wang, C.; Hughbanks, T. *Inorg. Chem.* **1995**, *34*, 5524.
- (3) Müller, U. *Inorganic Structural Chemistry*, Wiley: New York, 1993.
- (4) Hulliger, F. *J. Less-Common Met.* **1968**, *16*, 113.
- (5) Onken, H.; Vierheilig, K.; Hahn, H. *Z. Anorg. Allg. Chem.* **1964**, *333*, 267.
- (6) Haneveld, A. J. K.; Jellinek, F. *Recl. Trav. Chim. Pays-Bas* **1964**, *83*, 776.
- (7) Johnson, V.; Jeitschko, W. *J. Solid State Chem.* **1973**, *6*, 306.
- (8) Barthelat, J. C.; Jeannin, Y. *J. Less-Common Met.* **1972**, *26*, 273.
- (9) Wang, R.; Steinfink, H.; Bradley, W. F. *Inorg. Chem.* **1966**, *5*, 142.
- (10) Bensch, W.; Dürichen, P. *Acta Crystallogr., Sect. C: Cryst. Struct. Commun.* **1994**, *50*, 346.
- (11) Garcia, E.; Corbett, J. D. *J. Solid State Chem.* **1988**, *73*, 452.
- (12) Bolloré, G.; Ferguson, M.; Hushagen, R.; Mar, A. *Chem. Mater.* **1995**, *7*, 2229.
- (13) Náráy-Szabó, S. *Z. Kristallogr.* **1937**, *97*, 223.
- (14) Schachner, H.; Nowotny, H.; Kudielka, H. *Monatsh. Chem.* **1954**, *85*, 1140.
- (15) Smith, J. F.; Bailey, D. M. *Acta Crystallogr.* **1957**, *10*, 341.
- (16) POLSQ: Program for least-squares unit cell refinement. Modified by D. Cahen and D. Keszler, Northwestern University, 1983.
- (17) Yvon, K.; Jeitschko, W.; Parthé, E. *J. Appl. Crystallogr.* **1977**, *10*, 73.
- (18) Sheldrick, G. M. SHELXTL Version 5.0, Siemens Analytical X-ray Instruments, Inc., Madison, WI, 1994.
- (19) Sheldrick, G. M. *J. Appl. Crystallogr.*, in press.

- (20) *International Tables for X-ray Crystallography*; Wilson, A. J. C., Ed.; Kluwer: Dordrecht, The Netherlands, 1992; Vol. C.
- (21) Lam, R.; Mar, A. *Inorg. Chem.* 1996, 35, 6959.
- (22) Jellinek, F.; Hahn, H. *Naturwissenschaften* 1962, 49, 103.
- (23) Eisenmann, B.; Schäfer, H. *Angew. Chem. Int. Ed. Engl.* 1980, 19, 490.
- (24) Eisenmann, B.; Schäfer, H. *Z. Anorg. Allg. Chem.* 1982, 484, 142.
- (25) Hamon, P. M.; Guyader, J.; L'Haridon, P.; Laurent, Y. *Acta Crystallogr., Sect. B: Struct. Crystallogr. Cryst. Chem.* 1975, 31, 445.
- (26) Hurng, W.-M.; Corbett, J. D.; Wang, S.-L.; Jacobson, R. A. *Inorg. Chem.* 1987, 26, 2392.
- (27) Eisenmann, B.; Jordan, H.; Schäfer, H. *Z. Naturforsch., B: Anorg. Chem., Org. Chem.* 1984, 39, 864.
- (28) Eisenmann, B.; Jordan, H.; Schäfer, H. *Z. Naturforsch., B: Anorg. Chem., Org. Chem.* 1982, 37, 1221.
- (29) Eisenmann, B.; Schäfer, H. *Z. Naturforsch., B: Anorg. Chem., Org. Chem.* 1981, 36, 415.
- (30) Haneveld, A. J. K.; Jellinek, F. *J. Less-Common Met.* 1969, 18, 123.
- (31) Hulliger, F. *J. Less-Common Met.* 1973, 30, 397.
- (32) Ferguson, M. J.; Hushagen, R. W.; Mar, A. *Inorg. Chem.* 1996, 35, 4505.
- (33) Eisenmann, B.; Jordan, H.; Schäfer, H. *Z. Anorg. Allg. Chem.* 1986, 532, 73.
- (34) Eisenmann, B.; Jordan, H.; Schäfer, H. *Z. Naturforsch., B: Anorg. Chem., Org. Chem.* 1983, 38, 404.
- (35) Klein, J.; Eisenmann, B. *Mater. Res. Bull.* 1988, 23, 587.

- (36) Eisenmann, B.; Jordan, H.; Schäfer, H. *Z. Naturforsch., B: Anorg. Chem., Org. Chem.* **1984**, *39*, 1151.
- (37) Wojakowski, A. *J. Less-Common Met.* **1985**, *107*, 155.

CHAPTER 8

Conclusion

STRUCTURAL DIVERSITY

A series of new compounds containing a combination of electropositive ($M = \text{Ba}$, RE , Zr , Hf) and electronegative elements ($A = \text{Si}$, Ge , Sn ; $B = \text{As}$, Sb) have been synthesized and structurally characterized (Table 8–1), and their resistivity determined. Exploration of these polar intermetallic compounds provides a unique opportunity for studying bonding between main-group atoms (A – A , A – B , and B – B) as well as examining the extent to which they adhere to the Zintl concept. Furthermore, the use of less electropositive cations from the rare-earth series and the group 4 transition metals has led to the discovery of new compounds which serve to test the validity of the Zintl concept.

As shown in Table 8–1, the heavy pnictogens As and Sb have the propensity to form homoatomic (A – A , B – B) and heteroatomic bonds (A – B) when in combination with electropositive elements. The condensation of these heavy elements with the group 14 atoms in the present study has resulted in the formation of elaborate as well as lower-dimensional polyanionic networks. We observe a diverse collection of structural features, including isolated atoms, zigzag chains, ribbons of various widths, and two-dimensional square and corrugated nets. The occurrence of large channels (spanning 30

atoms) of different shapes in EuSn_3Sb_4 and $\text{Ba}_2\text{Sn}_3\text{Sb}_6$, as well as the intricate network of walls in $\text{RE}_6\text{Ge}_{5-x}\text{Sb}_{11+x}$ ($\text{RE} = \text{La-Nd, Sm, Gd-Dy}$), represent the versatility of the main-group atoms to form bonds with each other when provided with enough electrons by the cationic matrices.

The types of frameworks that are constructed occupy the whole spectrum of dimensionality. For instance, the compounds $\text{Ba}_{0.8}\text{Hf}_{12}\text{As}_{17.7}$, ZrGeSb , and $\text{ZrSn}_{0.4}\text{Sb}_{1.6}$ display one-dimensional networks of ribbons and atoms. Two-dimensional nets are observed in $\text{Ba}_3\text{Sn}_4\text{As}_6$ and $\text{ZrSi}_{0.7}\text{Sb}_{1.3}$, while three-dimensional channels and interconnecting walls are found in $\text{Ba}_2\text{Sn}_3\text{Sb}_6$, EuSn_3Sb_4 , and $\text{RE}_6\text{Ge}_{5-x}\text{Sb}_{11+x}$ ($\text{RE} = \text{La-Nd, Sm, Gd-Dy}$).

The remarkable versatility of As and Sb in forming polyanionic networks is attributed to their ability to form classical as well as nonclassical structural geometries. The present investigation supports Papoian and Hoffmann's conclusion¹ that hypervalent bonding becomes more prevalent as one goes down a group in the p -block. This is attributed to reduced s - p mixing of the valence orbitals in the heavier atoms, giving rise to unique atomic arrangements such as undistorted metallic networks. Table 8-1 also shows the kinds of geometries adopted by As and Sb in the current group of compounds. We see that, in the structures of arsenides and antimonides, classical geometries (nonbonded isolated atoms, bent, and trigonal pyramidal) occur as frequently as nonclassical types (square planar and square pyramidal). This is consistent with the vast number of other arsenide and antimonide structure types.

LIMITS OF ZINTL CONCEPT

Traditionally, the Zintl concept² has provided a deceptively simple and convenient approach for understanding and rationalizing the structure and bonding of a multitude of solid state compounds that consist of a combination of electropositive and electronegative elements. Effectively, it accounts for the tendency for electronegative main-group atoms to form localized covalent bonding when provided with electrons from electropositive cations. The existence of a vast number of structurally and compositionally diverse phases¹⁻⁹ that adhere to this set of valence rules is evidence of the usefulness of the scheme. However, there are limitations to the Zintl concept. Exceptions exist of compounds having seemingly Zintl-like compositions but which do not follow the octet rule. An example is provided by the compound $\text{Ba}_7\text{Ga}_4\text{Sb}_9$ ^{10,11} which appears that it should be a Zintl compound but in actuality, the concept fails to account for its structure. Theory points to the possibility of a pairing distortion in a part of the structure which effectively opens up a gap at the Fermi level, and induces a metal-to-insulator transition. Experimental results are being sought to confirm the suggestion of a change of bonding type in the compound.

In spite of the success that the Zintl concept has in establishing a correlation between the electronic and geometric structures of a large class of polar intermetallics, it tends to be overly simplistic. Although it serves well as a post-hoc method for rationalizing the bonding in numerous structures or as a “litmus test”¹² for evaluating the soundness of a crystal structure determination, the Zintl concept still lacks predictive value. This is partially due to the neglected consideration of the cations, which are often ignored since they merely act as spacers or fillers in Zintl structures. Furthermore, the

extent of charge transfer from cations to anions is often overestimated, which is not an unreasonable claim given the polarizing abilities of small, highly charged cations. Owing to these effects, the Zintl concept is limited in its ability to be used as a tool to predict global structures. For example, one can make an accurate prediction as to the types of bonds Si will form locally in the structures of the series $AESi_2$ ($AE = Ca, Sr, Ba$).² but their crystal structures, showing the arrangement of all polyanionic units, can only be determined by a structure determination. In fact, the structures of the three binary compounds differ from each other. Thus, the importance of cation-anion interactions, which have structure-determining effects in crystal structures, cannot be overlooked.

Table 8–1 shows that the structures of the compounds $Ba_3Sn_4As_6$, $Ba_2Sn_3Sb_6$, and $EuSn_3Sb_4$ can be rationalized by the Zintl set of rules. This confirms our original suspicion that these should form Zintl phases given the electronegativity difference between Ba (or Eu) and the other main-group atoms. $EuSn_3Sb_4$, which has the $SrSn_3Sb_4$ structure type, contains the same channels as observed in the related compound $Ba_2Sn_3Sb_6$. However, the size difference between Ba and Eu atoms has the effect of forming wide or narrow versions of the channels, respectively, in their respective structures. As less electropositive cations are used, such as those from the rare-earth series or group 4 transition metals, we see that the remaining compounds in Table 8–1 fail to follow the Zintl convention, even though examples exist of Zintl phases containing these cations.

The expectation that Zintl compounds are semiconducting is not realized with the present group of compounds, as $Ba_3Sn_4As_6$, $Ba_2Sn_3Sb_6$, and $EuSn_3Sb_4$ all show metallic behaviour. The phenomena in the latter two have been determined to be a result of

additional bonding interactions that arise from the joining of the channels, leading to band broadening and the disappearance of the band gaps in the two compounds.

FUTURE DIRECTIONS

It has been shown that the anionic substructures of Zintl-type compounds are highly sensitive to the types of cations used. Thus, it is natural to extend the current restriction to ternary systems to include more complicated quaternary combinations. Of interest will be the effect of reacting two vastly different cations with two main-group elements from the *p*-block. Their structures are expected to be highly complex, and will serve to further test the applicability of the Zintl concept. Owing to the greater number of components, these systems are expected to provide fertile ground for the discovery of novel compounds. A preliminary search of the system (alkali metal / rare-earth metal / group 14 / group 15), for example, revealed that there are currently no known compounds. Incorporation of a rare-earth component will make these systems ideal for electronic and magnetic property studies.

The systems (Ti, Zr, Hf / Si, Ge, Sn / P, As, Sb, Bi), which yielded the ZrSiS-type compounds $\text{ZrSi}_{0.7}\text{Sb}_{1.3}$ and ZrGeSb as well as the compound $\text{ZrSn}_{0.4}\text{Sb}_{1.6}$, deserve greater attention owing to the potential for these systems to be structurally rich. Resistivity measurements of the series can give interesting results considering that the compounds $\text{ZrSi}_{0.7}\text{Sb}_{1.3}$ and ZrGeSb contain one of the lowest valence electron counts in the large class of ZrSiS-type and PbFCI-type structures.

It will be worthwhile to measure the magnetic susceptibilities of the rare-earth series $RE_6Ge_{5-x}Sb_{11+x}$ ($RE = La-Nd, Sm, Gd-Dy$) and then complement those studies with neutron diffraction experiments. The extensive substitution range of these materials, whose structures contain stackings of trigonal prisms of rare-earth atoms, provide a curious system for studying magnetic interactions. The results from resistivity measurements already hint at potentially intriguing behaviour of these compounds in a magnetic field, showing transitions in the resistivity vs. temperature plots.

Table 8-1. Summary of Structural Features of Selected Arsenides and Antimonides

Compound	Anionic Network Features	Geometry of As/Sb ^a	Zintl Concept	Property
Ba ₃ Sn ₄ As ₆	2D corrugated nets	3b-trig. pyr.	Zintl compound ^b	metallic
Ba _{0.8} Hf ₁₂ As _{17.7}	isolated atoms, six-atom wide ribbons	0b-atom, 2b-bent, <u>4b-sq. planar</u>	fail	metallic
Ba ₂ Sn ₃ Sb ₆	zigzag chains, large open channels	2b-bent, 3b-trig. pyr.	(Ba ²⁺) ₂ [(Sn ¹⁻) ₂ (Sn ⁰)(Sb ⁰) ₄ (Sb ¹⁻) ₂] ⁴⁻	metallic
EuSn ₃ Sb ₄	large narrow channels	3b-trig. pyr.	(Eu ²⁺) [(Sn ¹⁻) ₂ (Sn ⁰)(Sb ⁰) ₄] ²⁻	metallic
RE ₆ Ge _{5-x} Sb _{11+x} (RE = La-Nd, Sm, Gd-Dy)	interconnecting walls, isolated atoms	0b-atom, 2b-bent, <u>3b-planar</u> , <u>4b-sq. planar</u> , <u>5b-sq. pyr.</u>	fail	metallic
ZrSi _{0.7} Sb _{1.3}	isolated atoms, 2D square nets	0b-atom, <u>4b-sq. planar</u>	fail	n/a
ZrGeSb	isolated atoms	0b-atom	fail	n/a
ZrSn _{0.4} Sb _{1.6}	four-atom wide ribbons	2b-bent, <u>4b-sq. planar</u>	fail	n/a

^a "Nonclassical" geometries are underlined.

^b Chemical formulation for Ba₃Sn₄As₆: [(Ba²⁺)_{0.15}(Ba²⁺)_{0.85}(Ba²⁺)₂][(Sn¹⁻)_{0.85}(Sn¹⁻)_{0.15}(Sn⁰)₄(As^{0.15-})(As^{0.85-})(As¹⁻)₄]⁶⁻

REFERENCES

- (1) Papoian, G. A.; Hoffmann, R. *Angew. Chem. Int. Ed.* **2000**, *39*, 2408.
- (2) Kauzlarich, S. M., Ed. *Chemistry, Structure, and Bonding of Zintl Phases and Ions*; VCH Publishers: New York, 1996.
- (3) Schäfer, H. *Annu. Rev. Mater. Sci.* **1985**, *15*, 1.
- (4) Corbett, J. D. *Chem. Rev.* **1985**, *85*, 383.
- (5) von Schnering, H. G. *Angew. Chem., Int. Ed. Engl.* **1981**, *20*, 33.
- (6) Kauzlarich, S. M. *Comments Inorg. Chem.* **1990**, *10*, 75.
- (7) Schäfer, H.; Eisenmann, B.; Müller, W. *Angew. Chem., Int. Ed. Engl.* **1973**, *12*, 694.
- (8) Nesper, R. *Angew. Chem., Int. Ed. Engl.* **1991**, *30*, 789.
- (9) Schäfer, H.; Eisenmann, B. *Rev. Inorg. Chem.* **1981**, *3*, 29.
- (10) Alemany, P.; Alvarez, S.; Hoffmann, R. *Inorg. Chem.* **1990**, *29*, 3070.
- (11) Cordier, G.; Schäfer, H.; Stelter, M. *Z. Anorg. Allg. Chem.* **1986**, *534*, 137.
- (12) Zhao, J.-T.; Corbett, J. D. *Inorg. Chem.* **1995**, *34*, 378.

APPENDIX

Table A-1. Powder X-Ray Diffraction Data for Ba₂Sn₃Sb₆ ^a

<i>hkl</i>	<i>d</i> _{obs} (Å)	<i>d</i> _{calc} (Å)	<i>I</i> / <i>I</i> ₀ ^b	<i>hkl</i>	<i>d</i> _{obs} (Å)	<i>d</i> _{calc} (Å)	<i>I</i> / <i>I</i> ₀ ^b
0 1 3	3.887	3.889	10	3 1 6	2.490	2.489	17
1 1 3	3.733	3.735	32	0 0 10	2.450	2.451	11
1 0 7	3.386	3.387	46	0 2 0	2.212	2.211	82
2 1 3	3.357	3.362	10	5 0 7	2.126	2.126	10
4 0 0	3.343	3.344	14	0 0 12	} 2.043	2.043	12
4 0 1	3.312	3.313	41	2 1 10		2.041	32
3 0 5	3.299	3.298	54	6 1 2	1.967	1.965	36
1 1 5	3.191	3.189	84	2 1 11	1.908	1.907	13
2 1 4	3.159	3.160	32	1 2 7	1.850	1.852	16
3 1 2	3.041	3.041	62	4 2 1	} 1.839	1.839	15
2 1 5	2.947	2.948	53	3 2 5		1.837	20
4 0 4	} 2.932	2.935	11	7 1 2	1.738	1.736	10
3 1 3		2.931	82	4 2 5	1.727	1.726	20
3 1 4	2.795	2.794	47	5 2 2	1.688	1.688	11
4 0 5	2.763	2.762	39	7 1 5	1.652	1.651	11

Table A-1. Powder X-Ray Diffraction Data for Ba₂Sn₃Sb₆^a (continued)

0 1 7	} 2.739	2.745	19	3 1 13	1.617	1.616	15
2 1 6		2.738	100	6 1 10	1.547	1.545	10
1 0 9	} 2.668	2.669	12	3 0 15	1.535	1.534	10
4 1 0		2.667	12	2 3 6	1.358	1.358	13
5 0 2	2.612	2.613	20	3 2 15	1.261	1.261	12
5 0 3	} 2.541	2.542	10				
2 1 7		2.540	12				

^a The cell parameters refined from the powder pattern, obtained on a Guinier camera at room temperature, are $a = 13.374(3)$ Å, $b = 4.423(1)$ Å, $c = 24.510(5)$ Å, $V = 1449.7(4)$ Å³.

^b The intensities were calculated from the crystal structure of Ba₂Sn₃Sb₆ with the use of the program LAZY-PULVERIX (Yvon, K.; Jeitschko, W.; Parthé, E. *J. Appl. Crystallogr.* 1977, 10, 73-74).

Table A-2. Anisotropic Displacement Parameters ^a (Å²) for Ba₂Sn₃Sb₆

Atom	U_{11}	U_{22}	U_{33}	U_{12}	U_{13}	U_{23}
Ba(1)	0.012(1)	0.007(1)	0.012(1)	0	0.0014(8)	0
Ba(2)	0.013(1)	0.005(1)	0.016(1)	0	0.0000(8)	0
Sn(1)	0.012(1)	0.008(1)	0.011(1)	0	0.0021(9)	0
Sn(2)	0.011(1)	0.008(1)	0.014(1)	0	0.000(1)	0
Sn(3)	0.013(1)	0.010(1)	0.018(1)	0	0.000(1)	0
Sb(1)	0.011(1)	0.007(1)	0.019(1)	0	-0.001(1)	0
Sb(2)	0.015(1)	0.009(1)	0.015(1)	0	0.004(1)	0
Sb(3)	0.016(1)	0.010(1)	0.010(1)	0	-0.002(1)	0
Sb(4)	0.013(1)	0.008(1)	0.014(1)	0	-0.001(1)	0
Sb(5)	0.015(1)	0.009(1)	0.013(1)	0	-0.001(1)	0
Sb(6)	0.012(1)	0.008(1)	0.015(1)	0	-0.000(1)	0

^a The form of the anisotropic displacement parameter is: $\exp[-2\pi^2(h^2a^{*2}U_{11} + k^2b^{*2}U_{22} + l^2c^{*2}U_{33} + 2hka^*b^*U_{12} + 2hla^*c^*U_{13} + 2klb^*c^*U_{23})]$.

Table A-3. Anisotropic Displacement Parameters ^a (Å²) for EuSn₃Sb₄

Atom	U_{11}	U_{22}	U_{33}	U_{12}	U_{13}	U_{23}
Eu	0.0153(4)	0.0133(4)	0.0193(3)	0	0.0005(3)	0
Sn(1)	0.0170(5)	0.0168(5)	0.0237(4)	0	-0.0013(4)	0
Sn(2)	0.0229(5)	0.0211(5)	0.0256(5)	0	-0.0012(4)	0
Sn(3)	0.0148(5)	0.0132(5)	0.0227(4)	0	-0.0007(3)	0
Sb(1)	0.0195(5)	0.0132(5)	0.0186(4)	0	0.0015(3)	0
Sb(2)	0.0131(4)	0.0158(5)	0.0258(5)	0	0.0004(3)	0
Sb(3)	0.0144(5)	0.0141(5)	0.0254(5)	0	-0.0013(3)	0
Sb(4)	0.0197(5)	0.0137(4)	0.0248(4)	0	0.0061(4)	0

^a The form of the anisotropic displacement parameter is: $\exp[-2\pi^2(h^2a^{*2}U_{11} + k^2b^{*2}U_{22} + l^2c^{*2}U_{33} + 2hka^*b^*U_{12} + 2hla^*c^*U_{13} + 2klb^*c^*U_{23})]$.

Table A-4. Anisotropic Displacement Parameters ^a (Å²) for Ba₃Sn₄As₆

Atom	U_{11}	U_{22}	U_{33}	U_{12}	U_{13}	U_{23}
Ba(1)	0.0093(4)	0.0128(4)	0.0142(4)	0.0017(3)	-0.0007(5)	-0.0006(5)
Ba(2)	0.0093(4)	0.0128(4)	0.0142(4)	0.0017(3)	-0.0007(5)	-0.0006(5)
Ba(3)	0.0115(4)	0.0143(4)	0.0218(4)	0.0021(3)	-0.0007(6)	-0.0007(5)
Ba(4)	0.0105(4)	0.0171(4)	0.0263(5)	0.0035(3)	-0.0046(7)	-0.0016(6)
Sn(1)	0.0082(4)	0.0121(4)	0.0114(4)	-0.0014(3)	0.0001(6)	0.0005(5)
Sn(2)	0.0082(4)	0.0121(4)	0.0114(4)	-0.0014(3)	0.0001(6)	0.0005(5)
Sn(3)	0.0101(4)	0.0116(4)	0.0128(4)	0.0005(3)	-0.0011(6)	-0.0002(5)
Sn(4)	0.0128(5)	0.0115(4)	0.0146(4)	-0.0002(3)	0.0001(6)	0.0001(5)
Sn(5)	0.0088(4)	0.0081(4)	0.0135(4)	0.0010(3)	-0.0005(6)	0.0000(5)
Sn(6)	0.0088(4)	0.0081(4)	0.0135(4)	0.0010(3)	-0.0005(6)	0.0000(5)
As(1)	0.0090(5)	0.0140(6)	0.0149(6)	0.0010(5)	0.0001(10)	0.0010(7)
As(2)	0.0087(6)	0.0255(7)	0.0146(6)	-0.0054(6)	-0.0012(10)	0.0016(8)
As(3)	0.0116(6)	0.0142(6)	0.0131(6)	-0.0003(5)	-0.0013(11)	-0.0007(9)
As(4)	0.0111(6)	0.0127(6)	0.0152(6)	0.0002(5)	-0.0022(11)	0.0023(9)
As(5)	0.0131(6)	0.0114(6)	0.0155(6)	0.0000(5)	-0.0016(12)	0.0002(10)
As(6)	0.0135(6)	0.0110(6)	0.0178(7)	-0.0009(5)	-0.0008(12)	-0.0017(10)

^a The form of the anisotropic displacement parameter is: $\exp[-2\pi^2(h^2a^{*2}U_{11} + k^2b^{*2}U_{22} + l^2c^{*2}U_{33} + 2hka^*b^*U_{12} + 2hla^*c^*U_{13} + 2klb^*c^*U_{23})]$.

Table A-5. Crystallographic Data for Ba₃Sn₄As₆ (subcell)

Formula	Ba ₃ Sn ₄ As ₆ (subcell)
Formula mass, amu	1336.30
Space group	$D_{2h}^{16} - Pnma$ (No. 62)
a , Å	9.7192(11) ^a
b , Å	4.3177(5) ^a
c , Å	18.3541(15) ^a
V , Å ³	770.22(14)
Z	2
T , °C	22
Diffractometer	Enraf-Nonius CAD4
ρ_{calc} , g cm ⁻³	5.760
Crystal dimensions, mm	Dark grey needle, 0.45 × 0.11 × 0.06 mm
Radiation	Graphite monochromated MoK α , $\lambda = 0.71073$ Å
$\mu(\text{MoK}\alpha)$, cm ⁻¹	266.6
Transmission factors ^b	0.158–0.300
Scan type	θ – 2θ
Scan speed, deg. min ⁻¹	1.7
Scan range, deg.	$0.5 + 0.344 \tan \theta$
2θ limits	$4^\circ \leq 2\theta(\text{MoK}\alpha) \leq 70^\circ$
Data collected	$-15 \leq h \leq 15, -6 \leq k \leq 6, -29 \leq l \leq 29$
No. of data collected	11023
No. of unique data, including $F_o^2 < 0$	1826 ($R_{\text{int}} = 0.0987$)

Table A-5. Crystallographic Data for Ba₃Sn₄As₆ (subcell) (continued)

No. of unique data, with $F_o^2 > 2\sigma(F_o^2)$	1540
No. of variables	50
Extinction coefficient ^c	0.0023(2)
$R(F)$ for $F_o^2 > 2\sigma(F_o^2)$ ^d	0.034
$R_w(F_o^2)$ ^e	0.074
Goodness of fit ^f	1.06
$(\Delta\rho)_{\max}, (\Delta\rho)_{\min}, e^{-\text{\AA}^{-3}}$	3.2, -2.2

^a Obtained from a refinement constrained so that $\alpha = \beta = \gamma = 90^\circ$.

^b A Gaussian-type absorption correction was applied, with the use of programs in the SHELXTL package (Sheldrick, G. M. SHELXTL Version 5.0, Siemens Analytical X-Ray Instruments, Inc., Madison, WI, 1994).

^c An extinction parameter x was refined, where F_c is multiplied by: $k[1 + 0.001 * x * F_c^2 * \lambda^3 / \sin(2\theta)]^{-1/4}$.

^d $R(F) = \sum ||F_o| - |F_c|| / \sum |F_o|$.

^e $R_w(F_o^2) = [\sum [w(F_o^2 - F_c^2)^2] / \sum wF_o^4]^{1/2}$; $w^{-1} = [\sigma^2(F_o^2) + (0.0206P)^2 + 3.8995P]$
where $P = [\max(F_o^2, 0) + 2F_c^2] / 3$.

^f $Goof = S = [\sum [w(F_o^2 - F_c^2)^2] / (n - p)]^{1/2}$ where n is the number of reflections and p is the total number of parameters refined.

Table A-6. Atomic Coordinates, Occupancies, and Equivalent Isotropic Displacement Parameters (\AA^2) for $\text{Ba}_3\text{Sn}_4\text{As}_6$ (subcell)

Atom	Wyckoff position, site symmetry	x	y	z	Occupancy	U_{eq}^a
Ba(<i>a</i>)	4 <i>c</i> . <i>m</i> .	0.44160(8)	¼	0.21232(4)	0.50	0.0148(1)
Ba(<i>b</i>)	4 <i>c</i> . <i>m</i> .	0.74331(4)	¼	0.54446(2)	1	0.0187(1)
Sn(<i>c</i>)	4 <i>c</i> . <i>m</i> .	0.00485(8)	¼	0.37447(5)	0.50	0.0140(2)
Sn(<i>d</i>)	4 <i>c</i> . <i>m</i> .	0.34661(4)	¼	0.63988(2)	1	0.0152(1)
Sn(<i>e</i>)	4 <i>c</i> . <i>m</i> .	0.36070(9)	¼	0.26275(5)	0.50	0.0136(2)
As(<i>f</i>)	4 <i>c</i> . <i>m</i> .	0.00171(7)	¼	0.10513(5)	1	0.0200(2)
As(<i>g</i>)	4 <i>c</i> . <i>m</i> .	0.11931(7)	¼	0.56658(4)	1	0.0143(1)
As(<i>h</i>)	4 <i>c</i> . <i>m</i> .	0.29501(7)	¼	0.77833(3)	1	0.0146(1)

^a U_{eq} is defined as one-third of the trace of the orthogonalized U_{ij} tensor.

Table A–7. Anisotropic Displacement Parameters ^a (Å²) for Ba₃Sn₄As₆ (subcell)

Atom	U_{11}	U_{22}	U_{33}	U_{12}	U_{13}	U_{23}
Ba(<i>a</i>)	0.0153(3)	0.0119(3)	0.0171(3)	0	–0.0013(2)	0
Ba(<i>b</i>)	0.0266(2)	0.0120(2)	0.0175(2)	0	0.00417(14)	0
Sn(<i>c</i>)	0.0127(3)	0.0128(4)	0.0165(3)	0	–0.0014(3)	0
Sn(<i>d</i>)	0.0148(2)	0.0180(2)	0.0127(2)	0	0.00004(14)	0
Sn(<i>e</i>)	0.0159(3)	0.0119(4)	0.0129(3)	0	–0.0008(3)	0
As(<i>f</i>)	0.0147(3)	0.0101(3)	0.0352(4)	0	–0.0025(3)	0
As(<i>g</i>)	0.0151(3)	0.0124(3)	0.0153(3)	0	0.0003(2)	0
As(<i>h</i>)	0.0179(3)	0.0137(3)	0.0122(3)	0	–0.0008(2)	0

^a The form of the anisotropic displacement parameter is: $\exp[-2\pi^2(h^2a^{*2}U_{11} + k^2b^{*2}U_{22} + l^2c^{*2}U_{33} + 2hka^*b^*U_{12} + 2hla^*c^*U_{13} + 2klb^*c^*U_{23})]$.

Table A-8. Powder X-Ray Diffraction Data for $\text{Ba}_{0.8}\text{Hf}_{12}\text{As}_{17.7}$ ^a

<i>hkl</i>	d_{obs} (Å)	d_{calc} (Å)	I/I_0 ^b	<i>hkl</i>	d_{obs} (Å)	d_{calc} (Å)	I/I_0 ^b
1 0 0	12.976	12.990	28	4 1 1	2.216	2.215	100
2 0 0	6.514	6.495	10	2 5 0	2.080	2.080	17
2 1 0	4.904	4.910	6	3 5 0	1.856	1.856	8
3 0 0	4.332	4.330	4	2 6 0	} 1.802	1.801	8
3 1 0	3.607	3.603	42	6 2 0		1.801	4
1 0 1	3.428	3.424	18	0 0 2	1.776	1.775	18
1 1 1	3.206	3.209	8	3 6 0	1.637	1.637	15
2 0 1	3.117	3.115	3	2 6 1	} 1.606	1.606	3
2 1 1	2.878	2.877	14	6 2 1		1.606	3
4 1 0	2.837	2.835	28	3 1 2	1.592	1.592	8
5 0 0	2.596	2.598	4	7 1 1	1.547	1.548	6
2 2 1	2.577	2.578	6	4 1 2	1.504	1.504	12
1 3 1	} 2.529	2.529	10	7 3 0	1.462	1.462	5
3 1 1		2.529	16	7 2 1	1.448	1.449	16
4 2 0	} 2.456	2.455	4	2 5 2	1.350	1.350	10
2 4 0		2.455	3	8 2 1	1.315	1.316	8
4 0 1	2.398	2.396	19	3 5 2	1.283	1.283	8
1 5 0	2.332	2.333	8	2 6 2	1.263	1.264	8
3 2 1	2.284	2.283	21	3 6 2	1.203	1.203	14

^a The cell parameters refined from the powder pattern, obtained on a Guinier camera at room temperature, are $a = 15.000(2)$ Å, $c = 3.550(1)$ Å, $V = 691.8(2)$ Å³.

Table A-8. Powder X-Ray Diffraction Data for $\text{Ba}_{0.8}\text{Hf}_{12}\text{As}_{17.7}$ ^a (continued)

^b The intensities were calculated from the crystal structure of $\text{Ba}_{0.8}\text{Hf}_{12}\text{As}_{17.7}$ with the use of the program LAZY-PULVERIX (Yvon, K.; Jeitschko, W.; Parthé, E. *J. Appl. Crystallogr.* 1977, 10, 73).

Table A-9. Anisotropic Displacement Parameters ^a (Å²) for Ba_{0.8}Hf₁₂As_{17.7}

Atom	U_{11}	U_{22}	U_{33}	U_{12}	U_{13}	U_{23}
Ba	0.015(3)	0.015(3)	0.07(2)	0.008(2)	0	0
Hf(1)	0.0042(4)	0.0033(4)	0.0052(4)	0.0020(4)	0	0
Hf(2)	0.0039(4)	0.0038(4)	0.0051(4)	0.0020(4)	0	0
As(1)	0.004(2)	0.004(2)	0.011(2)	0.002(2)	0	0
As(2)	0.002(1)	0.006(1)	0.007(1)	0.0009(9)	0	0
As(3)	0.002(1)	0.003(1)	0.0030(9)	0.0007(9)	0	0
As(4)	0.007(3)	0.008(3)	0.006(3)	0.005(3)	0	0

^a The form of the anisotropic displacement parameter is: $\exp[-2\pi^2(h^2a^{*2}U_{11} + k^2b^{*2}U_{22} + l^2c^{*2}U_{33} + 2hka^*b^*U_{12} + 2hla^*c^*U_{13} + 2klb^*c^*U_{23})]$.

Table A–10. Powder X-Ray Diffraction Data for $\text{La}_6\text{Ge}_{2.8(1)}\text{Sb}_{13.2(1)}$ ^a

<i>hkl</i>	d_{obs} (Å)	d_{calc} (Å)	I/I_0 ^b	<i>hkl</i>	d_{obs} (Å)	d_{calc} (Å)	I/I_0 ^b
1 0 1	4.287	4.275	3	1 3 12	1.752	1.751	2
1 1 0	4.030	4.021	2	1 1 14	1.743	1.743	2
0 1 7	3.648	3.644	2	2 1 9	1.735	1.734	2
0 3 1	3.591	3.587	4	2 4 0	} 1.692	1.692	4
1 1 4	3.462	3.457	4	2 0 10		1.691	2
0 0 8	3.387	3.385	6	1 6 1	} 1.667	1.666	3
0 3 3	3.364	3.359	29	1 0 15		1.666	3
1 2 3	3.173	3.169	37	2 4 4	1.642	1.642	3
0 3 5	3.013	3.009	24	0 2 16	1.616	1.616	3
0 1 9	2.896	2.899	6	2 2 10	1.614	1.614	13
1 0 7	2.884	2.884	100	2 4 6	1.584	1.585	1
1 2 5	2.870	2.870	5	1 5 10	1.578	1.577	2
1 3 2	2.722	2.720	9	1 4 13	1.542	1.544	3
0 4 0	2.717	2.714	8	1 6 7	1.533	1.533	7
0 0 10	2.706	2.708	3	2 5 1	1.531	1.530	5
1 1 8	2.589	2.589	12	0 5 13	1.502	1.503	3
1 3 4	2.568	2.569	97	0 7 5	1.490	1.491	2
0 4 4	2.518	2.519	5	2 3 11	1.482	1.483	18
1 0 9	2.470	2.470	9	2 5 5	1.475	1.475	2
0 2 10	2.422	2.423	18	1 5 12	1.471	1.471	4
1 3 6	2.366	2.365	5	1 6 9	1.459	1.460	2
0 4 6	2.326	2.326	2	1 7 2	1.451	1.452	2

Table A-10. Powder X-Ray Diffraction Data for $\text{La}_6\text{Ge}_{2.8(1)}\text{Sb}_{13.2(1)}$ ^a (continued)

1 4 1	2.292	2.291	3	1 3 16	1.444	1.445	2
0 0 12	2.257	2.256	2	2 0 14	1.443	1.442	8
1 4 3	2.229	2.228	2	1 2 17	1.441	1.441	15
2 0 0	} 2.166	2.164	37	1 7 4	1.427	1.427	9
0 5 1		2.164	7	2 5 7	1.425	1.425	8
1 3 8	2.147	2.147	2	1 7 6	} 1.388	1.389	3
0 3 11	2.036	2.035	20	2 6 0		1.388	6
0 5 5	2.013	2.015	2	3 2 3	1.378	1.378	3
1 4 7	1.978	1.977	5	2 1 15	1.375	1.375	2
1 1 12	1.968	1.968	3	1 5 14	1.370	1.370	16
1 5 0	1.942	1.941	3	0 0 20	1.354	1.354	2
1 3 10	1.939	1.938	6	3 0 7	1.352	1.352	14
0 0 14	1.935	1.934	9	1 7 8	1.340	1.341	2
0 5 7	1.894	1.893	10	3 3 2	1.332	1.334	2
2 3 1	1.854	1.853	2	2 6 6	1.327	1.327	2
2 0 8	1.823	1.823	2	1 3 18	1.322	1.323	8
2 3 3	1.820	1.819	12	3 3 4	1.314	1.315	15
0 6 0	1.810	1.810	6	1 2 19	1.313	1.313	2
1 5 6	1.783	1.783	10	0 7 11	1.313	1.312	3
0 1 15	1.781	1.781	2	1 6 13	1.302	1.303	2
1 2 13	1.773	1.774	3	2 2 16	1.295	1.295	3
2 3 5	1.757	1.757	10	1 8 3	1.282	1.282	9

Table A-10. Powder X-Ray Diffraction Data for $\text{La}_6\text{Ge}_{2.8(1)}\text{Sb}_{13.2(1)}$ ^a (continued)

^a The cell parameters refined from the powder pattern, obtained on a Guinier camera at room temperature, are $a = 4.3289(7)$ Å, $b = 10.857(1)$ Å, $c = 27.076(3)$ Å, and $V = 1272.6(2)$ Å³.

^b The intensities were calculated from the crystal structure of $\text{La}_6\text{Ge}_{2.8(1)}\text{Sb}_{13.2(1)}$ with the use of the program LAZY-PULVERIX (Yvon, K.; Jeitschko, W.; Parthé, E. *J. Appl. Crystallogr.* 1977, 10, 73-74).

Table A-11. Powder X-Ray Diffraction Data for $Ce_6Ge_{5-x}Sb_{1+x}$ ^a

<i>hkl</i>	<i>d</i> _{obs} (Å)	<i>d</i> _{calc} (Å)	<i>hkl</i> ^b	<i>hkl</i>	<i>d</i> _{obs} (Å)	<i>d</i> _{calc} (Å)	<i>hkl</i> ^b
1 0 1	4.254	4.243	3	2 3 5	1.743	1.742	10
1 1 0	3.999	3.990	2	1 3 12	1.734	1.733	2
0 1 7	3.611	3.605	2	1 1 14	1.726	1.725	2
0 3 1	3.556	3.548	4	2 1 9	1.719	1.720	3
1 1 4	3.435	3.428	4	2 4 0	} 1.677	1.678	4
1 0 5	} 3.354	3.352	2	2 0 10		1.676	2
0 0 8		3.349	6	0 6 6	1.662	1.661	1
0 3 3	3.329	3.323	28	1 0 15	} 1.649	1.649	3
1 2 3	3.146	3.141	37	1 6 1		1.649	3
0 3 5	2.979	2.977	24	2 4 4	1.626	1.627	3
0 1 9	2.869	2.869	6	2 2 10	} 1.599	1.600	13
1 0 7	2.860	2.858	100	0 2 16		1.599	3
1 2 5	2.844	2.844	5	2 4 6	1.570	1.570	2
1 3 2	2.695	2.694	10	1 5 10	1.559	1.561	2
0 4 0	2.686	2.685	8	1 4 13	1.527	1.528	3
0 0 10	2.679	2.679	3	1 6 7	} 1.517	1.517	7
1 1 8	2.566	2.565	12	2 5 1		1.517	5
1 3 4	2.546	2.544	97	0 5 13	1.487	1.487	3
0 4 4	2.493	2.492	5	0 7 5	1.474	1.475	2
1 0 9	2.448	2.447	10	2 3 11	1.469	1.469	18
0 2 10	2.398	2.397	18	2 5 5	1.462	1.461	2
1 3 6	2.342	2.342	5	1 5 12	1.456	1.456	4

Table A-11. Powder X-Ray Diffraction Data for $\text{Ce}_6\text{Ge}_{5-x}\text{Sb}_{11+x}$ ^a (continued)

0 4 6	2.303	2.301	2	1 6 9	1.444	1.445	2
1 4 1	2.270	2.269	3	1 7 2	1.436	1.437	2
0 0 12	2.232	2.233	2	2 0 14	1.429	1.429	8
1 4 3	2.208	2.206	2	1 2 17	1.426	1.426	15
2 0 0	2.150	2.149	37	1 7 4	} 1.412	1.412	9
0 5 1	2.142	2.141	7	2 5 7		1.412	8
1 3 8	2.128	2.126	2	2 6 0	} 1.374	1.375	6
0 3 11	2.015	2.014	20	1 7 6		1.375	3
1 4 7	1.958	1.957	5	3 2 3	1.367	1.368	3
1 1 12	1.948	1.948	3	2 1 15	1.362	1.362	2
1 5 0	1.922	1.921	3	1 5 14	1.356	1.356	16
1 3 10	1.920	1.919	6	3 0 7	1.342	1.342	14
0 0 14	1.914	1.914	9	0 0 20	1.338	1.340	2
0 5 7	1.873	1.873	10	3 3 2	1.323	1.323	2
2 3 1	1.838	1.838	2	2 6 6	1.314	1.314	2
2 0 8	1.807	1.808	2	1 3 18	1.308	1.309	8
2 3 3	1.805	1.804	12	3 3 4	1.305	1.304	15
0 6 0	1.790	1.790	6	0 7 11	1.298	1.298	3
1 5 6	1.765	1.765	10	1 6 13	1.288	1.289	2
0 1 15	1.762	1.762	2	2 2 16	1.281	1.283	3
1 2 13	1.756	1.756	3	1 8 3	1.268	1.268	9

^a The cell parameters refined from the powder pattern, obtained on a Guinier camera at room temperature, are $a = 4.2972(7)$ Å, $b = 10.740(1)$ Å, $c = 26.791(4)$ Å, and $V = 1236.4(2)$ Å³.

Table A-11. Powder X-Ray Diffraction Data for $\text{Ce}_6\text{Ge}_{5-x}\text{Sb}_{11+x}$ ^a (continued)

^b Theoretical intensity calculations were based on positional parameters obtained from the crystal structure of $\text{La}_6\text{Ge}_{2.8(1)}\text{Sb}_{13.2(1)}$ with the use of the program LAZY-PULVERIX (Yvon, K.; Jeitschko, W.; Parthé, E. *J. Appl. Crystallogr.* 1977, 10, 73-74).

Table A-12. Powder X-Ray Diffraction Data for $\text{Pr}_6\text{Ge}_{5-x}\text{Sb}_{1+x}$ ^a

<i>hkl</i>	d_{obs} (Å)	d_{calc} (Å)	I/I_0 ^b	<i>hkl</i>	d_{obs} (Å)	d_{calc} (Å)	I/I_0 ^b
1 0 1	4.226	4.214	4	2 3 1	1.826	1.826	2
1 1 0	3.975	3.963	2	2 0 8	1.796	1.796	2
0 1 7	3.590	3.583	2	2 3 3	1.793	1.792	11
0 3 1	3.536	3.527	4	0 6 0	1.780	1.779	6
1 1 4	3.412	3.405	4	1 5 6	1.754	1.754	10
1 0 5	} 3.334	3.330	2	1 2 13	1.745	1.745	4
0 0 8		3.328	6	2 3 5	1.731	1.731	11
0 3 3	3.309	3.303	28	1 3 12	1.722	1.723	2
1 2 3	3.124	3.120	43	1 1 14	1.714	1.715	2
0 3 5	2.961	2.959	26	2 1 9	1.709	1.708	3
0 1 9	2.852	2.851	6	2 4 0	1.665	1.667	4
1 0 7	2.839	2.839	100	1 6 1	} 1.638	1.639	4
1 2 5	2.830	2.825	6	1 0 15		1.639	3
1 3 2	2.678	2.677	12	2 4 4	1.616	1.617	3
0 4 0	2.671	2.669	9	2 2 10	1.588	1.590	15
0 0 10	2.664	2.663	3	0 2 16	1.587	1.589	3
1 1 8	2.550	2.549	14	1 5 10	1.550	1.552	2
1 3 4	2.529	2.528	99	1 4 13	1.518	1.519	2
0 4 4	2.479	2.477	6	1 6 7	} 1.507	1.508	7
1 0 9	2.433	2.431	9	2 5 1		1.507	5
0 2 10	2.384	2.383	21	0 5 13	1.478	1.478	3
1 3 6	2.328	2.327	5	0 7 5	1.466	1.466	2

Table A-12. Powder X-Ray Diffraction Data for $\text{Pr}_6\text{Ge}_{5-x}\text{Sb}_{11+x}$ ^a (continued)

1 4 1	2.256	2.255	3	2 3 11	1.459	1.460	17
0 0 12	2.220	2.219	2	2 5 5	1.451	1.452	2
1 4 3	2.194	2.193	2	1 5 12	1.447	1.447	5
2 0 0	2.135	2.134	38	1 6 9	1.435	1.436	3
0 5 1	2.131	2.128	7	1 7 2	1.428	1.428	2
1 3 8	2.113	2.112	2	1 3 16	} 1.421	1.421	2
1 0 11	2.106	2.105	2	2 0 14		1.420	8
0 3 11	2.002	2.001	19	1 2 17	1.417	1.418	17
0 5 5	1.983	1.982	2	1 7 4	} 1.403	1.404	9
1 4 7	1.945	1.945	5	2 5 7		1.403	9
1 1 12	1.936	1.936	4	2 6 0	} 1.366	1.367	6
1 5 0	1.910	1.910	2	1 7 6		1.366	3
1 3 10	1.907	1.907	6	3 2 3	1.358	1.358	4
0 0 14	1.902	1.902	9	2 1 15	1.353	1.354	3
0 5 7	1.862	1.862	10	1 5 14	1.347	1.348	17
				3 0 7	1.332	1.332	14

^a The cell parameters refined from the powder pattern, obtained on a Guinier camera at room temperature, are $a = 4.2674(9)$ Å, $b = 10.677(2)$ Å, $c = 26.626(5)$ Å, and $V = 1213.1(3)$ Å³.

^b Theoretical intensity calculations were based on positional parameters obtained from the crystal structure of $\text{Nd}_6\text{Ge}_{3.6(1)}\text{Sb}_{12.4(1)}$ with the use of the program LAZY-PULVERIX (Yvon, K.; Jeitschko, W.; Parthé, E. *J. Appl. Crystallogr.* 1977, 10, 73-74).

Table A-13. Powder X-Ray Diffraction Data for $\text{Nd}_6\text{Ge}_{3.6(1)}\text{Sb}_{12.4(1)}$ ^a

<i>hkl</i>	d_{obs} (Å)	d_{calc} (Å)	$ I_o$ ^b	<i>hkl</i>	d_{obs} (Å)	d_{calc} (Å)	$ I_o$ ^b
1 0 1	4.199	4.188	4	1 3 12	1.715	1.717	2
1 1 0	3.949	3.940	2	2 1 9	1.699	1.700	3
0 1 7	3.578	3.573	2	2 4 0	} 1.657	1.658	4
0 3 1	3.522	3.514	4	2 0 10		1.657	2
1 1 4	3.394	3.388	4	0 6 6	1.646	1.646	2
0 0 8	3.323	3.319	6	1 0 15	} 1.632	1.634	3
0 3 3	3.296	3.291	28	1 6 1		1.633	4
1 2 3	3.108	3.105	42	2 4 4	1.608	1.609	3
0 3 5	2.950	2.949	26	0 2 16	1.584	1.584	3
0 1 9	2.840	2.843	7	2 2 10	1.582	1.582	15
1 0 7	2.826	2.827	100	1 5 10	1.545	1.546	2
1 2 5	2.816	2.813	6	1 4 13	1.513	1.513	2
1 3 2	2.666	2.665	12	1 6 7	1.502	1.502	7
0 4 0	2.661	2.659	9	2 5 1	1.499	1.499	5
0 0 10	2.656	2.655	4	0 5 13	1.473	1.473	3
1 1 8	2.539	2.538	14	0 7 5	1.461	1.461	2
1 3 4	2.518	2.517	99	2 3 11	1.453	1.453	17
0 4 4	2.470	2.468	6	1 5 12	1.442	1.442	5
1 0 9	2.422	2.422	9	1 6 9	1.430	1.431	3
0 2 10	2.376	2.376	21	1 7 2	1.422	1.422	2
1 3 6	2.319	2.317	5	2 0 14	} 1.413	1.414	8
1 4 1	2.247	2.245	3	1 2 17		1.413	17

Table A-13. Powder X-Ray Diffraction Data for $\text{Nd}_6\text{Ge}_{3.6(1)}\text{Sb}_{12.4(1)}$ ^a (continued)

0 0 12	2.213	2.213	2	1 7 4	1.398	1.398	9
1 4 3	2.185	2.183	9	2 5 7	1.396	1.396	8
0 5 1	} 2.124	2.121	7	1 7 6		1.361	3
2 0 0		2.121	38	0 5 15	} 1.360	1.361	2
1 3 8	2.106	2.104	2	2 6 0			1.360
1 0 11	2.099	2.098	2	3 2 3	1.350	1.350	4
0 3 11	1.996	1.995	20	2 1 15	1.348	1.348	3
0 5 5	1.976	1.975	2	1 5 14	1.342	1.343	17
1 4 7	1.938	1.937	5	3 0 7	1.325	1.325	14
1 1 12	1.929	1.929	4	1 7 8	1.313	1.314	2
1 5 0		1.902	2	3 3 2	1.306	1.307	2
1 3 10	} 1.899	1.900	6	2 6 6	1.300	1.300	2
0 0 14		1.897	9	1 3 18	1.297	1.297	7
0 5 7	1.856	1.855	10	3 3 4	} 1.288	1.288	16
2 3 1	1.817	1.816	2	1 2 19		1.288	2
2 3 3	1.784	1.783	11	0 7 11	1.285	1.286	3
0 6 0	1.774	1.773	6	1 6 13	1.276	1.277	2
1 5 6	} 1.747	1.747	10	2 2 16	1.268	1.269	3
0 1 15		1.746	2	1 8 3	} 1.255	1.256	8
1 2 13	1.739	1.739	4	0 1 21		1.256	3
2 3 5	1.722	1.722	11				

^a The cell parameters refined from the powder pattern, obtained on a Guinier camera at room temperature, are $a = 4.2412(8)$ Å, $b = 10.637(2)$ Å, $c = 26.552(4)$ Å, and $V = 1197.8(3)$ Å³.

Table A-13. Powder X-Ray Diffraction Data for $\text{Nd}_6\text{Ge}_{3.6(1)}\text{Sb}_{12.4(1)}$ ^a (continued)

^b The intensities were calculated from the crystal structure of $\text{Nd}_6\text{Ge}_{3.6(1)}\text{Sb}_{12.4(1)}$ with the use of the program LAZY-PULVERIX (Yvon, K.; Jeitschko, W.; Parthé, E. *J. Appl. Crystallogr.* 1977, 10, 73-74).

Table A-14. Powder X-Ray Diffraction Data for $\text{Sm}_6\text{Ge}_{5-x}\text{Sb}_{1+x}$ ^a

<i>hkl</i>	d_{obs} (Å)	d_{calc} (Å)	III_o ^b	<i>hkl</i>	d_{obs} (Å)	d_{calc} (Å)	III_o ^b
1 0 1	4.149	4.142	4	2 3 5	} 1.704	1.704	11
1 1 0	3.897	3.897	2	1 3 12		1.702	2
0 1 7	3.547	3.545	2	1 1 14	1.694	1.695	2
0 3 1	3.485	3.482	4	2 1 9	1.685	1.683	3
1 1 4	3.356	3.354	4	2 0 10	} 1.640	1.641	2
0 0 8	3.295	3.294	6	2 4 0		1.641	4
1 0 5	3.281	3.282	2	0 6 6	1.631	1.631	2
0 3 3	3.263	3.261	28	1 0 15	1.620	1.620	3
1 2 3	3.074	3.074	42	1 6 1	1.617	1.617	4
0 3 5	2.923	2.923	26	2 4 4	1.592	1.592	3
0 1 9	2.821	2.821	7	0 2 16	1.572	1.572	3
1 0 7	2.802	2.801	100	2 2 10	1.566	1.567	15
1 2 5	2.786	2.786	7	1 5 10	1.532	1.532	2
1 3 2	2.638	2.638	12	1 4 13	1.500	1.500	2
0 0 10	} 2.634	2.635	4	1 6 7	1.488	1.488	7
0 4 0		2.634	9	2 5 1	1.485	1.484	5
1 1 8	2.516	2.516	14	0 5 13	1.461	1.461	3
1 3 4	2.493	2.493	99	0 7 5	1.448	1.447	2
0 4 4	2.447	2.446	6	2 3 11	1.439	1.439	17
1 0 9	2.402	2.401	9	1 5 12	1.430	1.429	5
0 2 10	2.359	2.357	22	1 6 9	1.417	1.417	3
1 3 6	2.297	2.296	5	1 7 2	1.408	1.409	2

Table A-14. Powder X-Ray Diffraction Data for $\text{Sm}_6\text{Ge}_{5-x}\text{Sb}_{11+x}$ ^a (continued)

1 4 1	2.225	2.223	3	1 3 16	1.405	1.405	2
0 0 12	2.197	2.196	2	1 2 17	} 1.401	1.402	17
1 4 3	2.164	2.162	2	2 0 14		1.401	8
0 5 1	2.101	2.101	7	1 7 4	1.385	1.385	9
2 0 0	2.099	2.097	38	2 5 7	1.382	1.383	9
1 3 8	2.085	2.085	2	0 5 15	} 1.348	1.349	2
1 0 11	2.080	2.080	2	1 7 6		1.348	3
0 3 11	1.980	1.979	20	2 6 0	1.346	1.346	6
0 5 5	1.958	1.957	2	2 1 15	} 1.335	1.336	3
1 4 7	1.920	1.919	5	3 2 3		1.336	4
1 1 12	1.914	1.913	4	1 5 14	1.331	1.331	18
1 3 10		1.883	6	0 0 20	1.317	1.317	2
1 5 0	} 1.884	1.883	2	3 0 7	1.310	1.311	14
0 0 14			1.882	9	1 7 8	1.301	1.302
0 5 7	1.840	1.839	10	3 3 2	1.292	1.293	2
2 3 1	1.796	1.796	2	1 3 18	1.285	1.286	7
2 0 8	1.770	1.769	2	1 2 19	1.276	1.277	2
2 3 3	1.764	1.764	11	0 7 11	} 1.274	1.275	3
0 6 0	1.756	1.756	6	3 3 4		1.274	16
0 1 15	1.735	1.733	2	2 2 16	1.257	1.258	3
1 5 6	1.730	1.731	10	0 1 21	1.246	1.246	3
1 2 13	1.725	1.724	4	1 8 3	1.243	1.244	8
0 5 9	1.711	1.710	2				

Table A-14. Powder X-Ray Diffraction Data for $\text{Sm}_6\text{Ge}_{5-x}\text{Sb}_{11+x}$ ^a (continued)

- ^a The cell parameters refined from the powder pattern, obtained on a Guinier camera at room temperature, are $a = 4.1942(7)$ Å, $b = 10.537(1)$ Å, $c = 26.350(3)$ Å, and $V = 1164.5(2)$ Å³.
- ^b Theoretical intensity calculations were based on positional parameters obtained from the crystal structure of $\text{Nd}_6\text{Ge}_{3.6(1)}\text{Sb}_{12.4(1)}$ with the use of the program LAZY-PULVERIX (Yvon, K.; Jeitschko, W.; Parthé, E. *J. Appl. Crystallogr.* 1977, 10, 73-74).

Table A-15. Powder X-Ray Diffraction Data for $\text{Gd}_6\text{Ge}_{4.3(1)}\text{Sb}_{11.7(1)}$ ^a

<i>hkl</i>	d_{obs} (Å)	d_{calc} (Å)	III_o^b	<i>hkl</i>	d_{obs} (Å)	d_{calc} (Å)	III_o^b
1 0 1	4.106	4.100	5	2 1 9	1.668	1.669	3
1 1 0	3.863	3.857	2	2 0 10	1.628	1.628	2
1 0 3	3.756	3.750	1	2 4 0	1.625	1.625	5
0 1 7	3.531	3.527	3	1 5 8	1.621	1.621	2
0 3 1	3.455	3.450	4	1 0 15	1.611	1.611	3
1 1 4	3.328	3.325	4	1 6 1	1.601	1.602	4
0 0 8	3.283	3.278	7	2 4 4	1.577	1.577	4
0 3 3	3.236	3.233	27	0 2 16	1.563	1.564	3
1 2 3	3.046	3.046	49	2 2 10	1.553	1.554	15
0 3 5	2.900	2.900	28	1 5 10	1.521	1.520	2
0 1 9	2.806	2.807	6	1 4 13	1.489	1.490	2
1 0 7	2.780	2.781	98	1 6 7	1.474	1.475	7
1 2 5	2.763	2.762	7	2 5 1	1.469	1.470	4
0 0 10	2.623	2.623	4	0 5 13	1.451	1.451	2
1 3 2	} 2.613	2.613	12	0 7 5	1.434	1.435	2
0 4 0		2.610	10	2 3 11	1.427	1.428	16
1 1 8	2.498	2.498	16	1 5 12	1.418	1.419	5
1 3 4	2.470	2.470	100	2 5 5	1.416	1.417	2
0 4 4	2.426	2.425	7	1 6 9	1.406	1.406	3
1 0 9	2.386	2.385	10	1 3 16	1.397	1.397	2
0 2 10	2.345	2.344	24	1 2 17	1.393	1.394	18
1 3 6	2.277	2.277	5	2 0 14	1.391	1.391	8

Table A-15. Powder X-Ray Diffraction Data for $\text{Gd}_6\text{Ge}_{4.3(1)}\text{Sb}_{11.7(1)}$ ^a (continued)

1 4 1	2.200	2.202	2	1 7 4	1.372	1.373	10
1 4 3	2.142	2.142	2	2 5 7	1.370	1.370	9
0 5 1	2.083	2.081	6	0 5 15	1.341	1.341	2
2 0 0	2.076	2.076	39	1 7 6	1.336	1.336	3
1 3 8	2.069	2.069	2	2 6 0	1.333	1.333	7
1 0 11	2.066	2.068	2	2 1 15	1.327	1.326	3
0 3 11	1.967	1.967	19	3 2 3	1.323	1.322	5
0 5 5	1.940	1.940	3	1 5 14	1.322	1.322	18
1 4 7	1.903	1.903	6	2 5 9	1.313	1.314	2
1 1 12	1.901	1.902	3	0 0 20	1.312	1.311	2
0 0 14	1.873	1.873	8	2 4 12	1.304	1.304	2
1 3 10	1.870	1.870	6	3 0 7	1.298	1.298	13
1 5 0	1.865	1.865	2	1 7 8	1.291	1.290	3
1 5 2	1.848	1.847	1	3 3 2	1.280	1.280	2
0 5 7	1.824	1.824	10	1 3 18	1.278	1.279	6
2 0 8	1.754	1.754	2	1 2 19	1.272	1.270	2
2 3 3	1.747	1.747	10	3 1 8	} 1.265	1.265	3
0 6 0	1.740	1.740	7	0 7 11		1.264	3
0 1 15	1.724	1.725	3	3 3 4	1.261	1.262	17
1 5 6	1.715	1.716	9	3 0 9	} 1.249	1.250	2
1 2 13	1.714	1.714	5	2 2 16		1.249	3
1 3 12	1.692	1.690	2	1 8 1	1.243	1.244	2
2 3 5	1.687	1.688	13	0 1 21	1.240	1.240	3
1 1 14	1.684	1.685	3	1 8 3	1.232	1.233	7

Table A-15. Powder X-Ray Diffraction Data for $\text{Gd}_6\text{Ge}_{4.3(1)}\text{Sb}_{11.7(1)}$ ^a (continued)

0 4 12	1.675	1.676	2
--------	-------	-------	---

^a The cell parameters refined from the powder pattern, obtained on a Guinier camera at room temperature, are $a = 4.1511(6)$ Å, $b = 10.440(1)$ Å, $c = 26.228(3)$ Å, and $V = 1136.7(2)$ Å³.

^b The intensities were calculated from the crystal structure of $\text{Gd}_6\text{Ge}_{4.3(1)}\text{Sb}_{11.7(1)}$ with the use of the program LAZY-PULVERIX (Yvon, K.; Jeitschko, W.; Parthé, E. *J. Appl. Crystallogr.* 1977, 10, 73-74).

Table A-16. Powder X-Ray Diffraction Data for $\text{Tb}_6\text{Ge}_{5-x}\text{Sb}_{11+x}$ ^a

<i>hkl</i>	d_{obs} (Å)	d_{calc} (Å)	$ I_o$ ^b	<i>hkl</i>	d_{obs} (Å)	d_{calc} (Å)	$ I_o$ ^b
1 0 1	4.086	4.080	5	1 5 6	} 1.707	1.708	9
1 1 0	3.845	3.838	2	1 2 13		1.707	5
1 0 3	3.736	3.732	1	2 3 5	1.679	1.680	13
0 1 7	3.520	3.514	3	1 1 14	1.678	1.679	3
0 3 1	3.439	3.434	4	0 4 12	1.670	1.669	2
1 1 4	3.311	3.310	4	2 1 9	1.661	1.661	3
0 0 8	3.270	3.267	7	2 0 10	1.620	1.620	2
1 0 5	3.244	3.241	1	2 4 0	1.616	1.617	5
0 3 3	3.221	3.219	26	1 5 8	1.614	1.614	2
1 2 3	3.034	3.031	48	1 0 15	1.605	1.606	3
0 3 5	2.889	2.888	28	1 6 1	1.594	1.594	4
0 1 9	2.799	2.797	6	2 4 4	1.569	1.569	4
1 0 7	2.772	2.770	97	0 2 16	1.558	1.558	3
1 2 5	2.753	2.750	7	2 2 10	1.547	1.547	15
0 0 10	2.615	2.614	4	1 5 10	1.514	1.514	2
1 3 2	} 2.602	2.601	12	1 6 7	1.468	1.469	7
0 4 0		2.598	10	2 5 1	1.462	1.463	4
1 1 8	2.490	2.488	16	0 5 13	1.445	1.445	2
1 3 4	2.461	2.459	100	0 7 5	1.427	1.428	2
0 4 4	2.416	2.414	7	2 3 11	1.421	1.422	16
1 0 9	2.378	2.376	10	1 5 12	1.413	1.413	5
0 2 10	2.338	2.335	24	2 5 5	1.410	1.411	2

Table A-16. Powder X-Ray Diffraction Data for $Tb_6Ge_{5-x}Sb_{11+x}$ ^a (continued)

1 3 6	2.268	2.267	5	1 6 9	1.399	1.400	3
0 0 12	2.178	2.178	1	1 3 16	1.391	1.391	2
1 4 3	2.134	2.132	2	1 2 17	1.388	1.389	18
0 5 1	2.073	2.072	6	2 0 14	1.385	1.385	8
2 0 0	2.066	2.065	38	1 7 4	1.365	1.366	10
1 3 8	} 2.062	2.060	2	2 5 7	1.363	1.364	9
1 0 11		2.060	2	1 7 6	1.329	1.330	3
0 3 11	1.961	1.960	19	2 6 0	1.327	1.327	7
0 5 5	1.932	1.932	3	2 1 15	1.320	1.321	3
1 4 7	} 1.896	1.895	6	1 5 14	} 1.316	1.317	18
1 1 12		1.894	3	3 2 3		1.316	5
0 0 14	1.868	1.867	8	0 0 20	1.306	1.307	2
1 3 10	1.864	1.862	6	2 4 12	1.299	1.298	2
1 5 2	1.841	1.838	1	3 0 7	1.291	1.292	13
0 5 7	1.816	1.816	10	1 7 8	1.284	1.285	3
2 0 8	1.744	1.746	2	1 3 18	1.273	1.274	6
2 3 3	1.738	1.738	10	1 2 19	1.266	1.266	2
0 6 0	1.731	1.732	7	3 1 8	} 1.259	1.259	3
0 1 15	1.717	1.719	3	0 7 11		1.259	3
				3 3 4	1.255	1.256	17

^a The cell parameters refined from the powder pattern, obtained on a Guinier camera at room temperature, are $a = 4.1305(8)$ Å, $b = 10.393(2)$ Å, $c = 26.139(4)$ Å, and $V = 1122.1(2)$ Å³.

Table A-16. Powder X-Ray Diffraction Data for $\text{Tb}_6\text{Ge}_{5-x}\text{Sb}_{11+x}$ ^a (continued)

^b Theoretical intensity calculations were based on positional parameters obtained from the crystal structure of $\text{Gd}_6\text{Ge}_{4.3(1)}\text{Sb}_{11.7(1)}$ with the use of the program LAZY-PULVERIX (Yvon, K.; Jeitschko, W.; Parthé, E. *J. Appl. Crystallogr.* 1977, 10, 73-74).

Table A-17. Powder X-Ray Diffraction Data for Dy₆Ge_{5-x}Sb_{11+x}^a

<i>hkl</i>	<i>d</i> _{obs} (Å)	<i>d</i> _{calc} (Å)	<i>I</i> / <i>I</i> ₀ ^b	<i>hkl</i>	<i>d</i> _{obs} (Å)	<i>d</i> _{calc} (Å)	<i>I</i> / <i>I</i> ₀ ^b
1 0 1	4.066	4.053	3	2 3 1	1.760	1.759	2
1 1 0	3.825	3.814	3	2 0 8	1.735	1.735	3
1 0 3	3.712	3.709	4	2 3 3	1.727	1.728	10
0 1 7	3.504	3.497	2	0 6 0	1.724	1.724	7
0 3 1	3.424	3.418	6	0 1 15	1.709	1.710	3
1 1 4	3.290	3.290	8	1 5 6	} 1.698	1.700	7
0 0 8	3.257	3.252	8	1 2 13		1.699	4
1 0 5	3.223	3.222	3	1 1 14	} 1.669	1.670	2
0 3 3	3.210	3.204	28	2 3 5		1.700	11
1 2 3	3.019	3.014	38	0 4 12	1.663	1.661	2
0 3 5	2.878	2.874	24	2 1 9	1.651	1.652	2
0 1 9	2.785	2.784	4	2 0 10	1.612	1.611	3
1 0 7	} 2.757	2.754	95	2 4 0	} 1.608	1.607	6
0 2 8		2.753	2	1 5 8		1.606	2
1 2 5	2.736	2.735	4	1 0 15	1.596	1.597	3
0 0 10	2.602	2.601	5	1 6 1	1.586	1.587	3
1 3 2	} 2.588	2.587	9	2 4 4	1.559	1.560	4
0 4 0		2.586	11	0 2 16	1.549	1.551	3
1 1 8	2.477	2.475	18	2 2 10	1.540	1.538	13
1 3 4	2.448	2.446	100	1 5 10	1.506	1.506	2
0 4 4	2.404	2.403	7	1 6 7	1.461	1.461	7
1 0 9	2.364	2.363	7	2 5 1	1.454	1.455	3

Table A-17. Powder X-Ray Diffraction Data for $\text{Dy}_6\text{Ge}_{5-x}\text{Sb}_{11+x}$ ^a (continued)

0 2 10	2.325	2.324	20	2 3 11	1.414	1.414	16
1 3 6	2.255	2.255	7	1 5 12	1.405	1.406	6
1 4 3	2.122	2.121	2	2 5 5	1.402	1.403	3
0 5 1	2.064	2.062	4	1 6 9	1.391	1.393	3
2 0 0	2.054	2.052	37	1 3 16	1.384	1.384	2
1 3 8	2.050	2.050	3	1 2 17	1.380	1.382	16
0 3 11	1.951	1.950	19	2 0 14	1.378	1.377	8
0 5 5	1.922	1.923	3	1 7 4	1.358	1.360	11
1 4 7	} 1.886	1.885	8	2 5 7	1.356	1.356	8
1 1 12		1.885	4	2 6 0	1.319	1.320	7
0 0 14	1.858	1.858	8	2 1 15	1.313	1.314	3
1 3 10	1.854	1.853	6	1 5 14	1.309	1.310	15
1 5 2	1.828	1.829	2	3 2 3	1.306	1.307	4
0 5 7	1.808	1.808	8	3 0 7	1.283	1.284	13

^a The cell parameters refined from the powder pattern, obtained on a Guinier camera at room temperature, are $a = 4.103(1)$ Å, $b = 10.345(2)$ Å, $c = 26.014(5)$ Å, and $V = 1104.2(3)$ Å³.

^b Theoretical intensity calculations were based on positional parameters obtained from the crystal structure of $\text{Gd}_6\text{Ge}_{4.3(1)}\text{Sb}_{11.7(1)}$ with the use of the program LAZY-PULVERIX (Yvon, K.; Jeitschko, W.; Parthé, E. *J. Appl. Crystallogr.* **1977**, *10*, 73-74).

Table A–18. Anisotropic Displacement Parameters a (\AA^2) for $\text{La}_6\text{Ge}_{2.8(1)}\text{Sb}_{13.2(1)}$,
 $\text{Nd}_6\text{Ge}_{3.6(1)}\text{Sb}_{12.4(1)}$, and $\text{Gd}_6\text{Ge}_{4.3(1)}\text{Sb}_{11.7(1)}$

Atom	U_{11}	U_{22}	U_{33}	U_{12}	U_{13}	U_{23}
$\text{La}_6\text{Ge}_{2.8(1)}\text{Sb}_{13.2(1)}$						
La(1)	0.0165(2)	0.0119(2)	0.0116(2)	0	0	0
La(2)	0.0174(2)	0.0127(2)	0.0121(2)	0.0007(1)	0	0
Sb(1)	0.0157(3)	0.0150(3)	0.0130(3)	0	0	0
Sb(2)	0.0225(2)	0.0134(2)	0.0147(2)	0.0014(1)	0	0
Sb(3)	0.0182(3)	0.0203(3)	0.0124(3)	0	0	0
Sb(4) ^b	0.0229(8)	0.0147(4)	0.0109(4)	0	0	0
Sb(5)	0.0325(4)	0.0158(3)	0.0260(4)	0	0	0
$M(1)^c$	0.0188(3)	0.0248(4)	0.0146(3)	0.0028(2)	0	0
$M(2)^d$	0.0244(9)	0.0239(7)	0.0164(8)	0	0	0
$\text{Nd}_6\text{Ge}_{3.6(1)}\text{Sb}_{12.4(1)}$						
Nd(1)	0.0137(2)	0.0111(2)	0.0125(2)	0	0	0
Nd(2)	0.0148(2)	0.0118(1)	0.01306(2)	0.0007(1)	0	0
Sb(1)	0.0133(3)	0.0138(2)	0.0138(3)	0	0	0
Sb(2)	0.0188(2)	0.0126(2)	0.0149(2)	0.0008(1)	0	0
Sb(3)	0.0159(3)	0.0210(3)	0.0135(3)	0	0	0
Sb(4) ^b	0.0205(9)	0.0140(4)	0.0117(4)	0	0	0
Sb(5)	0.0306(4)	0.0154(3)	0.0233(3)	0	0	0
$M(1)^c$	0.0157(3)	0.0197(3)	0.0154(3)	0.0017(2)	0	0
$M(2)^d$	0.024(1)	0.0255(9)	0.0168(9)	0	0	0

Table A-18. Anisotropic Displacement Parameters ^a (Å²) for La₆Ge_{2.8(1)}Sb_{13.2(1)},
Nd₆Ge_{3.6(1)}Sb_{12.4(1)}, and Gd₆Ge_{4.3(1)}Sb_{11.7(1)} (continued)

		Gd ₆ Ge _{4.3(1)} Sb _{11.7(1)}				
Gd(1)	0.0132(3)	0.0109(3)	0.0121(3)	0	0	0
Gd(2)	0.0146(2)	0.0122(2)	0.0129(2)	0.0006(2)	0	0
Sb(1)	0.0128(4)	0.0130(4)	0.0128(4)	0	0	0
Sb(2)	0.0164(3)	0.0124(3)	0.0136(3)	0.0005(2)	0	0
Sb(3)	0.0157(4)	0.0171(4)	0.0136(4)	0	0	0
Sb(4)	0.042(1)	0.0169(7)	0.0108(6)	0	0	0
Sb(5)	0.0269(6)	0.0174(5)	0.0250(6)	0	0	0
M(1) ^c	0.0153(5)	0.0166(5)	0.0157(5)	0.0009(3)	0	0
Ge(2) ^d	0.019(1)	0.036(4)	0.020(1)	0	0	0

^a The form of the anisotropic displacement parameter is: $\exp[-2\pi^2(h^2a^{*2}U_{11} + k^2b^{*2}U_{22} + l^2c^{*2}U_{33} + 2hka^*b^*U_{12} + 2hla^*c^*U_{13} + 2klb^*c^*U_{23})]$.

^b Occupancy fixed at 50%.

^b Site M(1) contains 61(3)% Ge(1), 39(2)% Sb(6) in La₆Ge_{2.8(1)}Sb_{13.2(1)}; 72(3)% Ge(1), 28(2)% Sb(6) in Nd₆Ge_{3.6(1)}Sb_{12.4(1)}; and 83(3)% Ge(1), 17(2)% Sb(6) in Gd₆Ge_{4.3(1)}Sb_{11.7(1)}.

^c Site M(2) contains 19(2)% Ge(2), 31(1)% Sb(7) in La₆Ge_{2.8(1)}Sb_{13.2(1)}; 36(2)% Ge(2), 14(1)% Sb(7) in Nd₆Ge_{3.6(1)}Sb_{12.4(1)}; and 50% Ge(2) in Gd₆Ge_{4.3(1)}Sb_{11.7(1)}. The remaining 50% represent vacancies.

Table A-19. Powder X-Ray Diffraction Data for $\text{ZrSi}_{0.7}\text{Sb}_{1.3}$ ^a

<i>hkl</i>	d_{obs} (Å)	d_{calc} (Å)	II_0 ^b	<i>hkl</i>	d_{obs} (Å)	d_{calc} (Å)	II_0 ^b
0 0 1	8.613	8.638	25	1 0 5	1.574	1.574	15
0 0 3	2.878	2.879	16	2 1 3	1.468	1.468	55
1 0 2	2.858	2.859	66	2 2 0	1.349	1.349	20
1 1 0	2.695	2.697	52	2 0 5	1.281	1.280	14
1 1 1	2.572	2.575	76	1 1 6	1.271	1.270	21
1 0 3	2.298	2.298	100	2 1 5	1.213	1.214	17
1 1 2	2.287	2.288	39	3 1 0	1.206	1.206	12
2 0 0	1.907	1.907	53	3 1 1	1.195	1.195	20
2 0 3	1.589	1.590	11	3 0 3	1.163	1.163	18
2 1 2	1.587	1.587	25	3 1 2	1.162	1.162	13

^a The cell parameters refined from the powder pattern, obtained on a Guinier camera at room temperature, are $a = 3.8146(6)$ Å, $c = 8.638(2)$ Å, $V = 125.69(4)$ Å³.

^b The intensities were calculated from the crystal structure of $\text{ZrSi}_{0.7}\text{Sb}_{1.3}$ with the use of the program LAZY-PULVERIX (Yvon, K.; Jeitschko, W.; Parthé, E. *J. Appl. Crystallogr.* 1977, 10, 73-74). Only those reflections with $II_0 > 10$ are listed.

Table A-20. Powder X-Ray Diffraction Data for ZrGeSb ^a

<i>hkl</i>	<i>d</i> _{obs} (Å)	<i>d</i> _{calc} (Å)	<i>I</i> / <i>I</i> ₀ ^b	<i>hkl</i>	<i>d</i> _{obs} (Å)	<i>d</i> _{calc} (Å)	<i>I</i> / <i>I</i> ₀ ^b
0 0 1	8.655	8.646	10	1 0 5	1.577	1.577	16
0 0 3	2.884	2.882	23	2 1 3	1.476	1.477	56
1 0 2	2.872	2.873	64	2 2 0	1.359	1.359	24
1 1 0	2.719	2.718	41	2 0 5	1.285	1.286	16
1 1 1	2.594	2.593	99	1 1 6	1.273	1.273	25
1 0 3	} 2.303	2.306	100	2 2 3	1.228	1.229	10
1 1 2		2.301	2.301	2 1 5	1.220	1.219	17
2 0 0	1.921	1.922	62	3 1 0	1.216	1.216	10
0 0 5	1.730	1.729	10	3 1 1	1.204	1.204	25
1 1 4	1.692	1.692	10	3 0 3	} 1.171	1.171	18
2 0 3	} 1.597	1.599	17	3 1 2		1.170	18
2 1 2		1.598	24				

^a The cell parameters refined from the powder pattern, obtained on a Guinier camera at room temperature, are $a = 3.8445(6)$ Å, $c = 8.646(2)$ Å, $V = 127.78(4)$ Å³.

^b The intensities were calculated from the crystal structure of ZrGeSb with the use of the program LAZY-PULVERIX (Yvon, K.; Jeitschko, W.; Parthé, E. *J. Appl. Crystallogr.* **1977**, *10*, 73-74). Only those reflections with $I/I_0 > 10$ are listed.

Table A-21. Powder X-Ray Diffraction Data for $\text{ZrSn}_{0.4}\text{Sb}_{1.6}$ ^a

<i>hkl</i>	d_{obs} (Å)	d_{calc} (Å)	I/I_0 ^b	<i>hkl</i>	d_{obs} (Å)	d_{calc} (Å)	I/I_0 ^b
1 0 3	2.965	2.966	62	3 1 4	1.580	1.580	10
1 1 2	2.836	2.834	85	2 1 5	1.577	1.577	18
2 1 0	2.691	2.689	94	1 2 4	1.504	1.504	11
2 1 1	2.594	2.592	64	3 2 2	1.467	1.467	35
1 1 3	2.375	2.375	100	5 1 1	1.360	1.360	20
3 0 1	—	2.367	11	5 1 2	—	1.322	10
2 1 2	2.354	2.354	11	2 2 5	1.298	1.299	20
1 0 4	2.309	2.309	19	1 1 7	1.291	1.292	10
3 0 2	2.181	2.182	55	4 1 5	1.263	1.264	24
0 2 0	1.982	1.982	42	2 3 0	1.243	1.243	12
0 1 5	—	1.748	13	1 3 3	1.206	1.207	17
2 0 5	1.719	1.719	21	1 1 8	—	1.149	10
1 2 3	1.648	1.648	23				

^a The cell parameters refined from the powder pattern, obtained on a Guinier camera at room temperature, are $a = 7.322(1)$ Å, $b = 3.9642(6)$ Å, $c = 9.734(1)$ Å, $V = 282.53(5)$ Å³.

^b The intensities were calculated from the crystal structure of $\text{ZrSn}_{0.4}\text{Sb}_{1.6}$ with the use of the program LAZY-PULVERIX (Yvon, K.; Jeitschko, W.; Parthé, E. *J. Appl. Crystallogr.* 1977, 10, 73-74). Only those reflections with $I/I_0 > 10$ are listed.

Table A-22. Anisotropic Displacement Parameters ^a (Å²) for ZrSi_{0.7}Sb_{1.3}, ZrGeSb, and ZrSn_{0.4}Sb_{1.6}

Atom	U_{11}	U_{22}	U_{33}	U_{12}	U_{13}	U_{23}
ZrSi _{0.74(2)} Sb _{1.26(1)}						
Zr	0.0058(2)	0.0058(2)	0.0045(2)	0	0	0
A ^b	0.0103(3)	0.0103(3)	0.0035(3)	0	0	0
Sb(2)	0.0055(2)	0.0055(2)	0.0056(2)	0	0	0
ZrGeSb						
Zr	0.0051(6)	0.0051(6)	0.0045(8)	0	0	0
Ge	0.0069(6)	0.0069(6)	0.0018(7)	0	0	0
Sb	0.0049(5)	0.0049(5)	0.0057(7)	0	0	0
ZrSn _{0.4} Sb _{1.6}						
Zr	0.0059(3)	0.0045(3)	0.0037(3)	0	-0.0001(2)	0
X(1) ^c	0.0078(3)	0.0057(3)	0.0036(3)	0	-0.0002(1)	0
X(2) ^c	0.0058(3)	0.0049(3)	0.0053(3)	0	0.0004(1)	0

^a The form of the anisotropic displacement parameter is: $\exp[-2\pi^2(h^2a^{*2}U_{11} + k^2b^{*2}U_{22} + l^2c^{*2}U_{33} + 2hka^*b^*U_{12} + 2hla^*c^*U_{13} + 2klb^*c^*U_{23})]$.

^b A contains 74(2)% Si and 26(1)% Sb(1).

^c Each site is occupied by 20% Sn and 80% Sb.